EXPLOITING GRAPHENE AS A THERAPEUTICS PLATFORM IN BIOLOGICAL SYSTEMS

A thesis submitted to the University of Manchester for the degree of Doctor of Philosophy in the Faculty of Biology, Medicine and Health

2016

Catriona McCallion
School of Health Sciences

FIGURES

TABLES

ABBREVIATIONS

AFM	Atomic force microscopy
ANOVA	Analysis of variance
ATP	Adenosine triphosphate
Boc	*Tert*-butyloxycarbonyl
BSA	Bovine serum albumin
CMC	Critical micelle condition
CLL	Chronic lymphocytic leukaemia
CLP	CNT-poly(lactide)
CNTs	Carbon nanotubes
Cy5	Cyanine 5
D	Diffusion coefficient
DCM	Dichloromethane
DFT	Density functional theory
DIPEA	N,N-Diisopropylethylamine
DLS	Dynamic light scattering
DMF	N,N-Dimethylformamide
DMSO	Dimethyl sulfoxide
DNA	Deoxyribonucleic acid
DOX	Doxorubicin
DPPC	Dipalmitoylphosphatidylcholine
EC_{50}	Drug concentration for half maximal response
EDC	*N*-(3-Dimethylaminopropyl)-*N'*-ethylcarbodiimide hydrochloride
EPR	Enhanced permeability and retention
FA	Folic acid
FAM	Fluorescein reporter
FBS	Foetal bovine serum
FDA	Federal drug association
FLG	Few layer graphene
FSC/SSC	Forward scatter counts/side scatter counts
GFNs	Graphene family of nanomaterials
GNR	Graphene nanoribbon
GONR	Graphene oxide nanoribbon
GO	Graphene oxide
GRAS	Generally recognised as safe
GrLP	h-Gr-PEG-poly(lactide)
GTrGO	Green tea rGO
h-Gr	Hydroxylated graphene
HMBA	N,N'-hexamethylenebisacrylamide
HRP	Horse radish peroxidase
HRTEM	High resolution TEM
HTrGO	High temperature rGO
HUVEC	Human vein endothelial cells
HZrGO	Hydrazine rGO
IC_{50}	Inhibitor concentration that reduces binding by half
IFN	Interferon
IPA	Isopropyl alcohol
LDH	Lactate dehydrogenase

mAb	Monoclonal antibody
MB	Molecular beacon
MRI	Magnetic resonance imaging
mRNA	Messenger RNA
MS	Mass spectroscopy
MWCNTs	Multi-walled carbon nanotubes
MWCO	Molecular weight cut-off
NaC	Sodium cholate
NIRF	Near infrared fluorescence
NLS	Nuclear localisation signal
NMP	*N*-methyl-2-pyrrolidone
NMR	Nuclear magnetic resonance
NO	Nitrous oxide
OTE	Off-target effect
OVA	Ovalbumin antigen
PBMCs	Peripheral blood mononuclear cells
PBS	Phosphate buffered saline
PBS/T	PBS-Tween
PCNA	Proliferating cell nuclear antigen
PDMAEMA	Poly(2-dimethylamino-ethylmethacrylate)
PDNA	Plasmid DNA
PEG	Polyethylene glycol
PEI	Polyethyleneimine
PHA	Phytohaemagglutanin
PI	Propidium iodide
PLA	Poly(lactide)
PTFE	Polytetrafluoroethylene
PTX	Paclitaxel
PVDF	Polyvinylidene difluoride
PVP	Polyvinylpyrrolidone
RBF	Round bottom flask
REC	Research Ethics Committee
RES	Reticuloendothelial system
rGO	Reduced graphene oxide
R_h	Hydrodynamic radius
RICS	Raster image correlation spectroscopy
RNA	Ribonucleic acid
ROI	Region of interest
ROS	Reactive oxygen species
RPMI	Roswell Park Memorial Institute medium
RT	Room temperature
TEMED	Tetramethylethylenediamine
SDBS	Sodium dodecylbenzenesulfonate
SDS	Sodium dodecylsulfate
SDS-PAGE	Sodium dodecylsulfate polyacrylamide gel electrophoresis
SEM	Scanning electron microscopy
SERS	Surface enhanced Raman spectroscopy
SGNFs	Stacked graphene nanofibres
siRNA	Short interfering RNA
SPECT/CT	Single photon emission computed tomography
SS	Disulphide bond
SWCNTs	Single walled carbon nanotubes
TBS	Tris-buffered saline

TFA	Trifluoroacetic acid
TEM	Transmission electron microscopy
Tris	Tris(hydroxymethyl)aminomethane
UV-Vis	Ultraviolet-Visible spectroscopy
uwGO	Unwashed GO
wGO	Washed GO
Val	Valine
VEGF	Vascular endothelial growth factor
XPS	X-ray photoelectron spectroscopy

Abstract

Since its isolation in 2004, the research landscape around graphene and other 2D materials has expanded rapidly and now encompasses fields as diverse as electronic engineering and drug delivery. For biomedical applications, one of the most desirable properties of the graphene family of nanomaterials (GFNs) is their 2D geometry; the high surface area to volume ratio that is characteristic of nanomaterials is taken to its extreme in a material that can be viewed as being entirely surface. This particular property alongside the versatility with which they may be functionalised both makes GFNs well positioned to function as the foundation of highly tailored and multifunctional therapeutics platforms.

In this project, two GFN types, namely pristine graphene and graphene oxide, were prepared to form suspensions suitable for application to therapeutics delivery. Firstly, experiments using four essential amino acids with pristine graphitic material were undertaken to assess whether graphene flakes could be suitably exfoliated and suspended using sonication in the presence of aqueous solutions of these biocompatible molecules. A positive correlation was found between the hydrophobicity of the amino acid and the presence of one or more aromatic rings in the amino acid, and the efficacy of exfoliation both in terms of concentration achieved in suspension and flake thinness. However, the system itself was found to be highly complex, both with regards to the sonication used to exfoliate the graphitic flakes, and the interactions between the amino acids and the flakes. These considerations limited the wider applicability of this form of graphene preparation for therapeutics delivery applications.

Secondly, work was performed on graphene oxide (GO), a GFN far more studied in the literature, but notoriously heterogeneous. Therefore much of the work completed focused on its characterisation. A combination of established and novel fluorescence-based characterisation methods were used to fully characterise three preparations of GO, before preliminary experiments were undertaken to test their interactions with cell components. The work showed that the inherent fluorescence of GO can be exploited to improve suspension characterisation; raster image correlation spectroscopy (RICS) was used to measure the apparent hydrodynamic

radii of the flakes and flow cytometry was used to provide insight into the interactions between GO flakes and serum components. Preliminary cellular experiments confirmed that flow cytometry could be also employed to assess particular graphene characteristics in the context of cell culture, demonstrating the relatively low toxicity of PEGylated GO compared to unfunctionalised GO.

Finally, as the therapeutics target for this project was leukaemia, a targeting ligand was designed and synthesised that could bind to CXCR4 – a receptor that is overexpressed on CLL B-cells, as well as many other cancer types. The ligand was synthesised such that it could easily be attached to GO, however its molecular structure is flexible enough that it can be attached to a number of different therapeutics materials. It was confirmed using both competition and functional assays that the molecule was antagonistic, and was able to deliver a conjugated fluorescent molecule specifically to the CXCR4 receptors on primary CLL B-cells.

The work presented in this thesis illustrates the complexity that affects the use of GFNs in biomedicine, but also confirms the potential for their future development. The field is still young, and therapeutics delivery is likely to benefit from advances in the preparation of pristine graphene, and from methods to minimise the heterogeneity of GO. These steps will support a route towards clinical application. In addition, as the field of 2D materials expands, other materials with enviable surface area to volume ratios may come to the fore. Furthermore, this thesis has shown the value of exploring novel approaches to the characterisation of GFNs, and has identified approaches that may be exploited to improve applications of GFNs in biomedicine. Additionally, the aim of using GFNs as a platform for a multifunctional therapeutics delivery vehicle was developed with regards to the attractive CXCL12/CXCR4 axis, which is relevant in a large number of disease states including over 20 cancers, by demonstrating a flexible targeting ligand that could be used to exploit the CXCR4 receptor as a drug delivery target.

DECLARATION

I hereby declare that no portion of the work referred to in this thesis has been submitted in support of an application for another degree or qualification of this or any other university or institute of learning.

COPYRIGHT STATEMENT

i. The author of this thesis (including any appendices and/or schedules to this thesis) owns certain copyright or related rights in it (the "Copyright") and she has given The University of Manchester certain rights to use such Copyright, including for administrative purposes.

ii. Copies of this thesis, either in full or in extracts and whether in hard or electronic copy, may be made **only** in accordance with the Copyright, Designs and Patents Act 1988 (as amended) and regulations issued under it or, where appropriate, in accordance with licensing agreements which the University has from time to time. This page must form part of any such copies made.

iii. The ownership of certain Copyright, patents, designs, trademarks and other intellectual property (the "Intellectual Property") and any reproductions of copyright works in the thesis, for example graphs and tables ("Reproductions"), which may be described in this thesis, may not be owned by the author and may be owned by third parties. Such Intellectual Property and Reproductions cannot and must not be made available for use without the prior written permission of the owner(s) of the relevant Intellectual Property and/or Reproductions.

iv. Further information on the conditions under which disclosure, publication and commercialisation of this thesis, the Copyright and any Intellectual Property and/or Reproductions described in it may take place is available in the University IP Policy (see http://documents.manchester.ac.uk/DocuInfo.aspx?DocID=2442), in any relevant Thesis restriction declarations deposited in the University Library, The University Library's regulations (see http://www.library.manchester.ac.uk/about/regulations) and in The University's policy on Presentation of Theses.

Acknowledgements

I'd firstly like to thank my supervisors, Dr Alain Pluen, Dr Sasha Golovanov and Dr John Burthem for their patience, guidance and endless coffees – John in particular ensured that I was never caffeine-free. I'd also like to thank Dr Karen Rees-Unwin and Dr Julie Adams for their kindness and patience during all their time spent teaching this physicist about cell biology. I'd like to give a special thank you to Dr Andrew Booth for all of the help and guidance during my foray into organic chemistry and for generally keeping me afloat during much of my PhD. I'd also like to thank Dr Aisling Miller, Tom Fallows, Anna Peters, Rob Woolfson and Peter Youle for the emergency chemistry conversations and willingness to lend equipment.

To all my friends – both inside science and out – who have been lovely and made Manchester a lovely place to be. In particular, Eve Blumson and Stacy Panova who have kept me sane through the majority of my PhD, and Amelia Bayliss for her endless support, wine, food and for generally being an amazing person. To all the NoWNanos for being awesome, and to Jo and everyone at aerial silks who helped me totally escape science at least once a week by encouraging me to fight gravity instead.

Finally, I'd like to thank my family who have loved and supported me throughout my education; my amazing partner, Markus Krumins, for all his love and support throughout my PhD, and for just making my life better; and the Krumins family for their warmth, kindness and incredible food.

RECENT PUBLICATIONS RELEVANT TO THIS STUDY

Presented in full as the introduction to this thesis:

[1] Graphene in therapeutics delivery: Problems, solutions and future opportunities
McCallion, C., Burthem, J., Rees-Unwin, K., Golovanov, A., Pluen, A., *Eur. J. Pharm. Biopharm*, **2016**, 104, 235-250

1 Introduction

European Journal of Pharmaceutics and Biopharmaceutics 104 (2016) 235–250

Contents lists available at ScienceDirect

European Journal of Pharmaceutics and Biopharmaceutics

journal homepage: www.elsevier.com/locate/ejpb

Review article

Graphene in therapeutics delivery: Problems, solutions and future opportunities

Catriona McCallion [a], John Burthem [c], Karen Rees-Unwin [c], Alexander Golovanov [b], Alain Pluen [a,*]

[a] Manchester Pharmacy School, University of Manchester, Manchester, UK
[b] Manchester Institute of Biotechnology, Faculty of Life Sciences, University of Manchester, Manchester, UK
[c] Institute of Cancer Sciences, University of Manchester, Manchester, UK

ARTICLE INFO

Article history:
Received 17 November 2015
Revised 12 April 2016
Accepted in revised form 18 April 2016
Available online 22 April 2016

Keywords:
Graphene
Drug delivery
Graphene oxide
Targeted drug delivery
Graphene nanomaterials
GFN
Gene delivery

ABSTRACT

Graphene based nanomaterials are being used experimentally to deliver therapeutic agents to cells or tissues both *in vitro* and *in vivo*. However, substantial challenges remain before moving to safe and effective use in humans. In particular, it is recognised that graphene molecules undergo complex interactions with solutes, proteins or cellular systems within the body, and that these interactions impact significantly on the behaviour or toxicity of the molecule. Approaches to overcome these problems include modification of the graphene or its combination with other molecules to accentuate favourable characteristics or modify adverse interactions. This has led to an emerging role for graphene as one part of highly-tailored multifunctional delivery vehicles. This review examines the knowledge that underpins present approaches to exploit graphene in therapeutics delivery, discussing both favourable and unfavourable aspects of graphene behaviour in biological systems and how these may be modified; then considers the present place of the molecule and the challenges for its further development.

Contents

* Corresponding author.
E-mail address: alain.pluen@manchester.ac.uk (A. Pluen).

http://dx.doi.org/10.1016/j.ejpb.2016.04.015
0939-6411/

1. Introduction

Since the isolation of graphene in 2004, potential uses of the material have expanded rapidly, and a wide range of biomedical applications are now proposed [1–23]. In this review, the physical and chemical properties of what will be referred to as *the graphene family of nanomaterials (GFNs)* [24] will be reviewed in the context of their potential role in therapeutics delivery – which includes drugs, biopharmaceuticals and genetic material.

The use of graphene in therapeutics delivery is based upon its particular properties. Its high surface-area to volume ratio, polyaromatic structure and the ease with which various forms can be functionalised offers capacity and flexibility for cargo loading, transport and targeting to tissues. Additionally, the ability to combine hydrophilic and hydrophobic regions on the surface of GFN flakes supports both their solubility within aqueous environments and their subsequent interaction with lipids in cell membranes. However, it is also recognised that graphene may have potential adverse interactions within biological environments that are highly relevant to biomedical applications. In particular, interactions between graphene and protein elements in biological fluids may significantly affect the physical properties of the molecule, potentially inducing damaging responses by the host immune system, while the membrane interactions and chemical properties of graphene have the potential to cause direct toxicity to target cells or to normal "bystander cells".

The review examines those qualities of GFNs that may make them attractive as therapeutics delivery vehicles, before considering how the varied properties of different graphene forms may affect their performance. Present and possible future applications in drug delivery are then considered.

2. Properties of graphene

2.1. The graphene family of nanomaterials

Graphene was first isolated using mechanical exfoliation in the now famous "scotch-tape" method [25] and is the first truly two-dimensional material. Each carbon atom of pristine graphene is bound to three others in a flat structure (sp^2 hybridised). This structure is the basis of many carbon materials, from graphite to carbon nanotubes (CNTs) and fullerenes, and underlies the distinctive honeycomb lattice structure of the molecule [16,28] (Fig. 1). The benzene-like structure of the hexagonal components of the lattice allows it to be thought of as a giant aromatic poly-molecule [16]. Even without further functionalisation, this structure confers properties that are useful in therapeutics delivery: aromatic molecules may bind to graphene through non-covalent interactions between their carbon rings (π–π stacking), and the large relative surface-area of the 2D geometry permits a single graphene flake to be decorated with a raft of different aromatic groups [26]. For pristine graphene, π–π stacking and hydrophobic interactions are the major source of binding for drugs and other molecules; however, for other graphene forms the additional presence of chemical functional groups provides a greater range of possible interactions (Fig. 3) [26,27].

2.2. Structural features and solubility of graphene

For use in therapeutics delivery, GFN flakes must be dispersed within biological fluids. In its pristine form graphene is hydrophobic; therefore, solubilisation is achieved through exfoliation of graphite layers in the presence of a non-polar solvent or surfactants

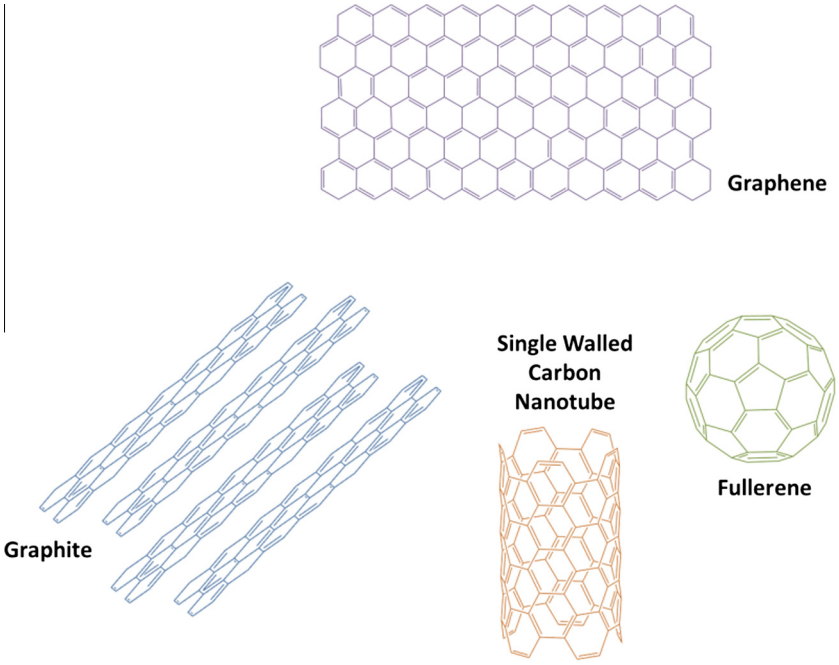

Fig. 1. sp^2 hybridization in graphene and other carbon allotropes. The honeycomb structure recognisable in the above materials derives from the sp^2 hybridized bonds between their constituent carbon atoms; graphene is often described as the structural precursor to graphite, CNTs and fullerenes.

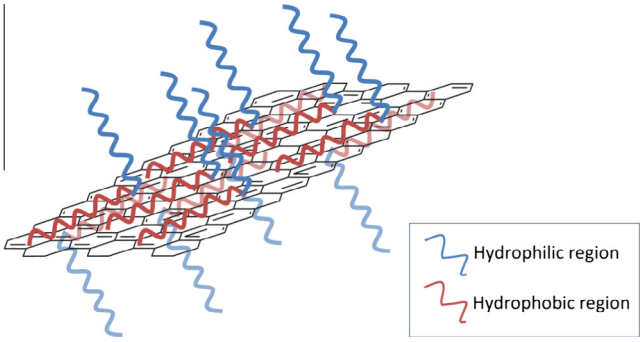

Fig. 2. Graphene solubilised using surfactant molecules; the hydrophobic regions cover most of the graphene flake surface, while the hydrophilic tail regions stretch out into the aqueous solution in which the flakes are suspended. The resultant flake's size and geometry will be significantly changed compared to a single bare graphene sheet.

[28]. Graphene prepared in this way retains particular physicochemical properties that include high electrical conductivity, low defect density, and sharp edges, but the graphene is generally very polydisperse, both in terms of the lateral dimensions of the flakes and the number of layers contained. To produce more uniform samples requires additional techniques such as centrifugation sectioning. Moreover, where surfactant is used, the majority of the polyaromatic graphene-surface becomes covered by surfactant molecules, potentially causing steric interference with other functional molecules and changing the geometry of the flakes by causing them to become thicker (Fig. 2). Similarly, residual molecules from non-polar solvents must be removed when transferring the flakes from that solvent into water, and a method of solubilising the flakes in water must still be found. Finally, both surfactants and residual non-polar solvent molecules adsorbed on the flake surface may contribute significantly to the toxicity of the preparation.

For these reasons, the introduction of pristine graphene in biomedical applications has been relatively limited, and alternative graphene forms have been preferred.

At present the most common preparation used is graphene oxide (GO). This preference derives in part from its favourable solubility, which is in turn due to its surface chemistry (for a detailed account see [27,29]). In brief, GO is predominantly prepared using a standard or modified Hummers' method, employing prolonged exposure to strong oxidants such as sulphuric acid, sodium nitrate and potassium permanganate, applied to bulk graphite, where the oxidation also aids the exfoliation of the graphite [27,30]. The chemical characteristics of the GO flakes are most commonly described by the Lerf–Klinowski model [27] (Fig. 3). That model considers the GO flake to be comprised of a typical flat sp^2 bonded honeycomb lattice with occasional defects, interrupted by sp^3 bonds that allow epoxides and alcohols to project from the planar surface, while flake edges are populated with carboxylic acids (Fig. 3). An alternative recent model agrees that oxygenated functional groups (mostly carboxylic acids) again predominantly occur on the edges of the flake, but suggests that the surface of the GO is

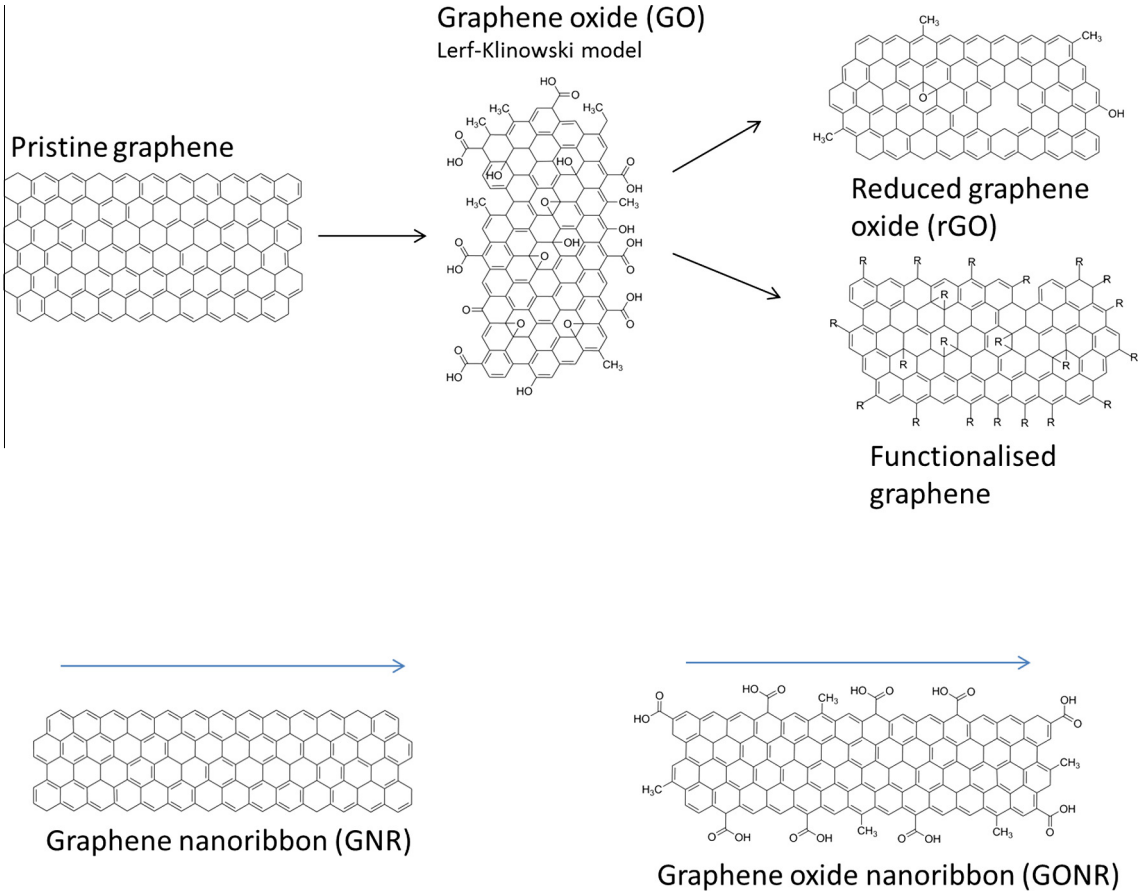

Fig. 3. Commonly used graphene forms. Pristine graphene is hydrophobic and so is often solubilised using the Hummer's method so that it is decorated with oxygenated functional groups. Graphene oxide is quite easy to prepare and so is often the precursor to other functionalised GFNs, or reduced to prepare a material that approximates pristine graphene. Graphene nanoribbons are often prepared by 'unzipping' carbon nanotubes, resulting in graphene with a very high aspect ratio. It has been shown that aspect ratio is one of the physicochemical properties of graphene that changes the behaviour of cells to which they are exposed.

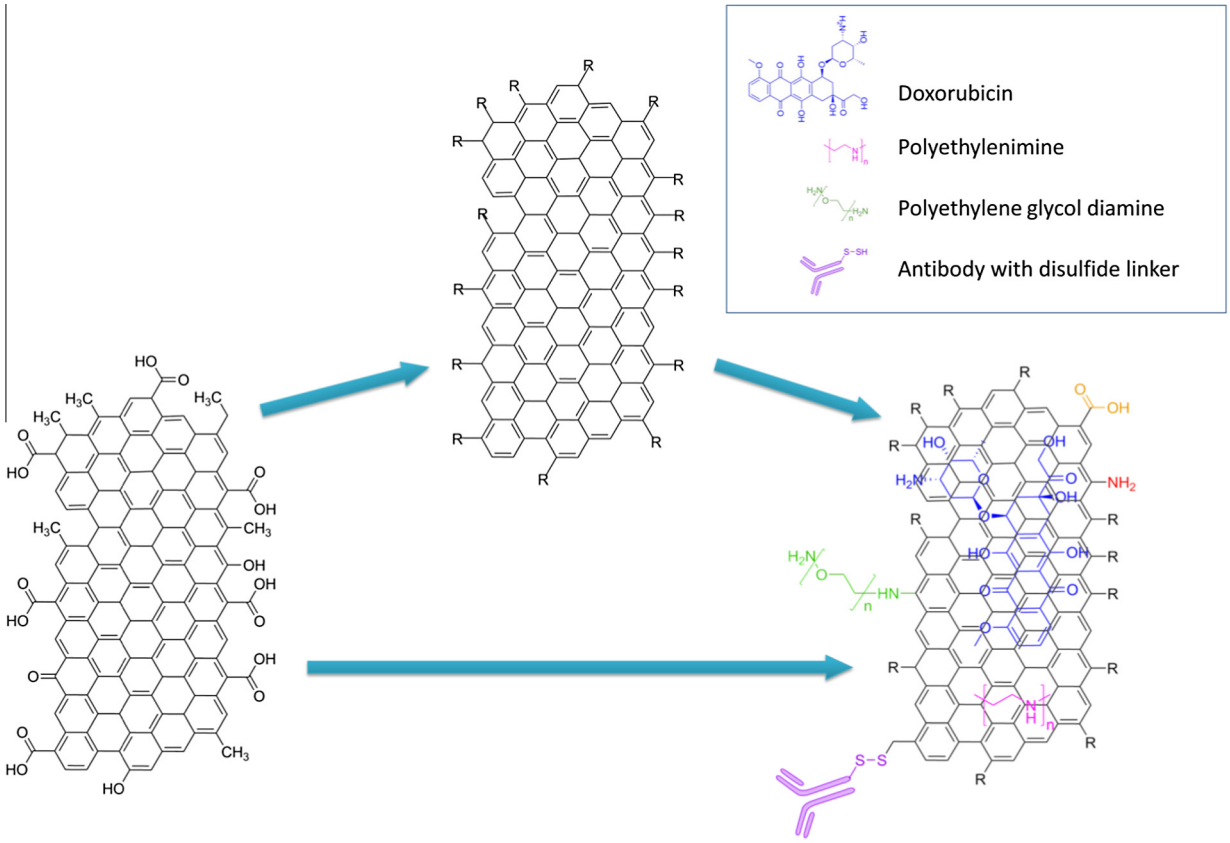

Fig. 4. GO loading and functionalisation: One of the benefits of using graphene oxide is the combination of a polyaromatic basal plane and the functional groups that extend from it. Once GO has been prepared, other molecules may be easily attached - hydrophobically, electrostatically, *via* π–π interactions or covalently; alternately, the functional groups may be chemically altered. The figure illustrates some of the myriad cargoes that have been loaded onto GO/functionalised graphene using the above techniques.

covered with highly oxidised aromatic carbonaceous fragments (oxidative debris) which effectively act as stabilising agents, solubilising the flakes in water [29]. Both models are supported by results of high-resolution transmission electron microscopy (HRTEM) [31].

2.3. Graphene as a therapeutics delivery vehicle

An ideal delivery vehicle will target therapeutic agents to their site of action and protect them from degradation, thereby reducing off-target effects (OTEs) and dilution, and potentially increasing efficacy [32–36]. This requires a stable and inert vehicle whose physicochemical properties permit its transport through complex physiological environments, while specific characteristics ensure cell-specific uptake and delivery [35,36]. Present trends favour highly tailored nanoparticles with control of each physicochemical property, from size, shape and zeta potential, through to nanoscale roughness.

In these respects, graphene may provide advantages over other carbon nanomaterials. GFNs may have lower toxicity [37–39], and highly flexible physicochemical properties that allow the different functional groups of the molecule to be modified and perform a range of different tasks [10,15,16,40–43] (Fig. 4). Many applications employ GO prepared by Hummer's method. The GO formed by this method retains many of the useful structural features of pristine graphene, including low dimensionality and the retention of isolated patches of the honeycomb structure that allow the attachment of water-insoluble drugs. The oxygenated functional groups including hydroxyls, epoxides and carboxyls render the material inherently hydrophilic reducing the need for additional solubilisation, and provide opportunity to bind additional functional molecules through covalent bonding or electrostatic interactions [15,26,27,44] (see Fig. 4). This functional flexibility is central to the role of GO in therapeutics delivery. However, this same flexibility also introduces a significant complexity: It is recognised that GO prepared using similar techniques by different laboratories may contain graphene flakes of polydisperse dimensions and layer number, and this may result in the reporting of contradictory results in apparently comparable studies [24,45]. Furthermore, full oxygenation of the graphene lattice is thermodynamically unfavourable; therefore, GO is heterogeneous in its surface chemistry and functionalisation may be subtly different between samples [27,31]. Finally, during the design of functionalised graphene, any modification made to the flake structure potentially alters other intrinsic properties, and may cause otherwise desirable features to become lost or masked as the modified nanoparticle effectively becomes a new material [36,46]. For instance, the addition of large polymers will increase the thickness of graphene flakes and may decrease their lateral sizes [47], producing a more spherical or globular nanoparticle, rather than the 2D geometry of unmodified graphene.

Despite improved understanding of the molecule therefore, predicting and controlling the behaviour of graphene in different environments remains a substantial challenge for investigators. To address these issues, methods are being developed to produce highly purified GO suspensions with increased biocompatibility and reduced polydispersity, together with the development of detailed protocols that describe the preparation of GO nanocomposites for biomedical applications [37,48]. In this review we have, where possible, sought to identify sources for any apparent

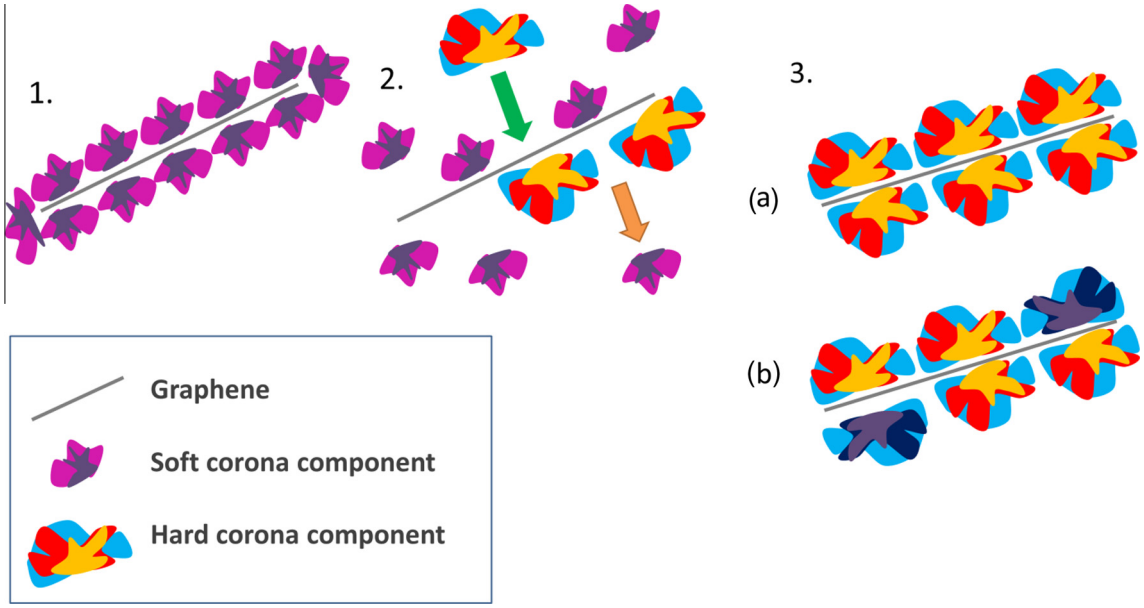

Fig. 5. Schematic of the formation of the protein corona about a flake of graphene (Vroman model). 1. Initially the soft corona is formed, made up of abundant proteins with high dissociation constants, i.e. are weakly bound. 2. Gradually the soft corona is replaced with less abundant proteins that have lower dissociation constants, making up the hard corona. 3. The hard corona may be made up of a complex mixture of proteins, that can vary depending on the region of the body and the physiological state of the human or animal into which the flakes have been introduced.

contradictions in the reported biological effects of different graphene forms or preparations, and to identify emerging the consensus views that presently drive research in this area.

3. The behaviour of graphene within biological environments

3.1. Graphene and biological fluids

Within cell culture media or biological fluids, it is recognised that all forms of graphene may potentially interact with components of the physiological media. These effects may dramatically alter the size, shape or surface chemistry of the 2D sheet [49,50]. Two aspects have particular importance: the behaviour of graphene as a colloid, and the formation on the graphene surface of a protein corona.

GFN suspensions are colloids; therefore, their ability to remain suspended in solution depends fundamentally on the interaction between their intrinsic surface chemistry and the chemical make-up of the suspending media. This problem is critical in physiological media where salts, ions and biomolecules may all interact with the graphene resulting in flocculation or aggregation of the previously suspended flakes. For example, while GO is known to be highly stable in water, when transferred to cell culture media or buffer it frequently undergoes aggregation [7,15,18,48,51] as ions and salts in the media screen its negative surface charge [52] (Fig. 5). Physical factors such as lateral size and flake thickness contribute to this stability. Smaller flakes have a lower probability of inter-flake interaction and aggregate less frequently [53]. Solubility may therefore be promoted by extensive washing and centrifugation, yielding suspensions of thin and laterally small flakes that contain fewer aggregates [37]. Increasingly however, additional functionalisation is also employed to stabilise GFNs in the presence of buffering agents. The most commonly used materials are PEG [10,49,52,54–57], chitosan [7,42,58,59], dextran [43,60,61] and serum proteins [62].

The formation of a protein corona is also a substantial complicating factor. When a nanoparticle is introduced to the body a protein corona forms as serum proteins adsorb to its surface. For GFN flakes this process is dependent on surface features that include chemistry, geometry and charge [63,64], as well as the proteins present and their respective concentrations [49,52,63,65]. The protein corona is considered to be formed of two components – the hard corona and the soft corona (Fig. 5). The soft corona is made up of highly abundant but weakly interacting proteins, whereas the hard corona is made up of less abundant proteins that have a higher affinity for the nanoparticle surface [64,66]; the soft corona that forms initially may become replaced over time through competitive binding [64]. The development of a corona may have positive effects – particle stability may be enhanced since proteins are predominantly adsorbed *via* their hydrophobic regions to the basal plane of the flake, with their charged hydrophilic regions directed to the exterior, and specific proteins have been used to coat GFNs before introducing them into physiological media [62,67,68]. However, adverse interactions also occur affecting biodistribution or interaction with cells of the immune system [52,64,65,69] or complement system [49,65], particularly in the case of proteins of the complement system. This latter interaction is one of the most significant problems associated with the formation of protein corona, and will be reviewed in the next section.

3.2. Inflammatory and immune responses to graphene

As with other assessments of the graphene–biological interface, host responses to different GFNs often appear contradictory. However it is clear that adverse systemic-responses may be evoked by graphene, and that these responses may be evoked either by GFN itself, or by any modifications made to it. The complexity of potential inflammatory interactions is illustrated by effects involving the protein corona (Section 3.1): Tan et al. [49] showed that in its native form, GO may bind the complement protein C3 which may then be cleaved inducing activation of the complement cascade. However following PEGylation of GO, steric repulsion hindered the attachment of larger proteins – modifying the nature of the protein corona such that the only detectable complement protein attached was C3/C3a(des-Arg). This process was reported to impair the normal interaction between C3a and its receptor,

potentially reducing any adverse complement-response to the graphene flake [53]. However, effects of the protein corona may be modified by any disease state in the recipient, potentially affecting outcome: Hajipour et al. [66] demonstrated that GO flakes exposed to serum proteins from patients experiencing a range of different disease states, induced different toxicities when introduced to cells *in vitro*.

Beyond the interaction with the protein corona, GO and pristine graphene are both recognised to be ingested by macrophages, inducing cell activation and secretion of pro-inflammatory cytokines [70–73]. These effects depend significantly on the geometry of the graphene flakes used. It has repeatedly been shown that the inflammatory response to graphene preparations becomes more pronounced as lateral flake-dimensions increase both *in vitro* and *in vivo*. In a study involving GO flakes of two distinct dimensions (approximately 350 nm and 2 μm), it was found that the larger flakes provoked a significantly increased secretion of inflammatory cytokines by macrophage cell lines *in vitro* [74]. Similarly *in vivo*, large flake size was shown to induce a more significant influx of lymphocytes and macrophages into adipose tissues following subcutaneous injection. TEM study revealed wrinkles in the structure of larger flakes following phagocytosis, and it was postulated that these forms are more chemically reactive since the bonds between carbon atoms in these regions become bent, causing the electron clouds of the carbon atoms to fall outside of the plane of the flake [80]. Such effects may differ however according to recipient species and the dose interval employed. The secretion of pro-inflammatory cytokines may be less marked in human cells [73] than in murine macrophages [70–72]; in a mouse model, multiple doses of small GO flakes resulted in the accumulation of inflammatory cells within hepatic tissues that were not observed with other flake size or dosing strategies [75].

The effects of graphene extend also to the adaptive immune system, where graphene has been shown to suppress interactions between dendritic cells and T lymphocytes [76]. Using an ovalbumin antigen (OVA) system, bone-marrow dendritic cells were used to stimulate T-lymphocytes in the presence of either GO or fullerenes (unfunctionalised or TRIS-functionalised). Low doses of fullerenes (6.25 μg/mL) increased IL-2 secretion by T-cells, whereas GO significantly reduced the T-cell activation at all concentrations. The authors used molecular modelling to demonstrate that GO strongly interacts with the LMP7 molecule (a critical immunoproteasome subunit) through charged residues; the corresponding interaction with the fullerenes was far weaker, being solely dependent on hydrophobic and π–π interactions, and was restricted by the smaller lateral dimensions of the fullerene [76]. Together, these studies highlight the importance of graphene preparation, cell model and experimental approach when evaluating graphene in a biological context.

Functionalisation of GFN flakes may be used to modify cell-induced inflammatory or immunological effects. Zhi et al. [77] coated GO flakes with polyvinylpyrrolidone (PVP), comparing the effects of native GO and PVP-GO *in vitro* using macrophages and immature dendritic cells (DCs) from healthy human volunteers. Both GO and PVP-GO were found to activate immature DCs, inducing dose-dependent maturation, up-regulation of activation markers, and secretion of inflammatory cytokines, causing dose-dependent release of pro-apoptotic cytokines by the T-lymphocytes. In each case however, native GO produced a more significant response than PVP-GO [77]. More recently, Paul et al.

Table 1
A summary of important results on immunogenicity of different graphene forms.

Refs.	Functionalisation	Geometry	Concentration	Response
Immunotoxicity				
[70]	Pristine graphene	150–200 nm Few layer	20 mg/kg; (murine model)	IL2, IL4, IL13, TGFB1 & TNF-α overexpression
[72]	Pristine graphene + pluronic F108 (1%)	10–100 s nm Few layer	20 μg/mL; primary murine macrophages & RAW264.7	IL-1α, IL-6, IL-10, TNF-α and GM-CSF, MCP-1, MIP-1α, MIP-1β & RANTES upregulation
[49]	GO	⩽3 μm 1–2 layers	0.4 mg/mL; primary human serum	Non-specific adsorption of serum proteins → complement cascade
	GO-PEG (biotin)	10–50 nm 1–2 layers	0.4 mg/mL; primary human serum	Specific adsorption: C3a(des-Arg), PF4, vitronectin, clusterin, thrombin & HRG
[71]	GO	⩽3 μm Few layer	5 or 100 μg/mL; RAW 264.7	TLR signalling cascades, IL-2, IL10, IFN-γ, TNF-α secretion
		10–100 s nm Few layer	5 or 100 μg/mL; RAW264.7	
[73]	GO	1.32 μm 270 nm	1–100 μg/mL; primary human macrophages & primary murine macrophages	Murine cells: 25 μg/mL – significant IL1β secretion Human cells: 100 μg/mL – CD86 expression Murine cells: 25 μg/mL – significant CD86 expression; 50–100 μg/mL – significant TNFα
		130 nm		Human cells: 100 μg/mL – CD86 expression Murine cells: 25 μg/mL – significant CD86 expression; 25–100 μg/mL – significant TNFα expression; 25–50 μg/mL – significant IL1β secretion
[74]	GO	2 μm	2 μg/mL; primary murine macrophages; subcutaneous injection (murine model)	TNF-α, TNF-γ, MCP and IL-6: significant secretion increase Significant migration of inflammation cells after 21 d
		350 nm		Inflammatory cytokines: no significant increase Some migration of inflammation cells after 21 d
[76]	GO	100 nm–μm	1–25 μg/mL; bone marrow-derived dendritic cells	Reduction in dendritic cells' stimulation of T-cells after OVA exposure
[83]	GO	nm to μm range Few layer	25–100 μg/mL; primary human dendritic cells & primary T-lymphocytes	100 μg/mL: significant TNF-α and IL-1β increase 25–100 μg/mL: significant IL-6 increase
	GO + polyvinylpyrrolidone (PVP)	100 s nm Few layer; 2.5 nm thick		50–100/mL: significant IL-6 increase

[78] prepared an injectable hydrogel-GO nanocomposite, in which the GO flakes were additionally functionalised with polyethylenimine (PEI), for the delivery of vascular endothelial growth factor (VEGF) post-myocardial infarction. The nanocomposite was tested *in vivo*, in an immunocompetent mouse model, and it was found that the composite produced negligible immunogenicity. It was suggested that the embedding of the GO flakes in a hydrogel caused a controlled release, which is akin to administering multiple low doses of the GO nanocomposite over time; the results demonstrate the potential of the method to minimise unwanted side effects while avoiding repeated administration. Sasidharan et al. [79] also demonstrated that functional modifications significantly modify immune responses observed *in vivo*. Employing few-layer pristine graphene flakes (*p*-FLGs) prepared using the arc discharge method, then used directly or functionalised with either carboxyl groups (FLG-COOH) and PEGylated (PEG-FLGs), the three preparations of flakes were administered to Swiss albino mice, and immunological and inflammatory cytokines were monitored 1 and 8 days following administration. All preparations led to acute altered expression of genes associated with inflammation and immune response. On day 1 almost all the gene expression levels were up-regulated – most significantly by *p*-FLGs – whereas on day 8, many had been down-regulated, and in those treated with FLG-PEG most gene-expression levels resembled the control at 8 days post-treatment. Histological samples following *p*-FLG and FLG-COOH exposure also showed evidence of inflammation, even after 90 days, whereas PEG-FLG did not.

A summary of immunogenic responses to GFNs reported in the literature is presented in Table 1.

3.3. Interaction of graphene with the blood components

Compatibility with blood components is required for effective drug-delivery in many contexts. A range of studies have therefore addressed this aspect.

GFNs can interact strongly with cell membranes, and may induce membrane-damage through the formation of reactive oxygen species (ROS). Red blood cells lack significant repair capability and have reduced capability to respond to oxidative stress. The premature breakdown of red cells (haemolysis) is therefore a sensitive indicator of damage induced by graphene [61,80–82]. Sasdiharan et al. [83] compared pristine graphene with GO; the pristine graphene was prepared using direct-current arc discharge evaporation of graphite (forming flakes with lateral dimensions in the hundreds of nanometres and sub-nanometre thicknesses), while to prepare the GO the pristine-graphene flakes were refluxed in nitric acid. Both GO and pristine graphene were found to aggregate in cell culture media, and the aggregates clustered around the erythrocytes on TEM images. However, neither preparation invoked significant haemolysis in the tested concentration range of 0–75 μg/mL. By contrast, Liao et al. [8] compared the haemocompatibility of GO, rGO and chitosan-coated GO: the GO was produced using a modified Hummers' method and rGO was produced by subjecting the GO to hydrothermal treatment at low pH (both being significantly different methods to those used by Sasidharan et al. [84]). Each preparation was observed to aggregate; however, in this case all samples invoked haemolysis, even at concentrations less than 50 μg/mL. This latter result was confirmed by other groups using a modified Hummers' method to prepare their suspensions [85]. When optical microscopy was used to evaluate graphene-induced morphological changes in erythrocytes exposed to a range of flake thicknesses and lateral sizes (prepared by varying sonication time and intensity with lateral sizes ranging from the nanometre range up to approximately 10 μm), it was shown that the most exfoliated GO flakes induced the most extensive membrane damage, while modified preparations (rGO and chitosan-coated GO) caused the least damage. The authors concluded that these results were due to the aggregation of both the modified preparations, and because chitosan prevented electrostatic interaction between the GO functional groups and the erythrocyte membranes. In addition to the methods used to prepare the different GFNs between reports, other methodological approaches may not have been equivalent in the different experimental systems. Standard methods suspend the particles in phosphate buffered saline (PBS) (as stated explicitly by Sasidharan et al. [83]), however other publications were less clear about the methods used, and potentially employed dispersion media containing adsorbents or ionic species that could affect the surface chemistry of the flakes, changing their interactions with red blood cells.

The activation of human platelets *in vitro* is a significant adverse effect of many substances introduced to the body. In early experiments GO prepared using a modified Hummers' method was reported to induce thrombosis following injection into mice, and it was concluded that the platelet aggregation was induced by their interaction with the negatively charged surface of the GO flakes [85] – similar to the effects of the negatively-charged surface of collagen *in vivo* [86]. rGO flakes which had fewer charged groups on their surface were shown to be less thrombogenic [85]. Testing this hypothesis further, the authors employed positively-charged flakes using rGO subsequently functionalised with amine groups (producing amine modified graphene (G-NH_2))[80]. Whereas GO was shown to induce platelet activation and aggregation at doses of only 10 μg/mL, G-NH_2 showed no significant effect at the same doses. The difference was further confirmed *in vivo*: doses of 250 μg/kg of GO induced thrombosis to a similar extent to those treated with the platelet activating agent collagen (200 μg/mL), while those treated with the same concentration of G-NH_2 showed no increased thrombotic tendency [80]. Other reports have demonstrated that alternative functionalisation could modify this effect: Chowdhury et al. [61] measured platelet factor 4 levels in whole blood taken from two donors and found that GO-Dextran at doses of 1–10 mg/mL caused no platelet activation. Similarly Shen et al. found that GO-Fe_3O_4 prepared either as nanoparticles or sheets did not invoke a thrombotic response [87].

3.4. Bioaccumulation of graphene

The kinetics of biodistribution, including excretion or bioaccumulation, of nanoparticles are significantly linked to both particle size and geometry: research using non-graphene nanoparticles has shown that particles with diameters less than 30 nm are rapidly excreted by the kidneys, while large particles (above 500 nm) are phagocytosed and cleared through the reticuloendothelial system (RES); particles of intermediate size may accumulate in the bone marrow, heart, stomach, kidneys, liver and spleen [52]. Similar processes appear to be reflected in the behaviour of graphene. Moore et al. found that large flakes of PEG- or polymer-functionalised hydroxylated-graphene were cleared more rapidly than similarly functionalised small CNTs, and that they accumulated in the organs of the RES rather than the brain tissue to which they had been targeted [23]. Flake geometry was also found to be crucial to accumulation. Shen et al. [87], using a murine model, compared GO-FE_3O_4 wrapped *nanoparticles* with graphene in sheet-like structure where FE_3O_4 was attached to the surface (*nanosheets*). Iron levels were used to track the distribution and excretion of each graphene form. For the *nanoparticle* form of GO-FE_3O_4 the iron levels returned to baseline after 14 days suggesting effective elimination; in contrast, iron levels in animals exposed to *nanosheets* remained elevated. This difference was reflected in the observed residence behaviour: both forms initially were concentrated in the lung and spleen before a steady increase in the liver; however, there was a sharp peak in kidney residence at

Table 2
Summary of a selection of results from the literature in which GFNs were found to induce ROS generation, including the concentration at which ROS generation became significant, compared to a control.

References	Significant concentration (μg/mL)	Functionalisation	Geometry	Cell type	Time (h)
Reactive oxygenated species generation					
[93]	10–100	Pristine	3–5 layer, 10–100 nm	PC12	24
[84]	50–100	Pristine	Single layer	Vero	24
	–	Carboxylated	>2.5 μm		
[9]	5–20	Pristine in pluronic F108	Few layer	RAW264.7	24–48
			0.5–1 μm		
[111]	10–100	rGO + BSA	11 nm	hMSCs	1
	10–100		91 nm		
	10–100		418 nm		
	100		3.8 μm		
[83]	75	Pristine	1–2 layer	RAW264.7	24
	–	Carboxylated	100 s of nm		
[99]	10	GO	0.4–0.8 μm	HUVECs	24
			0.2–0.8 μm		
		rGO	0.4–0.8 μm		
			0.2–0.8 μm		
[96]	100	rGO	50–200 nm × 10 μm	hMSCs	1
	10		Monolayer		5
	1				96
	100		Low aspect ratio. No other details		1
	10				24–96
[98]	10	GO	Monolayer	Murine spermatazoa	2
	10	rGO – N2H4	>1 μm		
	10	rGO – HT			
	–	rGO – GTP	Monolayer (with adsorbed GTPs)		

Table 3
Summary of a selection of results from the literature where membrane disruption by GFNs was investigated, including the concentration of GFNs at which membrane disruption became significant, compared to a control.

References	Significant concentration (μg/mL)	Functionalisation	Geometry	Cell type	Time (h)
Membrane disruption					
[93]	100	None – pristine	3–5 layer, 10–100 nm	PC12	24
[84]	None	Pristine	Single layer	Vero	24
		Carboxylated	>2.5 μm		
[83]	–	Pristine	1–2 layer	RAW264.7	24
		Carboxylated	100 s of nm		
[99]	5–10	GO	0.4–0.8 μm	HUVECs	24
	1–10				48
	1–10		0.2–0.8 μm		24
	1–10				48
	10	rGO	0.4–0.8 μm		24
	10				48
	10		0.2–0.8 μm		24
	1–10				48
[96]	100	rGO	50–200 nm × 10 μm	hMSCs	1
	10		Monolayer		5
	1				96
	100		Low aspect ratio. No other details		24–96
[103]	–	GO	700 × 200 nm	A549	–
			No thickness stated	MCF7	
	–		300 nm		–
			No thickness stated		
	–		200 nm		–
			No thickness stated		
	100		100 nm		72
			No thickness stated		
[101]	200–400	GO	125–220 nm × 500–2500 nm	HeLa	72
	–		Few layer	SKBR3	72
	–			mcf7	72

24 h for the *nanoparticle* form before rapidly decreasing (suggesting excretion), while *nanosheets* had steady and low residence in the kidney that increased sharply after 14 days.

Accumulation and aggregation of nanoparticles that cannot be degraded may induce the formation of granulomas through frustrated phagocytosis by macrophages – a process that is well recog-

Table 4
Summary of results from the literature in which the genotoxicity of GFNs was examined, including the concentration at which genotoxicity became significant, compared to a control.

References	Significant concentration (μg/mL)	Functionalisation	Geometry	Cell type	Time (h)
Genotoxicity					
[100]	0.1–100	rGO + BSA	11 nm	hMSCs	1
	1–100		91 nm		
	100		418 nm		
	100		3.8 μm		
[101]	1	rGO	50–200 nm × 10 μm	hMSCs	1
	0.1		Monolayer		5
	0.01				96
[103]	100	GO	Monolayer	Murine spermatazoa	2
	100	rGO – N2H4	>1 μm		
	100	rGO – HT			
	–	rGO – GTP	Monolayer (with adsorbed GTPs)		
[61]	100	GO	400–500 nm Few layer	7702-3d, MRC-5-3d, U937-3d	24
	–	GO-PEG	30 nm Few layer (1–2 nm)		–
	–	rGO-PEG	70 nm Few layer (4–5 nm)		
	200	GO-BSA	50 nm Few layer (10 nm)		48
	–	rGO-BSA	70 nm Few layer (15 nm)		–

nised for carbon nanotubes [38,88]. There has therefore been significant interest in the potential for degradation of graphene flakes and related carbon nanomaterials. Kotchey et al. demonstrated that horse radish peroxidase (HRP) was able to further oxidise GO, causing holes to form in its basal surface [89], while Kagan et al. reported that neutrophil myeloperoxidase could degrade shorter CNTs [90]. Additional evidence has been presented using *in vivo* models: Girish et al. [70] used Raman spectroscopy to show that carboxylated graphene introduced to mice by tail-vein injection aggregated and accumulated in the lung, liver, kidney and spleen, but was partially degraded over time, such that after 3 months the intensity of the graphene signal in the lungs was reduced – particularly around the edge regions – and within the spleen the characteristic Raman signal associated with amorphous carbon was observed at the edges of aggregates – indicating significant degradation. The same authors confirmed their findings using murine macrophages *in vitro*, confirming graphene uptake within 24 h and significant degradation of the endocytosed graphene flakes by the seventh day, with approximately 50% of the total area of the flakes showing some degradation.

Bioaccumulation may also be significantly affected by functionalisation of GFNs; for example, PEG is often used to increase the biocompatibility and circulation time of GO, but has low biodegradability and may therefore potentially increase the bioaccumulation of the graphene. Li et al. [55] compared non-functionalised GO with PEGylated GO (PEG-GO) using human macrophage, lung fibroblast and liver cell lines *in vitro*. The group confirmed that PEG-GO caused less direct toxicity, but also that it underwent less degradation. To address this, the group used disulphide bonds to covalently link the PEG to the GO, which may be cleaved by intracellular enzymes potentially allowing the GO to be degraded following its interaction with the target cell.

4. Cellular toxicity of graphene

4.1. Importance of both chemical and physical form

Cells may die through either of two main routes: programmed cell death (apoptosis) or spontaneous cell death (necrosis). For nanomaterials both mechanisms are relevant and relate to both structural and chemical properties. Apoptosis may be triggered by reactive oxygen species (ROS) (see Table 2) or other toxic elements associated with the particles, while necrosis may be induced by direct damage to the plasma membrane resulting from specific physical properties of the particles (see Table 3). In addition, if the nanoparticles are able to enter the nucleus, there is concern that they could interact directly with the cell's DNA, resulting in genotoxicity (see Table 4). Study of the cellular toxicity of GFNs has therefore focused on each of these processes, and has considered both the physical characteristics of the material (such as lateral size, layer number, shape and hydrophobicity) and important chemical properties including functionalisation and molecules associated with the preparation or delivery media.

The relative importance of these properties is not equally represented between the different graphene forms or target cell types or tissues. The importance of both the chemical and physical form of the flakes is notably shown in those studies where similar cell systems or models produce apparently contradictory results, and is particularly apparent *in vivo* where the complexity of the system and the range of cells exposed require a more holistic view of the toxicological profile of different graphene preparations. Therefore, while the following sections are split in terms of GFN surface chemistry, the significance of graphene flake geometry – particularly the importance of both lateral dimensions and layer number – cannot be understated in determining toxicity. In addition, since particle size and geometry vary substantially according to preparation methods, this introduces additional complexity to the assessment of graphene toxicity. For these reasons, the geometry of the flakes is highlighted within the sections, and the geometry and thickness of graphene preparations for the quoted publications are highlighted in Tables 2–4, which may be used for reference between studies.

4.2. Pristine graphene

Pristine graphene form has low intrinsic solubility and therefore requires additional solubilisation steps to support its use within biological systems, and the additional compounds required to achieve this may affect its toxicity. Both PEG and the block co-polymer surfactant Pluronic F108 are widely used in biomedicine to improve the biocompatibility of nano and microparticles, and

Pluronic F108 has previously been shown to improve the toxicological profile of CNTs [91]. For pristine graphene it is recognised that Pluronic F108 interacts through the hydrophobic regions of the flake while the hydrophilic PEG tail-regions of the molecule extend into the media [9]. Solubility is promoted by this, but the surface chemistry of the graphene flakes is significantly altered. The pristine-graphene/Pluronic F108 compound was found to induce the apoptotic death of murine macrophages in a time and dose dependent manner that was attributed to depletion of the mitochondrial membrane potential significantly increasing ROS within the cell and triggering apoptotic pathways [9]. This effect appears to derive from the graphene component rather than of the surfactant however, since in other studies using pristine graphene alone similar effects were observed, with reduced metabolic activity [83,92,93] caused by an increase in ROS, often leading to apoptosis and in some cases cytoskeletal dysfunction [83]. In contrast, the lactate dehydrogenase (LDH) leakage associated with cell necrosis was observed to be minimal [83,92] (although caution should be taken with this mode of assessing toxicity, as GFNs are known to interact with the assay by binding to LDH, and can therefore give false negative results).

Studies *in vivo* have supported the concept of significant toxicity for pristine graphene with organ-specific effects being identified. Sawosz et al. [94] investigated the effects of pristine graphene on chicken embryos. The graphene was introduced to the ovalbumin before fertilisation, and hence was present before the blood–brain barrier formed. The authors found that although there was no significant reduction in the weights of the liver, brain, heart or spleens of the embryos after 19 days of incubation, the survival rate significantly decreased for all concentrations (50–10000 μg/L). TEM images showed that tissue and cells in the cerebrum were found to have abnormal ultrastructure, believed to derive from strong interactions between the hydrophobic basal plane of the graphene and the lipid membranes within the cerebral milieu. Evidence of additional cellular disruption was demonstrated by the reduction of PCNA expression, which is associated with DNA synthesis and repair [94]. Similarly, Sasidharan et al. [79] demonstrated cellular damage from pristine graphene using a few-layer preparation (*p*-FLGs) prepared by the arc discharge method, to produce flakes of lateral dimensions 200–400 nm, to which they exposed *via* tail-vein injection, Swiss albino mice over a period of 3 months. Through serum biochemistry analysis it was found that alkaline phosphatase and blood urea nitrogen levels increased over the 90 days to levels significantly higher than the control, indicating hepatic injury.

4.3. Reduced graphene oxide

The reduction of GO to form rGO removes the majority of the oxygenated functional groups. However, unlike pristine graphene, residual oxygenated functional groups remain on rGO conferring distinctive properties to the material. Like pristine graphene, the hydrophobicity of the rGO allows it to interact directly with cells causing direct physical damage; however, the extent to which this occurs is dependent also on other properties of the flakes. Akhavan et al. showed that reduced dimensions in one or both of the lateral planes of rGO had substantial impact on the cytotoxicity the sheets [95,96]. Different preparations of rGO were all shown to disrupt cell membranes and induce ROS generation within primary mesenchymal stem-cells; however, toxicity was substantially greater when rGO was in nanoplatelet or nanoribbon form when compared with rGO that had large lateral dimensions. Other studies have confirmed this effect of particle dimension [97].

In addition, the surface chemistry of rGO may differ significantly depending on how it is prepared. Hashemi et al. [98] tested the viability of spermatozoa exposed to rGO prepared using one of three different methods: hydrazine (HZrGO), high temperature (HTrGO) or green tea polyphenol (GTrGO) reduction. Each preparation induced increased ROS levels and nitrous oxide (NO) production, causing DNA fragmentation and low ATP levels with reduced motion of the spermatozoa. However, this effect was more marked for HTrGO and HzrGO forms than for GTrGO. The authors suggested that residual green tea polyphenols adsorbed to the flake surfaces of GTrGO provided partial protection. An effect of the preparation method on the physical characteristics of the rGO was also noted: the most hydrophobic particles (HzrGO) were also the thinnest and sharpest, and had highest toxicity.

A further element in rGO toxicity may relate to the aggregation or sedimentation of the molecule and the nature of the target cell type. Liao et al. [8] compared the toxicity of rGO and GO using human erythrocytes and skin fibroblasts. They showed that while rGO induced less haemolysis, it was more toxic to fibroblasts. This was attributed to increased sedimentation and aggregation of rGO, causing much of it to settle on top of the adherent fibroblast layer, which the authors suggest may have restricted the cells' access to nutrients.

4.4. Graphene oxide

The toxicity associated with oxygenated functional groups present on GO flakes introduces potential toxicity. However, the extent of the toxicity caused by this oxygenation is unclear, with separate studies reporting different outcomes. Das et al. [99] prepared GO using a modified Hummers' method, flakes were exposed to hydrazine hydrate for different lengths of time, generating flakes that had different densities of oxygenated functional groups, with the least stable flakes being somewhat stabilised using ammonium hydroxide. Using a Human Umbilical Vein Endothelial Cell (HUVEC) model, the group demonstrated that a higher density of oxygenated functional groups was associated with increased levels of ROS and associated DNA-damage within cells (quantified using the oxidant-sensitive dye H_2-dichlorofluorescein, together with the assessment of heme oxygenase-1 and thioredoxin-reductase). The increase in ROS was associated with altered cell attachment, morphology, cell survival and proliferation [99]. However, in an alternative approach by Sasidharan et al. [84], GO was first reduced using thermal exfoliation, following which, the flakes were carboxylated to varying extents. The flakes were then tested using cultures of Vero (monkey kidney) cells, and the carboxylated flakes were shown to disperse well in media and to be taken up by the cells, with metabolic activity (assessed using Alamar Blue), membrane integrity (LDH release) and survival all unaffected.

As highlighted for other graphene preparations, shape and aspect ratio contribute significantly to the toxicity of GO [96,100,101]. Kimh Chng et al. [100] compared two GO samples of differing geometries, both prepared using the same modified Hummers' method; low aspect ratio flakes were derived from oxidised and exfoliated graphene nanofibres with dimensions 100×100 nm (nGO flakes), while high aspect ratio graphene oxide nanoribbons (GONRs) of dimensions 310×5000 nm prepared from "unzipped" multiwalled carbon nanotubes (MWCNTs). Using cytotoxicity assays involving A549 (lung epithelial) cells, dose-dependent toxicity was observed for both preparations; however, toxicity was consistently greater for GONRs compared with nGO flakes, with an almost fourfold difference in the concentration required for a significant toxic effect (detected by MTT and WST-8 assays). In a separate study, GONRs were submitted to sonication using different intensities or lengths of time. Longer sonication is associated with smaller flake size [8], decreased aspect ratios [100], and an increased number of structural defects [102]. Using two human carcinoma cell lines and *Oryzias Latipes* embryos, it was found these features were associated with greater toxicity to the cells [103].

It is however difficult entirely to deconvolute the different elements of the various studies. The effects of aspect ratio are intrinsically linked to different overall lateral sizes of the GO flakes, and the methods required for sample preparation carry a significant effect. The unzipping method of producing GNRs is reported to result in a high proportion of carbonyl groups situated along the GNR edge [100] – for nanoribbons this may contribute to the high toxicity observed [101]. Furthermore, residual contaminants associated with GO preparation may include metals and mellitic acids adsorbed to the flakes; the removal of these contaminants may require additional steps, such as hydrochloric acid treatment [104] and multiple washing steps [37]. In addition, without multiple centrifugation and washing steps, larger and thicker flakes, and unreacted graphite may remain in suspension; without carrying out such steps, it becomes difficult to pinpoint the causes for any observed toxicity.

In vivo studies have enabled the assessment of chronic effects of GO exposure, and of dosing strategy. A high dose of GO (500 μg/mL) administered to maternal mice during their lactation period caused developmental delay to offspring and morphological abnormalities of the intestinal Villi of the young mice [105]. Using a mouse model, Liu et al. [75] compared two different GO flake-sizes (greater or less than 1 μm) and a range of doses delivered either as single injections (0.3, 2.1 or 10 mg/kg) or as seven successive doses (0.3 mg/kg per dose, up to a total exposure of 2.1 mg/kg). For both flake sizes, the lower single doses (0.3–2.1 mg/kg) had low mortality rates and organ size was not affected; in contrast, the highest single dose (10 mg/kg) induced a very high mortality rate. Mice from the multiple-dose group also experienced high toxicity: three died before the end of the investigation, and the mice showed increased lung size with GO-filled macrophage nodules, in addition to significant swelling in the renal glomeruli with biochemical evidence of renal impairment. The mechanism of toxicity did not appear to be the same as was seen *in vitro*, since apoptosis in affected organs was not significantly different from that in the control group, and oxidative stress markers in the liver, spleen and lungs were found to be at normal levels, perhaps because of a protective effect of the serum proteins adsorbed to the GO flakes [75]. The authors concluded that multiple low doses of GO flakes may allow an acceptable toxicological profile.

4.5. Further-functionalised GFNs

In general, while the nature or extent of toxicity for pristine graphene, rGO or GO may vary, most native GFNs have been found to produce significant cytotoxic responses. This has prompted the use of functionalisation to reduce this effect. In biomedicine significant attention has focused on polyethylene glycol (PEG) [48,51,55,106,107]. This molecule may be attached covalently, with bonds that are cleavable [55] or non-cleavable, or through hydrophobic attachment as block co-polymers [48,107]. PEG is recognised to increase the circulation time and biocompatibility of graphene, and is widely used to functionalise micro and nanoparticles for therapeutics delivery. Attachment of dextran may also provide similar benefits [60,61,108]. The advantages of functionalisation using PEG were shown by Moore et al. [23], who used a hydroxyl-functionalised graphene that was complexed with PEG and poly(lactide) (GrLP). The toxicity of the complex was compared with hydroxylated graphene (h-Gr) *in vitro* using U138 human glioblastoma cells. The authors demonstrated dose-dependent toxicity for uncoated hydroxylated graphene commencing at concentrations of 50 μg/mL, whereas dose-dependent toxicity was not observed for GrLP at concentrations up to 250 μg/mL.

Kanakia et al. [108] used GO-dextran composites to perform a safety pharmacology assessment; the superior stability of the composite compared to unfunctionalised GO allowed them to test the maximum tolerable dose (MTD) without the restrictions imposed by the limited stability of native GO. The authors found that if the suspension was given as a rapid bolus injection, significant mortality was observed at concentrations $\geqslant$125 mg/kg, whereas similar mortality rates were only observed at concentrations $\geqslant$250 mg/kg when the dosage was given at a slower injection rate. When dosages exceeded 250 mg/kg, histological sections of the heart, liver, lung and kidney revealed adverse pathological responses, predominantly in the form of congested blood vessels. In contrast, lower concentrations had no significant impact on the cardiovascular system or on the blood composition. Interestingly, as the concentrations of GO-dextran increased, proportionally more of the suspension was rapidly excreted, whereas low concentration GO was found to accumulate in the organs both immediately after injection, and after 30 days. Similar results were reported by Yang et al. [109], who tracked the distribution of ^{125}I-PEG-GO in mice (either 4 or 20 mg/kg). Reflecting previous reports, the majority of the flakes were found to accumulate in the organs of the RES, before being excreted. Although GO-PEG aggregates were observed in histology sections of the liver taken at 3 days, most were cleared by 20 days with no injury to the liver, kidney or spleen observed up to 90 days. Using a novel radiolabelled preparation of chemically-functionalised graphene, Jasim et al. [110] employed whole body single photon emission computed tomography (SPECT/CT) imaging combined with Ramen spectroscopy. The authors demonstrated that following injection into blood the graphene sheets underwent renal clearance, with retained graphene being present initially in liver before later accumulation in spleen (24 h). The authors noted however that the results obtained in their own study differed from other reported studies of the fate of graphene flakes administered *in vivo*. They specifically identified differences in the nature of the graphene flakes used in the different studies. The authors of the study make the important point that graphene-flake geometry plays a major role in determining the fate of administered functionalised graphene, identifying an importance of particle dimension as a determinant of uptake by both cell type and tissue [110].

It has been shown also that the toxicity of functional molecules may be also be modified through their association with graphene flakes. This may be illustrated by the compound PEI, a cationic polymer useful in therapeutics delivery *in vitro*. The molecule is able to condense nucleic acids and to escape the endosomal vesicles using the proton sponge effect. The compound has not reached the clinic as it has significant cytotoxicity. However, when in complex with GO the toxicity is reduced, possibly due to the reduction in free branches of the PEI polymer [18].

Summaries of a range of toxicology results for various GFNs are presented in Tables 2–4.

5. Graphene: a therapeutic platform

5.1. Cargo attachment

The way in which a cargo is loaded onto or into therapeutics delivery vehicles influences how well the cargo is protected from degradation, how it may be released at its site of action, and even the size and shape of the vehicle itself. The flexibility of the graphene platform has allowed exploitation of each of these aspects.

Initial work with GFNs used drugs that interact directly with graphene sheets, often through their aromatic or hydrophobic regions [112]. For instance, SN38 binds to graphene by hydrophobic interactions and π–π stacking [51], while for doxorubicin (DOX) binding may additionally employ hydrogen bonding to oxygenated functional groups, allowing pH-controlled loading and release [44]; in both cases, drug effectiveness was increased com-

pared to exposure to the drug alone. Other biopharmaceuticals including genetic materials have been complexed to graphene to protect them from degradation. For single stranded nucleic acids this has employed adsorption through interaction of the nucleobases with the polyaromatic basal plane of graphene or other carbon nanomaterials [1,113–115]. The effectiveness of this approach was demonstrated by Lu et al. who adsorbed a molecular beacon (MB) to GO via π–π interactions. The adsorbed genetic material was shown to be protected from degradation (by the enzyme DNAse I), and to be successfully released within a HeLa cell model where the hairpin looped oligonucleotide was shown to fluoresce when in contact with its complementary sequence [5]. To deliver double-stranded nucleic acids further functionalisation is required, and compounds that are already used in gene therapy are often employed. Zhang et al. [16] used PEI to functionalise GO, permitting the condensation of double stranded Bcl-2 targeted siRNA (short interrupting RNA) to the functionalised graphene through electrostatic interactions. Exploiting the high surface area of graphene, the group was able additionally to load DOX onto the flakes, although they reported that sequential rather than co-delivery of DOX and siRNA was more effective [16]. Since that report, other groups have also used PEI-functionalised GO for gene delivery [15,17,18,116]; this and other cationic polymers are particularly attractive as they are able to facilitate the condensation and complexation of negatively charged nucleic acids, and may promote interactions with the negatively charged cell membranes.

The complexation of graphene and polymers or other functional species can significantly change the size and geometry of a graphene flake, as found by Kim et al. [47], who showed that after complexation with PEI and PEG, their rGO flakes became significantly smaller and more globular. The capability to intentionally modify vehicle-shape by tailored drug-binding was demonstrated by Yang et al. [112]. Low molecular weight PDMAEMA (Poly(2-di methylamino-ethylmethacrylate) was attached to GO flakes using disulphide bonds (denoted using SS). The favourable interactions between pDNA and the short PDMAEMA chains was then exploited to induce the formation of a complex nanoparticle, made up of multiple GO-SS-PDMAEMA sheets with pDNA macromolecules sandwiched between them. The starting sheets were approximately 10 nm in thickness with lateral dimensions around 500 nm before complexation with pDNA, but following pDNA complexation the resultant nanoparticle was globular with an average diameter of 86 nm. The particle therefore contained multiple plasmids and had a size that favoured its endocytosis, while cleavage of its disulphide bonds permitted fragmentation within the cell.

5.2. Cell targeting

Following attachment to graphene, the cargo must be transported to its target cell or the tissue where the compound should be preferentially taken up and released. Again the flexibility of the graphene platform has been used to support a range of approaches.

Passive targeting mechanisms are attractive since they do not require extensive functionalisation, and these have been exploited using a graphene platform. The enhanced permeability and retention (EPR) effect is a well-used phenomenon in which the over-vascularisation, leaky vasculature and reduced lymphatic drainage in cancerous tumours means that nanoparticles, including GFNs, delivered through the circulation tend to preferentially accumulate in the tumour. This has been effectively demonstrated by a number of groups [23,117,118], many of whom loaded their GFNs with labels to allow imaging *in vivo* – for example magnetic nanoparticles for magnetic resonance imaging (MRI) [118] or fluorescent moieties for near infrared fluorescence (NIRF) imaging [119]. In addition to illustrating the biodistribution of the flakes, such studies show the capacity of using GFNs as theranostic probes. The EPR effect may be made more specific through the use of additional physical methods. For example, the high infra-red absorption capacity of graphene or GO allows photothermal effects to be exploited for localised cell killing through hyperthermia, where the infrared light is applied only to the area being targeted [120–124]; localised heating through photothermal means has also been shown to increase cell permeability, additionally increasing the transfection efficiency of the graphene complexes in the region where the infrared light is applied [125]. Similarly, GFN-magnetic nanoparticle composites have also been prepared so that graphene particles can be specifically targeted using localised magnetic fields [120,126].

In a particularly interesting example, Feng et al. [121] used the difference in pH in the tumour microenvironment to change their GFN's propensity for uptake; the flakes were loaded with DOX and conjugated with PEG and a pH responsive polymer. In neutral or basic environments, the flakes were negatively charged, but when introduced to an acidic environment their charge becomes positive – making interaction with the negative cell membrane and subsequent endocytosis far more likely. The authors used fluorescence imaging and flow cytometry, in addition to the increase in cell death following DOX-loading, to illustrate a significant improvement in cell uptake and drug delivery in acidic conditions compared to neutral conditions. Finally, photothermal ablation was used to further enhance cancer cell killing, showing additional improvements on rates of cell death.

A more specific interaction with particular cells or tissue types may be achieved through the linkage of ligands that are recognised by cell-surface receptors. This method allows the targeting of graphene/drug complexes to particular cell types or tissues, and also may facilitate cell uptake and promote specific modes of intracellular trafficking. This active-targeting approach has been exemplified by studies that exploit the interaction between the folate molecule and its specific receptor. The folate receptor is widely expressed, but has overexpression on the surfaces of particular cancer cells [42,124,127]. Folate itself has no intrinsic toxicity and is thought to be taken up through receptor mediated endocytosis, possibly through a number of non-specific trafficking routes [128]. Its use as a targeting ligand therefore has provided a potential practical approach to therapy, but also as a paradigm approach for receptor-mediated targeting and intracellular drug-targeting. Zhang et al. used folate-conjugated carboxylated and sulfonated graphene to target the breast cancer cell line MCF-7, delivering mixed anti-cancer drugs doxorubicin and camptothecin bound to graphene [129]. The flakes were also conjugated with Rhodamine-B and fluorescence microscopy images show the flakes dispersed evenly through all the cells with no specific intracellular localisation. This is compared to images of A549 lung epithelial cells (on which folate receptors are not overexpressed), similarly treated with the flake complexes, where very weak fluorescence is observed in few cells. In addition, folate-conjugated flakes induced significantly greater toxicity than non-targeted flakes at 20 μg/mL – inducing a similar level of cytotoxicity as free DOX. These results have been confirmed by other groups in a range of different folate-receptor expressing cell lines such as HeLa [10] and HepG2 [40]. The transferrin receptor is similarly overexpressed by some cancer cells, hence Sasidharan et al. used transferrin as a targeting ligand conjugated to carboxylated graphene, which was introduced to the cancer cell line K562. Further, the authors used graphene's sensitivity to radiofrequency (RF) radiation to induce localised heating in a method similar to the more commonly used IR absorption mentioned above – selectively killing cancer cells, including those resistant to existent chemotherapy drugs. The strong response of graphene to RF is of particular importance due to its increased tissue penetration depth in comparison with IR [130].

Additional functional tags may direct specific routes of entry to cells or cellular organelles – in gene delivery this may be the nucleus. Molecules with mass less than 40–45 kDa can diffuse passively through the nuclear pore complex; however, larger macromolecules need to be actively transported. The most well understood mechanism for this is the classical nuclear import cycle, a receptor-driven process in which a cytoplasmic carrier protein recognises macromolecules for import, binds first with the target protein, then the appropriate receptor in the nuclear pore complex, at which point the trimeric complex translocates into the nucleus [131]. The proteins that are to be transported into the nucleus are recognised from the inclusion of a Nuclear Localisation Signal (NLS) sequence in their structure [131–133]. Such sequences have been incorporated into therapeutics delivery complexes, including in graphene research, although the efficacy of this process may be limited by cargo size [35]. In 2012 Ren et al. [15] further non-covalently functionalised a GO-PEI complex with NLS PV7 to increase the efficiency of the vehicle which was delivering plasmid DNA (enhanced green fluorescent protein) [15]. The percentage quantitative transfection in both 293T and HeLa cells was improved by up to around 7% and 20% respectively compared to complexes that did not include the NLS sequence.

5.3. Cargo delivery

Achieving targeted drug-effect for a transported therapeutic agent requires that it is effectively released at its site of action. The mechanism required to release the drug depends on the graphene preparation and method of linkage. For minimally functionalised GFNs, cargo is generally bound by hydrophobic or π–π interactions; these may be released following change to physicochemical properties within the environment, frequently making use of changing physiological characteristics taking place within the cell or competitive binding to ligand. Some of the first examples used changes in pH to alter bonding-affinity: DOX attached by hydrogen bonding to GO may be released by localised pH change within the cell [44]. In an adaptation of the same approach, pH change within the extracellular microenvironment was used to drive the controlled release of bioactive molecules outside of cells: the inhibitory-antibody anti-IL10R and the interferon IFNϒ were loaded directly onto graphene oxide flakes, both individually and in combination, with the aim of facilitating the slow release of the bound inhibitory-antibody and interferon within tissues to modify an immune response [134]. The antibody was found to be released in acidic environments but remain attached at neutral pH. Exposure to the biomolecule-GO complexes both individually and in combination was found to significantly increase the production of interleukin 12-B, confirming the successful release of the biomolecules.

For single stranded genetic material adsorbed to the basal plane of GFNs it has been demonstrated that release is promoted by competitive binding to the complementary nucleotide strand [4,5,135]. This process is believed also to underlie the observed release of an oligodeoxyribozyme from native GO, which was used to cleave the mRNA of Hepatitis C non-structural gene 3 (NS3) in a Hepatitis C infected liver cell line [135]. In this case, the genetic material was labelled with a fluorescein reporter (FAM), which was quenched while bound to the flakes, so that cargo release was confirmed by the recovery of the fluorescence. The FAM label revealed localisation of the deoxyribozyme in the perinuclear region, while NS3 gene and protein down-regulation suggested that release was associated with binding to NS3 mRNA [135].

For functionalised GFNs cargo delivery must be tailored to the binding method used to attach the cargo as well as any specific functionalisation methods employed to facilitate cell targeting [7,15–17,23,112,125,129]. This may be illustrated by the use of graphene-conjugated PEI. This combination facilitates the binding of genetic material such as siRNA to graphene [16], and through its positive surface charge can promote cell entry, and importantly, its unique properties can promote lysosomal escape through the proton sponge effect. Once the complex has escaped the lysosome, while no specific physical process is known to facilitate cargo release from PEI, the continued condensation of genetic material on the PEI-graphene complex may continue to protect it and facilitate its transport through the cytosol towards the nucleus. This functionalisation may also carry negative effects since GO-PEI that has not been further functionalised strongly interacts with serum components, affecting both particle size and stability and reducing the transfection efficiency [125]. The addition of PEG to GO-PEI has been demonstrated to increase the stability of the flakes, and to increase transfection efficiency in HELA cells. In this paper it was found that linking this to photo-thermal effects based on the high infrared absorption of GO further enhanced transfection efficiency: from approximately 6% to around 25% presenting an opportunity for localised delivery [125].

Several groups have encapsulated GFNs in hydrogels to promote the localised and controlled delivery of cargo, often leading to significantly improved delivery profiles compared to the native hydrogel [78,136–139]. Paul et al. [78] used a methacrylated gelatin (GelMA) hydrogel matrix, in which PEI-GO, loaded with a vascular endothelial growth factor-165 (VEGF) plasmid (pDNA), was embedded. The hydrogel was injectable allowing localised delivery to the desired tissue and through chemical and physical tuning was able to produce slow-release of the pDNA over a 72 h timescale. The pro-angiogenic properties of the preparation were confirmed i*n vitro* using a rat heart myoblast model, where a 33% increase in proliferation over the control groups was observed after 96 h. Using a microchannel approach to mirror wound healing with HUVEC cells, conditioned media from the experiment increased in number and enhanced HUVEC migration around the microchannel. Using a rat *in vivo* model of myocardial infarction, the fGO-hydrogel increased capillary density and reduced scar tissue formation with a significantly improved cardiac ejection fraction after days 3 and 14 compared with control groups suggesting that the system could promote the growth of vasculature following acute myocardial infarction.

Other groups have worked to produce GFN therapeutics delivery-vehicles that incorporate sustained release. Moore et al. [23] coated GO flakes with PLA-PEG, where the PLA was used to encapsulate and slowly release Paclitaxel (GrLP-PTX) to treat glioblastoma. CNTs were used as a comparator and were similarly functionalised (CLPs). Loading of cargo was much higher for graphene, which was attributed to its very high surface area, and release rates over the time course were slower. As shown in their previous paper [106], the release of the PTX is far more rapid for CLPs than for graphene flakes, with approximately 80% of the drug released in the first 25 h, compared to 6% released from GrLP-PTX in the first 20 h. Therefore, although the PTX is encapsulated within the PLA in both graphene and CNT, the difference in shape between CNTs and graphene may be a significant determinant of the release profiles, as the curved CNT surface may result in more widely spaced PLA brushes. This shows that while the GFNs are highly functionalised, such that many of the inherent GFN properties may be masked at the point of delivery, they can still make a significant difference in terms of the efficacy of vehicle.

6. Conclusion

Research into graphene's use as a therapeutics delivery vehicle has moved on to the point where increasingly highly functionalised flakes are being used alone and in combination with other

biomedical technologies, resulting in vehicles highly tailored to their individual aims. However the material itself is often still poorly defined; the initial suspensions are often polydisperse and preparation methods vary significantly between groups. In this review it has been shown that all the physicochemical properties of GFNs – both before and after functionalisation – can have a significant impact on their interaction with the physiological environment and the tissues that reside there. This is relevant to both the flake's toxicity and its ability to deliver therapeutics effectively.

From the literature reviewed in this article, however, some tentative conclusions may be found. In terms of geometry, flakes with sub-micron lateral dimensions that are still larger than 20 nm may invoke the least inflammatory and toxic responses and thin flakes (ie few layer or less) are also less toxic, given appropriate functionalisation. The flakes used should be appropriately functionalised: pristine graphene and rGO are highly hydrophobic, but even with mild surface functionalisation can still cause a significantly toxic response; despite the hydrophilicity of GO, most groups have found that the flakes need additional functionalisation to improve stability, and depending on the functionalisation used, the resultant flakes may be less toxic, immunogenic and thrombotic. An improvement in stability will also reduce bioaccumulation; however, GFNs have been shown to undergo biodegradation *in vitro* and *in vivo* – albeit over relatively long timescales. Mitigating the effect of GFN flake functionalisation on biodegradation is also important – as many of the materials used to improve circulation time may also result in bioaccumulation due to increased residency time. The use of multiple low doses of GFNs, either through repeated administration or by making use of technologies such as hydrogels to promote slow release, may result in lower toxicity and increased efficacy. With regard to delivery, although the EPR effect may be relied upon to promote increased GFN accumulation in tumour sites, for instance, making use of the flexibility in GFN functionalisation, many groups have used active targeting methods to direct the flakes to the point of action – both intracellularly and extracellularly. In terms of therapeutics delivery, although initial work focused on the use of GFNs' intrinsic physicochemical properties to both load and release therapeutics such as small molecule drugs or single stranded genetic material, increasingly flakes are being further functionalised, eg with polymers, to allow attachment and condensation of a greater range of therapeutics to be delivered. Such functionalisation may also be used to improve the flakes' efficacy – although care should be taken that polymers such as PEI that have been traditionally used in gene therapy, but have not reached the clinic due to their unfavourable toxicological profiles, are not depended on in GFN research – even if their attachment to GFNs mitigates their toxicity somewhat.

Acknowledgements

Funding: This work was supported by the EPSRC [grant number EP/G03737X/1] and Manchester Pharmacy School, University of Manchester, UK.

References

[1] S. Akca, A. Foroughi, D. Frochtzwajg, H.W.C. Postma, Competing interactions in DNA assembly on graphene, PLoS ONE 6 (2011).
[2] Y. Wang, Y. Li, L. Tang, J. Lu, J. Li, Application of graphene-modified electrode for selective detection of dopamine, Electrochem. Commun. 11 (2009) 889–892.
[3] S. He, B. Song, D. Li, C. Zhu, W. Qi, Y. Wen, et al., A graphene nanoprobe for rapid, sensitive, and multicolor fluorescent DNA analysis, Adv. Funct. Mater. 20 (2010) 453–459.
[4] C.-H. Lu, J. Li, J.-J. Liu, H.-H. Yang, X. Chen, G.-N. Chen, Increasing the sensitivity and single-base mismatch selectivity of the molecular beacon using graphene oxide as the "Nanoquencher", Chem. – Eur. J. 16 (2010) 4889–4894.
[5] C.-H. Lu, C.-L. Zhu, J. Li, J.-J. Liu, X. Chen, H.-H. Yang, Using graphene to protect DNA from cleavage during cellular delivery, Chem. Commun. 46 (2010) 3116–3118.
[6] T. Nelson, B. Zhang, O.V. Prezhdo, Detection of nucleic acids with graphene nanopores: Ab initio characterization of a novel sequencing device, Nano Lett. 10 (2010) 3237–3242.
[7] H. Bao, Y. Pan, Y. Ping, N.G. Sahoo, T. Wu, L. Li, et al., Chitosan-functionalized graphene oxide as a nanocarrier for drug and gene delivery, Small 7 (2011) 1569–1578.
[8] K.-H. Liao, Y.-S. Lin, C.W. Macosko, C.L. Haynes, Cytotoxicity of graphene oxide and graphene in human erythrocytes and skin fibroblasts, ACS Appl. Mater. Interfaces 3 (2011) 2607–2615.
[9] Y. Li, Y. Liu, Y. Fu, T. Wei, L. Le Guyader, G. Gao, et al., The triggering of apoptosis in macrophages by pristine graphene through the MAPK and TGF-beta signaling pathways, Biomaterials 33 (2012) 402–411.
[10] X.Y. Yang, G.L. Niu, X.F. Cao, Y.K. Wen, R. Xiang, H.Q. Duan, et al., The preparation of functionalized graphene oxide for targeted intracellular delivery of siRNA, J. Mater. Chem. 22 (2012) 6649–6654.
[11] W. Miao, G. Shim, S. Lee, S. Lee, Y.S. Choe, Y.-K. Oh, Safety and tumor tissue accumulation of pegylated graphene oxide nanosheets for co-delivery of anticancer drug and photosensitizer, Biomaterials 34 (2013) 3402–3410.
[12] S. Radic, N.K. Geitner, R. Podila, A. Kaekinen, P. Chen, P.C. Ke, et al., Competitive binding of natural amphiphiles with graphene derivatives, Sci Rep 3 (2013).
[13] Z. Liu, J.T. Robinson, S.M. Tabakman, K. Yang, H. Dai, Carbon materials for drug delivery & cancer therapy, Mater. Today 14 (2011) 316–323.
[14] K.S. Novoselov, V.I. Fal'ko, L. Colombo, P.R. Gellert, M.G. Schwab, K. Kim, A roadmap for graphene, Nature 490 (2012) 192–200.
[15] T.B. Ren, L. Li, X.J. Cai, H.Q. Dong, S.M. Liu, Y.Y. Li, Engineered polyethylenimine/graphene oxide nanocomposite for nuclear localized gene delivery, Polym. Chem. 3 (2012) 2561–2569.
[16] L. Zhang, Z. Lu, Q. Zhao, J. Huang, H. Shen, Z. Zhang, Enhanced chemotherapy efficacy by sequential delivery of siRNA and anticancer drugs using PEI-grafted graphene oxide, Small 7 (2011) 460–464.
[17] D. Yin, Y. Li, H. Lin, B. Guo, Y. Du, X. Li, et al., Functional graphene oxide as a plasmid-based Stat3 siRNA carrier inhibits mouse malignant melanoma growth in vivo, Nanotechnology 24 (2013).
[18] L. Feng, S. Zhang, Z. Liu, Graphene based gene transfection, Nanoscale 3 (2011) 1252–1257.
[19] K. Yang, L.Z. Feng, X.Z. Shi, Z. Liu, Nano-graphene in biomedicine: theranostic applications, Chem. Soc. Rev. 42 (2013) 530–547.
[20] Z.H. Sheng, X.Q. Zheng, J.Y. Xu, W.J. Bao, F.B. Wang, X.H. Xia, Electrochemical sensor based on nitrogen doped graphene: simultaneous determination of ascorbic acid, dopamine and uric acid, Biosens. Bioelectron. 34 (Apr 2012) 125–131.
[21] Y. Mao, Y. Bao, S.Y. Gan, F.H. Li, L. Niu, Electrochemical sensor for dopamine based on a novel graphene-molecular imprinted polymers composite recognition element, Biosens. Bioelectron. 28 (2011) 291–297.
[22] Y.H. He, M. Tsutsui, R.H. Scheicher, F. Bai, M. Taniguchi, T. Kawai, Thermophoretic manipulation of DNA translocation through nanopores, ACS Nano 7 (2013) 538–546.
[23] T.L. Moore, R. Podilakrishna, A. Rao, F. Alexis, Systemic administration of polymer-coated nano-graphene to deliver drugs to glioblastoma, Part. Part. Syst. Charact. 31 (2014) 886–894.
[24] V.C. Sanchez, A. Jachak, R.H. Hurt, A.B. Kane, Biological interactions of graphene-family nanomaterials: an interdisciplinary review, Chem. Res. Toxicol. 25 (2012) 15–34.
[25] A.K. Geim, K.S. Novoselov, The rise of graphene, Nat. Mater. 6 (2007) 183–191.
[26] K. Loh, Q. Bao, P. Ang, J. Yang, The chemistry of graphene, J. Mater. Chem. 20 (2010) 2277–2289.
[27] D.R. Dreyer, S. Park, C.W. Bielawski, R.S. Ruoff, The chemistry of graphene oxide, Chem. Soc. Rev. 39 (2010) 228–240.
[28] C.L. Fu, X.N. Yang, Molecular simulation of interfacial mechanics for solvent exfoliation of graphene from graphite, Carbon 55 (2013) 350–360.
[29] J.P. Rourke, P.A. Pandey, J.J. Moore, M. Bates, I.A. Kinloch, R.J. Young, et al., The real graphene oxide revealed: stripping the oxidative debris from the graphene-like sheets, Angewandte Chemie-Int. Ed. 50 (2011) 3173–3177.
[30] W.S. Hummers, R.E. Offeman, Preparation of graphitic oxide, J. Am. Chem. Soc. 80 (1958). pp. 1339–1339.
[31] N.R. Wilson, P.A. Pandey, R. Beanland, R.J. Young, I.A. Kinloch, L. Gong, et al., Graphene oxide: structural analysis and application as a highly transparent support for electron microscopy, ACS Nano 3 (2009) 2547–2556.
[32] A. Hatefi, B.F. Canine, Perspectives in vector development for systemic cancer gene therapy, Gene Therap. Molecul. Biol. 13 (2009) 15–19.
[33] A.P. Lam, D.A. Dean, Progress and prospects: nuclear import of nonviral vectors, Gene Ther. 17 (2010) 439–447.
[34] S.D. Li, L. Huang, Gene therapy progress and prospects: non-viral gene therapy by systemic delivery, Gene Ther. 13 (2006) 1313–1319.
[35] E. Mastrobattista, M. van der Aa, W.E. Hennink, D.J.A. Crommelin, Artificial viruses: a nanotechnological approach to gene delivery, Nat. Rev. Drug Discovery 5 (2006) 115–121.
[36] H. Hillaireau, P. Couvreur, Nanocarriers' entry into the cell: relevance to drug delivery, Cell. Mol. Life Sci. 66 (2009) 2873–2896.
[37] H. Ali-Boucetta, D. Bitounis, R. Raveendran-Nair, A. Servant, J. Van den Bossche, K. Kostarelos, Purified graphene oxide dispersions lack in vitro

cytotoxicity and in vivo pathogenicity, Adv. Healthcare Mater. 2 (2013) 433–441.
[38] D.M. Brown, I.A. Kinloch, U. Bangert, A.H. Windle, D.M. Walter, G.S. Walker, et al., An in vitro study of the potential of carbon nanotubes and nanofibres to induce inflammatory mediators and frustrated phagocytosis, Carbon 45 (2007) 1743–1756.
[39] K. Pulskamp, J.M. Woerle-Knirsch, F. Hennrich, K. Kern, H.F. Krug, Human lung epithelial cells show biphasic oxidative burst after single-walled carbon nanotube contact, Carbon 45 (2007) 2241–2249.
[40] X. Zhao, P. Liu, Biocompatible graphene oxide as a folate receptor-targeting drug delivery system for the controlled release of anti-cancer drugs, RSC Adv. 4 (2014) 24232–24239.
[41] D. Depan, J. Shah, R.D.K. Misra, Controlled release of drug from folate-decorated and graphene mediated drug delivery system: synthesis, loading efficiency, and drug release response, Mater. Sci. Eng. C – Mater. Biol. Applicat. 31 (2011) 1305–1312.
[42] H.L. Hu, C. Tang, C.H. Yin, Folate conjugated trimethyl chitosan/graphene oxide nanocomplexes as potential carriers for drug and gene delivery, Mater. Lett. 125 (2014) 82–85.
[43] M. Chu, C.Y. Dong, H.Y. Zhu, X.J. Cai, H.Q. Dong, T.B. Ren, et al., Biocompatible polyethylenimine-graft-dextran catiomer for highly efficient gene delivery assisted by a nuclear targeting ligand, Polym. Chem. 4 (2013) 2528–2539.
[44] X. Yang, X. Zhang, Z. Liu, Y. Ma, Y. Huang, Y. Chen, High-efficiency loading and controlled release of doxorubicin hydrochloride on graphene oxide, J. Phys. Chem. C 112 (2008) 17554–17558.
[45] A. Bianco, Graphene: safe or toxic? The two faces of the medal, Angewandte Chemie-Int. Ed. 52 (2013) 4986–4997.
[46] G. Sahay, D.Y. Alakhova, A.V. Kabanov, Endocytosis of nanomedicines, J. Control. Release 145 (2010) 182–195.
[47] H. Kim, W.J. Kim, Photothermally controlled gene delivery by reduced graphene oxide-polyethylenimine nanocomposite, Small 10 (2014) 117–126.
[48] K. Yang, L. Feng, H. Hong, W. Cai, Z. Liu, Preparation and functionalization of graphene nanocomposites for biomedical applications, Nat. Protoc. 8 (2013) 2392–2403.
[49] X.F. Tan, L.Z. Feng, J. Zhang, K. Yang, S. Zhang, Z. Liu, et al., Functionalization of graphene oxide generates a unique interface for selective serum protein interactions, ACS Appl. Mater. Interfaces 5 (2013) 1370–1377.
[50] Z.J. Ding, Z.J. Zhang, H.W. Ma, Y.Y. Chen, In vitro hemocompatibility and toxic mechanism of graphene oxide on human peripheral blood T lymphocytes and serum albumin, ACS Appl. Mater. Interfaces 6 (2014) 19797–19807.
[51] Z. Liu, J.T. Robinson, X. Sun, H. Dai, PEGylated nanographene oxide for delivery of water-insoluble cancer drugs, J. Am. Chem. Soc. 130 (2008) 10876.
[52] M. Rahman, S. Laurent, N. Tawil, L.H. Yahia, M. Mahmoudi, Protein-Nanoparticle Interactions, Springer, 2013.
[53] U. Khan, A. O'Neill, M. Lotya, S. De, J. Coleman, High-concentration solvent exfoliation of graphene, Small 6 (2010) 864–871.
[54] H.W. Yang, Y.J. Lu, K.J. Lin, S.C. Hsu, C.Y. Huang, S.H. She, et al., EGRF conjugated PEGylated nanographene oxide for targeted chemotherapy and photothermal therapy, Biomaterials 34 (2013) 7204–7214.
[55] Y.J. Li, L.Z. Feng, X.Z. Shi, X.J. Wang, Y.L. Yang, K. Yang, et al., Surface coating-dependent cytotoxicity and degradation of graphene derivatives: towards the design of non-toxic, degradable nano-graphene, Small 10 (2014) 1544–1554.
[56] T. Zhou, B. Zhang, P. Wei, Y.P. Du, H.J. Zhou, M.F. Yu, et al., Energy metabolism analysis reveals the mechanism of inhibition of breast cancer cell metastasis by PEG-modified graphene oxide nanosheets, Biomaterials 35 (2014) 9833–9843.
[57] A. Chandra, S. Deshpande, D.B. Shinde, V.K. Pillai, N. Singh, Mitigating the cytotoxicity of graphene quantum dots and enhancing their applications in bioimaging and drug delivery, ACS Macro Lett. 3 (2014) 1064–1068.
[58] X.F. Cao, S. Zheng, S.P. Zhang, Y.S. Wang, X.Y. Yang, H.Q. Duan, et al., Functionalized graphene oxide with hepatocyte targeting as anti-tumor drug and gene intracellular transporters, J. Nanosci. Nanotechnol. 15 (2015) 2052–2059.
[59] S.L. Yang, S.L. Luo, C.B. Liu, W.Z. Wei, Direct synthesis of graphene-chitosan composite and its application as an enzymeless methyl parathion sensor, Colloids Surfaces B – Biointerf. 96 (2012) 75–79.
[60] S. Zhang, K. Yang, L. Feng, Z. Liu, In vitro and in vivo behaviors of dextran functionalized graphene, Carbon 49 (2011) 4040–4049.
[61] S.M. Chowdhury, S. Kanakia, J.D. Toussaint, M.D. Frame, A.M. Dewar, K.R. Shroyer, et al., In vitro hematological and in vivo vasoactivity assessment of dextran functionalized graphene, Sci. Rep. 3 (2013).
[62] S. Jokar, A. Pourjavadi, M. Adeli, Albumin-graphene oxide conjugates; carriers for anticancer drugs, RSC Adv. 4 (2014) 33001–33006.
[63] X.-Q. Wei, L.-Y. Hao, X.-R. Shao, Q. Zhang, X.-Q. Jia, Z.-R. Zhang, et al., Insight into the interaction of graphene oxide with serum proteins and the impact of the degree of reduction and concentration, ACS Appl. Mater. Interfaces 7 (24) (2015) 13367–13374.
[64] Y.K. Lee, E.J. Choi, T.J. Webster, S.H. Kim, D. Khang, Effect of the protein corona on nanoparticles for modulating cytotoxicity and immunotoxicity, Int. J. Nanomed. 10 (2015) 97–112.
[65] H. Mao, W. Chen, S. Laurent, C. Thirifays, C. Burtea, F. Rezaee, et al., Hard corona composition and cellular toxicities of the graphene sheets, Colloids Surfaces B – Biointerf. 109 (2013) 212–218.
[66] M.J. Hajipour, J. Raheb, O. Akhavan, S. Arjmand, O. Mashinchian, M. Rahman, et al., Personalized disease-specific protein corona influences the therapeutic impact of graphene oxide, Nanoscale 7 (2015) 8978–8994.
[67] Y.F. Li, H.Y. Yuan, A. von dem Bussche, M. Creighton, R.H. Hurt, A.B. Kane, et al., Graphene microsheets enter cells through spontaneous membrane penetration at edge asperities and corner sites, Proc. Natl. Acad. Sci. USA 110 (2013) 12295–12300.
[68] Q. Mu, G. Su, L. Li, B.O. Gilbertson, L.H. Yu, Q. Zhang, et al., Size-dependent cell uptake of protein-coated graphene oxide nanosheets, ACS Appl. Mater. Interf. 4 (2012) 2259–2266.
[69] M. Mahmoudi, I. Lynch, M.R. Ejtehadi, M.P. Monopoli, F.B. Bombelli, S. Laurent, Protein-nanoparticle interactions: opportunities and challenges, Chem. Rev. 111 (2011) 5610–5637.
[70] C.M. Girish, A. Sasidharan, G.S. Gowd, S. Nair, M. Koyakutty, Confocal Raman imaging study showing macrophage mediated biodegradation of graphene in vivo, Adv. Healthcare Mater. 2 (2013) 1489–1500.
[71] G.-Y. Chen, H.-J. Yang, C.-H. Lu, Y.-C. Chao, S.-M. Hwang, C.-L. Chen, et al., Simultaneous induction of autophagy and toll-like receptor signaling pathways by graphene oxide, Biomaterials 33 (2012) 6559–6569.
[72] H. Zhou, K. Zhao, W. Li, N. Yang, Y. Liu, C. Chen, et al., The interactions between pristine graphene and macrophages and the production of cytokines/chemokines via TLR- and NF-kappa B-related signaling pathways, Biomaterials 33 (2012) 6933–6942.
[73] J. Russier, E. Treossi, A. Scarsi, F. Perrozzi, H. Dumortier, L. Ottaviano, et al., Evidencing the mask effect of graphene oxide: a comparative study on primary human and murine phagocytic cells, Nanoscale 5 (2013) 11234–11247.
[74] H. Yue, W. Wei, Z. Yue, B. Wang, N. Luo, Y. Gao, et al., The role of the lateral dimension of graphene oxide in the regulation of cellular responses, Biomaterials 33 (2012) 4013–4021.
[75] J.H. Liu, S.T. Yang, H.F. Wang, Y.L. Chang, A.N. Cao, Y.F. Liu, Effect of size and dose on the biodistribution of graphene oxide in mice, Nanomedicine 7 (2012) 1801–1812.
[76] A.V. Tkach, N. Yanamala, S. Stanley, M.R. Shurin, G.V. Shurin, E.R. Kisin, et al., Graphene oxide, but not fullerenes, targets immunoproteasomes and suppresses antigen presentation by dendritic cells, Small 9 (2013) 1686–1690.
[77] X. Zhi, H. Fang, C. Bao, G. Shen, J. Zhang, K. Wang, et al., The immunotoxicity of graphene oxides and the effect of PVP-coating, Biomaterials 34 (2013) 5254–5261.
[78] A. Paul, A. Hasan, H. Al Kindi, A.K. Gaharwar, V.T.S. Rao, M. Nikkhah, et al., Injectable graphene oxide/hydrogel-based angiogenic gene delivery system for vasculogenesis and cardiac repair, ACS Nano 8 (2014) 8050–8062.
[79] A. Sasidharan, S. Swaroop, C.K. Koduri, C.M. Girish, P. Chandran, L.S. Panchakarla, et al., Comparative in vivo toxicity, organ biodistribution and immune response of pristine, carboxylated and PEGylated few-layer graphene sheets in Swiss albino mice: a three month study, Carbon 95 (2015) 511–524.
[80] S.K. Singh, M.K. Singh, P.P. Kulkarni, V.K. Sonkar, J.J.A. Gracio, D. Dash, Amine-modified graphene. thrombo-protective safer alternative to graphene oxide for biomedical applications, ACS Nano 6 (2012) 2731–2740.
[81] X. Zhang, J. Yin, C. Peng, W. Hu, Z. Zhu, W. Li, et al., Distribution and biocompatibility studies of graphene oxide in mice after intravenous administration, Carbon 49 (2011) 986–995.
[82] H. Wu, H. Shi, Y. Wang, X. Jia, C. Tang, J. Zhang, et al., Hyaluronic acid conjugated graphene oxide for targeted drug delivery, Carbon 69 (2014) 379–389.
[83] A. Sasidharan, L.S. Panchakarla, A.R. Sadanandan, A. Ashokan, P. Chandran, C. M. Girish, et al., Hemocompatibility and macrophage response of pristine and functionalized graphene, Small 8 (2012) 1251–1263.
[84] A. Sasidharan, L.S. Panchakarla, P. Chandran, D. Menon, S. Nair, C.N.R. Rao, et al., Differential nano-bio interactions and toxicity effects of pristine versus functionalized graphene, Nanoscale 3 (2011) 2461–2464.
[85] S.K. Singh, M.K. Singh, M.K. Nayak, S. Kumari, S. Shrivastava, J.J.A. Gracio, et al., Thrombus inducing property of atomically thin graphene oxide sheets, ACS Nano 5 (2011) 4987–4996.
[86] G.D. Wilner, H.L. Nossel, E.C. Leroy, Aggregation of platelets by collagen, J. Clinic. Invest. 47 (1968) 2616.
[87] J.M. Shen, G. Huang, X. Zhou, J. Zou, Y. Yang, Y.F. Chen, et al., Safety evaluation of graphene oxide-based magnetic nanocomposites as MRI contrast agents and drug delivery vehicles, Rsc Adv. 4 (2014) 50464–50477.
[88] H. Ali-Boucetta, K.T. Al-Jamal, K.H. Muller, S.P. Li, A.E. Porter, A. Eddaoudi, et al., Cellular uptake and cytotoxic impact of chemically functionalized and polymer-coated carbon nanotubes, Small 7 (2011) 3230–3238.
[89] G.P. Kotchey, B.L. Allen, H. Vedala, N. Yanamala, A.A. Kapralov, Y.Y. Tyurina, et al., The enzymatic oxidation of graphene oxide, ACS Nano 5 (2011) 2098–2108.
[90] V.E. Kagan, N.V. Konduru, W. Feng, B.L. Allen, J. Conroy, Y. Volkov, et al., Carbon nanotubes degraded by neutrophil myeloperoxidase induce less pulmonary inflammation, Nat. Nanotechnol. 5 (2010) 354–359.
[91] X. Wang, T. Xia, M.C. Duch, Z. Ji, H. Zhang, R. Li, et al., Pluronic F108 coating decreases the lung fibrosis potential of multiwall carbon nanotubes by reducing lysosomal injury, Nano Lett. 12 (2012) 3050–3061.
[92] J.H. Lee, Y.C. Shin, O.S. Jin, E.J. Lee, D.W. Han, S.H. Kang, et al., Cytotoxicity evaluations of pristine graphene and carbon nanotubes in fibroblastic cells, J. Kor. Phys. Soc. 61 (2012) 873–877.
[93] Y. Zhang, S.F. Ali, E. Dervishi, Y. Xu, Z. Li, D. Casciano, et al., Cytotoxicity effects of graphene and single-wall carbon nanotubes in neural phaeochromocytoma-derived PC12 cells, ACS Nano 4 (2010) 3181–3186.

[94] E. Sawosz, S. Jaworski, M. Kutwin, A. Hotowy, M. Wierzbicki, M. Grodzik, et al., Toxicity of pristine graphene in experiments in a chicken embryo model, Int. J. Nanomed. 9 (2014) 3913–3922.
[95] O. Akhavan, E. Ghaderi, A. Akhavan, Size-dependent genotoxicity of graphene nanoplatelets in human stem cells, Biomaterials 33 (2012) 8017–8025.
[96] O. Akhavan, E. Ghaderi, H. Emamy, F. Akhavan, Genotoxicity of graphene nanoribbons in human mesenchymal stem cells, Carbon 54 (2013) 419–431.
[97] O.J. Yoon, I. Kim, I.Y. Sohn, T.T. Kieu, N.-E. Lee, Toxicity of graphene nanoflakes evaluated by cell-based electrochemical impedance biosensing, J. Biomed. Mater. Res., Part A 102 (2014) 2288–2294.
[98] E. Hashemi, O. Akhavan, M. Shamsara, R. Rahighi, A. Esfandiar, A.R. Tayefeh, Cyto and genotoxicities of graphene oxide and reduced graphene oxide sheets on spermatozoa, RSC Adv. 4 (2014) 27213–27223.
[99] S. Das, S. Singh, V. Singh, D. Joung, J.M. Dowding, D. Reid, et al., Oxygenated functional group density on graphene oxide: its effect on cell toxicity, Part. Part. Syst. Charact. 30 (2013) 148–157.
[100] E.L. Khim Chng, C.K. Chua, M. Pumera, Graphene oxide nanoribbons exhibit significantly greater toxicity than graphene oxide nanoplatelets, Nanoscale 6 (2014) 10792–10797.
[101] S.M. Chowdhury, G. Lalwani, K. Zhang, J.Y. Yang, K. Neville, B. Sitharaman, Cell specific cytotoxicity and uptake of graphene nanoribbons, Biomaterials 34 (2013) 283–293.
[102] Y. Si, E.T. Samulski, Synthesis of water soluble graphene, Nano Lett. 8 (2008) 1679–1682.
[103] S.M. Chowdhury, S. Dasgupta, A.E. McElroy, B. Sitharaman, Structural disruption increases toxicity of graphene nanoribbons, J. Appl. Toxicol. 34 (2014) 1235–1246.
[104] X. Sun, Z. Liu, K. Welsher, J.T. Robinson, A. Goodwin, S. Zaric, et al., Nano-graphene oxide for cellular imaging and drug delivery, Nano Res. 1 (2008) 203–212.
[105] C.H. Fu, T.L. Liu, L.L. Li, H.Y. Liu, Q.H. Liang, X.W. Meng, Effects of graphene oxide on the development of offspring mice in lactation period, Biomaterials 40 (2015) 23–31.
[106] T.L. Moore, J.E. Pitzer, R. Podila, X. Wang, R.L. Lewis, S.W. Grimes, et al., Multifunctional polymer-coated carbon nanotubes for safe drug delivery, Part. Part. Syst. Charact. 30 (2013) 365–373.
[107] Y. Talukdar, J.T. Rashkow, G. Lalwani, S. Kanakia, B. Sitharaman, The effects of graphene nanostructures on mesenchymal stem cells, Biomaterials 35 (2014) 4863–4877.
[108] S. Kanakia, J.D. Toussaint, S.M. Chowdhury, T. Tembulkar, S. Lee, Y.-P. Jiang, et al., Dose ranging, expanded acute toxicity and safety pharmacology studies for intravenously administered functionalized graphene nanoparticle formulations, Biomaterials 35 (2014) 7022–7031.
[109] K. Yang, J. Wan, S. Zhang, Y. Zhang, S.-T. Lee, Z. Liu, In vivo pharmacokinetics, long-term biodistribution, and toxicology of PEGylated graphene in mice, ACS Nano 5 (2011) 516–522.
[110] D.A. Jasim, C. Menard-Moyon, D. Begin, A. Bianco, K. Kostarelos, Tissue distribution and urinary excretion of intravenously administered chemically functionalized graphene oxide sheets, Chem. Sci. 6 (2015) 3952–3964.
[111] S.M. Chowdhury, P. Manepalli, B. Sitharaman, Graphene nanoribbons elicit cell specific uptake and delivery via activation of epidermal growth factor receptor enhanced by human papillomavirus E5 protein, Acta Biomater. 10 (2014) 4494–4504.
[112] X.C. Yang, N.N. Zhao, F.J. Xu, Biocleavable graphene oxide based-nanohybrids synthesized via ATRP for gene/drug delivery, Nanoscale 6 (2014) 6141–6150.
[113] Z.G. Liu, L. Zhao, Z. Zhou, T.Z. Sun, Y.G. Zu, Assembly of single-stranded DNA onto HOPG surface at different temperature: atomic force microscopy study, Scanning 34 (2012) 302–308.
[114] A.K. Manna, S.K. Pati, Theoretical understanding of single-stranded DNA assisted dispersion of graphene, J. Mater. Chem. B 1 (2013) 91–100.
[115] S. Husale, S. Sahoo, A. Radenovic, F. Traversi, P. Annibale, A. Kis, SsDNA binding reveals the atomic structure of graphene, Langmuir 26 (2010) 18078–18082.
[116] S.K. Tripathi, R. Goyal, K.C. Gupta, P. Kumar, Functionalized graphene oxide mediated nucleic acid delivery, Carbon 51 (2013) 224–235.
[117] K. Yang, S. Zhang, G. Zhang, X. Sun, S.-T. Lee, Z. Liu, Graphene in mice: ultrahigh in vivo tumor uptake and efficient photothermal therapy, Nano Lett. 10 (2010) 3318–3323.
[118] K. Yang, L. Hu, X. Ma, S. Ye, L. Cheng, X. Shi, et al., Multimodal imaging guided photothermal therapy using functionalized graphene nanosheets anchored with magnetic nanoparticles, Adv. Mater. 24 (2012) 1868–1872.
[119] Z. Yue, P. Lv, H. Yue, Y. Gao, D. Ma, W. Wei, et al., Inducible graphene oxide probe for high-specific tumor diagnosis, Chem. Commun. 49 (2013) 3902–3904.
[120] X.X. Ma, H.Q. Tao, K. Yang, L.Z. Feng, L. Cheng, X.Z. Shi, et al., A functionalized graphene oxide-iron oxide nanocomposite for magnetically targeted drug delivery, photothermal therapy, and magnetic resonance imaging, Nano Res. 5 (2012) 199–212.
[121] L.Z. Feng, K.Y. Li, X.Z. Shi, M. Gao, J. Liu, Z. Liu, Smart pH-responsive nanocarriers based on nano-graphene oxide for combined chemo- and photothermal therapy overcoming drug resistance, Adv. Healthcare Mater. 3 (2014) 1261–1271.
[122] W. Zhang, Z. Guo, D. Huang, Z. Liu, X. Guo, H. Zhong, Synergistic effect of chemo-photothermal therapy using PEGylated graphene oxide, Biomaterials 32 (2011) 8555–8561.
[123] W. Miao, G. Shim, G. Kim, S. Lee, H.-J. Lee, Y.B. Kim, et al., Image-guided synergistic photothermal therapy using photoresponsive imaging agent-loaded graphene-based nanosheets, J. Control. Release 211 (2015) 28–36.
[124] P. Huang, C. Xu, J. Lin, C. Wang, X. Wang, C. Zhang, et al., Folic acid-conjugated graphene oxide loaded with photosensitizers for targeting photodynamic therapy, Theranostics 1 (2011) 240–250.
[125] L. Feng, X. Yang, X. Shi, X. Tan, R. Peng, J. Wang, et al., Polyethylene glycol and polyethylenimine dual-functionalized nano-graphene oxide for photothermally enhanced gene delivery, Small 9 (2013) 1989–1997.
[126] Y. Zhou, Y. Wang, X. Zhang, J. Peng, H. Li, Z. Li, Preparation and characterization of photosensitive and magnetic targeting graphene oxide nanocomposite, J. Nanosci. Nanotechnol. 15 (2015) 2009–2014.
[127] Z. Wang, C. Zhou, J. Xia, B. Via, Y. Xia, F. Zhang, et al., Fabrication and characterization of a triple functionalization of graphene oxide with Fe_3O_4, folic acid and doxorubicin as dual-targeted drug nanocarrier, Colloids Surfaces B – Biointerf. 106 (2013) 60–65.
[128] S. Sabharanjak, S. Mayor, Folate receptor endocytosis and trafficking, Adv. Drug Deliv. Rev. 56 (2004) 1099–1109.
[129] L. Zhang, J. Xia, Q. Zhao, L. Liu, Z. Zhang, Functional graphene oxide as a nanocarrier for controlled loading and targeted delivery of mixed anticancer drugs, Small 6 (2010) 537–544.
[130] A. Sasidharan, A.J. Sivaram, A.P. Retnakumari, P. Chandran, G.L. Malarvizhi, S. Nair, et al., Radiofrequency ablation of drug-resistant cancer cells using molecularly targeted carboxyl-functionalized biodegradable graphene, Adv. Healthcare Mater. 4 (2015) 679–684.
[131] A. Lange, R.E. Mills, C.J. Lange, M. Stewart, S.E. Devine, A.H. Corbett, Classical nuclear localization signals: definition, function, and interaction with importin alpha, J. Biol. Chem. 282 (2007) 5101–5105.
[132] D. Lechardeur, A.S. Verkman, G.L. Lukacs, Intracellular routing of plasmid DNA during non-viral gene transfer, Adv. Drug Deliv. Rev. 57 (2005) 755–767.
[133] K.M. Wagstaff, D.A. Jans, Nucleocytoplasmic transport of DNA: enhancing non-viral gene transfer, Biochem. J. 406 (2007) 185–202.
[134] G. Ni, Y. Wang, X. Wu, X. Wang, S. Chen, X. Liu, Graphene oxide absorbed anti-IL10R antibodies enhance LPS induced immune responses in vitro and in vivo, Immunol. Lett. 148 (2012) 126–132.
[135] S. Kim, S.R. Ryoo, H.K. Na, Y.K. Kim, B.S. Choi, Y. Lee, et al., Deoxyribozyme-loaded nano-graphene oxide for simultaneous sensing and silencing of the hepatitis C virus gene in liver cells, Chem. Commun. 49 (2013) 8241–8243.
[136] E. Byun, H. Lee, Enhanced loading efficiency and sustained release of doxorubicin from hyaluronic acid/graphene oxide composite hydrogels by a mussel-inspired catecholamine, J. Nanosci. Nanotechnol. 14 (2014) 7395–7401.
[137] F.F. Song, W.K. Hu, L.Q. Xiao, Z. Cao, X.Q. Li, C. Zhang, et al., Enzymatically cross-linked hyaluronic acid/graphene oxide nanocomposite hydrogel with pH-responsive release, J. Biomater. Sci.-Polym. Ed. 26 (2015) 339–352.
[138] J.H. Wu, A.P. Chen, M. Qin, R. Huang, G. Zhang, B. Xue, et al., Hierarchical construction of a mechanically stable peptide-graphene oxide hybrid hydrogel for drug delivery and pulsatile triggered release in vivo, Nanoscale 7 (2015) 1655–1660.
[139] S. Fusco, H.W. Huang, K.E. Peyer, C. Peters, M. Haberli, A. Ulbers, et al., Shape-switching microrobots for medical applications: the influence of shape in drug delivery and locomotion, ACS Appl. Mater. Interf. 7 (2015) 6803–6811.

2 Project Outline

2.1 Drug delivery using nanotherapeutic agents

The use of nanoparticles as drug delivery agents has become a very popular area of research due to the promise of targeted delivery leading to increased efficacy and reduced off-target effects of the therapeutic cargo. In addition, the use of nanocarriers may improve the stability of hydrophobic drugs and protect drugs vulnerable to degradation. For biotherapeutics such as DNA and RNA this latter consideration is of particular importance, as is the their delivery not only to the target cells, but the specific intracellular compartment where they perform their action; a carefully designed drug delivery vehicle may provide these outcomes – by tailoring size, shape and surface chemistry, including the attachment of targeting ligands.

However, the design of a nanoparticle drug delivery system that can meet these ends faces significant challenges; the optimum nanocarrier would be stable and inert as it travels through the body, while being able to traverse the necessary physiological barriers and deliver their payload to both the target cells, and often the specific intracellular region necessary for therapeutic effect. The variation of uptake mechanisms, the complexity of the physiological environment and variation on cell type make the picture even more complex [2]. Size, shape and rigidity are all known to affect uptake depending on cell type, and hydrophobicity and charge both affect interactions with the cells and surrounding physiological environment [2, 3]. For these reasons, a plethora of different nanoparticles exist in the drug delivery research field that aim to overcome some of the challenges listed above, and provide specific solutions for particular disease targets. Some of the most commonly used nanoparticles for drug delivery are described below.

2.1.1 Liposomes

Some of the first drug delivery vehicles both conceived, and then to reach the clinic were liposomes, which are nanospheres constructed of a phospholipid bilayer with a hydrophobic core and a central hydrophilic region [4]. This structure emulates the membrane of eukaryotic cells, and it was thought that this may facilitate cell entry and endosomal escape [5]. The liposomal

structure also theoretically allows the inclusion of both hydrophilic and hydrophobic cargo in the core and membrane respectively – however hydrophobic drug loading into the membrane can often lead to reduced stability and increased leakage, so other loading mechanisms may need to be pursued [4]. Since their early development, liposomes have been optimised for increased stability, circulation lifetime and targeting, and both their structure and the loading mechanisms used have been improved to reduce leakage and improve drug release at the target [4]. Related nanocarriers include lipoplexes, which do not maintain the same well-ordered structure as liposomes, but whose cationic charge allows complexation with nucleic acid cargo [6]. Numerous types of liposomes and lipoplexes are commercially available and are routinely used *in vitro*, as well as in the clinic, with liposome formulations used for various cancers, meningitis, pain therapy and fungal infections, and a significant number in phase I and II clinical trials [4]. The majority of applications, however, remain small molecule drugs rather than biotherapeutics such as nucleic acids.

2.1.2 Viral-like nanoparticles and viral vectors

Other nanocarriers that have used nature as inspiration are viral vectors and viral-like nanoparticles; viral vectors are existent viruses that have been modified so that their pathogenic payload is removed, and replaced with the nucleic acid of choice, while viral-like nanoparticles make use of the proteinaceous material that makes up the body of a virus in a synthetic nanoparticle with inorgranic core [5]. While viral vectors and viral-like nanoparticles have been very successful in the transfection of genetic material, a number of concerns remain, including immunogenicity – with a severe immune response leading to the death of a patient taking part in a clinical trial [7], limitations on the cargo that can be delivered, and a lack of flexibility in modification – with attempts to modify their targeting leading to reduced efficiency or complete failure [7].

2.1.3 Polymeric nanoparticles

Polymeric nanoparticles were another of the first synthetic nanoparticles to be developed, along with liposomes. Biodegradable or non-biodegradable synthetic or natural polymers are used to complex with nucleic acids to form nanospheres in which the cargo is dispersed throughout the nanoparticle, or nanocapsules in which the polymer forms a shell around the encapsulated cargo [2]. This type of nanocarrier is highly versatile due to the sheer numbers of polymers available and their possible combinations [5]; however, some of the most commonly used synthetic non-degradable are HPMA (*N*-(2-hydroxypropyl)-methacrylamide copolymer), PVP (poly(vinylpirrolidone)) and PEG (polyethylene glycol) – as they cause no significant toxicity and are often in combination with other nanocarriers [5]. Natural polymers such as silk, chitosan, albumin and heparin have also been used extensively [5]. Many of the polymers used are cationic, which encourages both the condensation of nucleic acids and ionic interactions with the cell membrane, which may cause adsorption mediated cell-binding and uptake [2, 8]. The condensation of nucleic acids not only functions to protect them from nucleases, but also decreases their size, which may increase transfection efficiency by increasing cell uptake and facilitating easier traversal of other physiological barriers [2]. The polymers may facilitate endosomal escape *via* an interaction between the delivery compound and the changing pH of the endosome as it is trafficked towards the lysosomes; notably polyethylenimine (PEI) is thought to cause osmotic swelling and disintegration of the endosome membrane due to its high buffering capacity [9]. PEI has been found to have a high transfection efficiency *in vitro* and has reached phase I and II clinical trials, where it was again successful, but toxicity and bio-degradability proved problematic [2]. Lower molecular weight polymers were found to have lower toxicity than those with higher molecular weight; however, their transfection efficiency is also reduced [8].

Dendrimers are a type of polymeric nanoparticle whose hyperbranched structure forms a spherical shape that allows the entrapment of therapeutic cargo within their structure [5]. They are well-defined in terms of dispersity and versatile due to the functionality afforded by their

repeating polymeric units [5]; however, issues surrounding haemocompatibility and toxicity have led to challenges in their development and application [5].

2.1.4 Cell penetrating peptides

Cell penetrating peptides (CPPs) have been found to traverse the membrane in an energy and receptor independent manner, avoiding endocytosis, the subsequent endosomal entrapment and therefore lysosomal degradation. Traversal is facilitated by peptides and proteins with short but distinct domains of around 20-30 residues [10]. While the mechanism is poorly understood, it has been suggested that it is due to their strong affinity for the cellular lipid membrane; the mechanism is very efficient, targets the nucleus and works on a wide range of cells with no strict cargo limit and no immunogenic or inflammatory properties observed [10]. CPPs are based on sequences that exist in natural protein transduction domains that are often incorporated onto certain viral bodies, such as HIV-1 in the form of the Tat peptide [5, 11]. Cargo can be attached to the peptides *via* covalent or non-covalent means, with the latter often preferred, as it is less likely to interfere with the cargo's biological activity [5]. This latter approach often makes use of electrostatic interactions for complexation with nucleic acids [5]. The presence of cationic residues such as lysine and arginine appear to improve transfection efficiency, while the presence of histidine can promote endosomal escape in the same way as PEI [5] – as described earlier.

However, the attachment of larger cargoes such as DNA has led to the observation of endocytic pathways being used [10], and although peptides from L-amino acids are inherently biodegradable, if they contain a large number of exposed positive charges or hydrophobic regions, they may disrupt cell membranes – leading to cytotoxicity [8].

2.1.5 Carbon-based nanomaterials

Over the past decades, sp^2 carbon-based nanomaterials have drawn increasing attention in the biomedical sciences – in addition to graphene, carbon nanotubes have been used for a range of biomedical purposes *in vitro* including the delivery of nucleic acids and water insoluble drugs to

varying levels of success [12-15]. The attention is due in part to their low dimensionality, the ease with which they are functionalised and their relative biological purity – being composed primarily of carbon [13]. The two dimensional network of sp^2 hybridised carbon atoms that makes up graphene can be seen as the basis of all graphitic materials, including graphite, CNTs and buckyballs [16], where CNTs are a cylindrical carbon allotrope that can be viewed as a seamless rolled up sheet of single or few layer graphene [13]. The one dimensional nature of CNTs means that they may behave in a way that is distinct from spherical nanoparticles in a physiological environment [13]; indeed, single walled CNTs have been observed to passively translocate the cell membrane [17-19] therefore escaping endosomal entrapment. As with graphene, it has been found that the functionalisation of the CNT surface is of paramount importance in order to ensure their stability in physiological environments, reduce their toxicity and control their interactions with cells [12, 14, 18]. Nevertheless, concerns exist over toxicity *in vivo* induced by contamination by materials used in the preparation of CNTs and aggregation and bundling of the fibres [13, 20]. In addition, CNTs are often not able to protect their cargo, and may require additional functionalisation to do so; DNA adsorbed to CNTs' sidewalls has been observed to be cleaved by nucleases in the serum [12] and although some therapeutic cargo may be inserted into the core of the CNT, in general there needs to be some external stimulus for its release [21], and while triggered release is desirable, a lack of flexibility is less so.

Graphene maintains many of the desirable features of CNTs, such as low dimensionality, ease of functionalisation and relative chemical purity; however, it boasts a surface area that is double that of CNTs, lacks the fibrous geometry and is generally prepared without the use of metal catalysts that can become risks for toxicity. In relation to this project, it was hoped that minimally functionalised pristine graphene could replicate the ability of CNTs to passively traverse the cell membrane, thus evading endosomal entrapment. Such a feature would set pristine graphene apart from many of the other nanoparticles discussed in this section, since those are either primarily taken up by endocytosis or use mechanisms that are inherently toxic to escape the endosome. Finally Manchester was well-placed in terms of resources and expertise for graphene

research. It is for these reasons that graphene was chosen as the drug delivery vehicle to be investigated in this project.

2.2 Therapeutics targeting to chronic lymphocytic leukaemia

The choice of therapeutic target for the project was made to address clinical need, but also to provide a relevant model to test the particulate suspension of graphene. Control blood cells (PBMCs) are also relevant to the broader immune environment, containing macrophages and lymphocytes, known to perform phagocytosis and pinocytosis respectively. They are readily purified and maintained in culture and can be assessed using flow cytometry and microscopy. Chronic lymphocytic leukaemia (CLL) cells are neoplastic lymphocytes that are directly related to PBMCs, and as a therapeutic target have the benefits of being accessible to therapeutic agents both in the blood plasma and through the fenestrated architecture of the bone marrow vasculature [22], thereby overcoming issues of nanoparticle accessibility present in other disease targets.

Chronic lymphocytic leukaemia is a B-cell lymphoproliferative disorder and is the most common adult leukaemia in the Western world [23, 24]. The prognosis is highly variable, but approximately half of all sufferers experience progressive disease, and in a significant proportion of patients life expectancy may be only 2-3 years [23, 24]. Combination chemotherapies including anti-CD20 antibodies have led to improved response rates, but the disease predominantly affects older adults, who have co-morbidities and poor performance status, and therefore cannot tolerate these approaches [23]. A new generation of signal-kinase inhibitors (including Ibrutinib and Idelalisib) offer good response rates, but do not achieve cure, so ongoing treatment costs, emerging resistance and off target adverse effects are a significant problem [23, 25]. The formulation of targeted and effective treatment routes to provide high response rates while minimising side effects is therefore a significant clinical need. The CXCR4 chemokine receptor is over-expressed on CLL B-cells [26, 27], and has been a pharmaceutical target for the last 20 years due to its importance in a number of disease states, with some drugs currently in common use in

a clinical setting. By using the most common of the clinically approved CXCR4-targeting drugs AMD3100, as a foundation for the design, synthesis and characterisation of a targeting ligand for tailoring GO, it was hypothesised that the resultant drug would maintain high specificity and receptor affinity, forming the basis for future therapeutic targeting of CXCR4.

2.3 Project aims and objectives

Chapter 1 has shown that the use of GFNs in biomedical applications is a burgeoning area of research with significant potential, but remains a very young field. The 2D geometry of GFNs lends itself to their use as a platform for a highly functionalised therapeutics delivery vehicle that can be specifically targeted to disease cells. However, significant work remains to improve the homogeneity of the samples; before further functionalisation can take place in order to tailor the GFNs for their specific application, it is important that the material be very well defined before it can move further towards a place in the clinic.

From this background it was hypothesised that with the use of controlled preparation methods and extensive characterisation, employing a combination of established and novel techniques, graphene and related materials could be prepared appropriately for specific targeting to leukaemic cells.

In order to test this hypothesis, the aims of this project were as follows:

i. To investigate the use of amino acids as biocompatible exfoliating and suspending agents for pristine graphene.
ii. To prepare and characterise purified and functionalised GO tailored for use in therapeutics delivery.
iii. To design and synthesise a targeting ligand that could be conjugated to GFNs in order to provide targeted interaction with chronic lymphocytic leukaemia cells (CLL).

The details of these aims are illustrated in more depth below.

2.4 Preparation and characterisation of GFNs as therapeutics platform

As described in Chapter 1, reports regarding the interaction of GFNs with cellular and extracellular components both *in vitro* an *in vivo* can often be contradictory. These apparent contradictions in the literature are often due to the variations in preparation methods, which result in varied purity, degree and type of functionalisation, and geometry. In particular, while GO incorporates many desirable features such as hydrophilicity and the combination of polyaromaticity and oxygenated functional groups, it is known to be highly heterogeneous, both in terms of its physical and chemical properties.

In order to prepare and use a GFN therapeutics vehicle for use in CLL, two main avenues were pursued. Both avenues focused on the use of controlled systems and methods that would minimise heterogeneity.

The first focused on the preparation of pristine graphene with amino acids as biocompatible, small molecule exfoliating and suspending agents used alone in aqueous solution. Pristine graphene is less chemically heterogeneous than GO, and it was thought that the combination of hydrophobicity and its unique geometry may lead to the passive translocation of cell membranes, as has previously been observed with some CNTs. Using literature-standard models of exfoliation, a range of structurally related amino acids would be tested for their ability to exfoliate and suspend pristine graphene. By analysing the effect of sonication time, amino acid concentration and the variation in amino acid molecular structure on the suspensions' concentration and stability, and the flakes' thinness, an assessment of the best system could be performed.

The second avenue focused on the use of GO as a therapeutics delivery vehicle. Due to the known heterogeneity of GO suspensions after preparation with the Hummer's method (or variant), additional purification and significant characterisation using both traditional and novel methods would be undertaken to assess the viability of GO preparations for use in biomedical applications. The characterisation would focus on both the physicochemical characteristics of the flakes and their behaviour in diverse biologically relevant media. One of the benefits of GO is the

variety of chemical groups present on its surface, which can be used to tailor the flakes' functionality; therefore further functionalisation steps would be undertaken to improve the biocompatibility of the flakes. The interaction between the different GO preparations would then be analysed with regards to relevant cell culture models so that their suitability for use in targeting therapeutics against leukaemia could be assessed.

3 Preparation and characterisation of graphene using amino acids as exfoliating and suspending agents

3.1 Introduction

The field of graphene in therapeutics delivery is rapidly expanding, and much of the initial research has focused on GO due to its inherent solubility and the ease with which it can be functionalised (see Chapter 1). However the use of non-covalent functionalisation of pristine graphene is less developed – especially when using small molecules, which may conserve the quasi-2D nature of the graphene flakes. This Chapter presents a study in which amino acids were used as exfoliating and suspending agents for pristine graphene flakes in aqueous media.

3.1.1 Liquid exfoliation of graphene

Since its isolation in 2004 by micromechanical exfoliation, the methods for producing graphene have evolved, often with the routes being taken determined by the desired end application. For instance, when the aim is the production of electronic devices, direct deposition or preparation onto a substrate may be desirable, and therefore techniques such as chemical vapour deposition or annealing silicon carbide substrates may be used [28]. However, for applications such as composite production, printable electronics or use in the biomedical sphere, liquid phase exfoliation of graphene or GO is attractive. When the aim is to produce a suspension of pristine graphene, the most common route uses a disruptive physical technique such as sonication, in the presence of either solvents or surfactants with a high energetic affinity to the graphene basal plane to induce exfoliation and reduce the energetic cost of exfoliation respectively [28-30].

3.1.1.1 Sonication

While the oxidation of graphite results in the functionalisation of individual graphene flakes in the graphitic stack – leading to a reduction in the interflake interactions – such that the graphite oxide may be exfoliated simply by stirring [31], the strong interflake interactions present in pristine graphite mean that the mechanical force required to separate the flakes is more significant, therefore researchers turned to the use of ultrasonic exfoliation. Through investigation of ultrasonic exfoliation in water-surfactant systems using computational modelling, [32] reported that exfoliation occurs laterally (rather than perpendicular to the flake) and with each sidestep of the flakes with respect to one another, a surfactant molecule is required to 'lock' the flakes out of line with each other.

The process of ultrasonication is illustrated in Figure 3-1. As the liquid is subjected to ultrasonic vibrations, any gas dissolved in the liquid will act as weak points where bubbles can form due to the oscillating pressure and the coalescence of microbubbles, which will then oscillate in a series of compression and rarefaction events. The type of sonication that the system is subjected to can be broadly split into stable and inertial cavitation, as described in Figure 3-1. Inertial cavitation is often considered to be more aggressive than stable cavitation as the bubbles are often less stable and therefore more likely to undergo violent collapse, during which powerful microjets may be ejected [33, 34]. However, even in stable cavitation, the bubbles are likely to grow over time due to coalescence events, to a point at which they become unstable and undergo violent collapse; in addition, inertial cavitation may lead to the formation and retention of many microbubbles that are unlikely to produce such powerful microjets as the larger bubbles when they collapse – if they collapse at all [34].

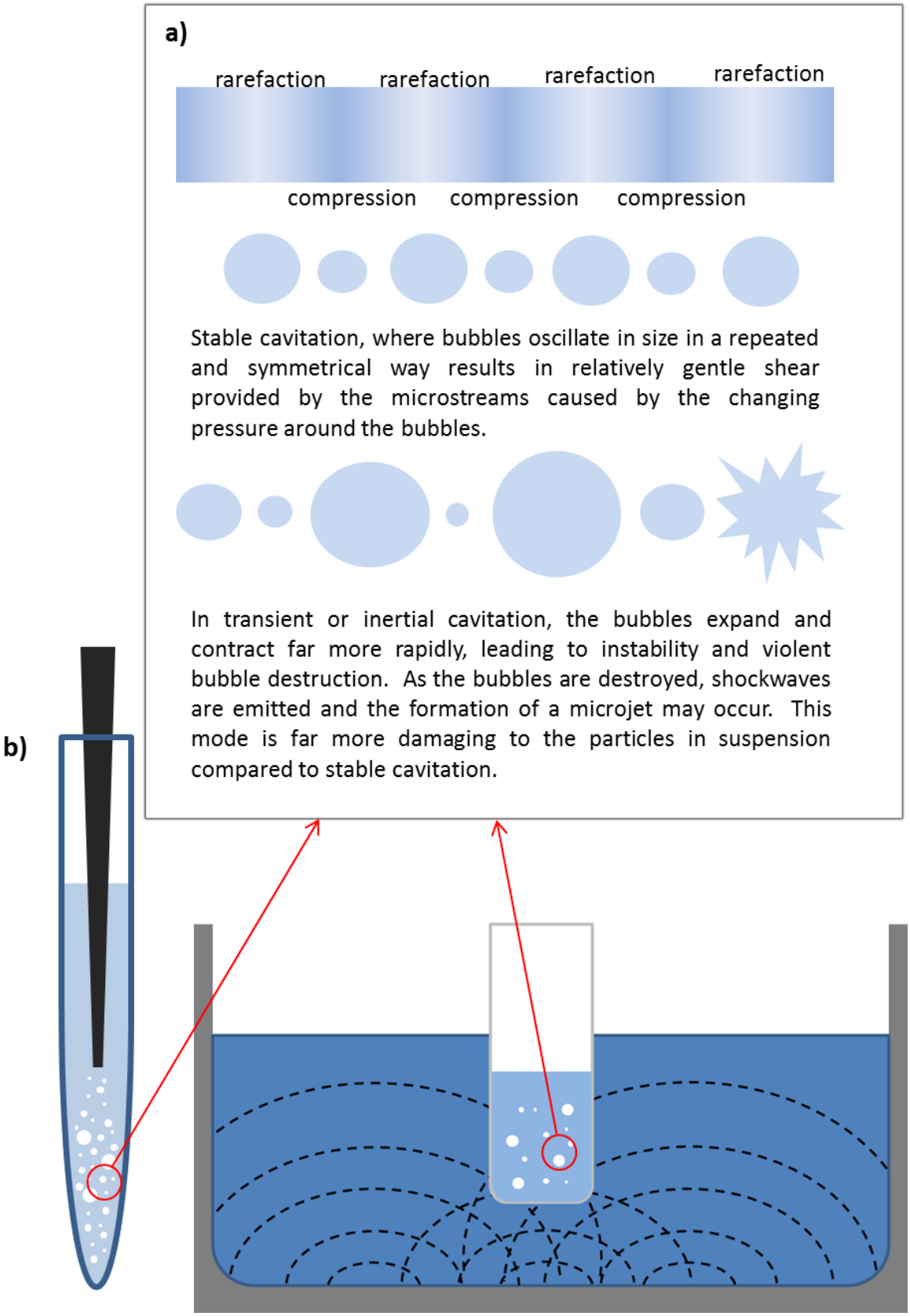

Figure 3-1 – A schematic representation of sonication mechanisms. a) Illustration of the mechanisms involved in ultrasonication adapted from Capelo-Martinez [33] b) illustration of probe and bath sonication

The modes of action for bath and probe sonication are illustrated in Figure 3-1. In bath sonication, a submerged vessel filled with the suspension to be sonicated is subjected to ultrasonic waves transmitted from the bottom of the bath, under which sits a signal transducer, and travel to the sample through the water. Interference can lead to regions of low and high amplitude within the bath, and reflection from the vessel surface can significantly reduce the intensity of the waves that reach the sample [33]. In contrast, the ultrasonic waves in direct probe sonication emanate from the probe itself, which expands and contracts at ultrasonic frequencies, leading to patterns of increased and reduced pressure that travel through the sample. While similar effects of interference may occur due to the reflection of the ultrasonic waves from the vessel walls, and inhomogeneities in the probe itself, the lack of barriers between the probe and the sample itself lead mean that the majority of the incident intensity is retained [33]. For this reason, bath sonication is considered to be significantly gentler than direct probe sonication, and researchers must balance the significantly reduced sonication times against the increased likelihood of scission and the introduction of defects in probe sonication. For biomedical applications, smaller lateral dimensions are often desirable; hence probe sonication is more suitable than for applications in electronics or composites.

3.1.2 Solvent systems and surfactants

Initial work to exfoliate and suspend pristine graphene often made use of organic solvents such as *N*-Methyl-2-pyrrolidone (NMP) [35], orthodichlorobenzene [36] and dimethylformamide (DMF) [37, 38] to make very high concentration suspensions of graphene platelets; however, the solvents' toxic nature and very high boiling points made them problematic for the applications for which they may be most desirable – including composite formation, printable electronics and biological applications, as the residual solvent is very difficult to remove [37]. Some attention turned to lower boiling point solvents, which would facilitate materials science applications, and it was found that suspensions of reasonably high concentration could be produced using solvents such as isopropyl alcohol (IPA) and chloroform [37], which should evaporate completely to leave

pristine graphene flakes without contamination. In addition, in the realm of printable electronics and biological applications, attention was turned to the use of suspending agents, including pyrene derivatives [39-43], and other relatively small molecules that included aromatic regions such as sodium cholate [44] and melamine [45], each of which make use of the presence of aromatic rings in the molecules' structure to increase lipophilicity and facilitate π-π stacking onto the pristine graphene flakes. Larger surfactant or polymer molecules such as sodium dodecylbenzylsulfate (SDBS) [46], dipalmitoylphosphatidylcholin (DPPC) [47], serum albumin [47] and block copolymers [48] have been used, but their large size arguably removes much of the desirable 2D geometry of the graphene flakes.

Amino acids have been used to coat various nanoparticles, both to improve their stability and to modify their interactions with the extracellular environment. Cai *et al.* [49] used aspartic acid, glycine, leucine, serine and lysine to coat gold nanoparticles, while Dubey *et al.* [50] covalently linked tyrosine and tryptophan to gold nanoparticles, with their hydrophobic aromatic regions extended outwards, and found that they were able to disrupt the formation of amyloid fibrils.

Within the field of graphene, Guo *et al.* [51] used tryptophan as a stabilising agent for rGO flakes by introducing tryptophan to a GO dispersion, and then reducing the GO using hydrazine hydrate at 90 °C. The dispersion prepared was shown to be dark in colour, and highly stable in aqueous media compared to GO reduced without the tryptophan. This paper showed the potential for amino acids to be used as stabilising agents for graphene derivatives, particularly minimally functionalised graphene flakes; however, it is unknown whether the hydrazine reduction step would have affected the tryptophan or its attachment to the GO flakes – either positively or negatively. Mallakpour *et al.* [52] used a range of aliphatic and aliphatic-aromatic amino acids to covalently functionalise GO using a nucleophilic substitution reaction that targeted the carboxylic acid and epoxy groups on the GO surface. In the paper it was reported that the stability of the suspensions were improved compared to GO without additional functionalisation; however, the

flakes functionalised with tyrosine exhibited a scrolled structure when their morphology was analysed.

In this work, the essential amino acids valine, phenylalanine, tyrosine and tryptophan were used as stabilising agents to exfoliate and suspend graphene flakes in water, with the aim of retaining the desirable flake-like geometry of the graphene and its pristine surface chemistry, while using suspending agents that were known to be biologically benign (GRAS by the FDA, USA). The interaction between various amino acids and graphene derivatives has been studied by various groups, most of whom focused on using theoretical methods such as density functional theory (DFT), with particular interest in applying the results to peptide adsorption (see Table 3-1). Very little work, besides that performed by Guo *et al.* [51], has been performed experimentally regarding their ability to exfoliate and suspend pristine graphene in aqueous solution.

In this project, initial work was performed on L-valine; while its small size renders valine largely water soluble, its structure consists of a hydrophilic and a hydrophobic region (Figure 3-2). It was therefore hypothesised that the hydrophobic region would interact with graphene's hydrophobic basal plane, and that the nucleating valine molecules would be stabilised on the flakes' surfaces *via* intermolecular hydrogen bonding, as occurs during valine's crystallisation [53]. Other structurally related amino acids with increasing partition coefficients (given in Table 3-2), and in which the structure included an aromatic ring were then assessed, to determine the effect of the molecular structure on the capacity to successfully exfoliate and suspend graphitic material.

Table 3-1 - Table of amino acid interaction energies with different forms of graphene. Values calculated theoretically using a range of models [54-56]

Amino Acid	Modelling method	Interaction energy (eV)	Intermolecular distance (Å)	Graphene type	Literature reference
Phenylalanine	Generalised gradient approximation & Møller-Plesset perturbation theory	0.25(0.62)	3.33	Pristine	[54]
Tyrosine		0.31(0.76)	3.34		
Tryptophan		0.42(0.84)	3.5		
Phenylalanine	Molecular dynamics in vacuum and water	-0.68 -0.12		Pristine	[55]
Tyrosine		-0.72 0.10			
Tryptophan		-0.80 -0.22			
Valine		-0.43 0.00			
Phenylalanine	Density functional theory (M05-2X & M06-2X)	0.149		Pristine	[56]
		0.209		GO	
Tyrosine		0.169		Pristine	
		0.398	1.88 (H-bond)	GO	
Tryptophan		0.249		Pristine	
		0.448	2.15 (H-bond)	GO	

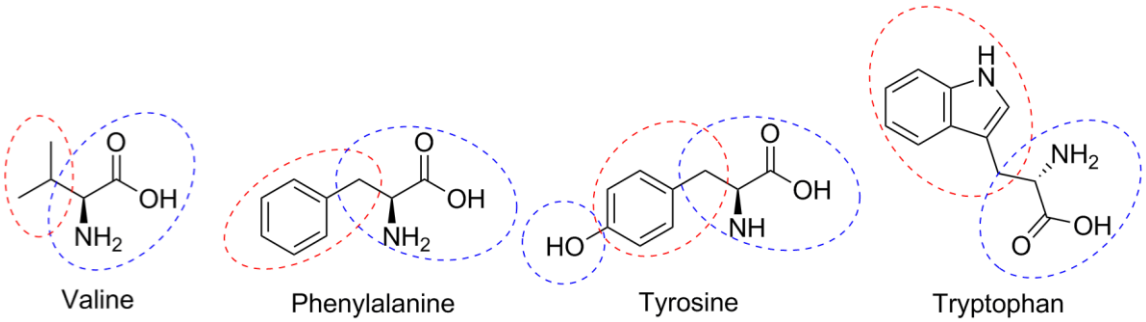

Figure 3-2 – Molecular structures of valine, phenylalanine, tyrosine and tryptophan. The amino acids used in this section to exfoliate and suspend graphene; hydrophobic regions are indicated in red, while hydrophilic are indicated in blue

Table 3-1 – Lipophilicities of valine, phenylalanine, tyrosine and tryptophan LogP values for the four amino acids used for exfoliation and suspension of graphene, reflecting their respective lipophilicities. LogP values were predicted using chemicalize.org and ChemAxon, 09/2016

Amino acid	LogP value
Valine	-1.95
Phenylalanine	-1.18
Tyrosine	-1.49
Tryptophan	-1.09

It was hypothesised that both as the LogP value of the amino acids increased (valine < tyrosine< phenylalanine < tryptophan) and as the structures included one or more aromatic regions the strength of the interaction would be enhanced. Many of the previous studies on the use of small molecule exfoliating and suspending agents has been most successful when using molecules with high LogP values and multiple aromatic rings in the structure; this is particularly apparent in the case of the pyrenes, but is also apparent in the use of sodium cholate (LogP = 2.48). The structural similarity of the molecules provided a controlled method of assessing the effects of each structural variation on the overall interaction of the molecules with the flakes and each other.

3.1.3 Characterisation of graphene suspensions

In this chapter pristine graphite and stacked graphene nanofibres (SGNFs) were used as starting materials for exfoliation and suspension using amino acids dissolved in water, where bath or probe sonication was used as the exfoliation method. The suspensions and the flakes were characterised using Ultraviolet-Visible Absorption Spectroscopy (UV-Vis), Dynamic Light Scattering (DLS) and Atomic Force Microscopy (AFM) respectively.

3.1.3.1 Scattering and absorption methods

Scattering and absorption methods of characterisation can provide information on two aspects of a suspension. They may be considered to be macroscopic characterisation methods, allowing a rapid view on the overall quality of a suspension; and as they interact with a large number of the flakes in suspension, the results provide a statistical overview of the flakes present.

One of the primary methods with which the graphene suspensions are characterised is by using their absorption spectrum in the UV-visible range. This characterisation technique is commonly used in a number of different fields, due to the wide availability of the equipment, its speed and ease of analysis. In the field of graphene, researchers firstly look for the characteristic spectrum shape to ensure that the suspension is indeed that of graphene; at approximately 265 nm a peak is observed that corresponds to the π-π^* transition of the C=C bond, followed by a tail that extends into the higher wavelengths [57, 58] – despite its thinness, the characteristic linear dispersion of the electrons present in graphene's polyaromatic basal plane mean that it absorbs strongly in the visible region [59]. This tail may then be used to determine the concentration that is present in the suspension, making use of the Beer-Lambert Law (Equation 1) [60].

Many reports in the literature describe the determination of the extinction coefficient for individual graphene suspensions at λ = 660 nm. In these reports the mass of graphene present in the samples was measured by filtering the suspension and weighing the flakes deposited, before measuring a calibration curve with known quantities of graphene present, as the extinction

coefficient at this wavelength was found to depend on the solvent or surfactant solution that the flakes were suspended in [30, 35, 44, 46, 61]. However, Backes *et al.* [60] found a widely applicable extinction coefficient of α_λ=4861 [$Lg^{-1}m^{-1}$] at λ = 750 nm, which remained accurate for a wide range of graphene suspensions, including both those in organic solvents and those that used surfactants or other stabilising agents in aqueous solution.

$$A = \alpha_\lambda C l \qquad \textbf{Equation 1}$$

where, α_λ = extinction coefficient [$Lg^{-1}m^{-1}$], C = concentration [gL^{-1}], A = absorbance

It is important to note that the concentration determined by this method is not solely that of single or few layer graphene flakes, but incorporates all suspended graphitic material – especially as A is contributed to both by absorbance and scattering. Very thick flakes would be expected to rapidly precipitate but any that remain in suspension would have a strong scattering contribution that is indistinguishable from the absorbance contribution in a standard UV-Vis spectrometer [60], therefore additional techniques such as AFM are generally considered to be necessary to determine the thicknesses of flakes in suspension.

It has also been found that the shape of the UV-vis spectrum can provide information about the quality of the flakes themselves. An empirical formula was derived by Backes *et al.* [60] (below), that can be used to determine the average number of graphene layers per flake from the shape of the suspension's absorption spectrum.

$$< N >= \left(35.7 \times \frac{\varepsilon_{550}}{\varepsilon_{325}}\right) - 14.8 \qquad \textbf{Equation 2}$$

Where ε_λ = absorption at the wavelength λ and <*N*> is the average number of layers that the flakes in suspension are comprised of. This equation was found to be robust regardless of the inclusion of scattering contributions, and hence can be used with a normal UV-vis spectrometer. The error associated with the equation is relatively large, at approximately 20%; however its use

can still give an approximation with regards to the flakes' relative thickness, particularly with regards to other suspensions measured in the same way.

3.1.3.2 Dynamic Light Scattering

Dynamic light scattering (DLS) is another commonly used measurement technique for characterising the size of both macromolecules and nanoparticles in suspension, including graphene. DLS depends on the scattering of laser light by small particles in suspension undergoing Brownian motion. The movement of the particles with respect to the incident light means that the scattered light is emitted with varying phase and frequency due to Doppler Broadening; the scattered light will therefore interfere either constructively or destructively with the incident light, resulting in a speckle pattern that changes over time, with the movement of the particles [62, 63]. Using this information, the apparent hydrodynamic radii of the flakes (R_h) is determined using the Stokes Einstein equation, and the volume fraction of the different sizes detected is found using Mie theory [62, 63].

Both the Stokes-Einstein equation and Mie theory assume that the particles present are hard spheres that scatter light elastically. This is a valid assumption for many nanoparticles and macromolecules, which are essentially globular; however, in the case of rods and flakes the assumption breaks down, as the diffusion coefficient may vary depending upon the direction that the body is moving in, and as variation due to rotational diffusion becomes significant, illustrated in Figure 3-3. For these reasons, the measurements found using DLS should be treated with care, and first correlated with measurements performed using direct measurement methods such as AFM [64]. In this chapter DLS is only used to assess the propensity for the flakes to aggregate of the flakes, rather than measure the individual flakes themselves.

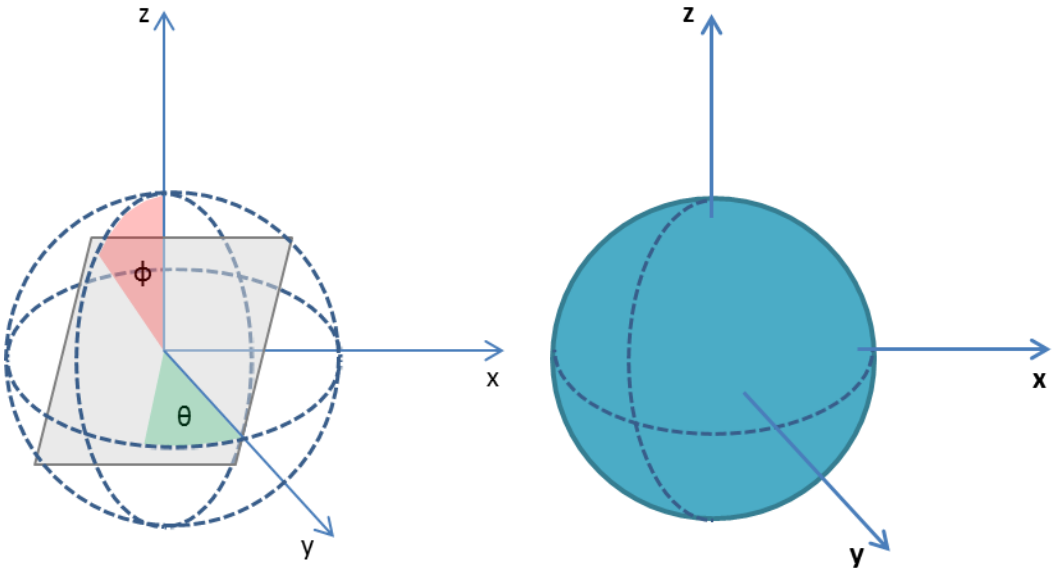

Figure 3-3 – Illustration of the diffusional degrees of freedom of a flake, compared to a sphere

3.1.3.3 Atomic force microscopy

Atomic force microscopy (AFM) is a form of scanning probe microscopy that is commonly used to assess the morphology of liquid exfoliated graphene by measuring the topography of a sample. A sharp tip mounted on a flexible cantilever raster-scans across a sample, and its topography is measured by assessing the movement of a laser spot on a photodetector that is bounced off the back of the cantilever, as shown in Figure 3-3. Atomic resolution can be obtained depending on the nature of the set-up, including the tip radius and vibration isolation of the microscope, however most set-ups can obtain resolution < 5 nm. From this information, the thickness and lateral dimensions of the flakes that have been prepared can be investigated, and which is important for suspensions that are to be used in biological applications, particularly as many suspensions of graphene prepared using liquid exfoliation are very polydisperse.

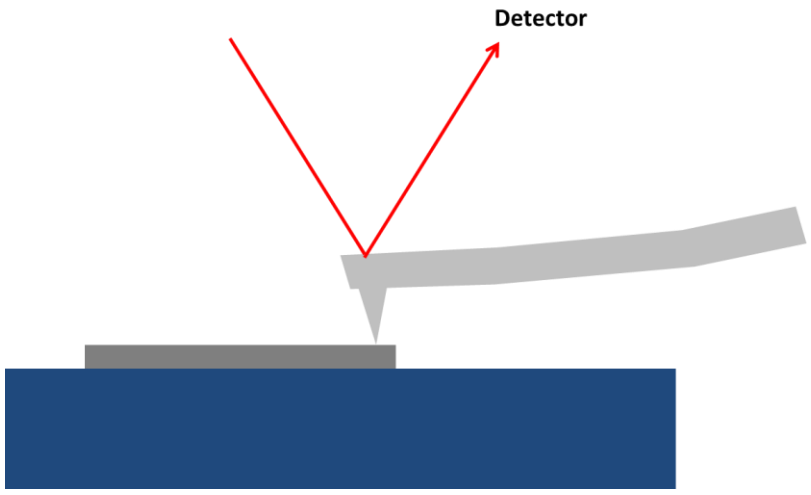

Figure 3-4 - Schematic of an AFM probe measuring the topography of an object. The change in position of the cantilever as the surface topography varies is recorded by the detector, allowing an image to be constructed of the sample surface.

There are various ways in which the AFM tip can interact with the sample as it scans across its surface, and the mode utilised is normally determined by the nature of the sample, in particular, its fragility; an extensive review of many commonly used modes is given by [65].

3.2 Aims & Objectives

The aim of this chapter was to determine whether the amino acids valine, phenylalanine, tyrosine and tryptophan can be used to suspend and exfoliate graphitic material to graphene in aqueous solution, and to investigate the ways in which their structure influences this outcome. In order to achieve this, iterative steps were performed to determine the most effective exfoliation protocol to be used with regards to sonication type and timescales, the optimum graphitic material to be used and the concentration of each amino acid. Finally both the resultant suspensions and the flakes within them were characterised for each of the amino acids used.

3.3 Experimental

3.3.1 Materials

3.3.1.1 Suspension preparation

Acid washed Stacked Graphene Platelet Nanofibres (SGNF) were purchased from Strem Chemicals, Inc., UK. Graphite powder (<45 μm, ≥ 99.99%), L-Valine, L-Tyrosine, L-Tryptophan and L-Phenylalanine from non-animal source, and Sodium Cholate were purchased from Sigma Aldrich, UK. All solutions were prepared in Milli-Q water. Bath sonication was performed in borosilicate glass round bottom flasks (RBFs) (Sigma Aldrich, UK), probe sonication was performed in 50 mL Falcon™ centrifuge tubes (Fisher Scientific, UK) and all suspensions were stored in Wheaton™ snap-cap borosilicate glass vials (Thomas Scientific, UK).

3.3.1.2 Graphene deposition

Gel-Pak films were received as a sample from Gel-Pak, a division of Delphon, USA. Nuclepore polycarbonate track-etch membrane filters were purchased from Whatman, GE Healthcare, UK. Silicon wafers (290 nm oxide layer) were purchased from IDB Technologies Ltd, UK.

3.3.2 Instrumentation

UV-Visible absorbance spectra were recorded using a Cary 60 UV-Vis Spectrophotometer (Agilent, USA). AFM was performed using a Bruker MultiMode (Bruker, UK) with a ContAI-G AFM probe, purchased from Budget Sensors (Windsor Scientific Ltd, UK) or a Bruker MultiMode8 (Bruker, UK) with Scanasyst-air probe (Bruker, UK). Supplier's probe dimensions are as follows: cantilever – 450 µm x 50 µm x 2 µm, tip height – 17 µm, tip radius < 10 nm; cantilever – 115 µm x 25 µm x 0.65 µm, tip height – 2.5-8.0 µm, tip radius 2 nm approx. respectively. Probe sonication was performed using a VCX130PB 130 W sonicator (Sonics & Materials Inc, USA) and bath sonication was performed using a Falc Labsonic LBS 1 sonication bath (Falc Instruments, Italy). Dynamic Light Scattering (DLS) was performed using Wyatt DynaPro Plate Reader II (Wyatt Technology Corporation, USA). Centrifugation was performed using an Eppendorf MiniSpin® (Fisher Scientific, UK) or Sigma 3-16KL bench top centrifuge (Sigma Aldrich, UK).

3.3.3 Methods

3.3.3.1 Graphene suspension preparation

Graphitic material (either SGNFs or graphite powder) and L-amino acids were weighed directly into a 40 mL centrifuge tube or RBF, for probe or bath sonication, respectively. For the highest concentrations of L-amino acid (in the case of L-valine), the graphitic material and amino acid powder were ground together using a tissue grinder and a small amount of water (2 mL), following which the paste was topped-up to the final volume with fresh Milli-Q water. For the lower final concentrations of L-amino acid, the full volume of water was added directly (40 mL).

3.3.3.1.1 Bath sonication

Glass round bottom flasks (RBFs) were used as extended sonication can cause localised heating and result in plastic tubes melting, both contaminating the suspension and allowing it to escape. All suspensions were kept in borosilicate glass vials following preparation. The RBFs containing graphitic suspensions to be sonicated were held in the sonication bath using a clamp stand; two

RBFs could fit into the bath at one time, and were placed as closely as possible to the optimum sonication region. The bath was regularly cooled using ice water, in order to prevent the temperature from rising above 35 °C. Sonication was performed at 59 kHz, 100% power and sonicated between 1-10 h, as indicated.

3.3.3.1.2 Probe sonication

Glass was not used for probe sonication as the probe sonicates at far higher power and can shatter the glass receptacle. All suspensions were kept in borosilicate glass vials following preparation. As sonication induces heating, the vessel was cooled by surrounding it with ice and the sonicator was kept on a duty cycle of 10 minutes sonication, 10 minutes break. The prepared graphitic suspensions in valine or sodium cholate solution were initially sonicated at 70% power for 10 minutes followed by 60% power for 80 minutes, and 50% power for 90 minutes; the mixture was then centrifuged at 50 x g for 30 minutes and 100 x g for 30 minutes successively, after which the supernatant was removed and sonicated for a further 180 minutes at 40% power. A small quantity of the suspension was removed every hour and fractioned using centrifugation to assess the efficacy of the sonication over time.

No improvement in the exfoliation or suspension of the flakes was observed after 3 h in the valine and sodium cholate suspensions (see Section 3.4.1.1), hence the suspensions in solutions of phenylalanine, tyrosine and tryptophan were sonicated for only 3 h in total: 70% power for 10 minutes, 60% power for 50 minutes, 50% power for 30 minutes before centrifugation at 50 x g for 30 minutes and 100 x g for 30 minutes successively, after which the supernatant was sonicated for a further 90 minutes at 50%.

3.3.3.1.3 Fractionation of graphene suspensions via centrifugation

Prepared suspensions of graphene were fractioned via centrifugation using a protocol adapted from Khan *et al.* [66]; briefly, suspensions were centrifuged in an Eppendorf MiniSpin® at 1610 x g (4900 RPM) for 30 minutes, the supernatant was collected (80% total volume) and aliquoted into

another vessel for analysis. The remaining suspension was topped-up with fresh stabilising agent (whichever was under investigation at the time) solution to reach its original volume and the sample was sonicated gently using a sonication bath (59Hz) for 10 minutes to resuspend the flakes. This procedure was then repeated at 918 x g (3700 RPM), 419 x g (2500 RPM) and 43 x g (800 RPM) respectively.

3.3.3.2 Characterisation of graphene suspensions in amino acid solutions

3.3.3.2.1 UV-Visible absorption spectroscopy

UV-Vis absorption spectroscopy was used both to monitor the concentration of the suspensions and to assess their quality. Absorption spectra of the suspensions were recorded between 200-800 nm in a quartz cuvette with path length of 1 cm. Water was used as a blank, which was subtracted prior to measurement. Stability measurements were performed after suspensions were left in borosilicate glass vials at 4 °C undisturbed for 4 weeks. Concentrations were determined using Equation 1, as described in Section 3.1.3.1, and yields were calculated using

$$Yield = 100 \times C_g \frac{V}{M_g} \qquad \text{Equation 3}$$

where C_g = concentration of graphene in suspension, M_g = mass of graphite initially added, V = volume of solvent.

3.3.3.2.2 Atomic force microscopy

Graphene suspensions in amino acid solutions were filtered onto Nuclepore Track Etched Membrane filters using vacuum filtration, following which the deposited flakes were washed with Milli-Q water and transferred onto silicon wafers with a 290 nm oxide layer using GelPak film.

The images were taken using both contact mode and the Bruker® ScanAsyst™ mode, which instead performs a very fast extension-retraction force curve at each measurement point, and will alter the position of the tip to compensate for any change in topography. In addition, the

ScanAsyst™ mode will automatically change parameters such as gain while the image is being recorded

3.3.3.2.3 Dynamic light scattering

In DLS, the changing intensity of the scattered laser light after its interaction with the sample is related to time using a correlation function, which defines the time taken for the intensity signal to become uncorrelated to its initial value. This is expressed as:

$$G^{(2)}(\tau) = < I(0)I(\tau) > = \lim_{T\to\infty} \frac{1}{2T} \int_{-T}^{T} I(t) \cdot I(t+\tau)dt \qquad \textbf{Equation 4}$$

$$G^{(2)}(\tau) = B(1 + f\left|g^{(1)}(\tau)\right|^2) \qquad \textbf{Equation 5}$$

Over time, this can be approximated to:

For a dilute monodisperse colloid, $g^{(1)}$ is:

$$g^{(1)}(\tau) = e^{-Q^2 Dt} \qquad \textbf{Equation 6}$$

Where I = intensity, D = the diffusion coefficient, t = time, τ = correlation time, B and f are experimental factors; $Q = \frac{4\pi n_0}{\lambda}\sin(\frac{\vartheta}{2})$ = strength of interaction between the light and the particle, n_0 = the refractive index of the medium, λ = wavelength of the incident light, ϑ = scattering angle.

From this, the diffusion coefficient can be related to the hydrodynamic radius of the particles using the Stokes-Einstein equation, below:

$$R_h = \frac{k_B T}{6\pi\eta_0 D}$$ Equation 7

Where k_B = Boltzmann's constant, 1.38 x 10^{-23} $m^2kgs^{-2}K^{-1}$, η_0 = solvent viscosity, T = absolute temperature.

For the experiments in this chapter, 100 µL of the suspensions was aliquoted into a black polystyrene 384 well microtitre plate with transparent bottom. All samples were measured in triplicate. An events schedule was set on the DynaPro plate reader using the Dynamics software which allowed automation of the readings. The laser was auto-attenuated for each reading and all acquisitions were performed over 10 s; 10 acquisitions were performed on each well and the temperature was maintained at 25 °C. The software enabled real-time data filters, and correlation function cut-offs were set at 0.93 and $1.33x10^6$ as the low and high passes respectively; peak radius cut-offs were set at 0.5 nm and 5 µm.

Analysis was performed using the Dynamics software, which makes use of CONTIN regularization analysis to fit the correlation curve and find the apparent hydrodynamic radius distribution. The region of the correlation curve that was used for the fitting was defined by the user. The accepted parameters were those in which the curve decayed such that its tail either reached 1.0 or was projected to, and where the residuals were minimised. From this curve, the programme produced a distribution of apparent hydrodynamic radii in the form of a histogram.

Stability measurements were performed after suspensions were left in borosilicate glass vials at 4°C undisturbed for 1 week. The correlation curve itself was also used as a method of analysis. Dynamic light scattering depends on the Doppler broadening of the monochromatic laser light scattered from the objects moving in suspension, and the random phase distribution of the scattered light caused by the objects moving randomly relative to one another, leading to a unique interference pattern, captured by the spectrophotometer [62, 63](illustrated in Figure

3-5). For suspensions where significant aggregation has occurred, the large aggregates may no longer move in the suspension in a Brownian (i.e. random) fashion, instead precipitating (Figure 3-5b); otherwise, they may take up the majority of the focal plane (Figure 3-5c). If a particle becomes so large that the phase distribution is no longer random, as multiple scattered light points emanate from the same particle, or if the particle movement is directional, the model used breaks down, which may be observed in the degradation of the correlation curve. For such suspensions the correlation curve is no longer sigmoidal – strong oscillations may be observed, the tail may no longer reach 1 or the decay region may be interrupted by significant peaks or troughs (Figure 3-6d). While the software used for this analysis provided residuals, unfortunately it did not give a χ^2 value for the fit – the value for which would be unlikely to reflect whether the

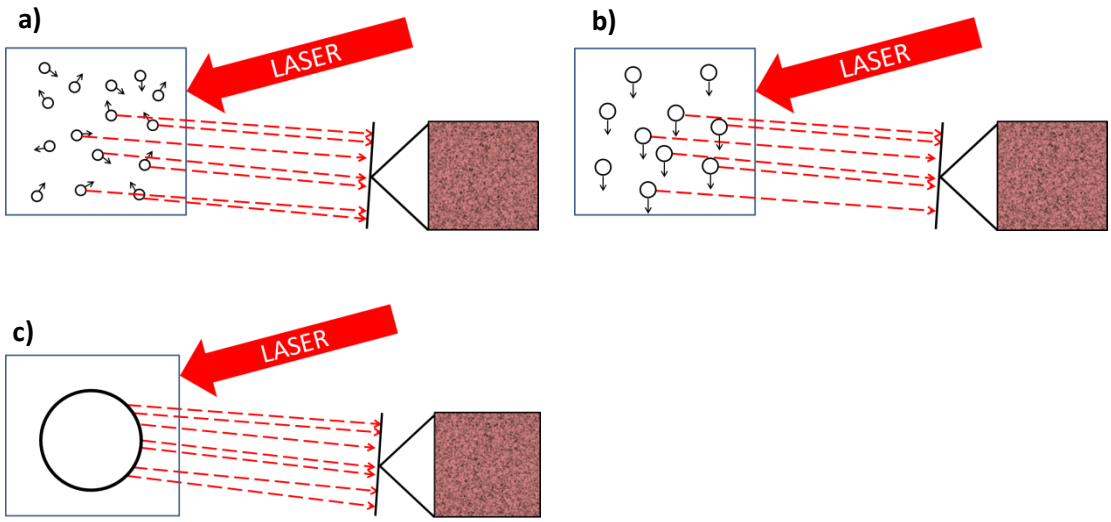

Figure 3-5 - Schematic of DLS function for different types of particle distributions. a) A well behaved suspension, where the particles are small compared to the laser point and present Brownian motion. b) Particles are still small compared to the laser, but are not well behaved; their motion is directional due to sedimentation. c) Particles are large compared to the laser point, meaning light scattered off the same particle may interfere with itself.

curve's baseline at 1 anyway, so qualitative assessments were made with regards to the curve, described in Figure 3-6. These distinctions were used as a method to judge the overall quality of the suspensions under measurement.

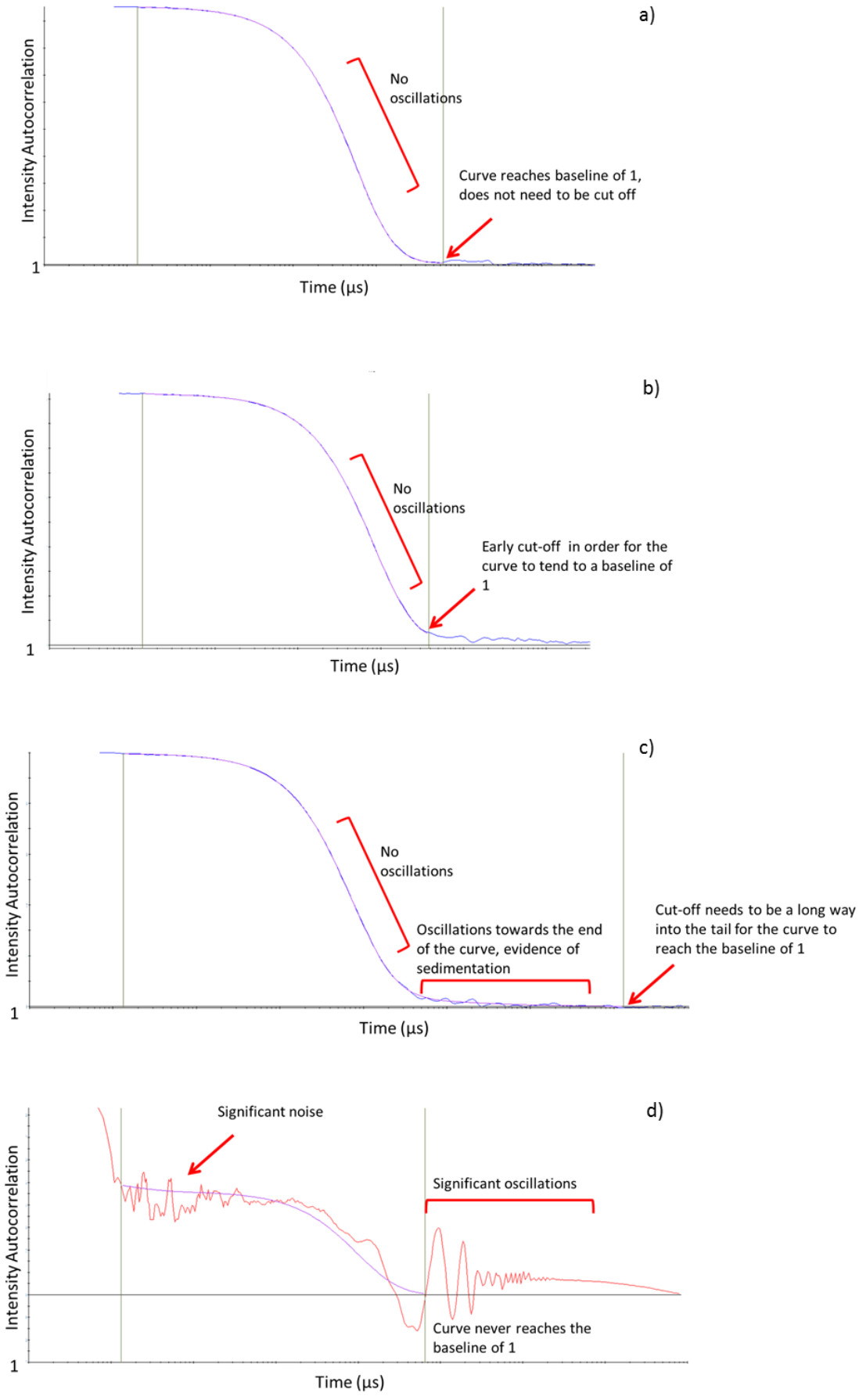

Figure 3-6 Representative examples of DLS correlation curves for different samples. a) Good, b) & c) Satisfactory, d) Bad

3.4 Results

3.4.1 Preliminary studies on the exfoliation and suspension of graphene using valine

The initial experiments performed utilised pristine graphite powder, which was exfoliated using bath sonication in aqueous valine solutions in the concentration range 0.022-680 mM. This includes saturated solutions of valine, as the solubility limit of valine in Milli-Q water is 474 mM [67]. Saturated solutions were included as it was thought that the presence of the graphitic material in the suspension may alter the behaviour of the valine. These experiments were performed in order to assess the best conditions to use when suspending the flakes, and used experimental methods and materials that are commonly used in the literature.

3.4.1.1 Analysis of suspension concentrations and flake thicknesses using UV-Visible absorption spectroscopy

Mixtures of pristine graphite powder and Milli-Q water in the presence of a range of valine concentrations underwent sonication for 10 hours, after which the concentration of the exfoliated flakes in suspension was determined using UV-Vis and the Beer-Lambert law, described in Section 3.1.3.1. A representative example of an absorption spectrum for a graphene

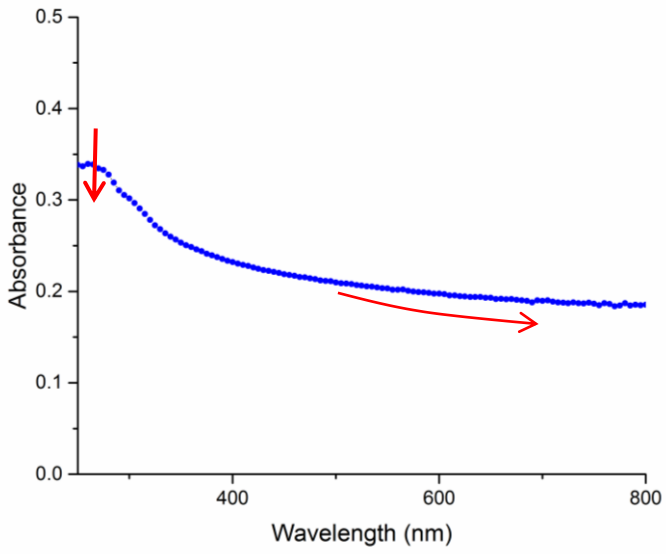

Figure 3-7 - A representative example of a graphene absorption spectrum in water following exfoliation by valine

suspension in valine solution is shown in Figure 3-7, with the characteristic peak and flattened tail indicated.

Figure 3-8 presents the yields of graphene-like material exfoliated and suspended in water as a function of valine concentrations directly after sonication; yields were calculated using Equation 3 in Section 3.3.3.2.1.

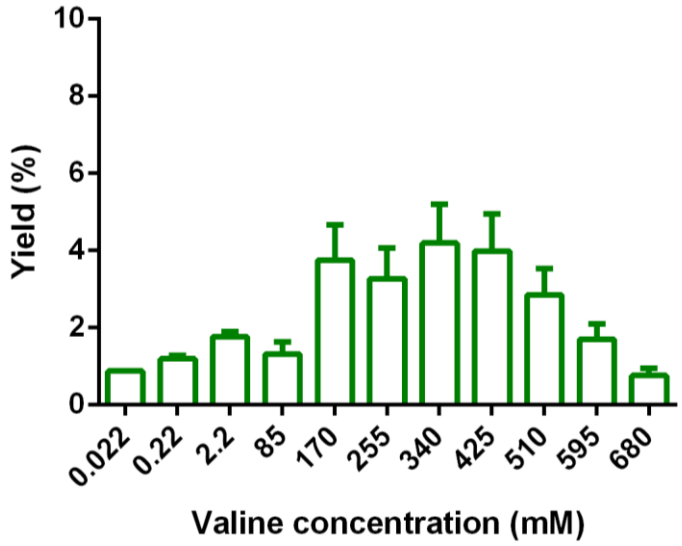

Figure 3-8– Valine-suspended graphene yields, at a range of valine concentrations (as shown), found by UV-Vis absorption spectroscopy. Yields were determined as a proportion of the mass of graphitic material originally put into the mixture. Error bars are taken as the standard deviation of triplicate measurements of different samples.

Figure 3-8 shows that the concentration of suspended graphene increases with increasing valine concentration up to 340 mM, which is a little below its solubility limit of 474 mM [67] at which point the yield plateaus and declines as the valine becomes increasingly unstable in solution. This relationship between graphene and its exfoliating and suspending agents, in which a peak in flake concentration is observed before a decline with increasing exfoliant concentrations, has been commonly observed, and is considered to indicate the optimum concentration of exfoliating and suspending agent [30, 46]. Therefore 340 mM was chosen as the valine concentration for subsequent experiments.

Unlike dispersions of pristine graphene in organic solvents or aqueous dispersions of graphene oxide, the yields for graphene exfoliated and suspended using stabilising agents are often quite low, with dispersions exfoliated and suspended with 1-pyrenesulfonic sodium salt and SDBS only reaching 7% w/v and 3% w/v respectively [35, 39]. Therefore the yields produced by valine were within the normal range for pristine graphene suspensions in aqueous solution.

Exfoliation using probe sonication

Following these initial experiments the use of the more aggressive probe sonication, described in Section 3.1.1.1, was assessed in solutions 340 mM valine solutions as a function of sonication time. In addition, SGNFs – which are a source of pristine graphitic material but with a standard diameter of 50 nm – were used instead of pristine graphite powder with the aim of reducing the polydispersity of the samples. As a control, sodium cholate (Figure 3-9) was used as an exfoliating and suspending agent at a concentration of 232 µM, as it is a relatively small molecule suspending agent that successfully exfoliated and suspended graphene, and was found to be most effective at this concentration [30].

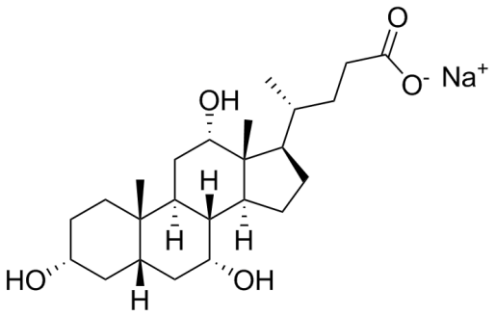

Figure 3-9 – Molecular structure of sodium cholate

Suspensions were probe sonicated over 6 h, and at each time point the graphene suspensions were fractioned using centrifugation, in order to separate the flakes according to their thicknesses [66]. The resulting fractions were assessed using UV-Vis spectroscopy (Figure 3-10 & Figure 3-11).

As the fractionation is considered to separate flakes depending on both their thickness and lateral dimensions, it could give a basic assessment of the quality of the suspensions. Hence, by

fractioning a small quantity of the suspensions at each hour in addition to finding the overall concentration, a measure of the proportion of the suspension that could be considered to be "good" quality (i.e. thin flakes) can be delivered. For both the sodium cholate suspensions and the valine suspensions, the thickest flakes – separated at 800 rpm – are the major species found in the suspension. Besides this, the flakes separated by centrifugation for 30 minutes at 419 x g, 918 x g and 1610 x g are relatively evenly split, and for the valine suspensions, the concentrations of each remain quite constant over the full 6 hours. At 5 hours of sonication, there is a sudden decrease in in flake concentration for all fractions in the suspension prepared using sodium cholate solution; the flakes noticeably aggregated and precipitated. While the mechanism behind this is unknown, sonication-induced aggregation has been observed in other systems [68, 69], and other graphene systems have been observed to drop in concentration after similar probe sonication timescales [29].

At 3 h there is a peak in the overall concentration of the suspension in valine solution, after which point a slight decrease is observed, and no overall improvement in the concentration of high quality flakes is seen (Figure 3-10). In addition, the suspensions prepared in sodium cholate solution became unstable after 4h. Therefore it was decided that the suspensions would be sonicated for 3 h; this time point is similar to that reported in the literature for liquid exfoliation of 2D materials such as graphene using direct probe sonication [64].

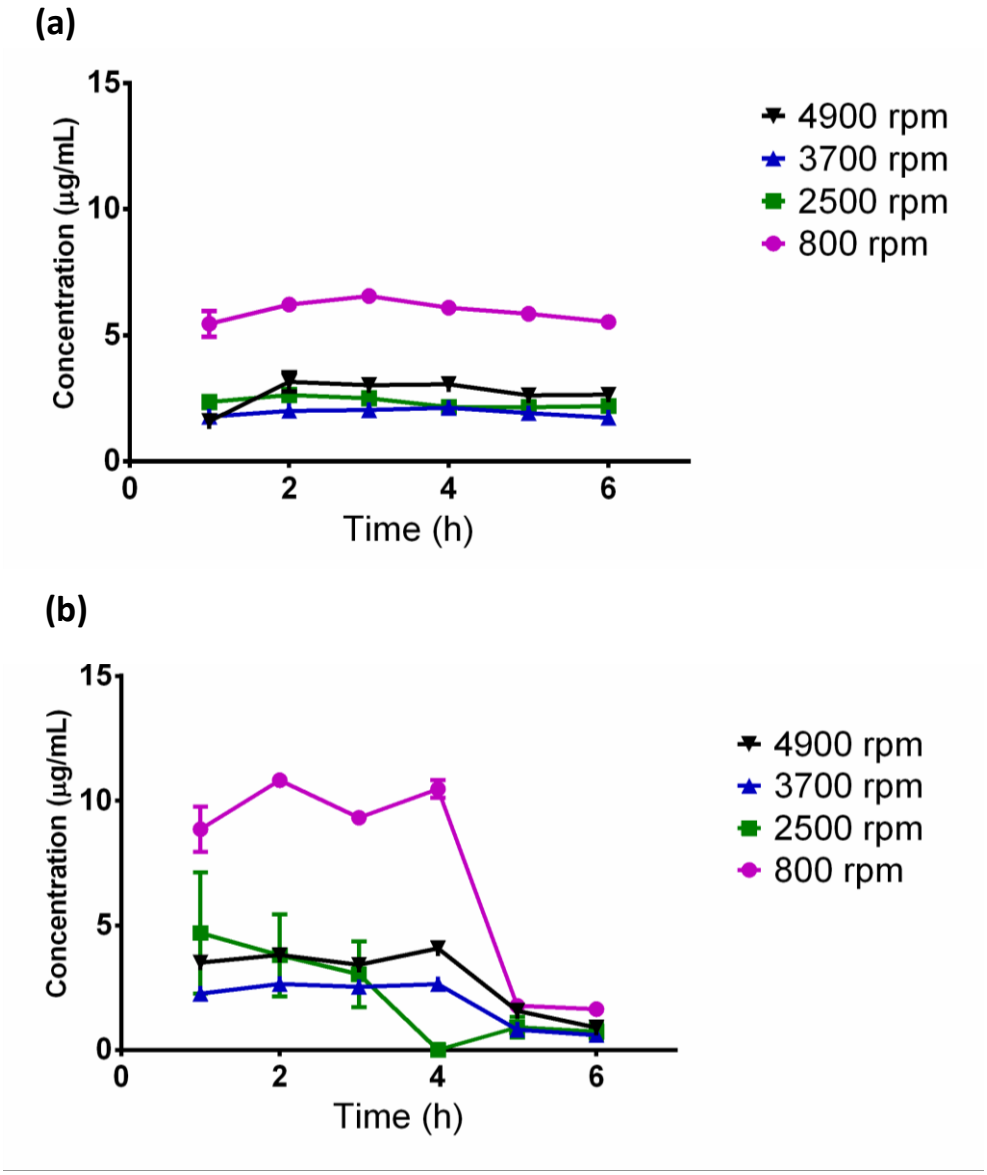

Figure 3-10 – Concentrations of graphene in probe sonicated suspensions as a function of sonication time, separated by flake quality using sequential fractioning. Different colours represent the different centrifugation rotation speeds at which the samples were fractioned. For (a) valine and (b) the control sodium cholate. Calculated using UV-Vis spectroscopy.

Determination of flake thickness using UV-Vis

Figure 3-11 shows the UV-vis spectra of the fractioned suspensions at each sonication time point, normalised with respect to the absorption at 800 nm for ease of comparability. This wavelength was chosen as it is the maximum wavelength for which the absorption was measured, and would minimise spectrum cross-over. The shape of the normalised UV-Vis spectra for the centrifuged fractions differs significantly depending upon the centrifugation rate, with the fractions from the lowest rate possessing a far flatter spectrum compared to those fractioned at the highest rate (Figure 3-11). This is in agreement with the relationship determined by Backes *et al.* [60], described in detail in Section 3.1.3.1, which can be used to determine the average number of graphene layers per flake from the shape of a suspension's absorption spectrum. Using Equation 1, the average flake thickness for the fractioned spectra at 3 h sonication was calculated (Figure

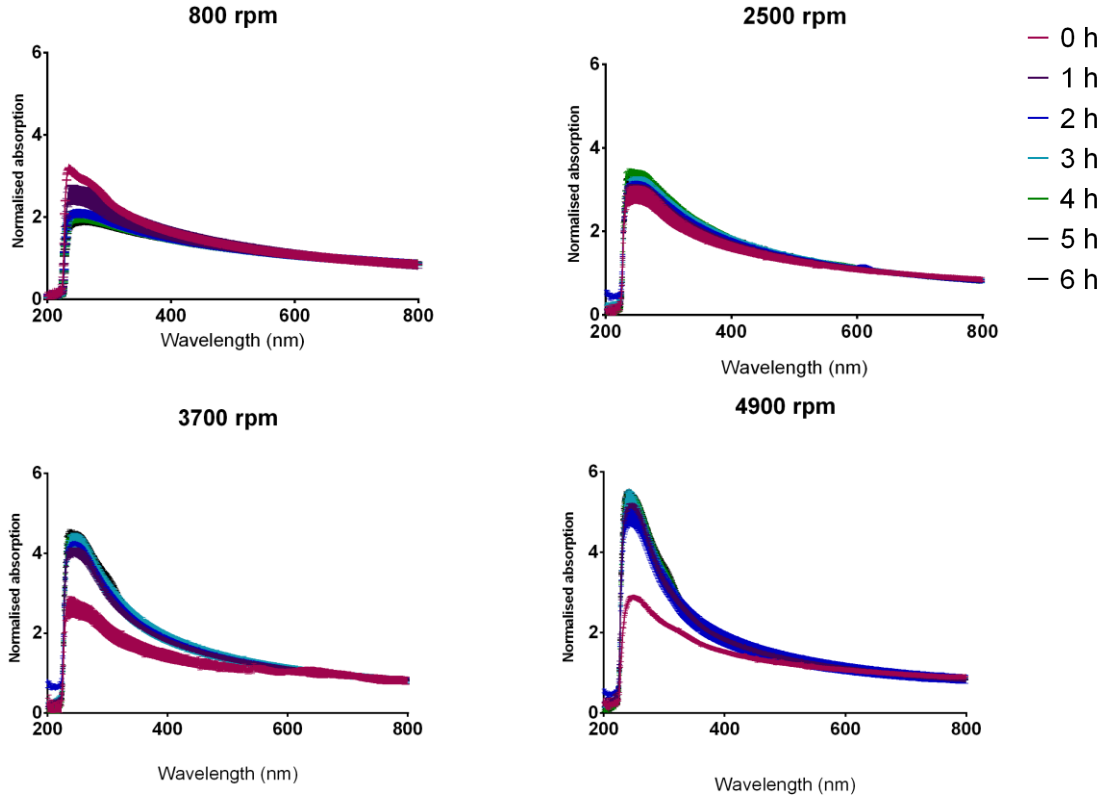

Figure 3-11 - Normalised UV-Vis spectra of valine suspensions, fractioned using centrifugation, the rates of which are indicated above each graph. The different colours of trace indicate the times at which the samples were taken over the 6 h of sonication.

3-12). Figure 3-12 clearly shows that the fractions produced at the highest rate of centrifugation contained the thinnest flakes, as expected, and that the suspensions may be comprised of flakes of reasonably high quality, with the majority of the flakes being under 10 layers.

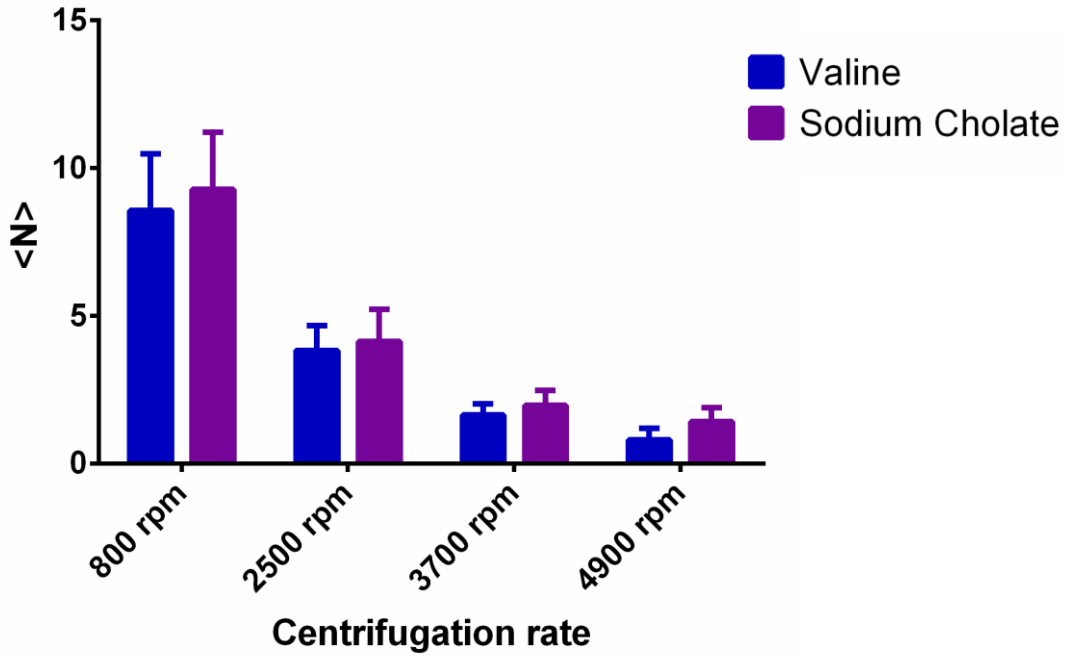

Figure 3-12 - Flake thickness, calculated using UV-Vis absorption spectroscopy. The values were calculated using empirical formula reported in Backes *et al.* [60], found for each centrifuged fraction. Sodium cholate was used as a control to compare with the valine suspensions.

Subsequently the morphology of the flakes was to be directly assessed using AFM, in order to confirm the results produced by analysing the shape of the UV-vis spectrum and to give greater insight into the properties of the suspension components.

3.4.1.2 Assessment of flake morphology by AFM

The assessment of the flake morphology is of particular importance as the flake size, thickness and geometry are all significant determinants of the way in which graphene may interact with a biological system, and each of these properties can be measured directly using AFM.

AFM is a surface technique, therefore interference from residual crystals of exfoliating and suspending agents needed to be avoided. For this reason, both valine and sodium cholate graphene suspensions were not directly drop-cast or spin coated, and instead were filtered and washed before transferral to the silicon wafer using non-adhesive films, as described in Section 3.3.3.2.2. Figure 3-13 presents representative AFM images for both the preparations; flakes of lateral dimensions close to 50 nm were observed dispersed across the surface of the substrates for both preparations. This correlates well with the expected dimensions from the pristine SGNFs used as a start material.

The distribution of thicknesses of the flakes was calculated using the built-in analysis capabilities of the software used (Gwyddion). The distribution of valine exfoliated and suspended flakes shown in Figure 3-13e) shows that valine was capable of exfoliating the flakes such that they are moderately thin (multilayer) flakes, but polydisperse, while the flake thickness distribution shown in Figure 3-13f) indicates that sodium cholate was able to predominantly produce few layer graphene, with a tail of flakes with larger thicknesses. While a single layer of graphene is calculated as having a thickness of 0.34 nm – equal to the extension of the π orbitals out of plane [70] – graphene and graphitic layer thicknesses have been measured by different groups to be between 0.5-1 nm using AFM [59, 71]; the variation in measured thickness depends upon the interaction between the AFM tip and the flake surface, including the presence of any adsorbed molecules – particularly water molecules. Therefore, the thinnest flakes would be at least three layers thick, with the mean thickness between 8-16 layers. The suspensions were not fractionated before deposition and characterisation by AFM.

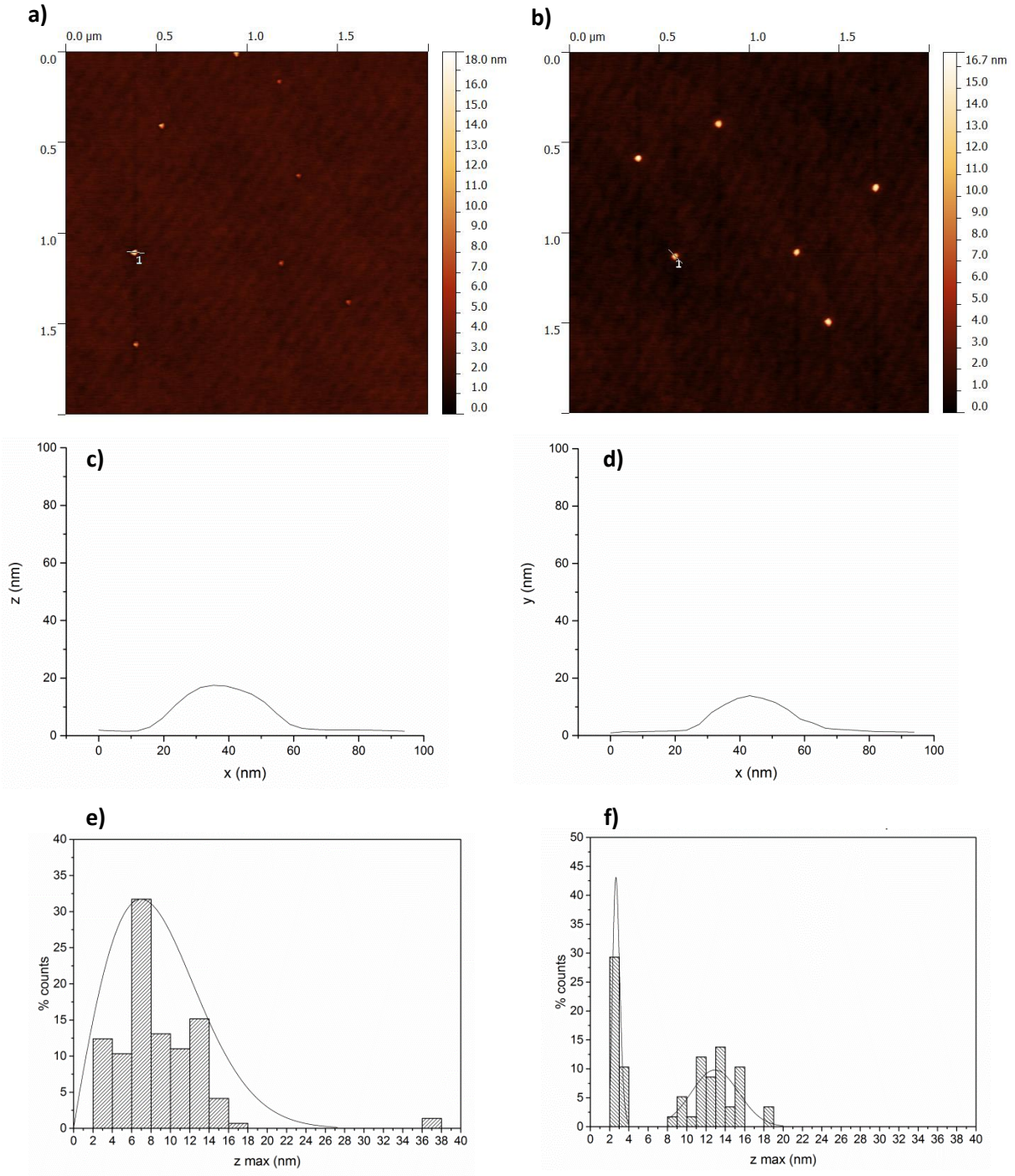

Figure 3-13 – AFM images of graphene flakes exfoliated and suspended in a) L-valine solution; b) sodium cholate solution after deposition onto silicon wafers using Gel Pak®. Profiles of the indicated flakes are shown in c) valine; d) sodium cholate. The distribution thicknesses of the flakes, gathered from several AFM images similar to a) and b) are shown in e) valine; f) sodium cholate. The thinnest flakes are few-layer, whereas no single-layer flakes were observed for either preparation

It should be noted that the Gel-Pak® method of flake transferral onto the substrates may not result in a representative distribution of the flakes present on the filter where they were initially deposited; it is unknown whether the film may be more effective at picking up the larger or the smaller flakes. However, as both the valine and sodium cholate preparations were transferred in this way, it is unlikely that there would be a significant difference in the way that the film interacts with the two preparations, and therefore the distributions seen are likely to be representative relative to each other.

3.4.1.3 Summary

Results from Section 3.4.1.1 (Figure 3-8) demonstrate that valine is able to exfoliate and suspend graphitic materials to a concentration within the range produced by other groups. However, after further investigation of the flake morphologies, shown in Section 3.4.1.2 (Figure 3-13), it became apparent that the flakes produced were of a thickness that was not commensurate with the term "graphene", as many of the flakes had eight or more layers in them. As described in the Introduction, the thickness of the flakes can significantly affect their toxicological profile, with thicker flakes more likely result in negative outcomes, particularly *in vivo* [72, 73]. In addition, the concentrations of valine that were used were incredibly high. This may be related to the related to the very low LogP value of valine – an indication of its lipophilicity – which may indicate its likelihood of interaction with the graphene flakes. In comparison, sodium cholate has a far higher LogP value of 2.48, and its most effective concentration is three orders of magnitude lower. Having such significant concentrations of suspending agents present is problematic for the point at which flakes are introduced to cells, and the weak hydrophobic interactions between the valine and the flake basal plane mean that it is not clear whether the flakes would remain stable if their diluent were changed.

The preliminary work with valine and sodium cholate guided the choice of molecules to be used in the subsequent studies; the two molecules are structurally significantly different, and have very different values of lipophilicity. The choice of molecules to be investigated subsequently aimed to

choose structures that could be viewed as intermediate between the two – retaining biological benignity and the small size associated with amino acids, but gaining in lipophilicity. L-phenylalanine, L-tyrosine and L-tryptophan were chosen as they are structurally related to valine, but the presence of aromatic ring(s) in their structures leads to increasing lipophilicity. These aromatic regions also allow π-π interactions with the polyaromatic basal plane of the graphene flakes.

3.4.2 Aromatic amino acids as alternative suspending agents

In this section of the work, the protocol for exfoliation of graphene flakes developed with valine and sodium cholate is again used for the determination of the efficacy of exfoliation and suspension of graphene using phenylalanine, tyrosine and tryptophan.

3.4.2.1 Suspension characterisation

The concentration range of the aromatic amino acids used was kept consistent across the three amino acids, and therefore its upper limit was determined by the amino acid with the lowest solubility limit; in this case that was tyrosine, which has a solubility limit of 2.5 mM in pure water [74], while the solubility limits of phenylalanine and tryptophan are 179 mM and 55 mM respectively in pure water [74]. While its polarity is higher than either of the other molecules, the strength of the intermolecular ionic bonds leads to difficulty in its dissolution [75].

3.4.2.1.1 Analysis of suspension concentration and stability

Stacked graphene nanofibres were probe sonicated in aromatic amino acid solutions with concentrations ranging from 0-2.2 mM. The concentration of the resultant suspensions was measured immediately after preparation, and re-measured 4 weeks after preparation to assess the stability of the suspensions (Figure 3-14). With respect to these experiments, stability was defined as the propensity for the flakes to remain in suspension, and for the flakes that had settled to the bottom of the container to be redispersed when agitated.

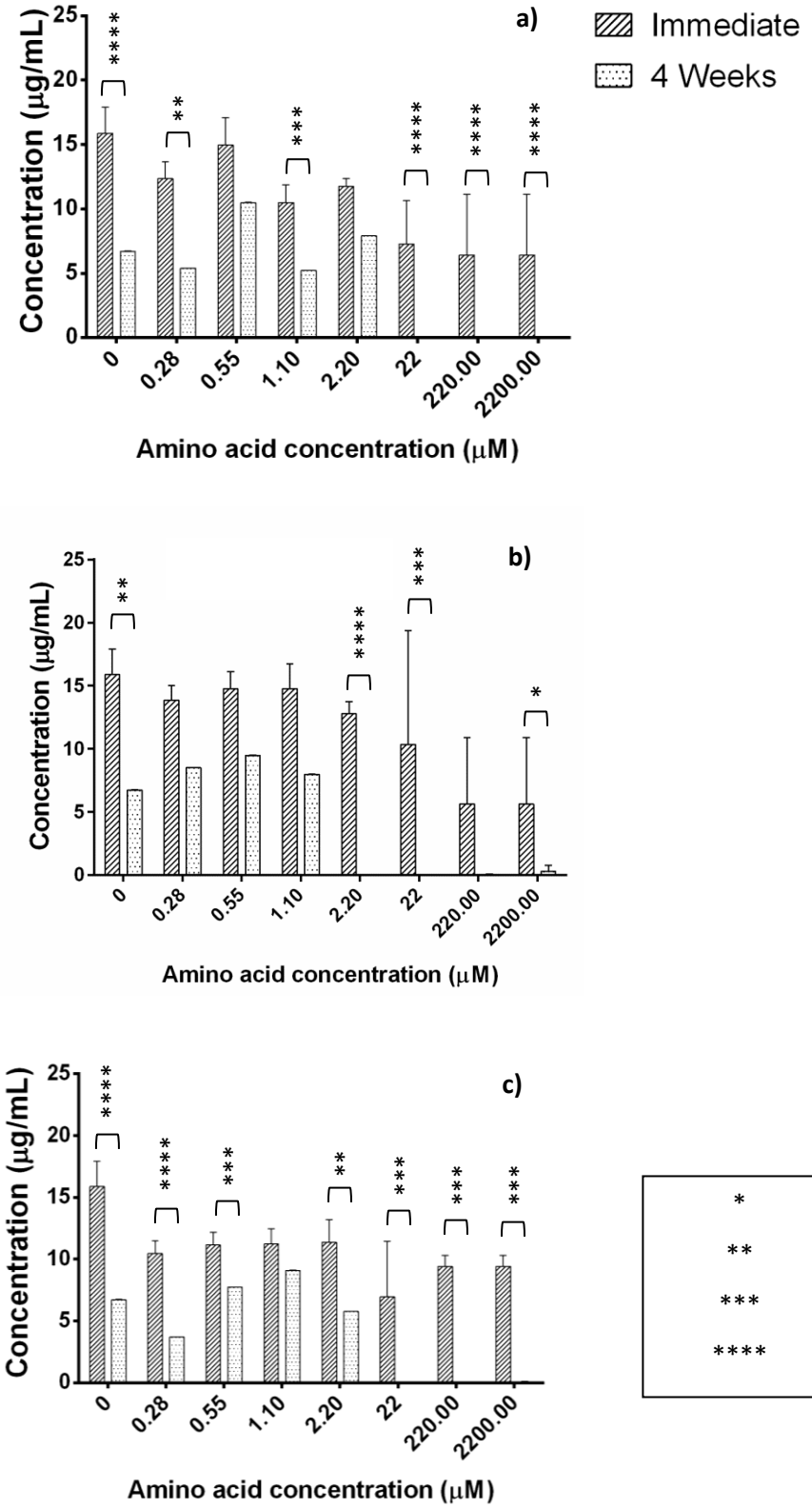

Figure 3-14– Concentrations of graphene prepared from stacked graphite nanofibres, exfoliated in a) phenylalanine; b) tyrosine c) tryptophan solutions, determined using UV-Vis absorption spectroscopy. Each graph shows the immediate graphene concentration and that after 4 weeks for a range of concentrations of the amino acids, where the errors were calculated as the standard deviation of measurements from three different samples. Two way ANOVA was performed using Sidak's multiple comparisons test and the significance levels are indicted.

Figure 3-14 illustrates that for each of the molecules tested the graphene suspension concentration was found to be dependent upon the concentration of amino acid present in solution, with the highest concentrations produced for amino acid concentrations ≤ 2.2 μM. After 4 weeks, the suspensions prepared with amino acid concentrations of concentrations ≥ 22 μM had decreased by > 99% for all three molecules. For the preparations made with amino acid concentrations under this value, the percentage decrease in suspension concentration ranged between 6%-60%.

As some of the concentrations of amino acids being tested were very small, a test suspension prepared in pure water without any suspending agents was prepared as a comparison. In the absence of exfoliating and suspending agents, graphene flakes were still observed at a concentration of 15.87 μg/mL immediately after preparation; interestingly, this is higher than that provided by any of the amino acids, at any concentration (see Figure 3-14). While a significant difference is observed in the suspension concentration after 4 weeks, this was also the case for the majority of the other preparations, and the concentration of flakes that remained in suspension after 4 weeks for the pure water preparation (6.73 μg/mL) was significantly higher than that prepared in amino acid solutions with concentrations ≥ 2.2 mM for all three amino acids. This result is surprising, as the nanofibres themselves were considered to be pristine graphene, the flakes should be hydrophobic and therefore would not be expected to be exfoliated or remain in suspension in pure water.

Furthermore, Figure 3-14 shows an unexpected decrease in initial exfoliation and suspension efficacy, and stability over time with increasing amino acid concentration. The concentrations of graphene present in the suspensions prepared with the highest concentrations of of amino acids (0.022-2.2 mM) are close to 0 μg/mL at 4 weeks. Whereas in the earlier work with valine the drop-off in exfoliation efficacy occurred close to the solubility limit of the molecule (Section

3.4.1.1, Figure 3-8), with each of the aromatic amino acids the 4 week suspension concentration decreases significantly before the flake solubility limit has been reached.

The concentrations of graphene in suspension at 4 weeks were measured without disturbing the vessel, therefore this change in graphene concentration may indicate that aggregation is occurring. This correlated with the visible appearance of black aggregates that precipitated at the bottom of the vessels in the suspensions prepared with the highest concentrations of phenylalanine, tyrosine and tryptophan. The appearance of black aggregates in the suspensions which were prepared with the highest aromatic amino acid concentrations often occurred within far shorter timescales than a week – in some cases within 24 h. The aggregates were not easily redispersed, even with agitation, indicating that the aggregation was irreversible.

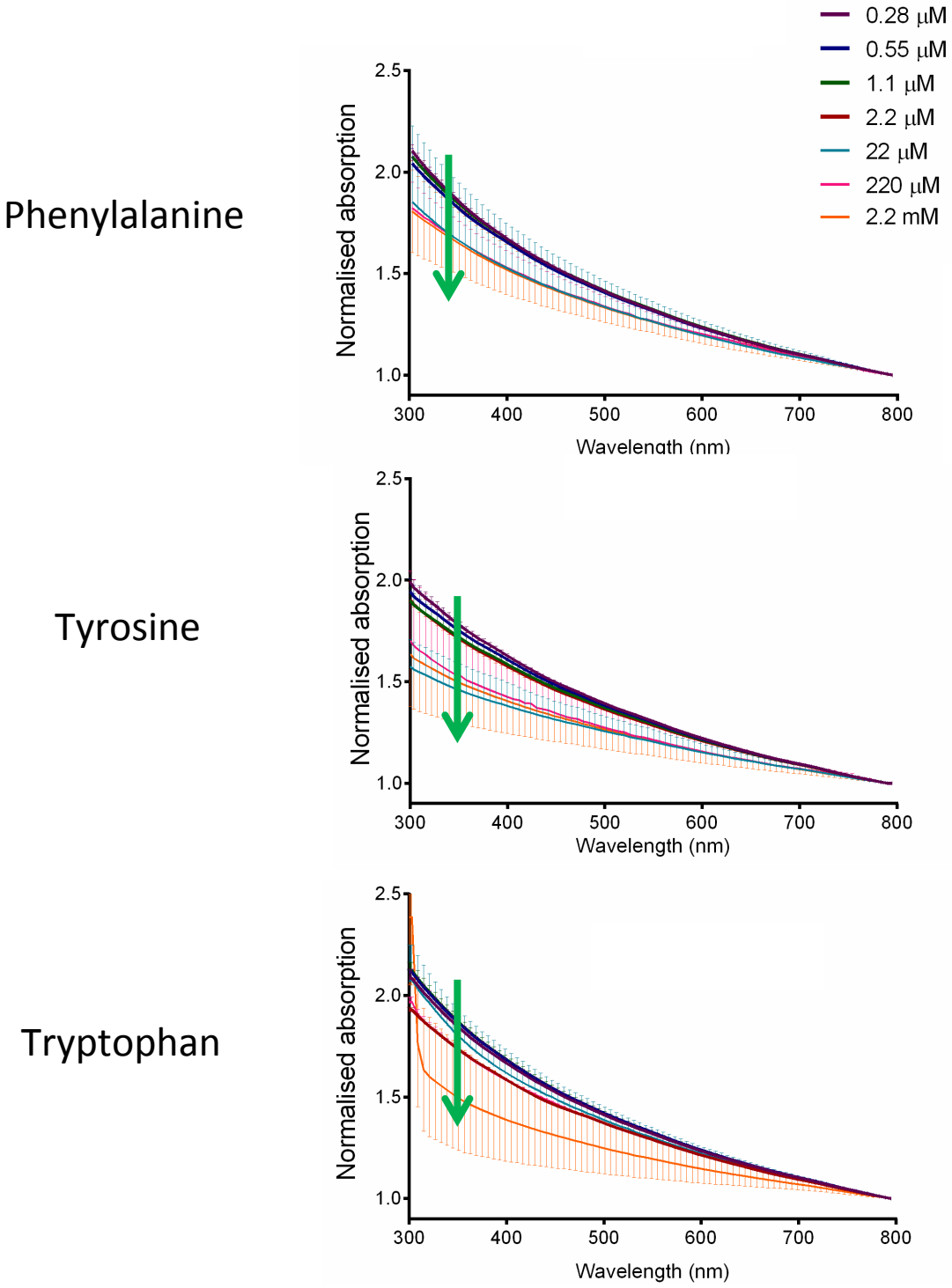

Figure 3-15 - Normalised UV-Vis spectra of suspensions for phenylalanine, tyrosine and tryptophan at varying amino acid concentrations – taken immediately after suspension preparation. Errors were calculated as the standard deviation of the measurements from three samples.

The shape of the UV-vis absorption spectra recorded directly after suspension preparation were also analysed to assess any change with amino acid concentration. The spectra were normalised with respect to their absorption at 800 nm and the shapes of the graphs compared, shown in Figure 3-15. With increasing amino acid concentrations, the curves became flatter in shape – indicated by the green arrows, which give the direction of increasing concentration and decreasing gradient.

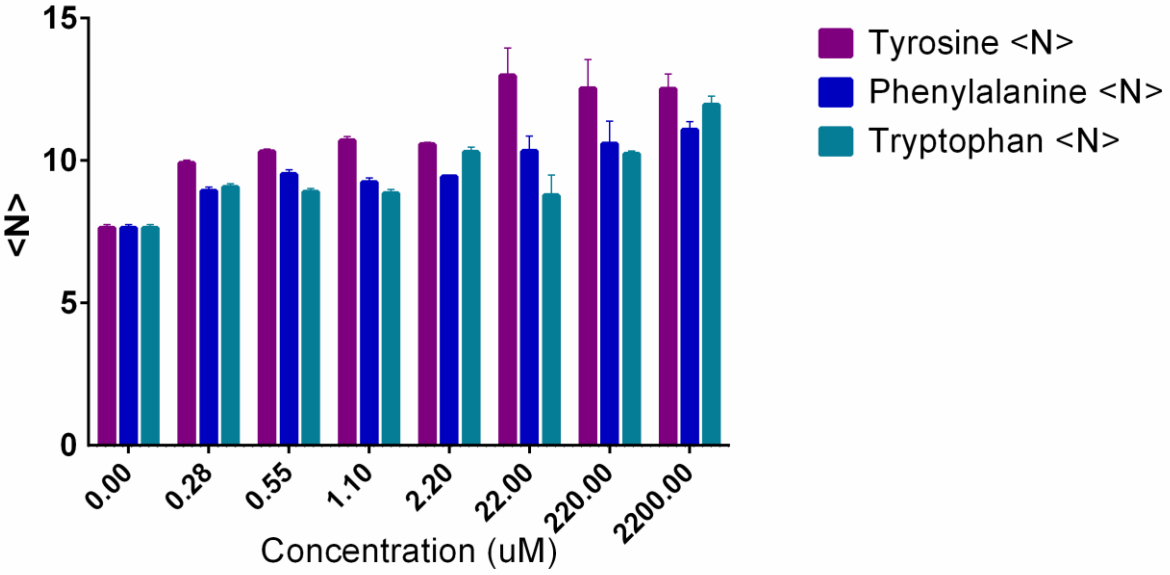

Figure 3-16 – Average flake thickness – calculated using Equation 2 – for the graphene suspensions prepared using phenylalanine, tyrosine and tryptophan without centrifugation fractioning and at varying concentrations of amino acid solution. Different amino acids are indicated using different colours. Errors were calculated as the standard deviation between the 3 repeats taken.

The change in shape dependent upon concentration of amino acid is most noticeable in tyrosine and phenylalanine, while some difference can be observed in tryptophan, although the shape of the curve associated with the suspension with 2.2 mM tryptophan is noticeably affected by the strong absorption of the amino acid itself at low wavelengths (below around 320 nm). The highest concentrations of amino acid also led to strong variations in the spectra, indicated by the large error bars present on the curves. This indicates the relative irreproducibility of the preparations, which may be linked to their instability.

Further to this, the UV-Vis absorption spectra taken immediately after suspension preparation were analysed to find the approximate flake thickness using Equation 2 – shown in Figure 4-16. As suggested by Figure 3-15, increasing amino acid concentration is positively correlated with flake thickness – including those suspensions prepared in pure water, which produced the thinnest flakes.

In addition, the suspensions prepared in tyrosine solution consistently produced thicker flakes than either phenylalanine or tryptophan. As stated earlier, tyrosine has a far lower solubility limit than either phenylalanine or tryptophan (2.5 mM compared to 179 mM and 55 mM), despite their similar structures and tyrosine's superior polarity – this is due to the OH group that stretches off its aromatic ring, and its propensity to form intermolecular ionic bonds. It therefore follows that a decrease in stability of the suspensions and an increase in the thickness of the flakes should occur at lower concentrations of tyrosine than either phenylalanine or tryptophan.

3.4.2.1.2 Analysis of the suspension dynamics at the highest concentrations of amino acids

The results in Section 3.4.2.1.1 suggest that with increasing amino acid concentration, the suspensions become increasingly unstable, leading to precipitation, which may have been due to aggregation. The suspensions that were observed to be least stable, those prepared with 0.22 and 2.2 mM amino acid concentrations, were therefore further investigated using DLS. In this case the lack of stability i.e. the propensity of the flakes to form aggregates that could not be resuspended, was investigated. The precipitation was observed to occur very rapidly in these preparations, with the majority of the flakes no longer in suspension after 24 h in some samples. Therefore the measurements were taken directly after preparation and after 1 week, during which the suspensions were left unagitated in a cold room. Suspensions were gently agitated directly before measurement in order to ensure the presence of some disperse particles, and to investigate whether the aggregation was reversible or not.

In addition to the measurements of the apparent hydrodynamic radii for the objects present in the suspension, each of the correlation curves was assessed in terms of quality, as described in Section 3.3.3.2.3. The proportions of measurements marked bad, satisfactory or good therefore give additional information in terms of the aggregation or precipitation of the graphene suspensions, and are shown in Figure 3-17.

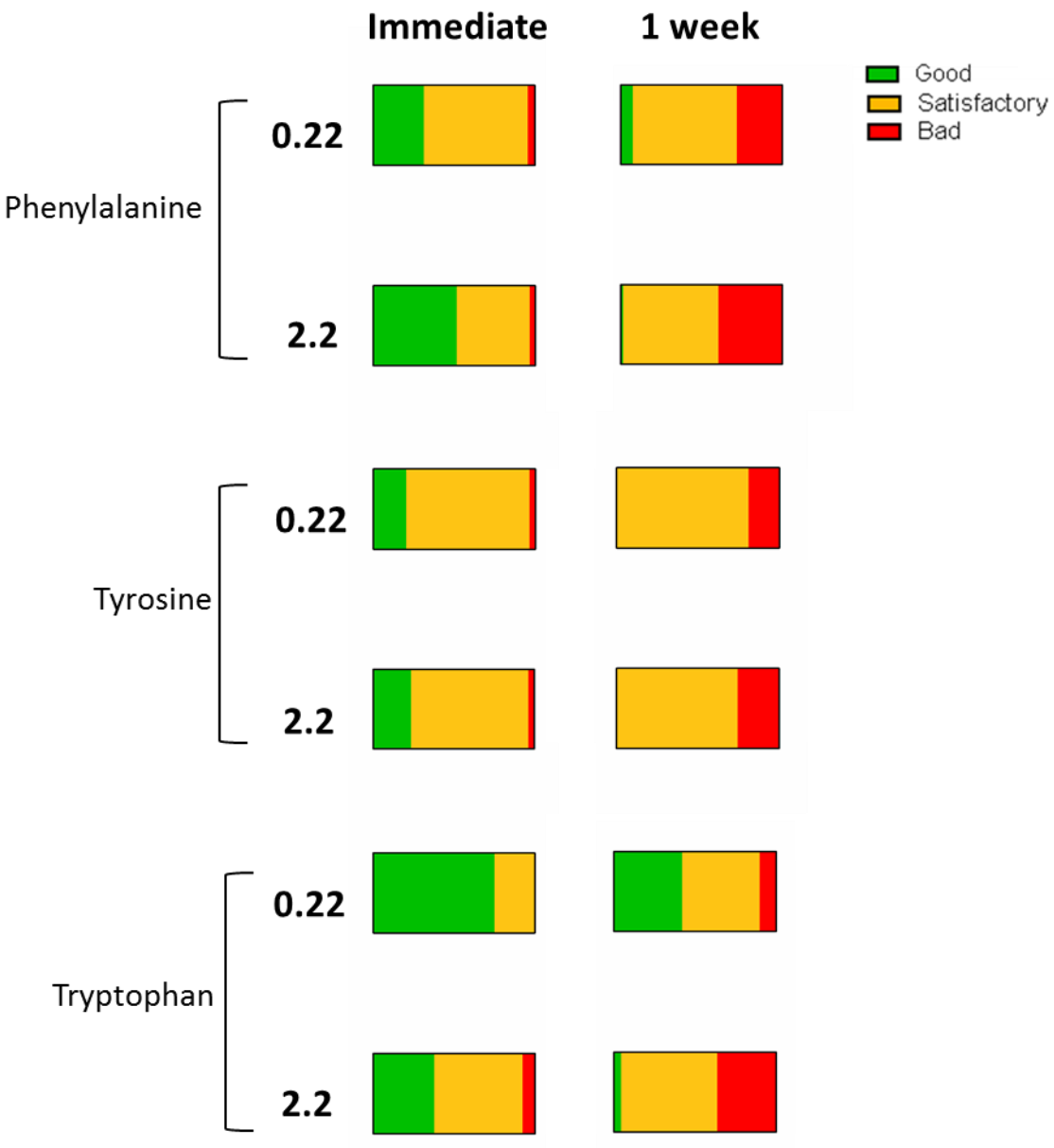

Figure 3-17 - Correlation curve quality, determined for each set of measurements and for each sample both immediately after preparation and after 1 week. Quantities were determined as a proportion of the total number of records taken.

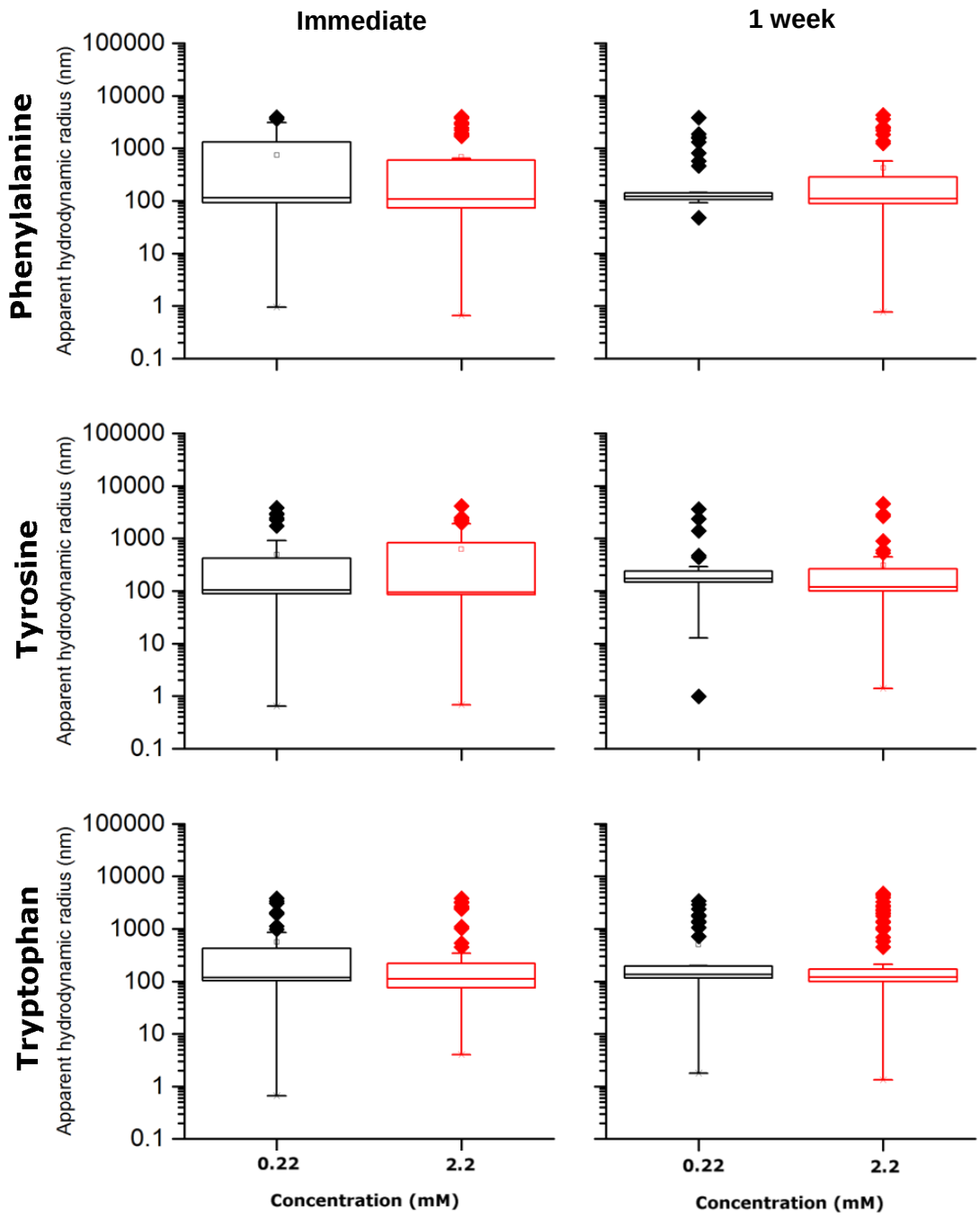

Figure 3-18 – The apparent hydrodynamic radius distribution, measured using DLS, both immediately after preparation and 1 week later. Extended bars represent the 1st and 4th quartiles of the distribution, box edges represent the 2nd and 3rd, the horizontal line in the body of the box is the median, the hollow squares represent the geometric mean and solid diamonds represent outliers

For all the suspensions there is both a significant difference in the quality of the suspensions for the different amino acid types, and a clear change in quality over time, with more measurements determined to be only satisfactory or bad after 1 week. This demonstrates the formation of large objects or aggregates. The suspensions prepared using tryptophan appear to be of a better quality, both immediately after preparation and at 1 week, but the most significant change in suspension quality over time is found in phenylalanine.

The distributions of hydrodynamic radii are shown in Figure 3-18 – these were determined using the *good* or *satisfactory* curves, with those considered to be *bad* not used. It should be noted that even after immediate preparation, the apparent hydrodynamic radii of the flakes were in the order of 100 nm. This is significantly larger than was expected, as the flakes used for the preparation had radii of approximately 25 nm; although their oblate geometry means that some discrepancy may be anticipated, it is still predicted that the apparent hydrodynamic radius would be close to that of the flake's solvent sphere, illustrated in Figure 3-3 in Section 3.1.3.2.

After the suspensions had been left for 1 week, the vast majority of the flakes had aggregated into dark black precipitates that sat at the bottom of the glass vessel in which they had been kept. For the majority, the solution was entirely transparent, with no suggestion of any particles remaining in suspension. This is in accordance with the UV-vis absorbance measurements performed in Section 3.4.2.1.1, shown in Figure 3-14. Immediately before the suspensions were aliquoted into the wells, they were gently agitated to resuspend the particles, and separate any that were only loosely bound together.

As seen from Figure 3-17, in the second set of measurements many of the results were rejected, due to their poor correlation curves, the presence of which was likely to have been due to large objects being present, as described in Section 3.3.3.2.3. This suggests that many of the flakes

could not be easily resuspended, and the distributions of radii recorded by the DLS only represent those objects that remained relatively stable in suspension.

A non-parametric ranked significance test (Mann-Whitney) was performed to assess whether the distributions varied significantly over time for each preparation; the difference was found to not be significant ($P \geq 0.05$) for any of the preparations, and for each the median at 1 week was very similar to the immediate median. For many of the distributions, however – particularly those prepared with the highest concentrations of amino acid – the distributions became tighter over time, with fewer flakes of the smallest sizes or the largest being observed. The decrease in the number of smaller particles in addition to the larger may be due to a process similar to Ostwald Ripening.

Finally, these results (Figure 3-17) suggest significant aggregation occurs over the 1 week period and that the resultant particles are both large and not easily re-dispersed. This trend is most significant for the suspensions prepared with 2.2 mM amino acid solutions, with particularly significant changes observed in those prepared with phenylalanine and tryptophan, whereas the suspensions prepared with tyrosine were of the worst quality immediately after preparation, but did not degrade as significantly.

3.4.2.2 Analysis of the morphology of aromatic amino acid suspended flakes

The aim in preparing the suspensions using the amino acids was for their use as therapeutic delivery vehicles, for which the suspensions must be stable and the flakes therein should be thin – up to few layer – and their lateral dimensions relatively monodisperse. The instability of the suspensions prepared with higher amino acid concentrations – investigated in the previous Section – makes them inappropriate for use in biological applications. From the UV-vis measurements performed in Section 3.4.2.1, the initial concentration and 4 week stability (Figure 3-14) and the theoretical flake thickness (Figure 4-16) of the suspensions prepared in 0.55 µM solutions of aromatic amino acids were considered to be the most promising and therefore these

suspensions were taken forwards for investigation into the morphologies of the flakes using AFM. Both the thickness and lateral dimensions of the flakes are of particular importance with regards to cellular toxicity [72, 73], and can be easily quantified using this method.

3.4.2.2.1 Atomic force microscopy

The flakes were deposited onto the substrates for AFM were prepared in the same way as both valine and sodium cholate for comparability, despite the much lower concentrations of amino acids reducing the problem of residual crystals interfering with the measurements.

A representative AFM image for one of the samples is shown in Figure 3-19. While the observed flakes are similar to those observed in the valine and sodium cholate prepared suspensions (Section 3.4.1.2, Figure 3-13), and those of the other samples, it is noticeable that many more flakes have far smaller lateral dimensions.

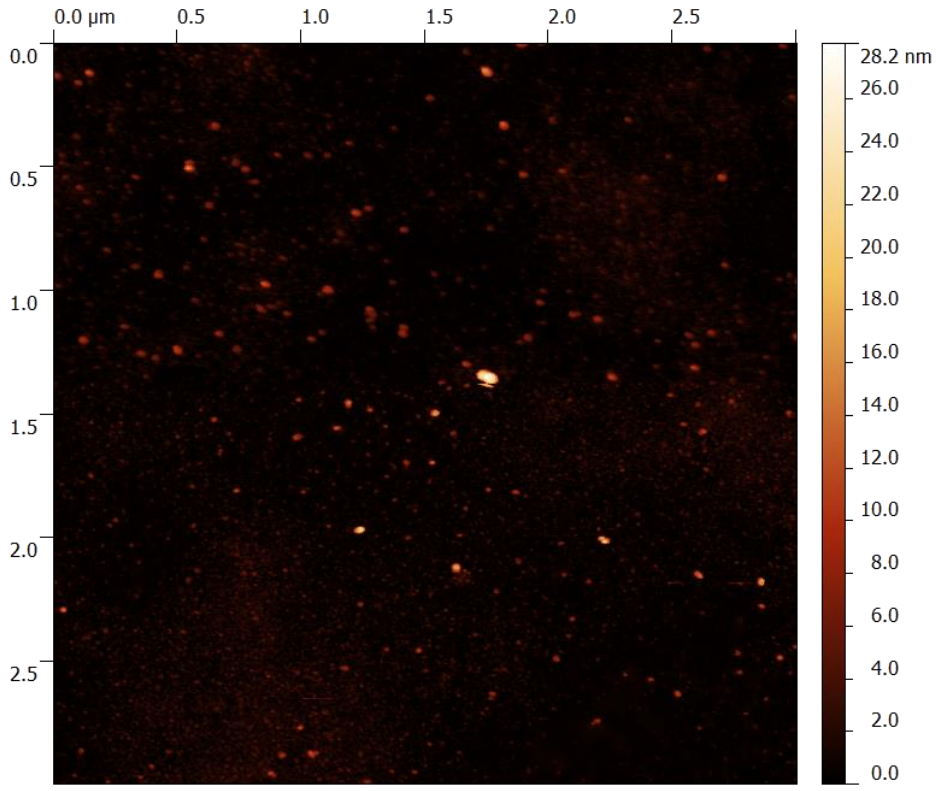

Figure 3-19 – A representative AFM image of graphene flakes exfoliated and suspended in 0.55 µM phenylalanine solution. This image is representative of those taken from the other amino acid suspensions. Deposition onto silicon dioxide wafer again used GEL Pak®.

Flake thicknesses

The flakes were marked using height thresholding, through which the distribution of their thicknesses was found – presented in Figure 3-20– where they are compared to the thicknesses predicted for each preparation using the UV-vis absorption spectrum (Section 3.4.2.1.1, Figure 4-16). For each sample, the mean flake thickness measured using AFM was found to be within the predicted range, calculated using the graphene layer thicknesses reported in the literature using AFM [59, 71], suggesting that the method is a reliable predictor for flake thicknesses in the system tested.

All three preparations examined led to thinner flakes being prepared than those observed with valine exfoliation and suspension (average: 8.87 nm), but remained thicker than those prepared using sodium cholate (main peak average: 2.82 nm). These results all agree with previously predicted interaction energies between the amino acids and graphene flakes [54-56], and the highest lipophilicities (Table 3-1) as it may be predicted that the molecules with the highest interaction energy and highest lipophilicity would provide the environment most favourable to the exfoliation of graphene flakes. Between the three aromatic amino acids, the mean flake thickness for the tyrosine preparation was the highest, while that for tryptophan was lowest (see Table 3-4).

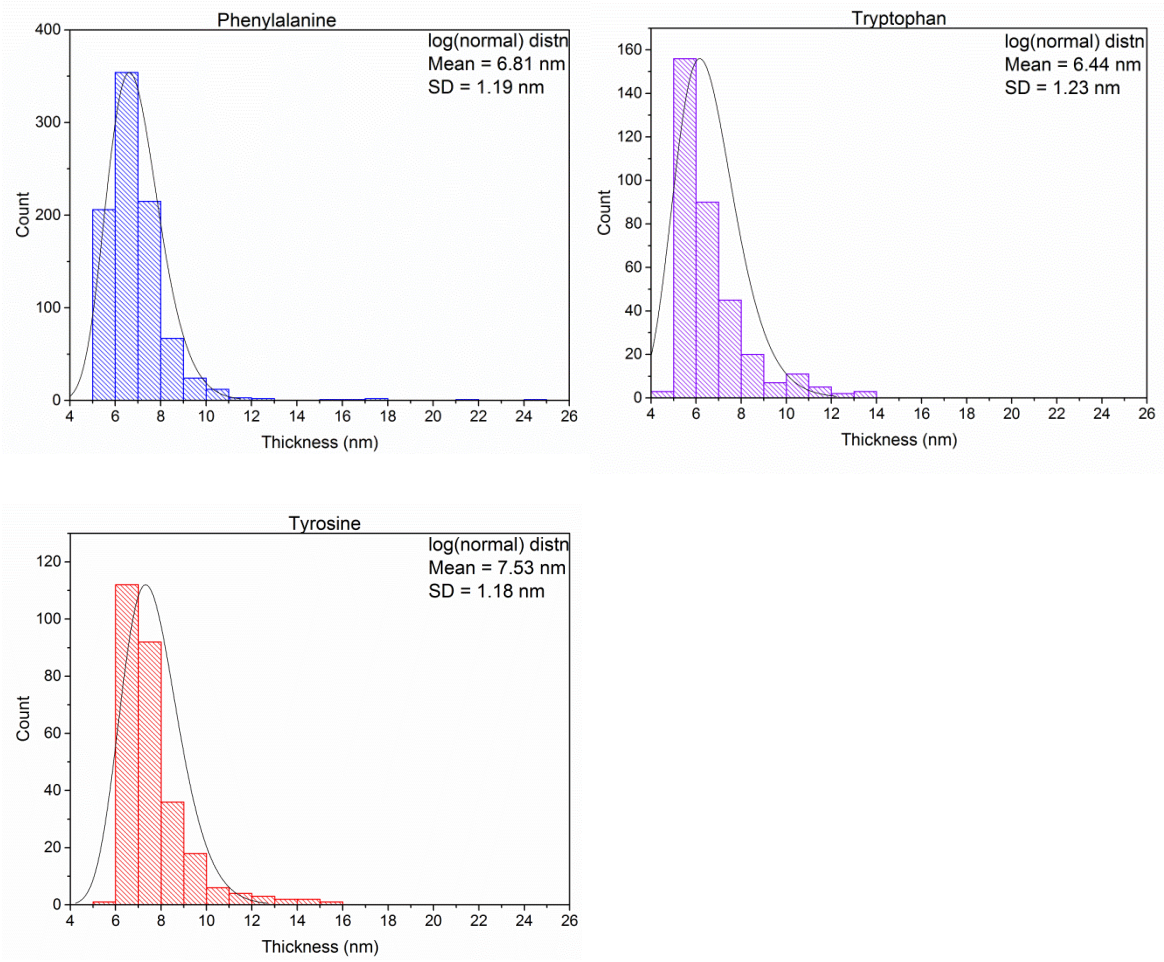

Figure 3-20 – Distribution of flake thicknesses calculated from the AFM images taken of graphene suspensions in phenylalanine, tyrosine and tryptophan solution. The amino acid concentration was 0.55 µM in each case.

Table 3-2 - Flake thicknesses found using AFM compared to the predicted thickness found by interrogating the UV-vis spectrum. The predicted range was calculated by multiplying the predicted <N> by the layer thicknesses reported in the literature when using AFM

Amino acid	Mean thickness (nm)	Estimated <N> (AFM)	Predicted thickness (nm)	Estimated <N> (UV-vis)
Tryptophan	6.44	6-12	4.3-8.6	9
Phenylalanine	6.81	7-13	4.6-9.2	9
Tyrosine	7.53	8-15	5-10	10

Flake lateral dimensions

As the AFM images appeared to shown far more flakes with very small lateral dimensions compared to those observed after exfoliation and suspension with either sodium cholate or valine, the flake lateral dimensions were also investigated using AFM, and the distributions are shown in Figure 3-21. As the same exfoliation technique was used as in the experiments carried out using valine and sodium cholate, it was expected that the flake diameters would also be

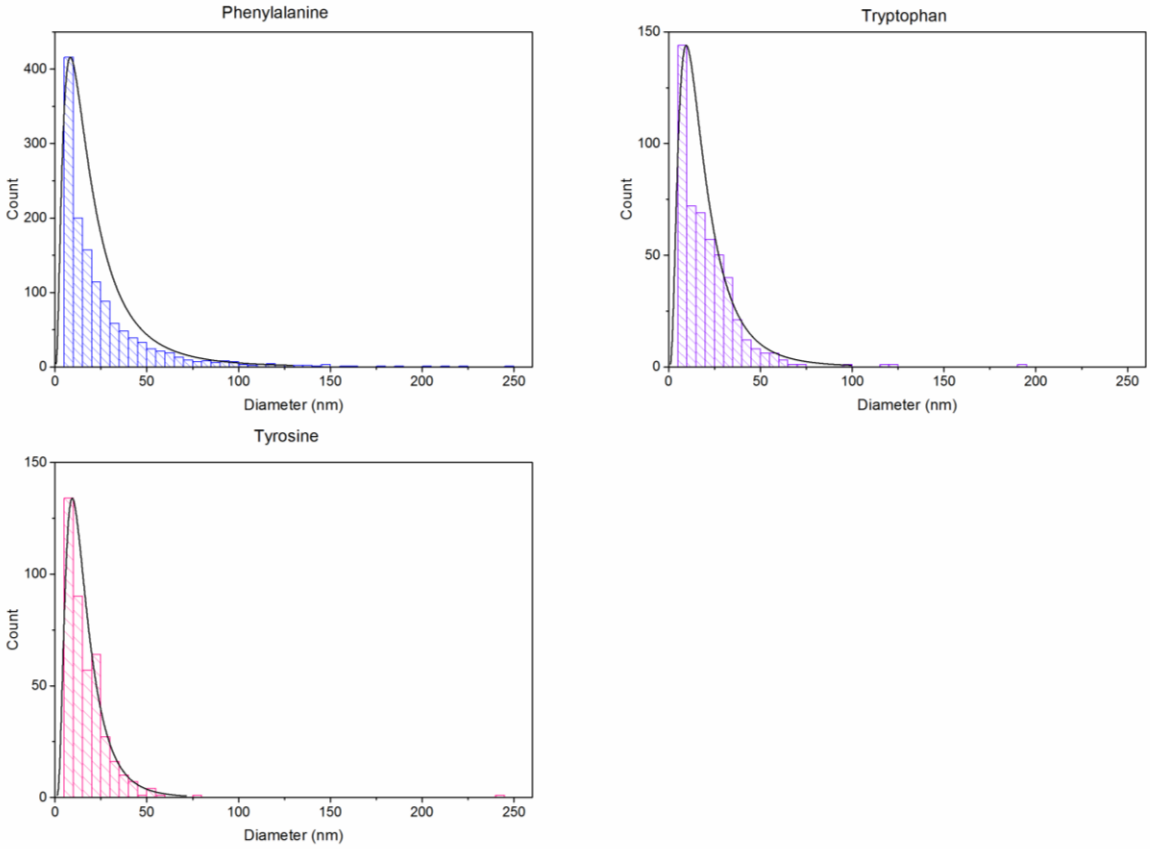

Figure 3-21 - Flake diameters, found using AFM, for graphene exfoliated using phenylalanine, tyrosine or tryptophan. A log(normal) distribution was fitted to each.

Table 3-3 – Mean diameter and SD for the flake distributions, prepared using the three aromatic amino acids as exfoliating and suspending agents.

Sample	Mean diameter (nm)	Standard deviation (nm)
Phenylalanine	16.9	2.32
Tyrosine	13.9	1.87
Tryptophan	16.0	2.05

similar. However, unlike the flakes observed in Section 3.4.1.2, Figure 3-13, the mean flake diameters for each of the preparations, given in Table 3-4, were found to be 3-3.6 times smaller than the expected 50 nm.

3.4.2.3 Summary

Following the preliminary experiments with valine and sodium cholate, phenylalanine, tyrosine and tryptophan were chosen as new exfoliating and suspending agents for graphene in aqueous solution. The same protocol as used in Section 3.4.1 with valine and sodium cholate was followed, utilising probe sonication and SGNFs as the graphitic starting material. While the graphene suspension concentrations using the new amino acids were higher than those produced using valine, and required lower concentrations of the amino acids, two unexpected results were observed. Firstly, in pure water the SGNFs could be exfoliated and suspended, and remained somewhat stable over 4 weeks. Secondly as the concentrations of the amino acids were increased beyond 1.1 μM, the concentrations of suspended graphene decreased, and the suspensions became very unstable over time.

Further investigations of the suspensions prepared using the highest concentrations of the amino acids were performed using DLS. For all preparations, it was found that the objects observed immediately after preparation had apparent hydrodynamic radii that were far larger than would be expected given the original 50 nm diameter of the flakes used, and after only 1 week the majority of the flakes were in large aggregates that could not be easily redispersed.

AFM analysis of the morphology of the flakes prepared in the suspensions judged to be of the highest quality in terms of initial graphene concentration and stability (0.55 μM) was undertaken. The thickness of the flakes was lower than that of those prepared using valine, but no single or bi-layer flakes were observed, with most remaining few-multilayer. In addition, the lateral dimensions of the flakes were also far smaller than that expected, with the majority of the flakes with diameters significantly lower than 50 nm.

3.5 Discussion

Over the course of this work it was found that the amino acids valine, phenylalanine, tyrosine and tryptophan could exfoliate and suspend graphitic materials in aqueous solution, and that the nature of their interactions may be complex and highly dependent upon both the graphitic material and amino acid intermolecular interactions. The efficacy of the exfoliating and suspending agents was assessed in terms of the graphene suspension concentration and stability, the concentration of the amino acids needed to suspend the flakes, and the flakes' morphology – particularly with regard to their thicknesses.

The aromatic amino acids were found to produce suspensions of higher a concentration made up of thinner flakes than those produced by valine, however this was complicated by the severe instability of the flakes at the highest concentrations of aromatic amino acids (0.022-2.2 mM), the ability to exfoliate and suspend flakes in pure water and the severely reduced flake lateral dimensions observed using AFM. However, within these results, tryptophan was still found to produce the most stable suspensions, even at high concentrations, and the thinnest flakes at 0.55 µM, as measured by AFM. As tryptophan has the highest lipophilicity (logP = -1.09), and its structure includes two aromatic rings, this outcome supports the importance of both of these properties when choosing an exfoliating and suspending agent for graphene, despite the complexity of the system. The results also support the importance of differentiating between the lipophilicity and solubility limit of a molecule proposed as an exfoliating and suspending agent; tyrosine had the lowest solubility limit of the three molecules, and was found to produce the least stable suspensions and thickest flakes at 0.55 µM.

3.5.1 Concentration and stability

Initial work focused on the use of valine as an exfoliating and suspending agent, and while it was found to successfully exfoliate and suspend both graphite powder and SGNFs, the concentrations of valine needed to obtain the most significant concentrations of suspended GNPs were very high

(340 mM – three orders of magnitude higher than the most effective concentration of sodium cholate [30]). Subsequent experiments involved the use of aromatic amino acids (phenylalanine, tyrosine, and tryptophan); these molecules were chosen due to the similarity in their molecular structures to valine, and their increased lipophilicity – due to the inclusion of aromatic rings within their structures.

The relationship between amino acid concentration and graphene suspension concentration for the three aromatic amino acids was found to be quite different to that found using valine. For the suspensions prepared using valine, an identifiable peak in graphene suspension concentration was observed close to the solubility limit of valine, similar to the trends observed for suspensions with sodium dodecylbenzenesulfate [35], sodium deoxycholate, sodium dodecyl sulphate and hexadecyltrimethylammonium bromide [76], for which the peak often lay near the critical micelle concentration (CMC). Whereas the immediate suspension concentration did not have a very strong trend with respect to amino acid concentration for any of the three aromatic amino acids, there was a tendency for lower suspension concentrations to be produced for amino acid concentrations ≥ 2.2 μM. This tendency became more pronounced over time, with close to 0 wt% of the graphene left in suspension for these concentrations after 4 weeks.

After 4 weeks the suspensions prepared with the concentrations of aromatic amino acids in the range 0-0.22 μM presented a decrease in suspension concentration comparable to that published in the literature – ranging between a 6-65 wt% decrease for the different suspensions. Over a similar time frame, Lotya *et al.* [30] found that samples of graphene suspended with SDBS decreased in concentration by 65 wt%, and while it was found that 80% of graphene flakes prepared with Tween-80 or Triton-X 100 remained in suspension after 20 days by Wang *et al.* [76], visible agglomerates and sedimentation of Triton-X 100 suspended graphene was observed by Lee *et al.* [77] This was compared to a suspension prepared using sodium cholate, where the suspension mostly remained well-dispersed. In this work, a sharp drop-off in suspension concentration at 4 weeks was observed at concentrations ≥ 2.2 μM, which is significantly lower

than the amino acids' solubility limits. This was accompanied by visible aggregates of graphitic material observed at the bottom of the vial.

Investigation with DLS confirmed the instability of the flakes at the highest concentrations of the three amino acids, and the inability to easily redisperse the flakes after aggregation suggested that it was not reversible. Even immediately after preparation, the apparent hydrodynamic radii of the flakes were observed to be far larger than expected based on the flake diameters, although it should be noted that DLS is dependent upon observed diffusion times, which will be affected by any molecules surrounding the surface, including multiple layers of the amino acids in solution. It has been reported previously that both phenylalanine and tyrosine will spontaneously form fibrils, in both ddH_2O and human serum, at concentrations as low as 1 mM – which is within the range in question [78, 79]. In addition, the work in which Mallakpour *et al.* [52] covalently functionalised GO flakes with a range of amino acids illustrated the propensity for tyrosine-functionalisation to lead to unexpected flake scrolling; while the functionalisation route described in this paper is distinct to that used in this Chapter – depending on covalent functionalisation of GO rather than hydrophobic and π-π interactions with pristine graphitic material – it may be that a similar process occurred in the suspensions prepared here. Of note is that in the work by Mallakpour *et al.* [52], phenylalanine was found to produce very stable suspensions, and no scrolling was observed when flake morphology was investigated.

An additional surprising result was that the SGNF flakes could be exfoliated and suspended in pure water; this was unexpected as the flakes are unfunctionalised, and therefore should be hydrophobic. It is thought that this could have been due to the effects of sonication on the flakes in the system, as sonication is known to introduce defects and disorder in the basal plane of graphene flakes, in addition to causing lateral scission [80, 81]. Furthermore, sonication has been reported induce the appearance of oxygenated functional species on exfoliated graphene, with significant oxygenation observed at only 60 minutes of probe sonication in NMP [82]. Even without sonication, the theoretical structure of graphene with a zig-zag edge that includes

hanging σ and π bonds is very unstable, and difficult to observe experimentally; it is more likely the edges will be hydrogenated, which will affect its interaction with surrounding solvents [83]. For very small flakes, with a high edge:basal plane ratio, and that may be undergoing scission during the sonication process, these aspects may strongly affect its solubility profile, and may have led to the unusual experimental outcomes observed for flake suspensions in pure water. The consideration that additional scission or the creation of defects through sonication was occurring was supported by the subsequent work using AFM to characterise the flakes' morphologies.

In addition, it should be noted that the concentrations of aromatic amino acids investigated were limited by the solubility limit of the least stable molecule - tyrosine. While the approach allowed direct comparability between the three molecules at their respective molar concentrations, it meant that the interaction between the suspended graphitic material and phenylalanine and tryptophan was not investigated up to their respective solubility limits. In order to fully investigate both the amino acids' intermolecular interactions and their interactions with the suspended graphitic material, future work would require that work be done up to and beyond the solubility limit of each of the amino acids.

3.5.2 Flake morphology

The thicknesses of the flakes exfoliated and suspended in valine solution, measured using AFM, were far thicker (mean thickness 8.87 nm – equivalent to 8 ≤ layers ≤ 16) than either the literature standard alternative used as a control (sodium cholate – major peak at 2.84 nm, 3 ≤ layers ≤ 6), or than would be desired

The morphology of the flakes in suspensions of aromatic amino acids was then investigated, where the suspensions used were those that produced the highest initial concentrations of flakes and presented the best stability – and therefore were the best candidates for use as a preparation for therapeutics delivery. The flakes were found to be thinner than those produced using valine,

but also of far smaller lateral dimensions – indicating that significant scission may have been taking place during the sonication process, which supports the hypothesis that the flakes were able to be suspended in pure water due to scission or the introduction of defects. While scission and the introduction of both defects and disorder is known to occur during the sonication of graphene and its derivatives (as described above), it was far more significant than that which was observed during the experiments with either valine or sodium cholate.

As mentioned in Section 3.1, probe sonication is the most aggressive form of sonication, and it is hypothesised that the sonication may have been in the inertial rather than stable cavitation regime (described in Figure 3-1, Section 3.1.1.1), which may be even more aggressive. This is further supported by the observation that the probe became severely damaged over time, with pits and cracks appearing at the probe's tip; physical damage of this kind is often observed in in sonication probes, and is one of the downsides of using this technique compared to bath sonication [33]. This change in the probe's physical form may have led to inhomogeneity in its action, or may have indicated that the regime in which the sonication was taking place was highly aggressive.

It should also be noted, however, that the AFMs used to image the flakes produced by valine and sodium cholate and those used to image the flakes prepared using the aromatic amino acids were different. The AFM used to image the flakes that had been suspended using the aromatic amino acids was located on a lower floor to that used for valine and sodium cholate, and was operated on an isolation table with air cushioning – both of which can lead to reductions in external vibrations and give a better signal to noise ratio. The reduction in the noise levels, therefore, may have led to better topographical resolution of the smaller flakes that may also have been present in the valine and sodium cholate preparations.

From this work, it may be concluded that the use of probe sonication as a method for the liquid exfoliation of graphene may be questionable; the decision to use SGNFs with pre-defined diameters was taken specifically to improve how well-defined the flakes are so that they may be

used in biological applications. With such an aggressive technique being used – made more unpredictable by the damage incurred to the tip over time – this aspect of control is reduced. In addition, the very small lateral dimensions of the resultant flakes may be of concern with regards to their potential toxicity, as such small flakes have previously been observed to enter the nucleus and cause genotoxicity in certain cell types [84, 85]. Finally, the increased ratio of edge groups to basal plane, and the possibility that both disorder and defects in the plane of the flakes could have been incurred [80, 82] means that the interaction with the exfoliating and suspending agents becomes more unpredictable.

Over recent years, there has been interest in using more gentle methods of exfoliation that do not include the use of sonication, including shear mixing and ball milling. Whereas initial work in liquid exfoliation of graphene moved from the use of bath sonication to direct probe sonication in order to reduce processing times and improve exfoliation efficiency, the problems of scission and the introduction of defects have resulted in some movement away from sonication entirely. Ball milling of graphene has been utilised by a number of groups to produce graphene suspensions of high quality, but often low concentration [45, 86]. High shear methods of exfoliation have also been highlighted by a number of groups, but particularly championed by J. Coleman's group in Dublin [87], who have used the method as a way of producing large, low defect graphene flakes, which are particularly desirable in composite or electronics usage. Whereas initial work involving the use of graphene and high shear mixing was often to aid mixture into composites after initial graphene exfoliation, it has been found that shear mixing alone may be able to exfoliate and suspend graphene without the use of sonication [88, 89]. Further, Varrla *et al.* [90] showed that the turbulence associated with a domestic kitchen blender can be sufficient to prepare a mixed suspension that includes few layer graphene flakes, if the interaction energy between the exfoliating and suspending agent and the graphene flakes is sufficiently high. In this work a mixture of ionic and anionic surfactants found in household detergent were used – which are inappropriate for biomedical applications – however the experiments illustrate the potential of other, less aggressive techniques than the widely used sonication methods.

3.6 Future work

Exfoliation of 2D materials including graphene using sonication requires significant investigation into the effects of all the parameters that surround the technique, in order to assess how best these factors should be controlled to make preparations optimal and reproducible. This is particularly important for probe sonication due to the aggressiveness of the technique. Work investigating the effect of probe placement within the sample, temperature, solvent gas content and time taken to sonicate the suspensions would support development of a more complete protocol in future work. This is of particular importance regarding effects on flake morphology, and may provide information not only on whether the technique is suitable for graphene exfoliation, but also the causes of some of the observed effects.

If future work were to be carried out on this area of the project, a more gentle method such as shear mixing, undertaken over very long time periods, may be desirable in order to avoid the problems of scission observed in these experiments. In this way, the lateral dimensions of the flakes make be preserved; while it is not known whether such a technique would be able to produce the same levels of exfoliation, even after long time periods, success in suspending graphene using ball milling and melamine [45] suggests that the approach could be successful.

In addition, TEM images of the agglomerates observed at the higher concentrations of amino acids would be informative in assessing whether this was due to similar flake behaviour as that observed by Mallakpour *et al* [52].

Due to the presence of predominantly multilayer flakes following exfoliation, the very small lateral dimensions caused by aggressive sonication and the problems with regards to stability, it was decided that, as the focus turned to the use of graphene as a therapeutics delivery vehicle, GO would be used instead of amino acid suspended graphene. As described in the Introduction, GO is the most developed of all the graphene derivatives in the field of therapeutics delivery in

the literature, and therefore was considered to be favourable in terms of developing the project towards its goal of therapeutics delivery.

4 Preparation and characterisation of graphene oxide for use in biomedical applications

As the preparations of pristine graphene using amino acids from Chapter 3 were considered to be unsuitable for use as therapeutics delivery vehicles, graphene oxide (GO) was chosen as an alternative graphene-based delivery vehicle for targeting CLL cells. GO has been far more widely used in the biomedical sphere than pristine graphene, as described in the Introduction, and the oxygenated functional groups of its structure provide convenient modes of attaching both therapeutic cargo and targeting ligands.

4.1.1 The Hummer's method of preparing graphene oxide and existent characterisation techniques

Graphene oxide is predominantly synthesised using the Hummer's method or some modification of the procedure. As illustrated in Figure 5-1, the method involves the treatment of graphite flakes with sodium nitrate, potassium permanganate and sulphuric acid before adding water, following which the mixture is stirred for long periods of time. The reaction is often terminated using hydrogen peroxide and most procedures will also involve the use of multiple centrifugation steps to remove both the oxidative starting materials and any unreacted graphite or unexfoliated flakes of graphite oxide [31, 58, 91]. The resulting suspension is distinguished from pristine graphene by its hydrophilicity, insulating properties and fluorescence.

As described in the Introduction, even individual GO flakes are highly heterogeneous in terms of their surface chemistry, and GO suspensions are also highly polydisperse with regards to flake sizes; furthermore, residual contaminants from the oxidation process can often remain. The characteristics of the flakes often also vary significantly between preparations – even when prepared by the same group or company. This is problematic in terms of their use in biomedical applications.

Any nanoparticles used in biological applications must be very highly characterised to allow observed behaviour to be correlated with the starting physicochemical properties; therefore, even though the suspensions to be used in this work were purchased from a supplier that is a member of the Europe-wide Graphene Flagship project and works closely with members of the research community (Graphenea^{TM}), the flakes were extensively characterised and purified in-

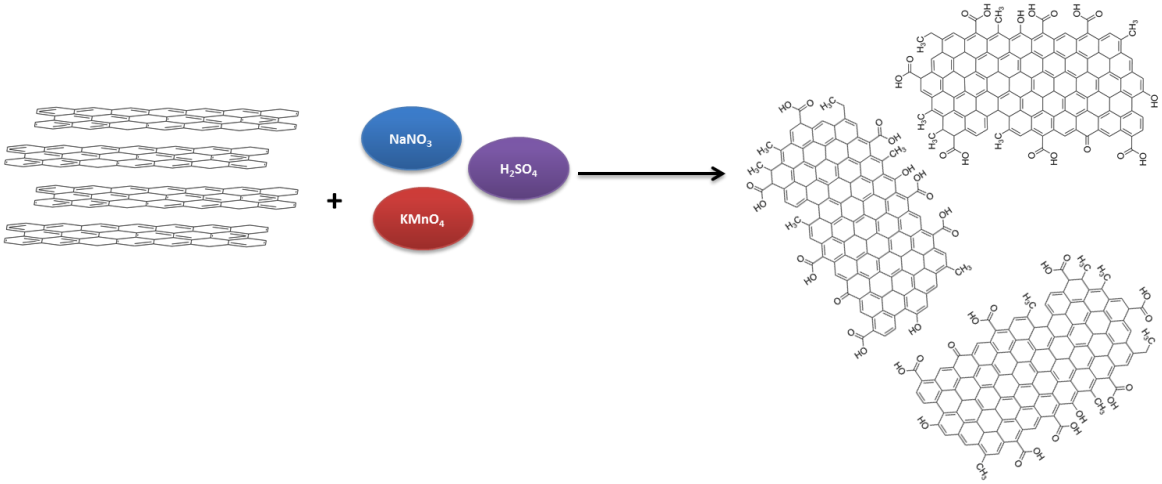

Figure 4-1 - A schematic of the Hummer's method

house. GO is traditionally characterised using a mixture of techniques, including AFM, optical microscopy, DLS, UV-Vis and X-ray photoelectron Spectroscopy (XPS); however, these techniques often do not give a full picture of a sample, both with regards to the size of the flakes and their behaviour in complex and biologically relevant media. In particular, AFM and DLS are limited with regards to the sizes of the flakes that can be easily observed. DLS cannot be used for objects with lateral dimensions > 5 µm and often does not easily measure objects with sizes > 1 µm. AFM is time consuming and most set-ups cannot reliably measure areas larger than 10x10 µm, making it difficult to collect images on a large sample of objects or measure flakes with larger lateral dimensions. In addition, both AFM and optical microscopy require the immobilisation of the flakes on a substrate, and therefore cannot be used to determine the behaviour of flakes in suspension.

4.1.2 Photoluminescence and the structure of graphene oxide

The structure of GO flakes leads to significant difference in optoelectronic properties in comparison to pristine graphene. There remains debate in the scientific community over the exact structure of GO [92], with two main models that are generally proposed. The first is the Lerf-Klinowski structure – in which the polyaromatic basal plane of graphene is heterogeneously functionalised with hydroxyl, epoxy and carboxylic acid groups [31, 93]. The second is the two component model of a weakly oxidised basal plane exhibiting carboxylic acids at the flake edges and adsorbed highly functionalised oxidative debris on its surface [94]. Depending on the model used, the optoelectronic properties of GO, and the way in which they differ from pristine graphene may be explained – in particular, its insulating and photoluminescent properties.

In the Lerf-Klinowski model, whereas the sp^2-hybridised carbon structure leads to the electrons obeying a linear dispersion relation in pristine graphene, the presence of oxygenated functional groups interrupts this structure with sp^3 domains, creating isolated sp^2 clusters and leading to the flakes' insulating properties [93, 95]. The heterogeneity of the flake functionalisation means that these clusters are of various different sizes; it is thought that the photoluminescence of GO derives from electron-hole pair recombination in these isolated electronic states [93].

In the two-component model, the photoluminescent properties are derived from the oxidative debris that exists on the weakly oxidised graphene flake surfaces [94], where the broadband photoluminescence is due to the heterogeneous nature of the oxidative debris. This model was proposed after experimental evidence in which oxidative debris and weakly oxidised graphene sheets could be separated following base washing with NaOH solution [94]. After this separation, the oxidative debris was found to exhibit significantly stronger fluorescence intensity, with an emission peak blue-shifted in comparison to the original GO, while the poorly oxidised flakes exhibit no fluorescence. These observations were considered to be due to quenching phenomena when the debris was adsorbed [96].

Recent work reported the high resolution structural characterisation of GO suggests that the structure is closer to the Lerf-Klinowski model. High resolution transmission electron microscopy was performed under elevated temperatures to remove surface contaminants that are ubiquitous on GO (and, to a lesser extent pristine graphene) under atmospheric conditions, and often prevent in-depth characterisation of the flake structure. The observations presented support a nano-crystalline structure (of approximately 2 nm^2 grain size), separated by defects, including both oxygenated functional groups and > 6 member rings [97]. This supports a model similar to the Lerf-Klinowski structure, and the challenge to the two-component model that rather than removing adsorbed material, base-washing fundamentally changes the structure of the GO flakes [92].

Despite the controversy surrounding the structure of GO and the related potential origins of its fluorescence, the fact that as-prepared GO exhibits broadband photoluminescence is broadly acknowledged, although the flakes' capacity to quench fluorescence is more commonly used in biomedical applications [93, 98-100]. The fluorescence has been reported to have been excited from anywhere between 325-600 nm with the resultant emission ranges between 400-1100 nm [101-103]. Peak fluorescence was observed between 700-850 nm after excitation between 580-600 nm by Luo *et al* [102], while peak fluorescence was observed by Shang *et al.* [104] between 600-680 nm following excitation between 380-440 nm. GO fluorescence has been used for the detection of flake internalisation into phagocytic cells using both optical microscopy and flow cytometry [105] delivery to cells using optical microscopy following conjugation with PEG and a CD19 targeting antibody [106], demonstrating the robustness of the property following further functionalisation of the flakes. The inherent fluorescence of GO expands the number of techniques available for characterisation of the flakes; Singh *et al.* [107] used flow cytometry to characterise GO flake characteristics, and while the forward and side scatter was primarily used for size distribution analysis, the fluorescence profile was noted as a method to assess the flakes' surface chemistry – with diminishing fluorescence intensity following treatment with hydrazine hydrate.

Raster image correlation spectroscopy (RICS) is a fluorescence technique used for measuring the size and movement characteristics of fluorescent bodies; the technique has been used in applications as broad as cell trafficking studies and protein aggregation [108, 109], and can measure a far broader range of object sizes than techniques such as DLS. While its use has been reported regarding the interaction between GO flakes and fluorescently labelled BSA, its use to characterise GO flakes alone has not been demonstrated. By harnessing the inherent fluorescence of GO, characterisation techniques such as RICS and flow cytometry can be used to give a more complete characterisation of the flakes in suspension before their introduction to cells.

4.1.3 Cellular studies

The aim of this project was to prepare GFN-based therapeutics delivery vehicles, using leukaemia as a disease model; therefore preliminary work to investigate the interaction of GO with cellular components focused on relevant leukaemic cells and primary white blood cells from normal donors. As described in Chapter1, the reported interaction between GO and cellular components has varied widely, and often contradictory conclusions have been drawn regarding the behaviour of GO with cells [110, 111]. The cell models chosen were the K562 myelogenous cell line and primary peripheral blood mononuclear cells (PBMCs). K562s were selected as a well-characterised cell line derived from myeloid lineage bone marrow cells from a chronic myeloid leukaemia case, and expressing the oncogene BCR/ABL1, which presents a clear therapeutic target [112, 113]. They provided a uniform population of cells to support testing of both apoptosis and proliferation. PBMCs are primary mononuclear cells purified from the blood of normal donors; the mixed population of cells contains lymphocytes (T-cells and B-cells capable of micropinocytosis) and phagocytic monocyte and macrophage cells. These primary human cells are more sensitive to spontaneous and induced apoptosis and can be induced to proliferate; in addition the presence of phagocytic cells provides a more realistic environment for the investigation of the flakes' interactions with cellular components present in the blood, particularly in the event of aggregation.

4.2 Aims & Objectives

The aim for this Chapter was to prepare GO such that it would be suitable for use as a therapeutics delivery vehicle to leukaemic cells. To this end, the samples had to be highly characterised, both in terms of the flakes' physical properties such as geometry and surface chemistry, and regarding the suspension behaviour in the presence of biologically relevant media such as saline, PBS and BSA solution. The existing GO characterisation methods were limited, both in terms of the size range that could be accessed, and the often protracted timescales required. By using the inherent fluorescence of GO, we aimed to find methods that could address the shortfalls in other characterisation methods and provide a fully characterised GO sample before its introduction into cell culture. To achieve these aims, the GO samples were characterised using the traditional methods, before using two methods (Raster Image Correlation Spectroscopy – RICS – and Flow Cytometry) that are dependent upon the fluorescence of the GO flakes, and offered the potential to capture the full size range of the flakes under investigation, and their interactions with complex media respectively, including media containing serum proteins. The instability of GO without further functionalisation in biologically relevant media has been widely reported, hence it was expected that further functionalisation would be necessary before introduction of the suspensions to cells; standard functionalisation approaches using polyethylene glycol (PEG) were pursued and characterisation of both the flakes' surface chemistry and their behaviour in suspension were explored using both traditional methods and fluorescence-based approaches. Finally, preliminary cell culture experiments were undertaken to assess the difference in the behaviour of the different GO types with cell components.

4.3 Experimental

4.3.1 Materials

Graphene oxide dispersions in water were purchased from Graphenea Inc. (Spain). Poly(ethylene oxide), 4-arm, amine-terminated (average M_n 10000; typically 10000-12000), *N*-(3-Dimethylaminopropyl)-*N'*-ethylcarbodiimide hydrochloride (EDC) and the Kaiser Test Kit were all purchased from Sigma Aldrich® Co. (UK). Poly(ethylene oxide), 4-arm, amine-terminated (average M_n 2000) was purchased from JenKem Technology (USA); PEG_8-biotin and PEG_{11} diamine were purchased from Polypure (Norway). Vivaspin centrifuge ultrafiltration tubes with 30 kDa MWCO membranes were purchased from Sartorius (UK). Corning™ Falcon™ round-bottom polystyrene tubes for FACS analysis were purchased from Fisher Scientific® (UK).

4.3.1.1 Cell culture materials

Primary PBMCs were collected from healthy volunteers with full Research Ethics Committee (REC) approval for use in evaluation of new treatment strategies (REC reference 10/H1017/73). All samples had been collected with full consent for research use and are stored in pseudo-anonymised form with identity traced only through the collecting medical institution (Manchester Royal Infirmary, custodian Dr John Burthem). There are no direct or indirect medical implications for donors.

RPMI 1640 (without L-Glutamine), Penicillin-Streptomycin, L-Glutamine and Foetal Bovine Serum (FBS) were all purchased from Invitrogen™, ThermoFisher (UK). Corning® multi-well plates were purchased from Sigma Aldrich® Co. (UK). Anti-CD3 antibody [UCHT1] conjugated with PerCP/Cy5.5®, anti-CD14 [MEM15] conjugated with FITC, anti-CD19 antibody [SJ25-C1] conjugated with PE/Cy7® and propidium iodide were all purchased from Abcam (UK). Giemsa stain was purchased from Sigma Aldrich® (UK).

4.3.2 Instrumentation

Sonication and DLS instrumentation as described in Section 3.3.2. Raster Image Correlation Spectroscopy was performed using a Zeiss LSM510 confocal laser scanning microscope with a c-Apochromat 40x/NA 1.2 water-immersion objective, and samples were excited at λ_{ex} = 488 nm; spectra were analysed using the in-house software ManICS. Flow cytometry was performed using a BD FACSCanto™ II flow cytometer with two lasers (488 nm solid state and 633 nm HeNe) and analysed using BD FACSDiva™ and Flowing Software v 2.5. X-ray photoelectron spectroscopy was performed at the National EPSRC XPS Users' Service (NEXUS) at Newcastle University and analysed using Casa XPS software. Atomic force microscopy was performed in air using a Bruker MultiMode8 in ScanAsyst mode using a ScanAsyst-air probe; images were analysed using Gwyddion software. Spin coating onto silicon substrates with a 290 nm oxide layer was performed using a Laurell Technologies WS-650-23 spin coater and brightfield reflective optical microscopy was performed using a Nikon Eclipse LV100ND upright reflective microscope; digital images were captured using NIS-Elements®. Cell visualisation was performed on an Olympus IX70 phase contrast inverted microscope and a Zeiss Observer.Z1 differential interference contrast microscope.

4.3.3 Chemical methods

4.3.3.1 Graphene oxide purification

GO was first centrifuged at low speed (3893 x g) for 2 h and the supernatant retained to remove any aggregates or unoxidised graphitic material [73]. The suspension was then subjected to 5% HCl solution [101] to remove any residual metal ions from the suspension, which may have been left over from the initial oxidation process; the solution was left stirring at room temperature (RT) for 2 h, following which the suspension was diluted using Milli-Q water and then subjected to repeated washing steps *via* centrifugation at 17000 x g for 45 minutes per step with distilled warm water until the supernatant reached neutral pH both to remove residual HCl, the metal ion-chlorides and any other by-products of the Hummer's method such as mellitic acids [73].

4.3.3.2 PEGylation

The protocol followed was based on that detailed by Yang *et al.* [114], with some modifications to increase the affinity of the GO to the PEG chains and decrease the chance of crosslinking between the GO flakes. GO suspensions in distilled water were stirred in the presence of 1-Ethyl-3-(3-

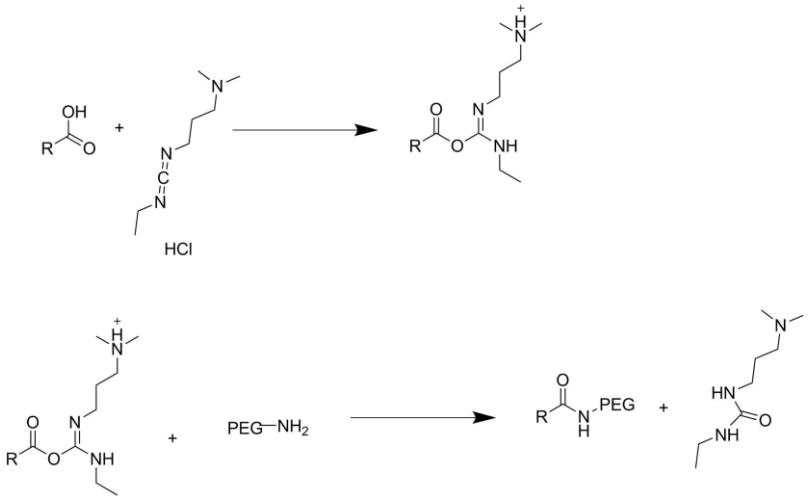

Figure 4-2 - Formation of an amide bond using EDC chemistry.

dimethylaminopropyl)carbodiimide (EDC) in order to activate the carboxyl groups present on the GO, making them susceptible to amide coupling, as shown in Figure 5-2. EDC is very hygroscopic and degrades in the presence of water, so the container was left to equilibrate to RT before opening to minimise the formation of condensation inside the container.

Amine-terminated PEG of varying sizes was mixed with a small amount of distilled water and the activated GO was slowly added to the PEG using a peristaltic pump while undergoing bath sonication. This step was performed so that the activated GO was introduced to an excess of PEG in order to minimise cross-linking.

Sonication was performed for 70 minutes, following which the mixture was left stirring overnight. The suspension was then repeatedly washed in a Vivaspin™ filter centrifuge tube. The GO tended to stick in the filters, hence the suspensions needed to be regularly agitated during filtration. Washing continued until the filtrate was free of residual PEG chains, tested using the Kaiser Test kit as described in the manufacturer's protocol: briefly, a drop of KCN and pyridine was added,

followed by a drop of ninhydrin in n-butanol, then phenol in n-butanol to the test mixture and heat to 110^{o}C for 5 minutes. Pure water was used as a negative control. A colour change to deep blue/purple (referred to as Ruhemann's purple) indicates the presence of primary amines, in which case the suspension would need further washing.

4.3.4 Characterisation methods

4.3.4.1 Brightfield reflective optical microscopy

Suspensions were deposited onto silicon wafers with a 290 nm oxide layer using spin coating. The substrates were first cleaned by submerging them in acetone, followed by distilled water, then isopropyl alcohol and sonicating in a bath for 10 minutes. The substrates were dried in a warming oven to remove any residue of the respective solvents. The GO suspensions were diluted to approximately 800 µg/mL if possible, and a droplet of the suspension large enough to cover the surface of the substrate was pipetted on top following vacuum fixation in the spin coater. The substrate was then spun at 3000 rpm for 2 minutes under nitrogen. The dry substrate was visualised using white light reflective optical microscopy with a Nikon Eclipse LV100ND microscope with digital camera attachment. The images were captured using NIS-Elements® software, using which colour balance was adjusted for optimal contrast.

Images were analysed using ImageJ (NIH, USA). For samples in which there was not a significant degree of overlap, automatic particle sizing was used. In order to perform a thresholding operation the colour balance was adjusted to reduce the green and red contributions, following which the image was transformed into 16 bit greyscale before using the thresholding operation. In images with a high degree of overlap, manual particle sizing was used.

4.3.4.2 Atomic force microscopy

AFM was performed on the same samples as those used in the optical microscopy experiments. Microscopy was performed using a Bruker Multimode in ScanAsyst mode, as described in Chapter

3, Section 3.3.3.2.2. Image analysis was performed using Gwyddion SPM analysis software, using automatic thresholding techniques for particle analysis.

4.3.4.3 X-ray photoelectron spectroscopy

X-ray photoelectron spectroscopy (XPS) employs x-ray illumination of a sample to liberate electrons from the sample surface so that their binding energy can be assessed; in this case the x-ray source was an Al Kα source, with an energy of $h\nu$ = 1486.6 eV. The energy of the released

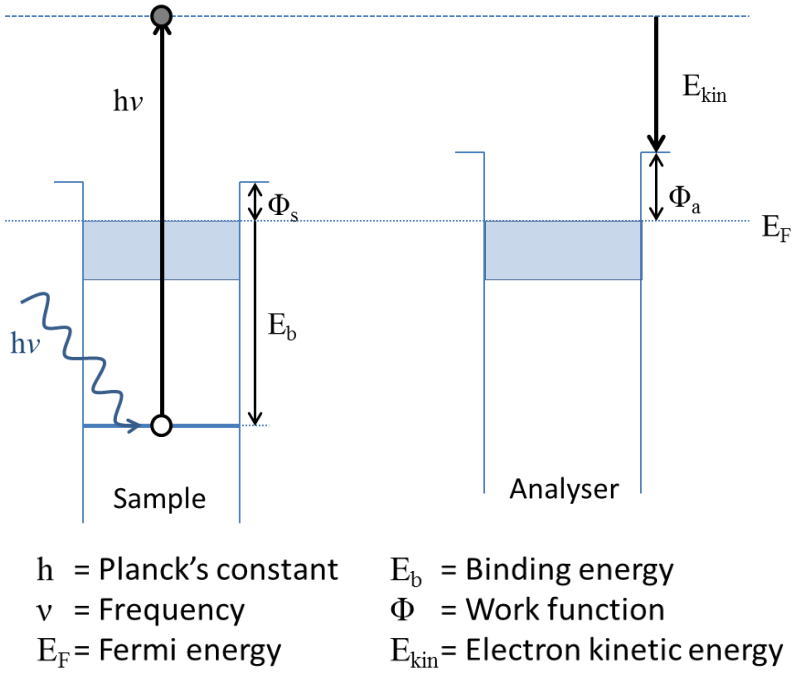

Figure 4-3 – An illustration of the underlying concept of XPS. By illuminating the sample with an x-ray of known energy ($h\nu$) and measuring the energy of the emitted electrons (E_{kin}), their binding energies (E_b) can be found. Figure adapted from Hofman [115].

electrons is characteristic to the elements present and the way in which they are bound to their neighbouring atoms. The technique is limited to surface analysis, however the 2D structure of graphene and GO means that the technique is well suited to the material [115]. The resultant spectra provide information on the energy of the electrons that have been emitted and the counts per second (CPS) – i.e. the number of electrons hitting the detector – to give information on the relative abundance of the particular element detected [115]. Figure 5-4 illustrates the underlying concept of the technique. For each sample, the energy required to liberate an electron is determined by its binding energy (E_b) and the work function (Φ_s) of the sample – determined by various properties of the sample surface including its crystal face and any contamination [116]. The energy left over will be transformed into the kinetic energy of the

electron as it moves towards the analyser. Once there, the particle must overcome the analyser's work function (Φ_a), following which the residual energy will be detected.

Samples were prepared by drop-casting aqueous suspensions directly onto silicon wafers with an oxide layer of 290 nm. Drop-casting continued until the entire wafer was covered with a complete layer that was thick enough to completely obscure the silicon wafer surface and looked dark brown to the naked eye.

XPS was performed by Nexus Newcastle using a Kratos Axis Nova XPS system. Measurements were repeated in 3 different positions across the sample and charge compensation was used in all measurements due to the insulating nature of both the GO and the substrate. The spectra analysed were those with the clearest spectrum that related most closely to the known functional groups: charge compensation is known to cause peak shift to lower binding energies (around 3 eV is typical in this system [private communication, Dr Jose Portoles, NEXUS, University of Newcastle]), and in a sample such as GO that is heterogeneous on a local scale, differential charging may be observed [117]. All spectra were analysed using CasaXPS™.

4.3.4.4 UV-Visible absorption spectroscopy

As-prepared suspensions were aliquoted into a quartz cuvette and measured as described in Chapter 3, Section 3.3.3.2.1.

4.3.4.5 Dynamic light scattering

GO samples of varying surface chemistries were prepared as described in Section 4.3.3 and kept as suspensions in aqueous media. Samples were diluted to approximately 50 µg/mL, and 100 µL was analysed in triplicate. Data acquisition and analysis was performed as described in Chapter 3, Section 3.3.3.2.3.

4.3.4.6 Raster image correlation spectroscopy

An in-depth description of the theory behind RICS can be found in papers by Digman *et al.* [118, 119]; confocal microscopy utilises a raster-scanning laser to create fluorescence images, which allows RICS to make use of the hidden time structure present in the images. Three levels of coarseness in the time structure are present within the images made by a confocal microscope – microsecond, millisecond and second, defined by the pixel dwell time, the line rate and the frame rate respectively, as illustrated in Figure 5-5.

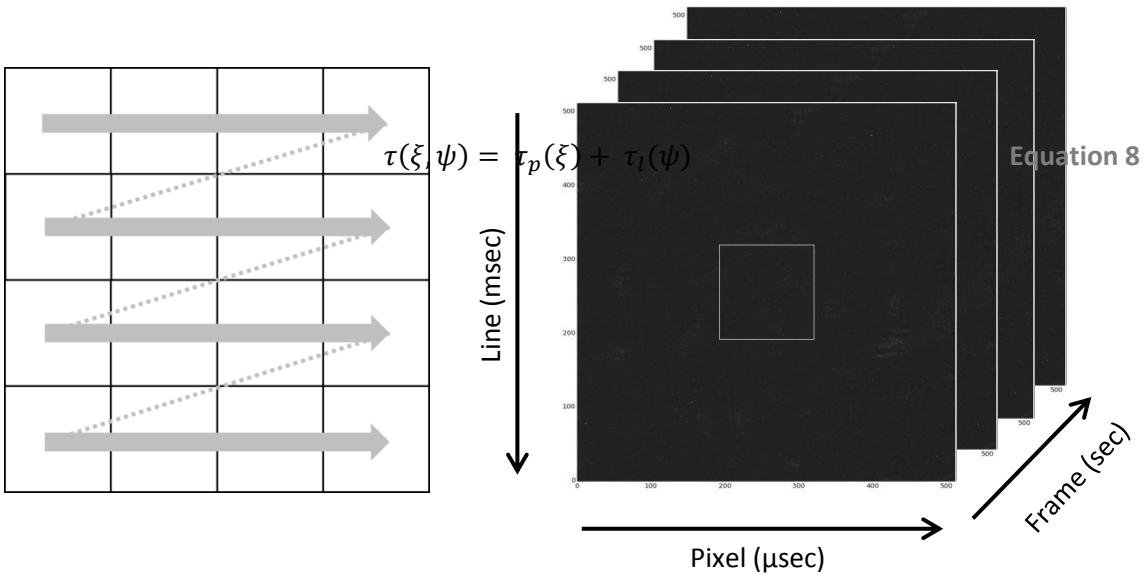

$$\tau(\xi, \psi) = \tau_p(\xi) + \tau_l(\psi) \quad \text{Equation 8}$$

Figure 4-4 – An illustration of the underlying concept behind RICS. A schematic view of the a) raster scanning pattern that the laser uses to form a 2D image and b) a temporal z-stack of images, in which the three levels of temporal coarseness are indicated. Adapted from Digman *et al.* [118].

To gather this information, the technique uses the scan function:

where τ_p = pixel dwell time, τ_l = line rate, ξ = the spatial displacement in the x-direction, ψ = spatial displacement in the y-direction in a raster image.

From Equation 8 a 2D autocorrelation can be built:

$$G_s(\xi,\psi) = G(\xi,\psi)\cdot G(\xi,\psi) = \frac{\langle \delta I(x,y)\delta I(x+\xi,y+\psi)\rangle_{x,y}}{\langle I(x,y)\rangle^2_{x,y}} \qquad \textbf{Equation 9}$$

where $I(x,y)$ = pixel fluorescence intensity, $\delta I(x,y) = I(x,y) - \langle I(x,y)\rangle_{x,y}$ = the fluorescence intensity variation around the mean. From this, an autocorrelation function for 3D diffusion can be built:

$$G(\xi,\psi) = \frac{\gamma}{N}\left(1+\frac{4D(\tau_p\xi+\tau_l\psi)}{\omega_0^2}\right)\cdot\left(1+\frac{4D(\tau_p\xi+\tau_l\psi)}{\omega_z^2}\right)^{-1/2} \qquad \textbf{Equation 10}$$

where D = diffusion coefficient, N = number of particles in a confocal volume, $\gamma = \frac{1}{\sqrt{8}}$, ω_0 = lateral beam waist and ω_z = axial beam waist. This is fitted using the Levenberg-Marquardt algorithm, giving the diffusion coefficient, number of particles and goodness of fit (R^2) for each ROI interrogated. From the diffusion coefficient, the apparent hydrodynamic radius will be calculated using the Stokes-Einstein equation (Equation 7).

Suspensions were prepared at concentrations of approximately 50 µg/mL, and 300 µL was aliquoted into a Lab-Tek Nunc® 8-well chamber slide (Fisher Scientific, UK). Fluorescence images were taken following excitation with a 488 nm argon laser (30 mW), and measured with a broadband filter. A stack 30 images was acquired per sample. The region of interest was approximately 28x28 µm with a pixel size of 54.9 nm and pixel dwell time of 6.4 µs, giving a line-time of 7.7 ms and a frame time of 3.94 s. All experiments were performed at 21°C in a climatically controlled environment.

4.3.4.7 Flow cytometry

4.3.4.7.1 GO samples alone

For the study of graphene alone, preparations were tested in the absence of cells, but within different buffers (NaCl, PBS, BSA in PBS) to assess the variation in flake behaviour using light scatter properties – i.e. forward and side scatter counts (FSC/SSC) – and also fluorescence properties of the suspensions. Variations in these properties were used to identify the changes in interflake interactions and their interaction with serum components.

Flow cytometry was performed on samples suspended in the media under investigation. Each sample was aliquoted into the FACS tubes to a volume of 400 µL. The tube was then inserted into the sample loader and run until 10000 events had been recorded (or as many could be before the sample volume was exhausted). Side scatter and forward scatter measurements were recorded, and the results presented on a scatter plot, while fluorescence measurements were recorded and presented on a histogram.

4.3.4.7.2 Cell samples

Cells were harvested from their multi-well plate by gently pipetting up-and-down to remove any that were lightly adhered to the bottom of the wells; some macrophages and nurse-like cells are likely to have remained firmly adhered and may not have been fully represented in the samples. Resuspended cells were then aliquoted into the FACS tubes and washed once with cold PBS, and kept on ice until measurement by flow cytometry

PBMCs contain a mixed population of T-cells, B-cells, monocyte macrophages and natural killer cells. Each cell set has a characteristic forward and side scatter pattern that allows specific gating using the flow cytometry software. In an initial experiment, fluorescent antibodies recognising receptors characteristically expressed on the surfaces of different cells (anti-CD3-PerCP-Cy5.5 for T-cells, anti-CD19-PE for B-cells and anti-CD14-FITC for monocytes and macrophages) were incubated with freshly harvested PBMCs and run through the flow cytometer. By gating using the fluorescent populations for each respective channel, the respective populations could be

highlighted on the scatter plot as illustrated in Figure 5-6, and these gates used for subsequent experiments. This also shows that the majority of the cells are T and B cell lymphocytes.

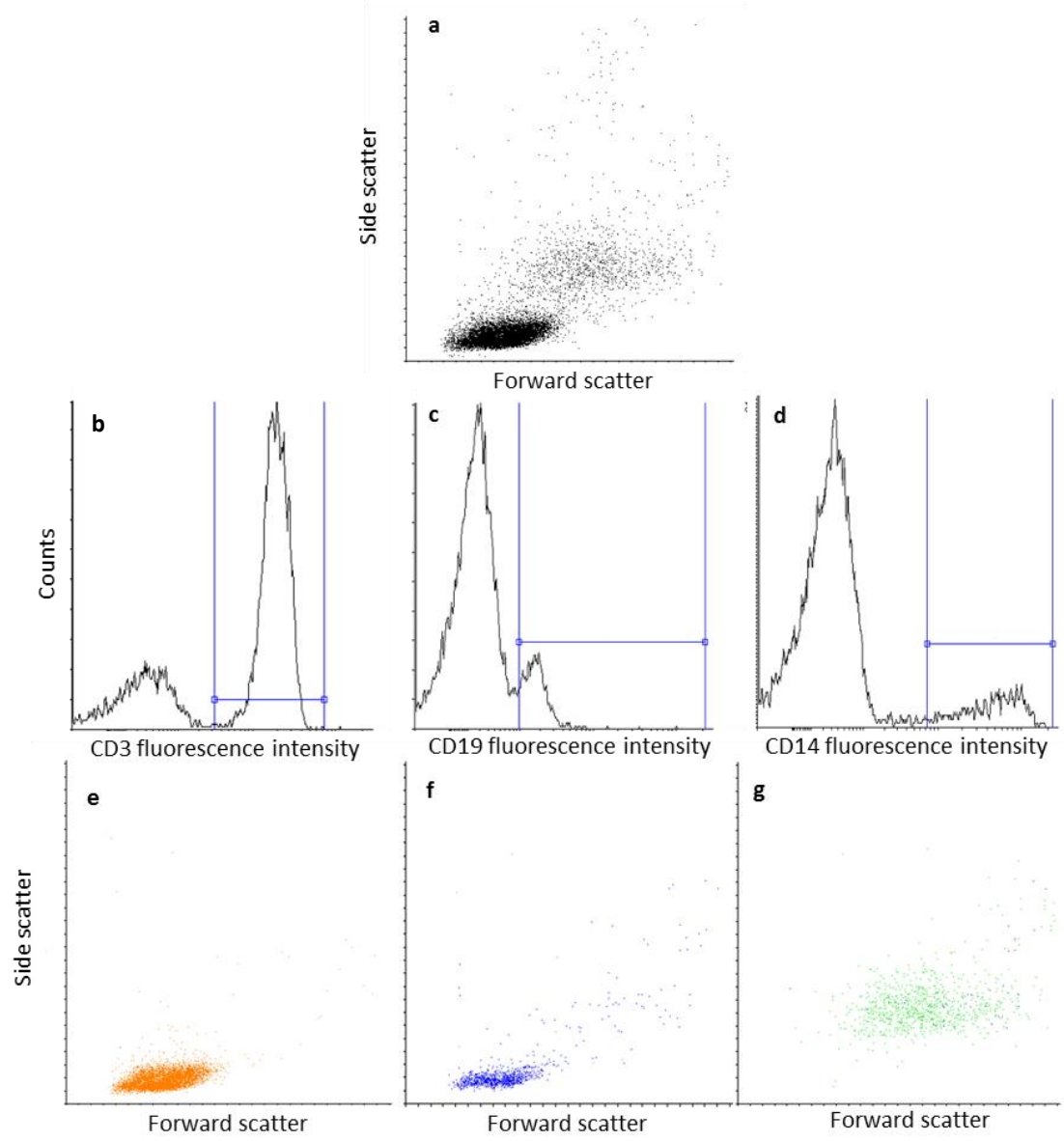

Figure 4-5 – Flow cytometric gating using antibody fluorescence to separate different white cell populations in a PBMC culture. Cell populations were gated according to the fluorescence intensity of the respective cell surface markers, and their populations highlighted on the forward/side scatter plot, allowing population separation without staining. a) Full forward and side scatter plot showing all the cell populations b) anti-CD3 fluorescence gating for T-cells, c) anti-CD19 fluorescence gating for B-cells, d) anti-CD14 gating for monocytes and the FSC/SSC profiles highlighted using the fluorescence gating: e) T-cells, f) B-cells, g) monocytes

Similarly, gating could be used to separate live and dead cells; PBMCs were incubated with 0-5 µg/mL Etoposide, and stained with propidium iodide – a molecule that displays typical fluorescence when bound to nucleic acids that is excluded from live cells but freely enters dead

cells, and therefore can be used as an indicator of cell death. By again gating on the fluorescent population, as shown in Figure 5-7, the distinct forward and side scatter profile of the dead cells was observed. This gating strategy was confirmed by observing the change in gate population with increasing etoposide dose, as illustrated in Figure 5-8. Gating was predominantly used to identify this population in subsequent experiments.

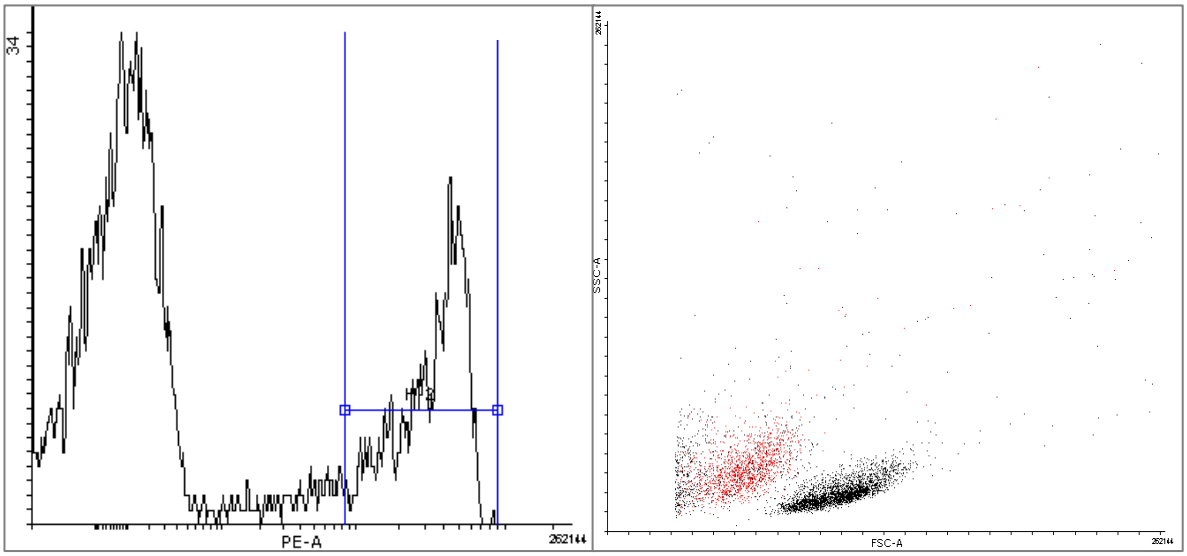

Figure 4-6 – Flow cytometric analysis of PBMCs treated with etoposide and stained with PI. The region of high PI fluorescence (shown on the left) was gated and marked red to confirm the region in which the dead cells lay on the scatter plot (right)

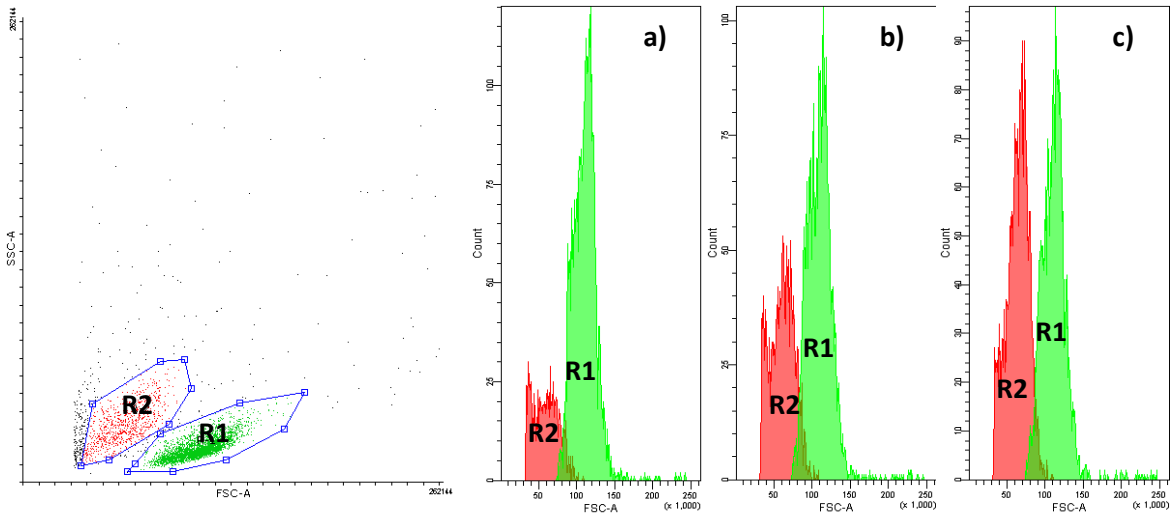

Figure 4-7 – PBMCs gated for live and dead populations at different concentrations of etoposide a) Control, b) 2.5 µg/mL etoposide c) 5 µg/mL etoposide. Measured using the gating strategy indicated in Figure 4-6

4.3.5 Cell culture and toxicity

4.3.5.1 Cell culture

4.3.5.1.1 K562

K562, an immortalised suspension chronic myeloid leukaemia cell line, was used in this project. The cells were cultured in RPMI-1640 medium with 10% v/v FBS, 1% v/v Penicillin-Streptomycin and 1% v/v L-Glutamine (complete medium) and incubated at 37^{o}C in a humidified 5% CO_2 incubator. Before use, the complete medium was warmed to 37^{o}C in a warming bath.

K562 cells were initially subcultured three times a week, to a 1:3 dilution with fresh culture medium.

4.3.5.1.2 Peripheral blood mononuclear cells

Peripheral blood mononuclear cells (PBMCs) were obtained by fractioning heparinised whole blood from healthy volunteers to remove erythrocytes, neutrophils and most platelets (leaving lymphocytes, monocytes and some natural killer cells).

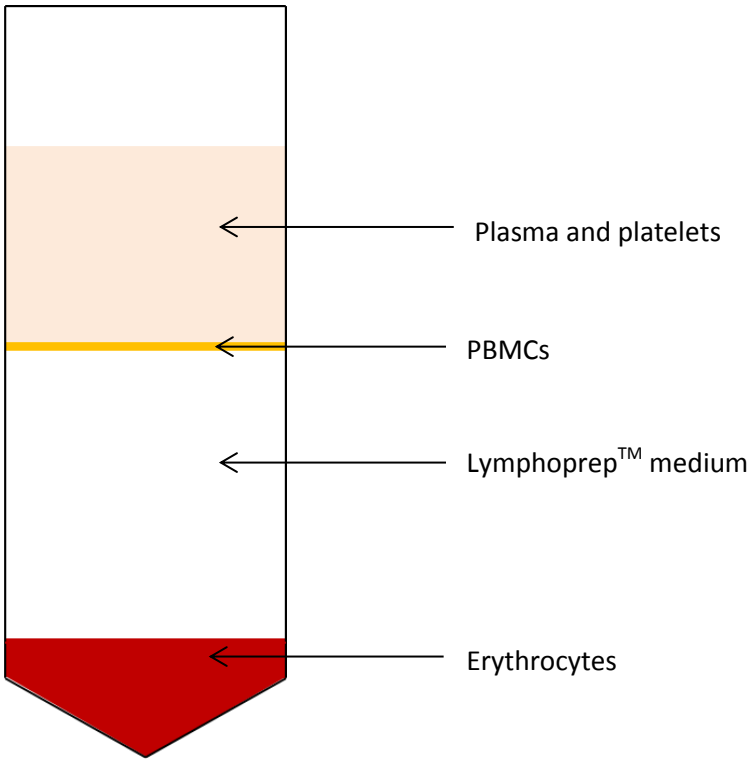

Figure 4-8 - Schematic of a whole blood sample after centrifugation in the Lymphoprep™ medium

A variation on the manufacturer's suggested protocol was used to separate PBMCs from whole blood using density gradient centrifugation. Approximately 10 mL Lymphoprep™ was aliquoted into a 50 mL centrifugation tube (Falcon) and an equal volume of whole blood was gently layered on top, with the side of the centrifuge tube used to aid the gentle layering, ensuring minimal mixing of the Lymphoprep™ and whole blood. The layered mixture was then centrifuged at 800x g for 20 min at RT with slow acceleration and deceleration. Following centrifugation, the PBMCs form a visible band at the sample/medium interface, where the upper layer is plasma and platelets (illustrated in Figure 5-9). PBMCs were removed from the band at the interface using a sterile plastic Pasteur pipette (BRAND® pipette, Sigma Aldrich, UK), taking care to avoid taking up the Lymphoprep™ medium or the plasma – usually some platelets remained in the culture, but became non-viable after a short period of time and were engulfed by macrophages. The extracted cells were pipetted into a 15 mL volume centrifuge tube (Falcon) and diluted with RPMI

complete at 37 °C. The cells were then washed by centrifuging at 250xg for 10 minutes to form a pellet, discarding the supernatant and resuspending in 5 mL warm RPMI complete to count. The resuspended cells were normally diluted at around 1:9 before counting. After cells were counted, they were further diluted in warm RPMI complete to the desired cell concentration and cultured in either a cell culture flask or multiwell plate and incubated at 37°C in a humidified 5% CO_2 incubator.

4.3.5.1.3 Treatment with GO

Cells were plated at a density of 1 x 10^6 cells/mL in 300 µL a 96 well plate and cultured overnight before treatment with the relevant preparation of GO at the indicated concentration. GO preparations were resuspended in RPMI complete by centrifuging in vivaspin centrifuge tubes and topping up with RPMI twice, in order to remove the majority of the water in which they were previously suspended. Concentrations were adjusted such that the final concentration could be achieved by adding 5 µL of the suspension. Cells were incubated with the GO preparations in an incubator at 37^{o}C with 5% CO_2 and extracted at the timepoints indicated

4.3.5.1.4 Stimulation into proliferation using PHA

In order to assess the toxicity of graphene preparations when proliferating, phytohemagglutanin (PHA) was used to stimulate the PBMCs into proliferation. PBMC were cultured as described in 4.3.5.1.3, treated with 0.5 µg/mL PHA and cultured for 24 h before treatment with GO as in Section 4.3.5.1.2.

4.3.5.1.5 Cell counting and Trypan Blue assay

Both K562 cells and PBMCs were counted using a haemocytometer and the K562s were stained with Trypan Blue dye to assess their viability. A moistened coverslip was placed on the haemocytometer chambers and 10 µL of the sample was pipetted into one of the chambers of the haemocytometer by placing the pipette tip at the edge of the coverslip and allowing the slowly

deposited sample to be drawn under the coverslip by capillary action until it covered the entire grid.

A counting chamber in a haemocytometer is divided as shown in Figure 5-10. The chamber contains four major squares, A, B, C, D, at its four corners, which each measure 1 mm x 1 mm x 0.1 mm. These are further divided into 64 minor squares to aid counting. The number of cells in a major square was counted by summing the number of cells in each of the minor squares. This was performed for each of the four major squares and an average was taken. Non-viable cells were judged to be those that could not exclude the Trypan Blue dye, hence to find the viability, the process was repeated, but only the cells stained by the Trypan Blue dye were counted.

The number of cells in 1mL of the culture can then be calculated using the following equation:

$$Average\ number\ of\ cells\ per\ major\ square\ \times 1 \times 10^4\ \times dilution\ factor$$

The percentage cell viability is then defined as:

$$\frac{Total\ number\ of\ cells}{Number\ of\ non-viable\ cells} \times 100$$

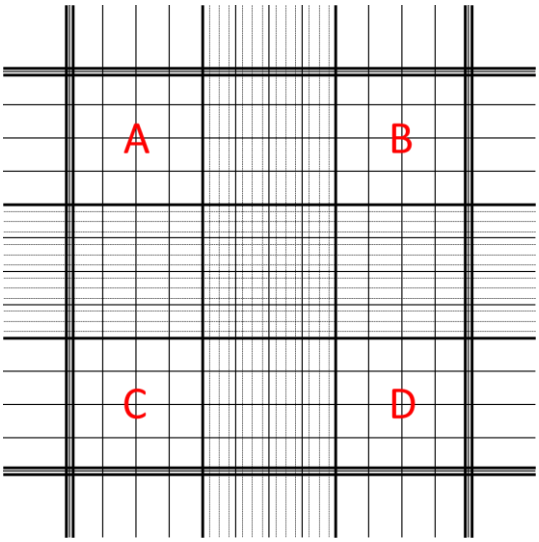

Figure 4-9 - Schematic of the counting region of a haemocytometer

4.3.5.1.6 Alamar Blue assay

PBMCs stimulated into proliferation do not have the same forward and side scatter profiles as those at rest, hence Alamar Blue was used as the primary method to assess the cells' metabolic health after treatment with GO when proliferating. The assay was used as described in the manufacturer's protocol, briefly: a 1:9 dilution of Alamar Blue was added to the cells cultured as described in Section 4.3.5.1.3 at the time points indicated and incubated for 4 h in the cell culture incubator. Absorbance was measured at 570 nm and 600 nm (used as a reference); Alamar blue in RPMI complete alone, and with the relevant concentration of GO sample were used as controls.

4.3.5.1.7 Giemsa Staining

For the 7 day cultures, cells were fixed and stained to improve visualisation of nuclei and cytoplasms. Media and the majority of the lymphocytes were removed by aspiration and the remaining cells were stained according to the manufacturer's protocol, briefly: cells were fixed by aliquoting methanol directly into the wells and incubating for 5-7 min. Methanol was aspirated from the wells and the cells were allowed to air-dry. Giemsa stain was diluted 1 in 20 with ddH_2O, aliquoted directly onto the fixed cells and incubated for 30 min. After incubation the stain was aspirated from the cells, which were then rinsed with ddH_2O and air dried before visualisation using brightfield phase contrast microscopy.

4.3.6 Statistical methods

Statistical analysis was performed using the in-built analysis operations in GraphPad Prism (GraphPad Software, Inc., USA) or Origin Pro (OriginLab Corporation, USA). Most populations were found to be non-normal (skewed) and of different sample sizes, therefore non-parametric tests were predominantly used. For comparisons between only two samples, the Mann-Whitney test was employed, whereas for multiple comparisons, the Kruskall-Wallis test was employed; these tests can be seen as non-parametric extensions of the t-test and ANOVA respectively.

4.4 Results

Two GO preparations were initially characterised: as-bought GO (from this point referred to as uwGO) and washed GO (from this point referred to as wGO). The washing procedure (described in Section 4.3.3.1) was performed with the aim of limiting the presence of contaminants and thicker or unreacted flakes, and therefore producing a less heterogeneous suspension that would be more biocompatible.

4.4.1 Preliminary graphene oxide characterisation before functionalisation

Initial characterisation of the uwGO and wGO flakes was performed using traditional methods that have been widely described in the literature [59, 64, 120-123]; the limits of these methods are illustrated, and then compared with the results of the novel fluorescence techniques used in this thesis. The methods used are predominantly focused on the flakes' physical properties, such as size and thickness, as well as the suspension behaviour in varying media, including media with serum present.

4.4.1.1 Traditional characterisation techniques

4.4.1.1.1 Flake morphology

AFM is widely used to characterise both the thickness and the lateral dimensions of GO flakes, but cannot easily capture images of objects with lateral dimensions > 10 µm, which is often the case in a highly polydisperse GO suspension. Reflective optical microscopy can be used in parallel to allow the measurement of larger flakes; all flakes were measured following deposition onto a silicon wafer with a 290 nm oxide layer, which allows easy visualisation of the flakes immobilised on its surface using reflective optical microscopy [59, 124].

The limits of AFM measurements of GO flake dimensions, and the additional information gained from optical microscopy used in parallel are illustrated in Figure 5-11. The image shows an optical microscope image of uwGO on the substrate, with the AFM cantilever visible, and (inset) three stitched AFM images of 10x10 µm each that cover only a small region of one of the larger flakes present on the substrate.

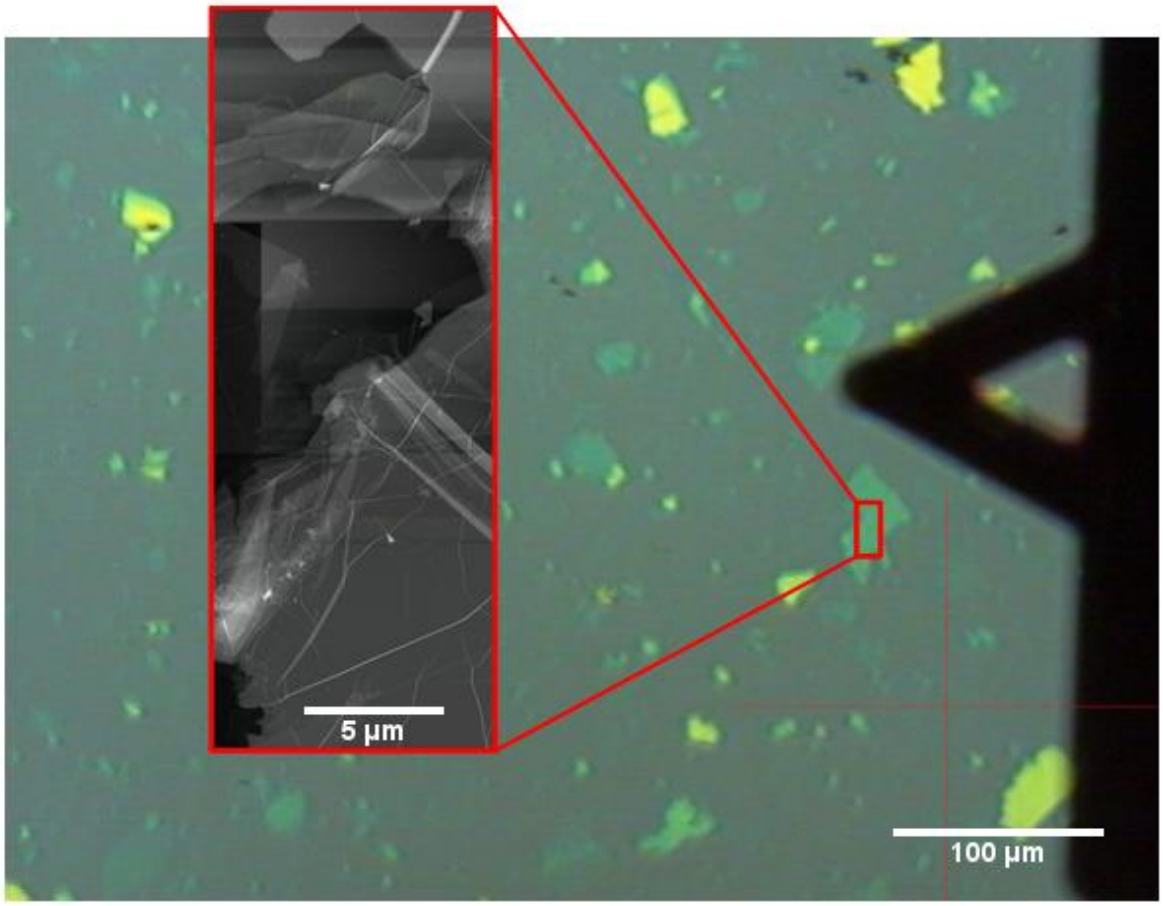

Figure 4-10 – Illustration of the limits of AFM and optical microscopy. Reflective optical microscope image and corresponding AFM image of a GO flake deposited on a silicon oxide substrate, taken using the optical microscope attached to the AFM.

Flake dimensions using optical microscopy

A representative optical microscopy image of wGO following purification is shown in Figure 5-12a. The colours of the flakes indicate their thickness; those with the highest contrast from the background, including black flakes are very thick multilayer flakes, whereas those that do not present a significant contrast from the background are far thinner single or few layer flakes. It is

particularly apparent in Figure 5-12a that the spin-coating process can result in a great deal of flake overlap, which can lead to difficulties in distinguishing between flakes for particle analysis. The distribution of lateral dimensions calculated is given in Figure 5-12b for uwGO and wGO; lateral dimensions are found using the flakes' major axes. The distributions are significantly different (Mann-Whitney $P < 0.0001$), with the uwGO having a median lateral dimension of 2.4 µm, while that of wGO is 1.0 µm. Both preparations, however, have outlier flakes with dimensions > 100 µm.

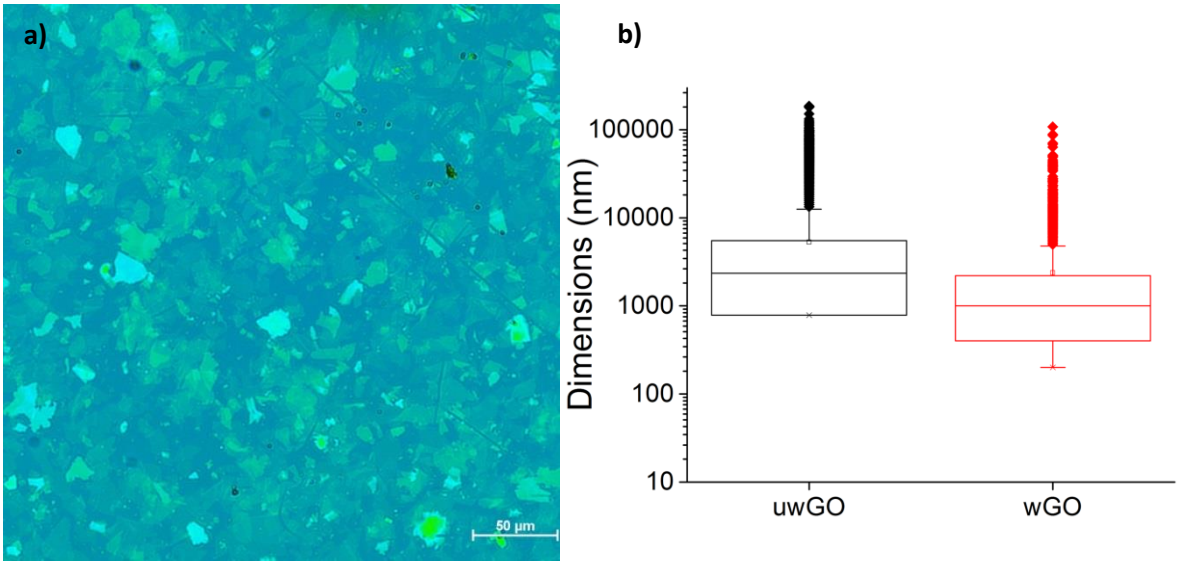

Figure 4-11 – uwGO and wGO lateral dimensions using optical microscopy. a) A representative image of wGO; b) uwGO and wGO flake size distributions found using reflective optical microscopy, presented using a box and whisker plot where the extended whiskers represent the edges of the 1st and 4th quartiles, the box edges the 2nd and 3rd quartiles, the bisecting line is the median, the x is the geometric mean and the □ the arithmetic mean, while the solid diamonds are the outliers.

Flake dimensions using AFM

AFM images were taken of the regions between the large flakes visible on the optical microscope, as the technique is unsuitable for imaging such large flakes. Representative images for both uwGO and wGO are shown in Figure 5-13. For uwGO (Figure 5-13a) a range of flake sizes are observed, but many are large and most are single layered. As seen with the optical microscopy

images, some overlap of the flakes from the spin-coating process is observed (indicated by the blue arrows). This can be distinguished from thicker, multilayer – possibly unreacted – flakes, which are indicated with red arrows by the similarity in the size, shape, orientation and the high degree of overlap of the flakes, suggesting that they have come from the same flake initially.

Additional small raised round features are apparent on some of the flakes – particularly those that are multilayer. This is often indicative of residual contamination from the chemicals used in the oxidation process [private communication, Dr Maria Iliut, University of Manchester].

The wGO sample, shown in Figure 5-13, is very similar to uwGO, predominantly single-layered flakes with a range of flake sizes are observed. However, fewer thick or aggregated flakes are observed, and while several bright spots may indicate the possible presence of remaining contaminants, these are less common than in the uwGO sample. This illustrates that post-washing, the samples appear to be of a higher quality with somewhat reduced heterogeneity, and possibly contain fewer contaminants that could affect its toxicological profile.

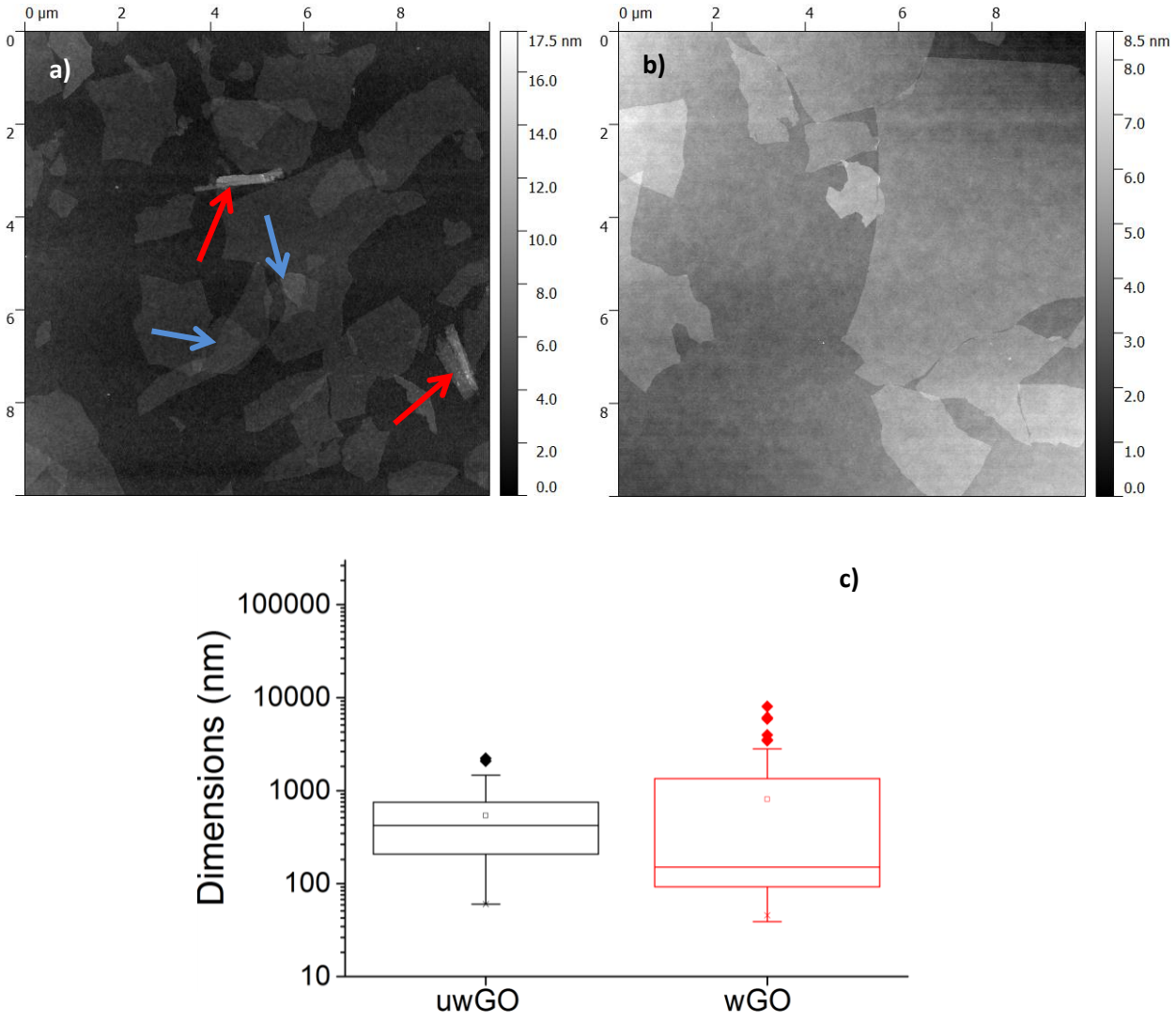

Figure 4-12 – uwGO and wGO lateral dimensions found using AFM. Representative images of a) uwGO b) wGO and c) flake lateral dimension distributions, found using AFM and represented using a box and whisker plot, in which the whiskers represent the 1st and 4th quartiles, the box encompasses the 2nd and 3rd quartiles, bisected by the median, the geometric mean is represented by x and the arithmetic mean by □. The solid diamonds are outliers.

As with the optical microscopy images, particle analysis was used to measure the flake dimensions (of the two major axes, as before) for both preparations, the distributions of which are also shown in Figure 5-13c. While the median for the uwGO distribution appears to be greater than that of wGO (0.423 vs 0.151 µm respectively), the distribution itself is tighter for the uwGO preparation. However, the regions in which AFM is performed are restricted by the suitability of the flakes present – i.e. if very large or thick flakes are present then AFM cannot be easily performed – and therefore should be taken in combination with the results given through optical microscopy.

The images taken using AFM and reflective optical microscopy have given some detail about the exact morphology of the flakes present in suspension, including their shape, lateral dimensions, thickness and some information about the presence of any contaminants present on the flake surfaces. By using the two techniques in parallel, a more representative picture has been built up of the morphologies of the flakes present in suspension that is reflective of the heterogeneity of the samples. However, the limitations imposed by both – and AFM in particular – make it difficult to discern whether the overall distribution gives a representative view of the flake size distributions.

4.4.1.1.2 Scattering techniques for characterisation of flake size and behaviour in suspension

Scattering techniques such as DLS are often used as a rapid method to gain a statistical overview of the graphene flake sizes in a suspension [64, 125, 126]; the method can also provide information on changing flake behaviour including aggregation – as described in Chapter 3. However, the oblate geometry of the GO flakes is more extreme than that of the flakes prepared in Chapter 3, and the optical microscopy observations have shown that many of the lateral dimensions of the flakes exceed 100 µm (Figure 5-12), which is far outside of the limits of the technique. In the literature it is generally suggested that DLS results be calibrated against those provided by a direct imaging technique such as TEM, AFM or optical microscopy [64].

Both the uwGO and wGO preparations were analysed using DLS, and the results are presented in Figure 4-13. Saline at physiological concentration (150 mM), PBS (150 mM, pH 7.4) and BSA dispersed in PBS were chosen in order to assess how the apparent hydrodynamic radii of the flakes changed in the presence of ions, buffering agents and proteins used commonly in cell culture. The quality of the correlation curves was assessed and is presented in the same format as used previously, and placed below the graph that presents the distributions.

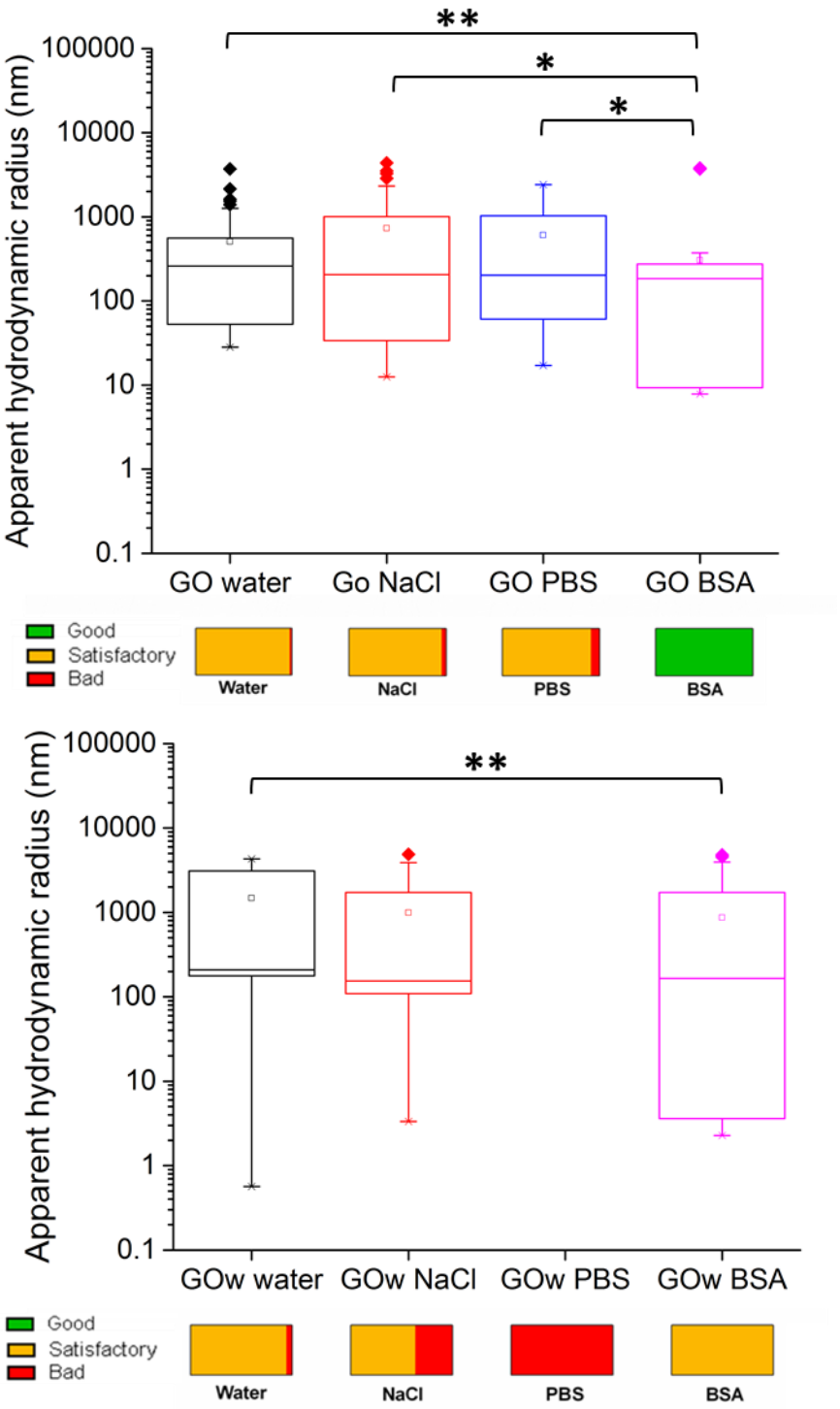

Figure 4-13 - Distribution of apparent hydrodynamic radii for uwGO and wGO found using DLS. a) uwGO suspension and b) wGO suspension, represented using box and whisker plots, along with the quality of the suspensions, as found using the correlation curve method described in Section 3.3.3.2.3. The whiskers of the plots describe the 1st and 4th quartiles of the distribution, and the box describes the 2nd and 3rd quartiles, bisected by the median; the geometric mean is represented with x and the arithmetic mean by □. Outliers are represented using solid diamonds. Significance levels are indicated for the different dispersion media for the two preparations, where ∗∗ is P ≤ 0.01 and ∗ is P ≤ 0.1. The R_h distributions for the uwGO and wGO in water are significantly different (P ≤ 0.1).

Apparent hydrodynamic radii of the GO preparations

If the flake sizes found using AFM in Section 4.4.1.1.1 (Figure 5-13), are converted into R_h by assuming that the lateral dimensions define the size of the solvent sphere inhabited by the flakes in suspension, the distributions are significantly different for both preparations (uwGO: Mann-Whitney, $P < 0.05$; wGO: Mann-Whitney, $P < 0.0001$), despite the size range in which both the techniques being similar. The method by which DLS functions means that the sample size is far higher than the AFM imaging provided, therefore the size distribution may be more representative; however, the oblate geometry of the flakes is known to lead to lead to discrepancies in the measurements [64]. As expected, the distributions do not capture the contribution of the flakes with far larger lateral dimensions, observed using optical microscopy (Section 4.4.1.1.1, Figure 5-12).

In the R_h distribution measured for the wGO preparation (Figure 4-13) very small R_h were observed for both the preparations in water and NaCl preparations, far smaller than were observed in AFM, or than could reasonably be considered to be GO fragments ($R_h < 1$ nm). The oblate geometry of the flakes may lead to contributions from other degrees of freedom of the flakes in suspension, including edge-on diffusion and flake bending and wrinkling, however this has not been confirmed.

The relationship between suspension quality and dispersion media

As shown in Figure 4-13 for both preparations, the majority of the correlation curves could only be deemed to be satisfactory, even when the suspensions were in water where the flakes appeared stable. When dispersed in saline and PBS, the quality of the as purchased GO suspensions becomes slightly worse, but when mixed in a 10% BSA solution, which was prepared in 150 mM PBS, the correlation curves become substantially better, with all of them judged as *good*. In contrast, the washed GO suspensions become significantly worse in the presence of

ionic species and buffering agents, with all of the curves rejected for the acquisitions in PBS, and the overall quality not significantly improved by the presence of BSA.

Variation in apparent hydrodynamic radii with changing dispersion media

As illustrated in Figure 4-13, for both preparations, the median apparent hydrodynamic radius (R_h) remains relatively unchanged in all media, and the overall distribution does not change significantly for the uwGO in water, saline and PBS, but the distribution in BSA presents a significant difference from all the other preparations (Kruskal-Wallis multiple comparisons). For wGO, only the distribution in water and that in BSA differed significantly from each other (Kruskall-Wallis multiple comparisons).

For both uwGO and wGO dispersed in BSA solution there is a significant change in the skewness of the distributions. It was considered that this observation was likely to be due to free BSA monomers and aggregated species. BSA is also known to interact with the basal plane of graphene and GO [127, 128], and the interaction between GO flakes and macromolecules have been reported to alter their geometry, making the particles less oblate and more globular while reducing their lateral dimensions [129].

To investigate whether any interaction between the flakes and BSA could be observed, the range $0 \leq R_h \leq 500$ nm was further examined for both preparations in histogram form (shown in Figure 8-1, in the Appendix). In the uwGO distributions, very small objects appear in the water, saline and PBS preparations, but all have $R_h \geq 10$ nm and their relative abundance is 10-20% of all counts, whereas for the BSA mixture the total percentage is close to 50%. The BSA monomer is known to be 3.4 nm [130], therefore a peak in the 0-20 nm region would correlate well with both monomeric and aggregated BSA species.

In addition, whereas the preparations dispersed in water, saline or PBS appear to have a flattened log(normal) distribution for $0 \leq R_h \leq 500$ nm, the dispersion in BSA suspension appears to have two distinct distributions; there is a tight distribution of very small objects in the 0-20 nm region, followed by another broader distribution centred around 200-300 nm. In the region 0.5

≤ R_h ≤ 4 µm there are far fewer objects observed compared to the other dispersion media. Statistically, this is better reflected by the geometric mean than the median, which seems to be quite static for all the samples. A similar investigation was undertaken for wGO (Figure 8-2, Appendix). For the preparations of washed GO in BSA a similar contribution between 0-10 nm appears, indicating that this is indeed the BSA in solution; however, the same gap in sizes does not appear at R_h ≥ 500 nm for this preparation as observed with unwashed GO. In addition, the largely flat distribution in the range 0 ≤ R_h ≤ 500 nm observed for the preparations of unwashed GO in water and saline does not appear for the washed GO preparations. Instead, a distinct population between 100-200 nm appears for all the preparations, similar to that seen with unwashed GO in BSA.

It can be concluded from the results presented in both this Section and Section 4.4.1.1.1 that none of the traditional methods used here can provide full characterisation of GO flakes as is necessary for their use in biomedical applications. In particular, measuring the lateral dimensions of the flakes present in a preparation is hampered due to the heterogeneity of the sample, and the size limits of the techniques used. Therefore an alternative approach was assessed that exploited the inherent fluorescence of GO so that Raster Image Correlation Spectroscopy (RICS) and flow cytometry could be used.

4.4.1.2 Using graphene oxide's inherent fluorescence for characterisation

4.4.1.2.1 Raster image correlation spectroscopy as an improved method for flake size characterisation

RICS is a technique used to measure the dynamics of fluorescent or fluorescently labelled body using a confocal microscope. By using both raster scanning of the laser and sequential image stacking of a 2D focal region, the technique is able to measure the dynamics of small, rapidly moving bodies and larger, slower moving bodies [119]. The technique therefore is able to measure the dynamics of particles within a wider size range, and in more complex or viscous media than DLS. It was therefore considered that the technique may be more appropriate than

either the combination of optical microscopy and AFM or DLS for giving a broad and high throughput measurement of flake lateral dimensions.

As with DLS, RICS makes use of the Stokes-Einstein relationship (Equation 7) to find the apparent hydrodynamic radius from the diffusion coefficient (D). The in-house software that was used produced a diffusion coefficient for each tile of the region of interest (ROI) interrogated, which was then converted to an apparent hydrodynamic radius (as described in Section 4.3.4.6).

The R_h distribution for both GO and washed GO is presented in Figure 4-15. The distributions are significantly different (P < 0.0001, Mann-Whitney test), with the washed GO presenting a significantly smaller median R_h and a tighter size distribution. While the R_h distribution for wGO is not significantly different to that captured by DLS, for the unwashed GO it is (P < 0.0001, Mann-Whitney test).

The technique was able to capture a far larger distribution of flake sizes than DLS, as it captures flake sizes stretching up to 80 µm in the unwashed GO preparation – which is within the size range captured by optical microscopy, but no other technique.

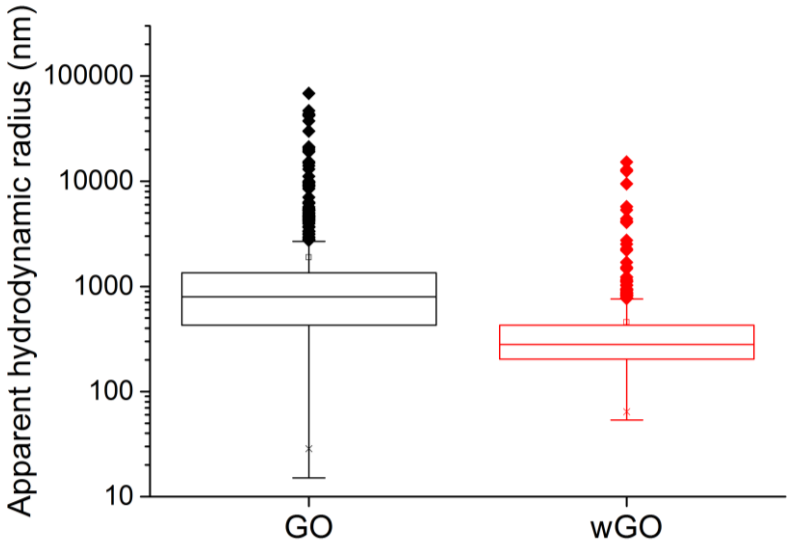

Figure 4-14 - Apparent hydrodynamic radius distributions of uwGO and wGO, found using RICS, illustrated using a box and whisker plot, with the whiskers representing the 1st and 4th quartiles, and the box the 2nd and 3rd quartiles bisected by the median. □ is the arithmetic mean and x is the geometric mean, while the solid diamonds represent outliers.

The distributions are significantly different (Mann-Whitney, $P < 0.0001$). Interestingly, smaller R_h values were observed in the unwashed GO preparation than in the washed preparation. This relationship conflicts with both the AFM measurements, and particularly with the DLS. For wGO, while the range minimum is within the same order of magnitude as measured using AFM, it is two or three times the size.

For each value of *D*, the software produced an R^2 value, based upon the goodness of fit to the 2D autocorrelation curve. Any measurement where the R^2 value dipped below 0.65 was rejected; when the GO and wGO suspensions were dispersed in saline or PBS, none of the measurements gained R^2 values within the acceptable range. This meant that the technique could not be used to assess the distribution of Rh in these media. In addition, the fluorescence intensity of the flakes decreased considerably in the BSA suspensions, so that flakes could not be easily identified and R^2 values were again low.

Flow cytometric analysis was proposed in order to assess the behaviour of the flakes in saline, PBS and BSA solution.

4.4.1.2.2 Flow cytometry: using scatter and fluorescence to determine flake interactions with their surrounding media

Flow cytometry is a technique commonly used in the biological sciences to characterise cells, through light scatter and fluorescence. Objects (generally cells) pass through a flow cell encounter laser light for fluorescence studies and white light to assess scatter. Flow cytometry has previously also been used to assess the size distribution of GO flakes in suspension, predominantly employing the scatter characteristics of the flakes to analyse the flake size distribution [107]. In the present study, the technique was used primarily to assess the behaviour change of the flakes in different dispersion media. It was considered that the combination of fluorescence and scatter measurements could provide a more thorough characterisation of the suspensions, and allows comparison with both DLS and RICS. In addition, characterisation using

flow cytometry prior to introduction into cells provides a set of measurements that may allow the identification and differentiation of flakes during the subsequent cell characterisation experiments.

4.4.1.2.2.1 Forward and side scatter

The geometry and behaviour of GO suspensions undergoing flow cytometric analysis is very different to that of cells; while Singh *et al.* [107] used platelets as a cellular comparison for their GO suspensions due to their oblate nature, flakes in a high quality GO suspension will be far thinner, and in the case of the flakes analysed here, their lateral dimensions are far more polydisperse. The occurrence of aggregation makes the situation again more complex; however, while the angle dependency of non-spherical particles is complex, non-spherical particles – including oblate particles – are generally found to have higher side scatter than spherical particles of equivalent size [131, 132].

The fluorescence, forward and side scatter distributions were investigated for both GO and washed GO in a range of media, including those investigated using both DLS and RICS. The behaviour of the suspension in Human AB serum was also investigated – Human AB serum has a more complex protein composition than BSA and so was used to extend observations made when the flakes were mixed with BSA.

The scatter plots for the different preparations of GO are shown in Figure 4-16 (very similar distributions are observed for the washed preparation). Very little difference can be observed between the different distributions; this is again reflected when the forward and side scatter counts are plotted separately (Figure 4-17). No significant variation in the forward or side scatter distributions was observed for GO in the various media other than for Human AB (Kruskal-Wallis non-parametric multiple comparisons test, $P > 0.5$).

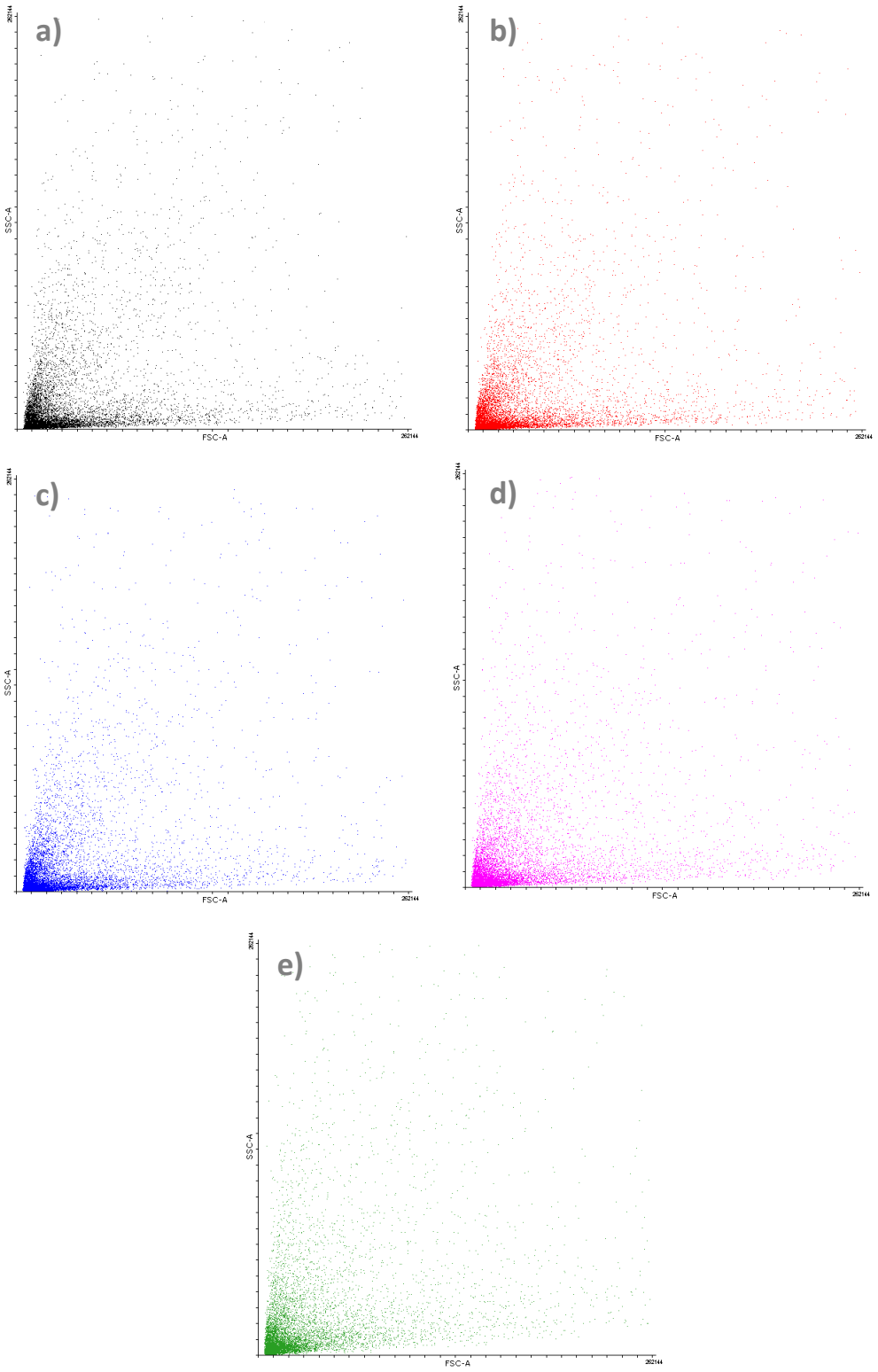

Figure 4-15 - Scatter plot distributions for uwGO measured using flow cytometry in a) water b) NaCl c) PBS d) BSA e) Human AB, showing very little difference in the forward and side scatter distributions for uwGO in different dispersion media.

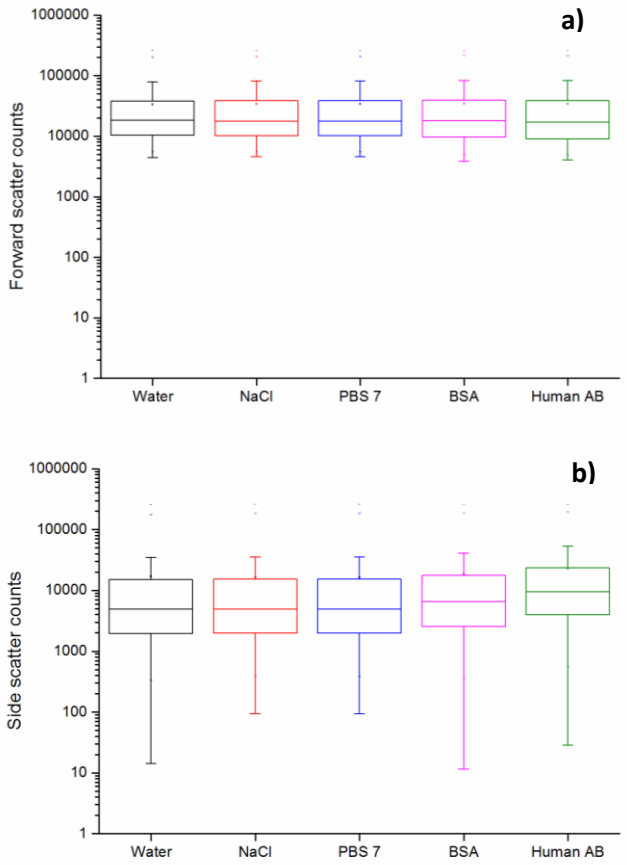

Figure 4-16 – a) forward and b) side scatter distributions for uwGO suspensions in a range of media, measured using flow cytometry; the distributions show very little difference in the forward and side scatter profiles of uwGO in the range of dispersion media. Distributions are represented using box and whisker plots, with the whiskers representing the 1st and 4th quartile and the box representing the 2nd and 3rd, bisected by the median. □ is the arithmetic mean and x is the geometric mean.

4.4.1.2.2.2 Fluorescence distributions

The fluorescence distributions of the same scatter plots shown in Figure 4-16 were investigated; both uwGO and wGO was found to have the highest emission intensity in the 660-750 nm region, therefore the fluorescence distributions recorded were those measured though this channel. The overall fluorescence intensity distributions for the suspensions are shown in Figure 4-18.

There is only a slight decrease in fluorescence intensity for the suspensions in NaCl and PBS. More significant is the change observed following the addition of BSA or Human AB serum to the suspensions; the median fluorescence intensity is observed to decrease significantly ($P < 0.0001$, Kruskal-Wallis), and the tail extend to far lower intensities. The same level of significance is observed for wGO. The intensity histogram for GO in BSA is also shown in Figure 4-18, in which

no obvious second non-fluorescent population is observed, an expected result if the BSA alone was registering as separate non-fluorescent objects on the flow cytometer. This is further confirmed by the scatter plot and fluorescence intensity histogram of BSA alone, shown in Figure 4-18. While many of the objects observed in the blank BSA solution – thought to be protein aggregates – sit within the same FSC/SSC region as the majority of the GO flakes, the fluorescence intensity is significantly lower than that of the GO sample, which only has a small tail in the region where the peak of the BSA distribution is.

These observations suggest that the GO flakes in both the suspensions mixed with BSA and Human AB serum are interacting with the proteins present in the suspension, and the proteins are decreasing the GO fluorescence, through unknown quenching mechanisms.

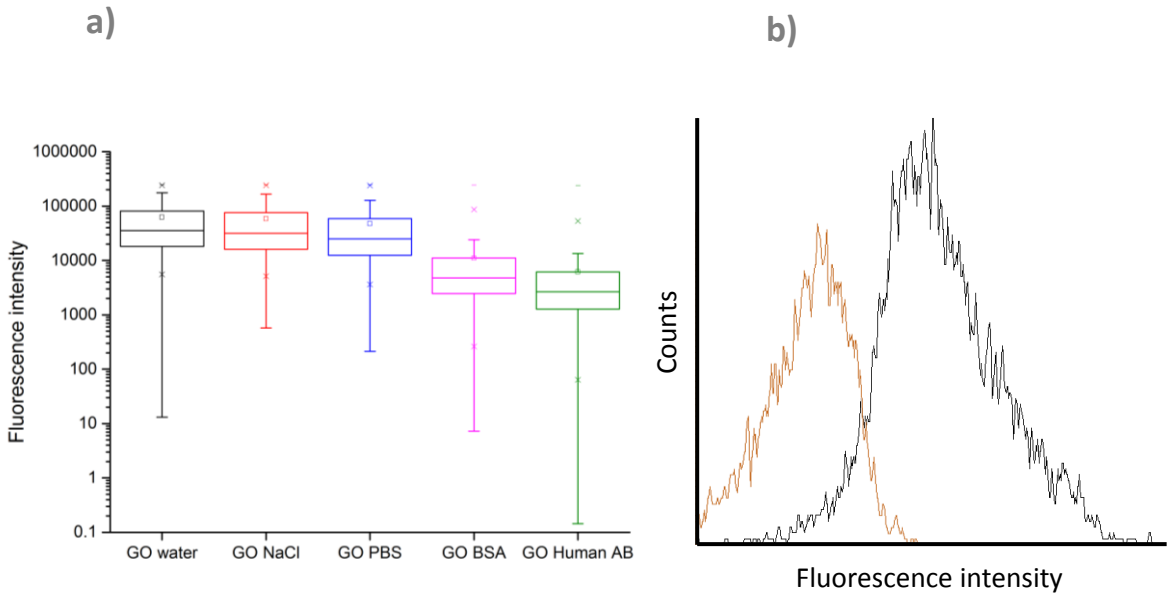

Figure 4-17 – Illustration of GO fluorescence quenching in solution with serum components using flow cytometry a) Fluorescence intensity distributions for GO in different media; Distributions are represented using box and whisker plots, with the whiskers representing the 1st and 4th quartile and the box representing the 2nd and 3rd, bisected by the median. □ is the arithmetic mean and x is the geometric mean. b) Fluorescent intensity distribution for GO in BSA (black) and fluorescence intensity distribution for BSA alone (orange).

To further investigate the fluorescence properties of the suspension, the forward/side scatter plots were divided into quadrants with regards to their forward and side scatter, and their fluorescence distributions were measured. An example of one of the forward/side scatter plots divided into four quadrants (low FSC & SSC; low FSC high SSC; high SSC low FSC; high SSC & FSC) is shown in Figure 4-19, and the respective fluorescence distributions for each of the quadrants in each of the preparations are shown in Figure 4-20.

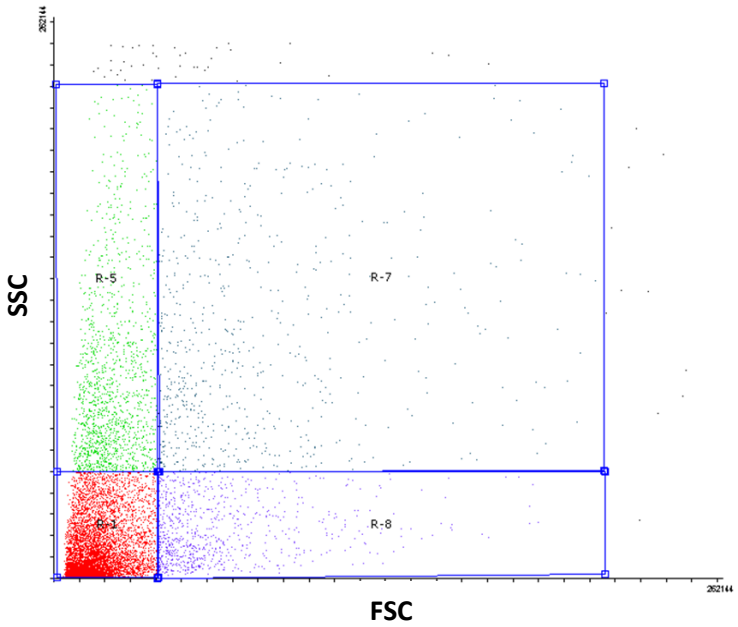

Figure 4-18 - Representative example of a scatter plot, measured using flow cytometry, in which the quadrants used in the figures that follow are illustrated

For all the samples, increasing forward and side scatter both result in increased fluorescence intensity – with the highest average fluorescence intensity observed in the quadrant with high FSC & SSC, and the lowest in the quadrant with low FSC & SSC. The data suggest that the larger GO objects exhibit the highest fluorescence intensity, as the increasing particle size is correlated with an increased asymmetry in scattering angle dependence – therefore the flakes with the highest side scatter are also expected to be large [131].

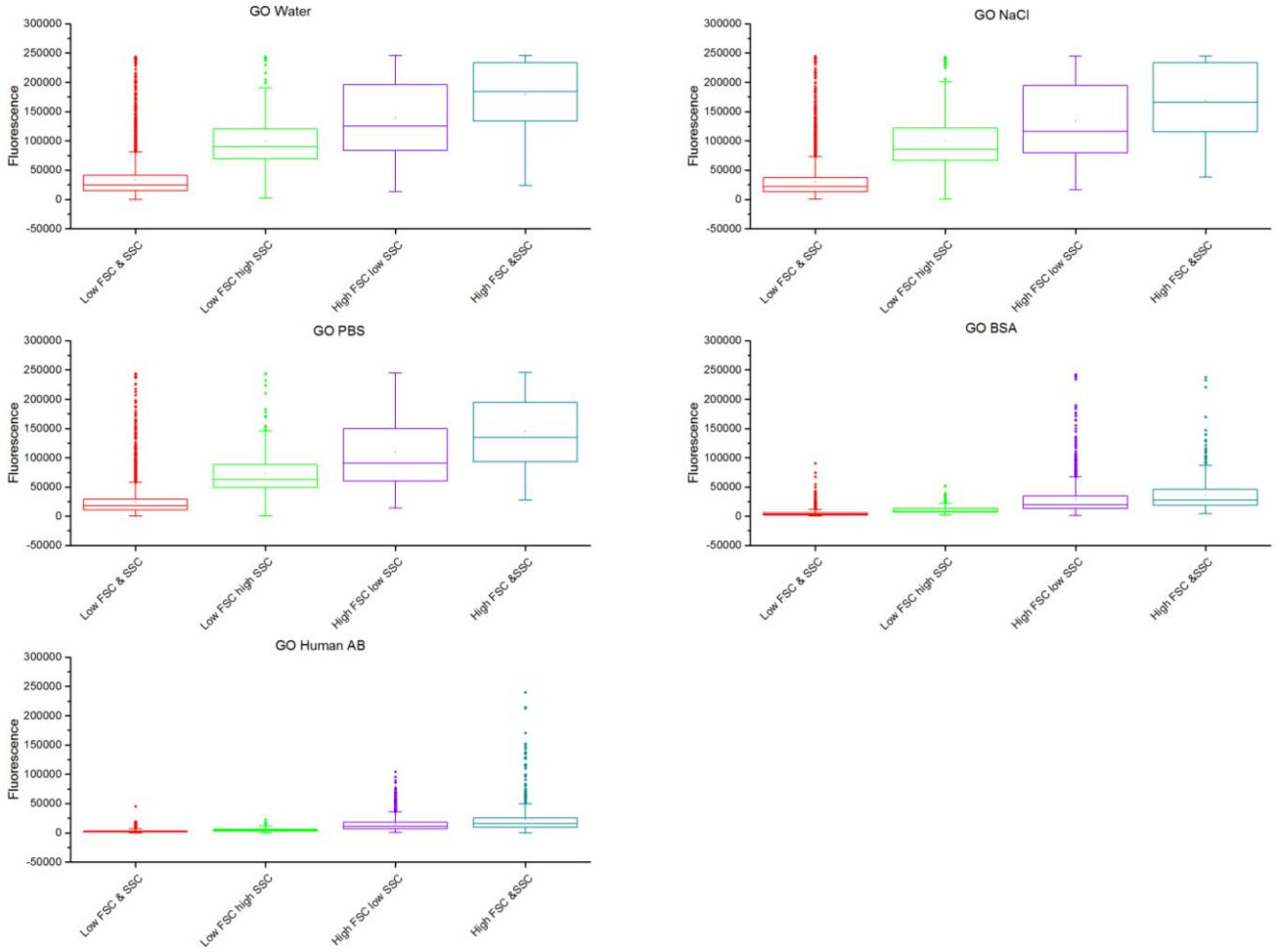

Figure 4-19 – Illustration of the variation in fluorescence intensity depending on FSC/SSC profile and dispersion media. Fluorescence distributions for each preparation of uwGO divided into quadrants of varying forward and side scatter, measured using flow cytometry. Data represented in box and whisker plots, with the whiskers representing the 1st and 4th quartile and the box representing the 2nd and 3rd, bisected by the median. □ is the arithmetic mean and x is the geometric mean. Solid diamonds are outliers.

When the distributions are subdivided according to their forward and side scatter, a clearer difference in fluorescence intensity between the GO flakes in water and those in PBS is observed, particularly the distributions in the quadrant with high FSC & SSC. In the case of both BSA and Human AB serum, the same trend of fluorescence quenching is observed again, and besides the outliers, there is very little variation in fluorescence between the quadrants – in stark contrast with the other preparations.

By using the inherent fluorescence of the GO flakes, it has been shown that GO flakes interact strongly with serum proteins that are present both in many *in vitro* preparations (BSA) and *in vivo* (Human AB serum). Alongside the results found using RICS, these results show that the inherent fluorescence of the GO flakes can be used to characterise its physical properties and interaction with biological media before use in biomedical applications.

Following the development of two effective methods of analysing the characteristics of GO flakes using the inherent fluorescence of the flakes, the samples were functionalised in preparation for introduction to cells. The methods developed could then be applied to the functionalised GO samples, and in the case of flow cytometry, used to investigate the interaction with the cells.

4.4.2 Graphene oxide functionalisation

Polyethylene glycol has been used by a number of groups to functionalise GO flakes to improve their stability and biocompatibility, and to tailor their functionality [128, 133-136], as described in detail in the Introduction Chapter. The use of PEG is known, in particular, to counter the adsorption of serum proteins onto GO [136] and has been used widely with bio-nanoparticles for this purpose. In this Section GO flakes were PEGylated with 10 kDa branched PEG with primary amine termini to improve their stability in biologically relevant media. The inclusion of the weakly positive amine functional groups was appealing both with regards to easy attachment of other functional molecules including targeting ligands, and because previous work had suggested that amine functionalised GO was less thrombogenic [137], which is important for the intended function of the flakes.

4.4.2.1 Flake surface chemistry

After the PEG conjugation step, the surface chemistry of both the functionalised and unfunctionalised GO flakes was assessed using XPS. This allowed the characterisation of any changes in the abundances of oxygenated functional groups and residual contaminants following the washing step to be assessed, and to confirm that PEGylation had occurred after the conjugation step by interrogating the bonding types present. A detailed description of the method and its mechanism is given in Section 4.3.4.3.

Initially a survey spectrum was taken, and the peaks associated with specific elements present integrated to give the overall elemental composition of the samples. Figure 5-21 shows a typical spectrum from GO, with the peaks highlighted and labelled. For each sample the observed abundances of each of the chemical elements are presented in Table 4-1.

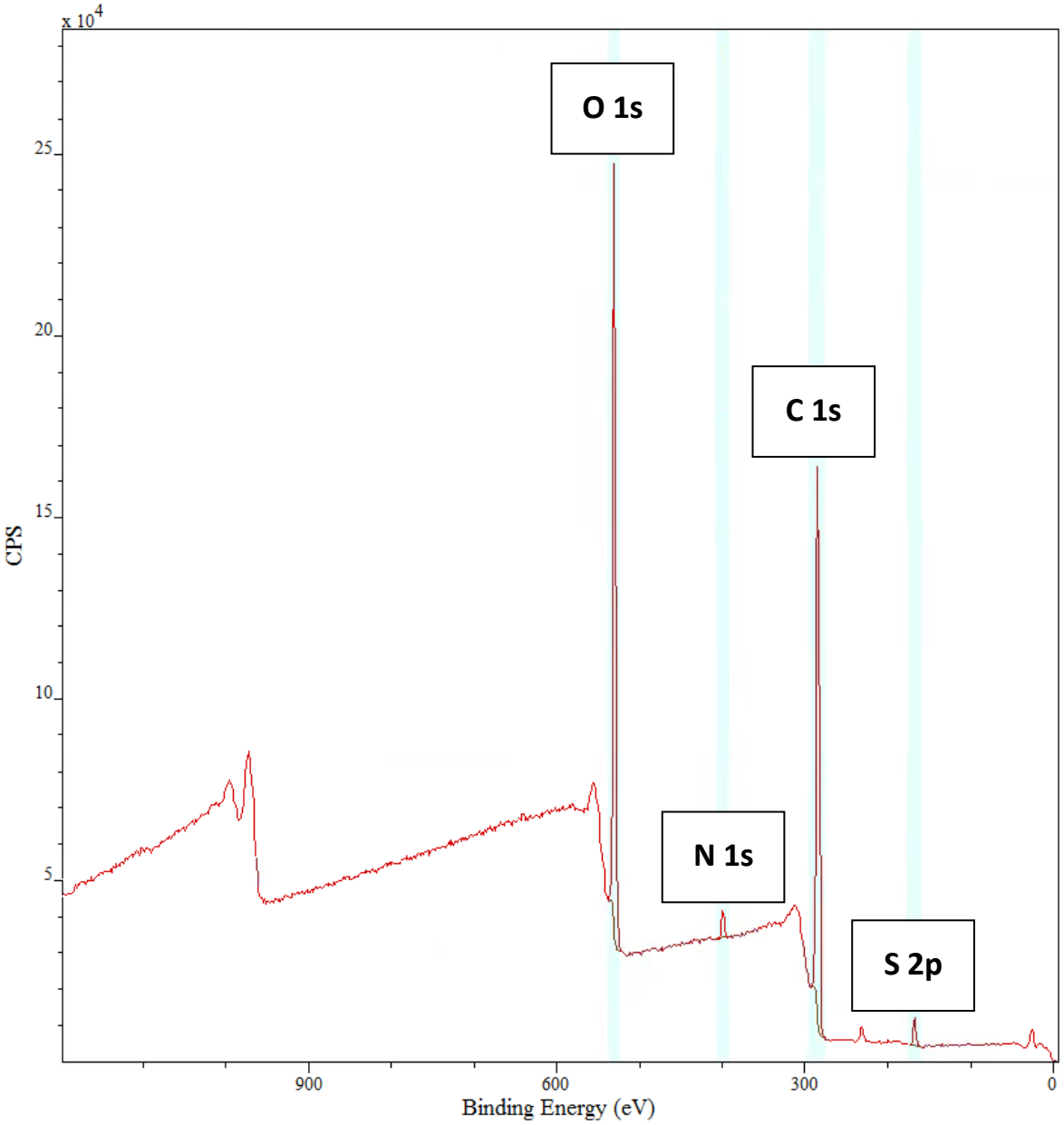

Figure 4-20 - Representative survey spectrum from GO showing the peaks from O 1s, C1s, N1s and S2p transitions, measured using XPS

Table 4-1 - Relative abundances of elements present in the samples of GO, as determined using XPS.

	uwGO	wGO	PEG-GO
	Relative abundancy (at%)		
O 1s	29.46	29.07	29.04
C 1s	67.24	68.57	69.00
N 1s	1.78	1.50	1.46
S 2p	1.55	0.85	0.50

The molecular structure of GO is formed entirely of carbon and oxygen, therefore any other elements present are contaminants, likely to have remained from the oxidation process, described in Figure 5-1; the HCl washing step that was performed was designed to remove residual contaminants. From Table 4-1, there is a decrease in the presence of nitrogenous and sulphuric impurities present after the washing step for GO; however, contaminants still remain. Therefore, despite treatment with HCl and multiple washing steps, the wGO retains some of the impurities associated with the oxidising process.

With respect to the PEGylated GO, the relative abundances of carbon, oxygen and nitrogen were not found to change significantly from the either of the unfunctionalised GO samples. While it may be expected that the abundances of O and N should change upon functionalisation, the structure and size of the PEG that was used to functionalise the GO flakes makes the relative stability in elemental abundances unsurprising – the amine termini of the PEG make up approximately 0.002 at% of the overall structure and the polyethylene glycol chains have an atomic ratio of approximately 2:1 carbon to oxygen, which is similar to that found in GO. Some sulphur contaminants still remain, and although the relative abundance has again decreased compared to the unfunctionalised GO preparations, it is not known if this is only relative to the addition of the PEG.

Further to this initial analysis, the photoelectron energy peaks were analysed to provide information on the abundances of the binding types that were present. This analysis gave information both on the different functional groups present before and after the washing steps were performed, but also whether the flakes were successfully functionalised.

Figure 4-22 shows the structure of the C1s peak for the unwashed GO sample, the structure of which is characteristic of GO samples [138-144]. The structure observed in the washed GO sample was very similar to the unwashed GO; however there were some decreases in the abundances of the various bonding types – as listed in Table 4-2. A decrease in the overall number of oxygenated functional groups and a relative increase in the number of C=C bonds were observed.

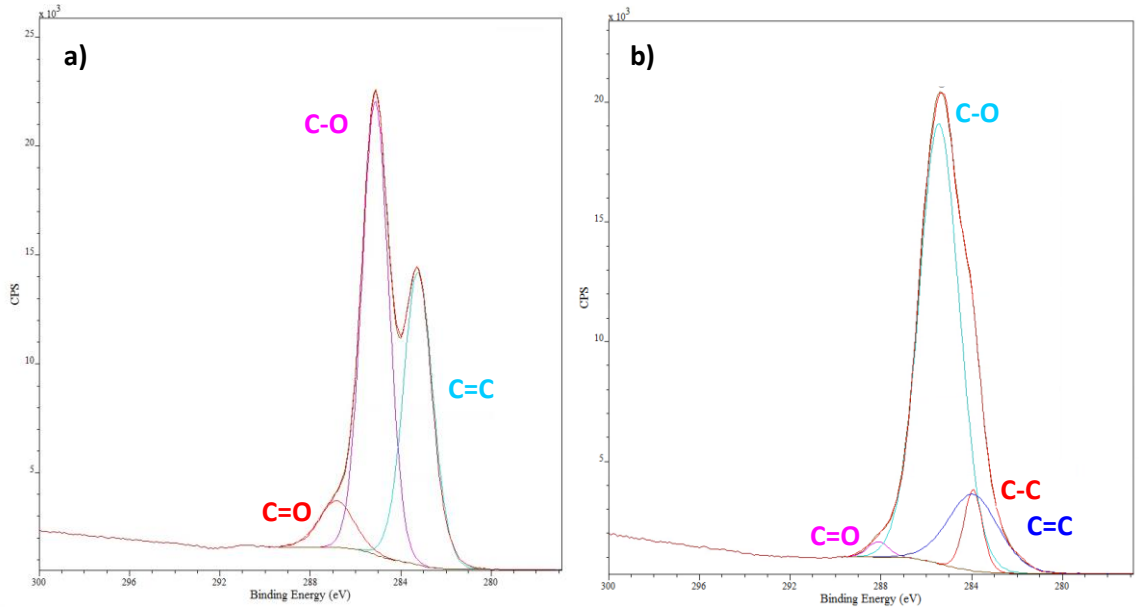

Figure 4-21 – Analysis of the C1s peak to find the relative abundances of the different molecular groups contributing to the transition. Fitting for a) GO and b) PEG-GO with the contributions from transitions in different functional groups labelled.

The C1s transition peak shape for PEGylated GO is shown in Figure 4-22b; the peak changes shape significantly, becoming a single peak rather than bimodal. This shape transition is indicative of the change in relative abundances of carbon bonding types present on the flakes. While the absolute abundance of the C=O or C=C groups should not change during amidation, the addition of the PEG will result in the relative abundances of C-C and C-O increasing. This confirms the successful conjugation of the PEG to the GO flakes.

Following confirmation of the successful PEGylation of the GO flakes, the suspensions were characterised using both traditional and fluorescence methods.

Table 4-2 - Percentage contribution of different functional groups to the C 1s peak for uwGO, wGO and PEG-GO, measured using XPS

Sample	Functional group	% contribution to C1s peak	Position (eV)
Unwashed graphene oxide	C-O	50.01	286.0
	C=C	43.39	284.1
	C=O	6.60	287.7
	C-C	-	-
Washed graphene oxide	C-O	47.84	286.8
	C=C	47.37	284.7
	C=O	4.79	288.7
	C-C	-	-
PEGylated GO	C-O	75.59	285.4
	C=C	16.53	283.9
	C=O	1.37	288.1
	C-C	6.51	283.9

4.4.2.2 Characterisation of functionalised GO using established methods

As before, the suspensions were spin coated onto silicon wafers with an oxide layer to assess their morphology; representative optical microscopy images are shown in Figure 4-23. Measurements of the flakes were taken of the flakes' lateral dimensions using both the optical microscopy images and AFM images, the distributions for which are shown in Figure 4-24.

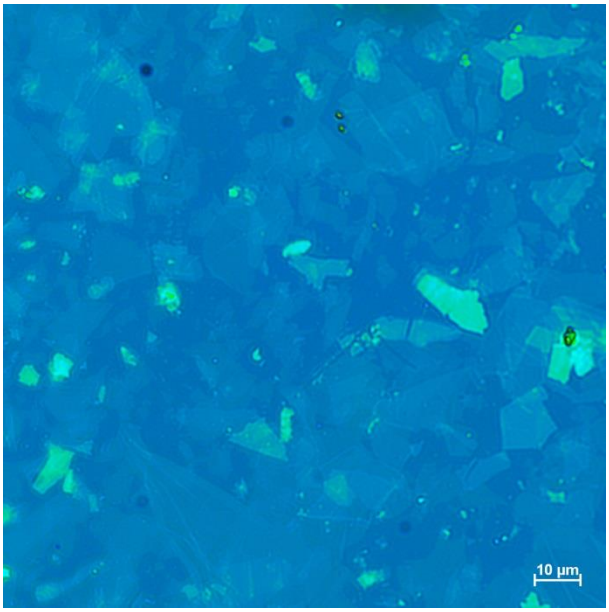

Figure 4-22 – A representative example of a reflective optical microscope image of GO-PEG 10 kDa spin-coated onto SiO_2 wafer. Colour balanced for contrast

The distributions again reinforced the limits of both techniques, and the necessity that they be used in parallel for flake characterisation, as shown in Figure 4-24. As the flakes were sonicated during the PEGylation process, it was surprising that some of the flakes remained so large, with lateral dimensions up to 30 µm.

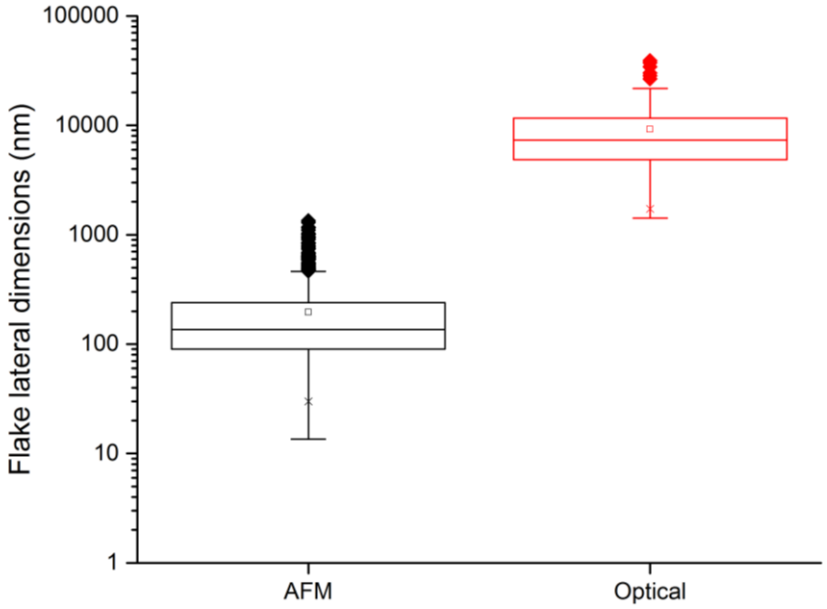

Figure 4-23 – PEG-GO flake lateral dimension distributions measured using optical microscopy and AFM measurements. Distributions are represented using box and whisker plots, with the whiskers representing the 1st and 4th quartile and the box representing the 2nd and 3rd, bisected by the median. □ is the arithmetic mean and x is the geometric mean, and the solid diamonds are outliers.

The AFM images also provided information on the extent of the flake functionalisation. The linkage of the PEG molecules to the GO flakes can be observed on large flakes as small features spread across the flake surface. Notably, GO flakes are expected to predominantly present carboxylic acid groups at their edges [31], the majority of the observed PEG chains are across their surfaces. In addition, on the large flakes where it is easiest to observe the functional molecules, the coverage appears sparse.

Conjugation with PEG chains is performed in order to make the flakes more stable in biologically relevant media, in order to avoid aggregation and recognition by macrophages. Therefore, in order to assess the success of the functionalisation, the flakes were measured both using traditional scattering methods and the fluorescence techniques developed in Section 4.4.1.

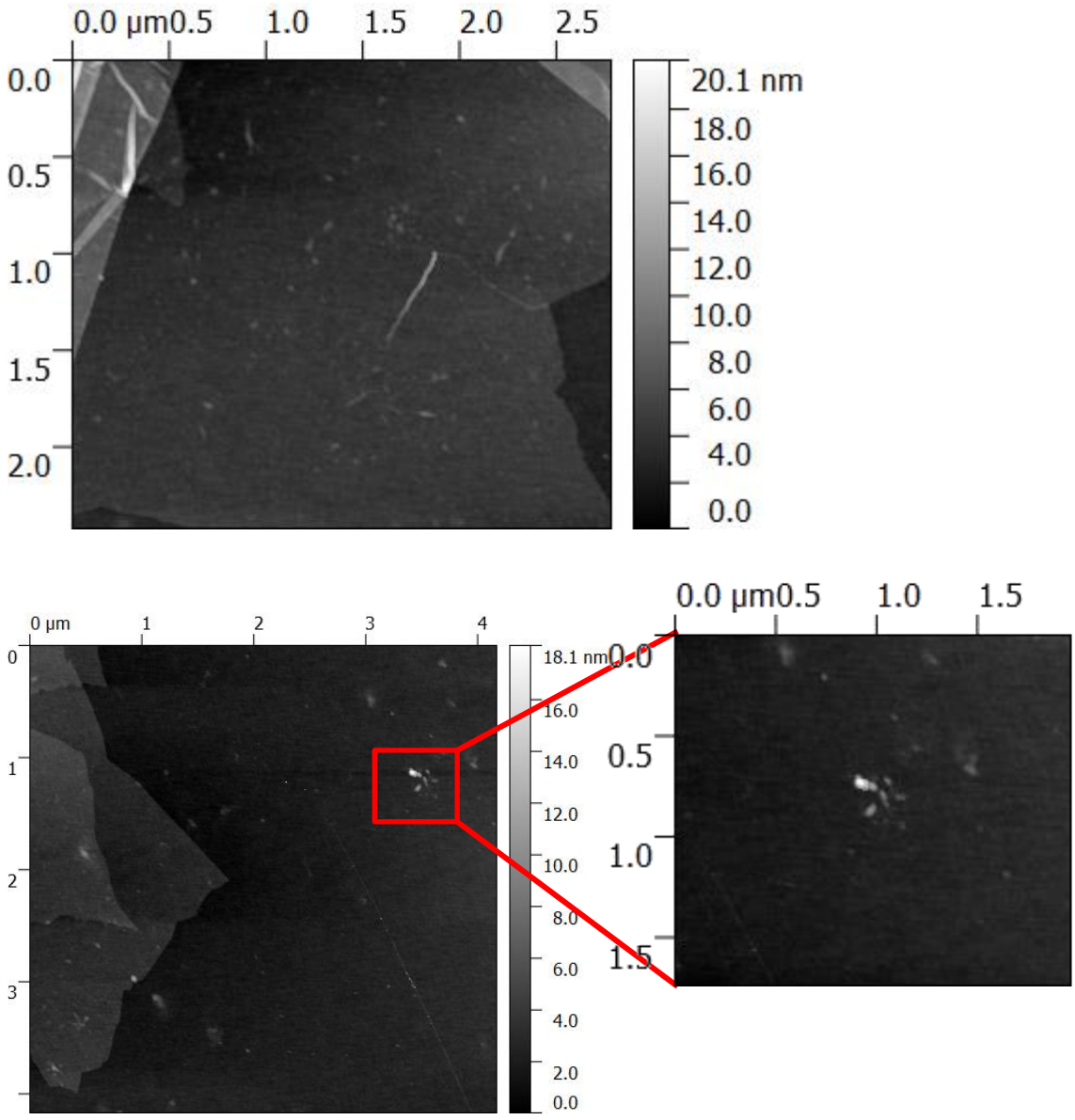

Figure 4-24 – Representative AFM images of GO-PEG 10 kDa, Functionalisation appears to be sparse and predominantly across the basal plane of the flakes. A region that could either be PEG functionalisation or small but highly functionalised flake(s) is highlighted.

4.4.2.2.1 Scattering methods for characterisation of flake size and behaviour in suspension

Following functionalisation, the suspensions were assessed using DLS in water, saline and PBS. The median flake size remained very similar to that measured for the wGO (208.5 nm), but the whole distribution appears to be tighter – with fewer very large or very small flakes observed. When functionalised GO was measured in saline, PBS and BSA, the distributions became broader, with more of the measured R_h in the range 0.2-5 µm, but also $R_h \leq 10$ nm, with the lower range limit at sub-nanometre levels for both NaCl and PBS. The BSA distribution showed a similar trend to that seen with uwGO and wGO (Figure 4-13) – the overall quality of the suspension improves and the distribution itself becomes broader to incorporate smaller sized objects.

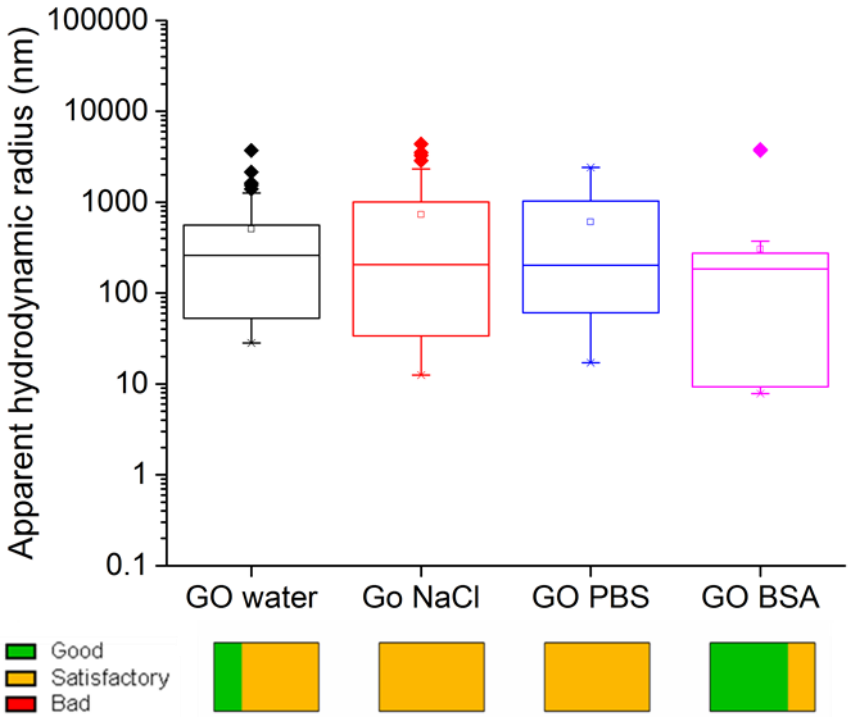

Figure 4-25 - Distribution of apparent hydrodynamic radii present in GO functionalised with 10 kDa PEG, measured using DLS in different media. Distributions are represented using box and whisker plots, with the whiskers representing the 1st and 4th quartile and the box representing the 2nd and 3rd, bisected by the median. □ is the arithmetic mean and x is the geometric mean, and the solid diamonds are outliers.

The quality of the DLS correlation curves (illustrated below the distributions in Figure 4-26) were again used to assess the quality of the suspensions, and in all the dispersion media more of the measurements were found to be *good* than for the uwGO or wGO and none were rejected. To investigate these observations further, and to gather a more representative distribution of flake sizes, the fluorescence techniques developed in Section 4.4.1.2 are used on the PEGylated suspensions.

4.4.2.3 Characterisation of functionalised GO using fluorescence techniques

In Section 4.4.1 it was demonstrated that by using the inherent fluorescence of the GO flakes, characterisation of both the flake sizes in a suspension, and their interactions with the surrounding media can be performed, and that this assessment offers some advantages when compared to many of the more established characterisation methods. The same characterisation techniques were therefore used to investigate the PEGylated flake sizes and their behaviour in physiologically relevant media.

4.4.2.3.1 Raster Image Correlation Spectroscopy for characterisation of PEGylated GO

RICS was again used to characterise the distribution of flake sizes present in suspension. Measurements were performed both in water and in double strength saline solution, to investigate whether aggregation occurred; the distributions are presented in Figure 4-27.

Despite the oxidative functional groups of the GO being utilised for the functionalisation, the flakes retain their fluorescence, with a strong signal obtained with a stack of 30 images taken – the same parameters used for unfunctionalised GO. Again, the distribution captured the larger flakes with lateral dimensions > 10 µm observed in the optical microscopy as well as the nanoscale objects found using AFM. The median R_h of the PEGylated flakes in water was 519 nm, which was larger than the washed GO, which had a median of 281 nm (Section 4.4.1.2.1 and Figure 4-15), some discrepancies also arise between the measurements performed using RICS and those found using AFM, as the lower limit of the range found using RICS does not include the flake

sizes observed using AFM (Figure 4-25). The lower limit of the AFM images is in the order of 10 nm (if working with the model of diffusion within a solvent sphere, this corresponds to R_h = 5nm), whereas for RICS the lower limit is close to 50 nm, which is an order of magnitude larger.

Unlike the unPEGylated GO, the R_h of the PEGylated flakes could still be measured after resuspension in saline solution. The median flake size and the lower limit of the range both decrease (median R_h = 395.15 nm) compared to the dispersion in water and there are fewer of the largest outliers (flakes with R_h > 10 µm). While these results suggest that a change does occur when the suspension is in the presence of ionic species, the expected change would be the observation of more objects with larger R_h as aggregates form.

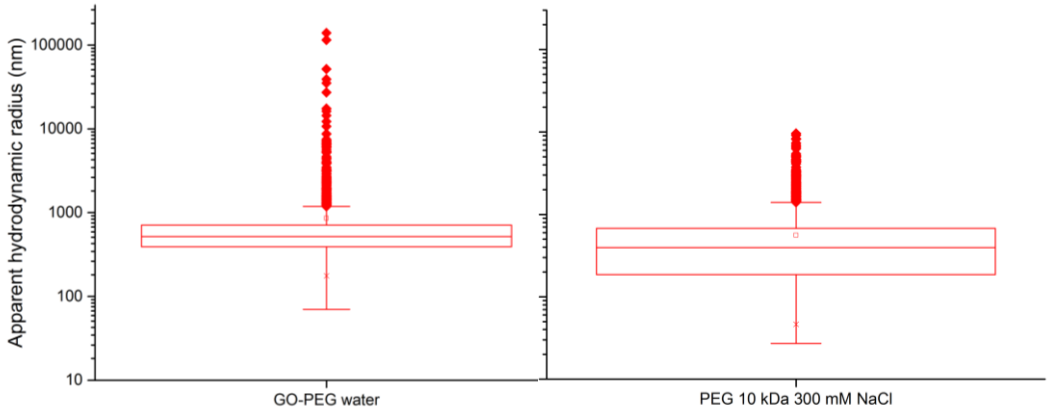

Figure 4-26 - Apparent hydrodynamic radii of GO-PEG measured using RICS, in a) water and b) 300 mM NaCl. Distributions are represented using box and whisker plots, with the whiskers representing the 1st and 4th quartile and the box representing the 2nd and 3rd, bisected by the median. □ is the arithmetic mean and x is the geometric mean, and the solid diamonds are outliers.

4.4.3 Cellular interactions

Responses to nanoparticles can vary significantly between cell types, as described in Chapter 1. As leukaemia was being used as the target for therapeutics delivery in this project, initial studies into the interaction between GO and PEG-GO and different cellular environments employed the K562 cell line, which is a well-characterised leukaemia-derived cell type with predictable proliferative behaviour, together with primary peripheral blood mononuclear cells from healthy donors, which included both normal lymphocytes and relevant phagocytic cell types.

4.4.3.1 GO interactions with K562 cells

Preliminary experiments used the K562 cell line and GO at a wide range of concentrations, assessing the cell count and viability.

Cells were extracted from culture after 24, 48 and 120 h, stained with Trypan Blue and counted using a haemocytometer, as described in section 4.3.5.1.2. The total cell count at 24, 48 and 120 h is presented in Figure 4-28; the trend shows no evidence of proliferation in the first 48 h either for untreated cells or any of the GO concentrations; however, after 120 h there is a significant decrease in cell number with increasing GO concentration, with a concentration of 75 µg/mL preventing any increase in cell number. Untreated K562s have a mean doubling time of 12 h [112], but this can vary significantly [145-147], and the cells were not in log phase growth when treated with the GO. In this experiment, the cells entered log phase growth after 48 h, indicated by the cell number at 120 h in the untreated sample increasing to approximately eight times that observed at 24 h. Cells in log phase growth are particularly sensitive to toxicity, therefore the effects of GO are more easily observed during this phase of their growth.

Simultaneously with the evaluation of cell number, a Trypan Blue exclusion assay was performed to assess cell viability, the results of which are shown in Figure 4-29. A correlation between cell viability and GO concentration is observed; however, increased cell death is induced only at higher concentrations of GO; this suggests that cell proliferation is more sensitive than viability to the effects of GO. This difference in sensitivity is frequently observed in toxicity studies since cell

division depends on a range of processes that include survival, metabolic activity and cell cycle entry.

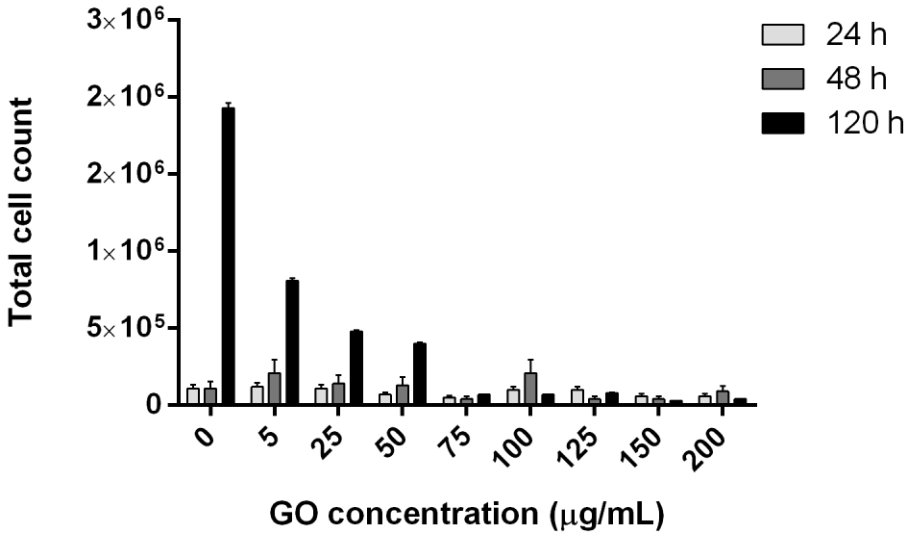

Figure 4-27 – The relationship between K562 cell number and GO concentration over time. Cells were counted at 24 h, 48 h and 120 h using a haemocytometer; the relative standard deviation between the four quadrants was taken as the error on the mean.

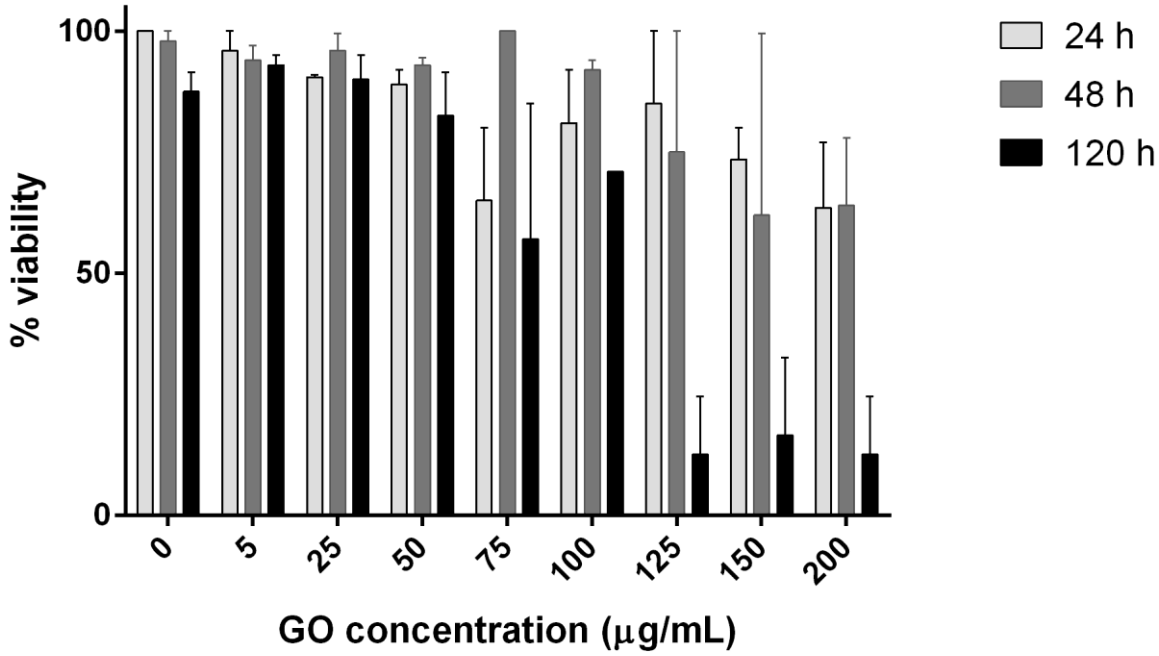

Figure 4-28 – The relationship between K562 cell viability and GO concentration over time. Viability was assessed using Trypan Blue exclusion and haemocytometer counting, and the error on the mean was found by taking the standard deviation between the four quadrants of the haemocytometer.

4.4.3.2 Studies with primary peripheral blood mononuclear cells

Having established initial toxicity and dose ranges using K562 cells, the effects of GO were then tested against primary peripheral blood mononuclear cells (PBMCs), comparing GO and GO-PEG 10 kDa. Primary cell cultures are less well-defined than cell lines; but represent more biologically relevant model, particularly given the presence of macrophages, which are of particular importance to nanoparticle studies, since particles that are engulfed by macrophages cannot interact with their target cells. All samples were taken from adult male healthy volunteers to minimise the variability between samples.

4.4.3.2.1 Morphological cell studies using brightfield microscopy

The morphology of the cells was first investigated using a phase contrast microscopy. Figure 4-31 demonstrates the difference in appearance of PBMCs in culture with either GO or PEG-GO suspensions. In the cultures treated with PEG-GO, the suspension cannot be seen, suggesting that the flakes are highly disperse and single to few-layer; no aggregates are observed. In the culture treated with unfunctionalised GO, the media is no longer clear, partially obscuring the cells with the aggregates of GO present in the media. In addition, the macrophages are seen to have very dark intracellular regions, representing aggregates that have been engulfed by the macrophages (white arrows in Figure 4-31). The lymphocytes in the cultures did not present dark regions that would suggest uptake or colocalisation of either form of GO, but in GO-treated cultures they were observed to cluster around the phagocytic cells, suggesting an activated state (Figure 4-30). The activation of the lymphocytes could represent a direct effect of the GO, or could be secondary to macrophage activation and cytokine release, of which there have been limited reports in the literature [105].

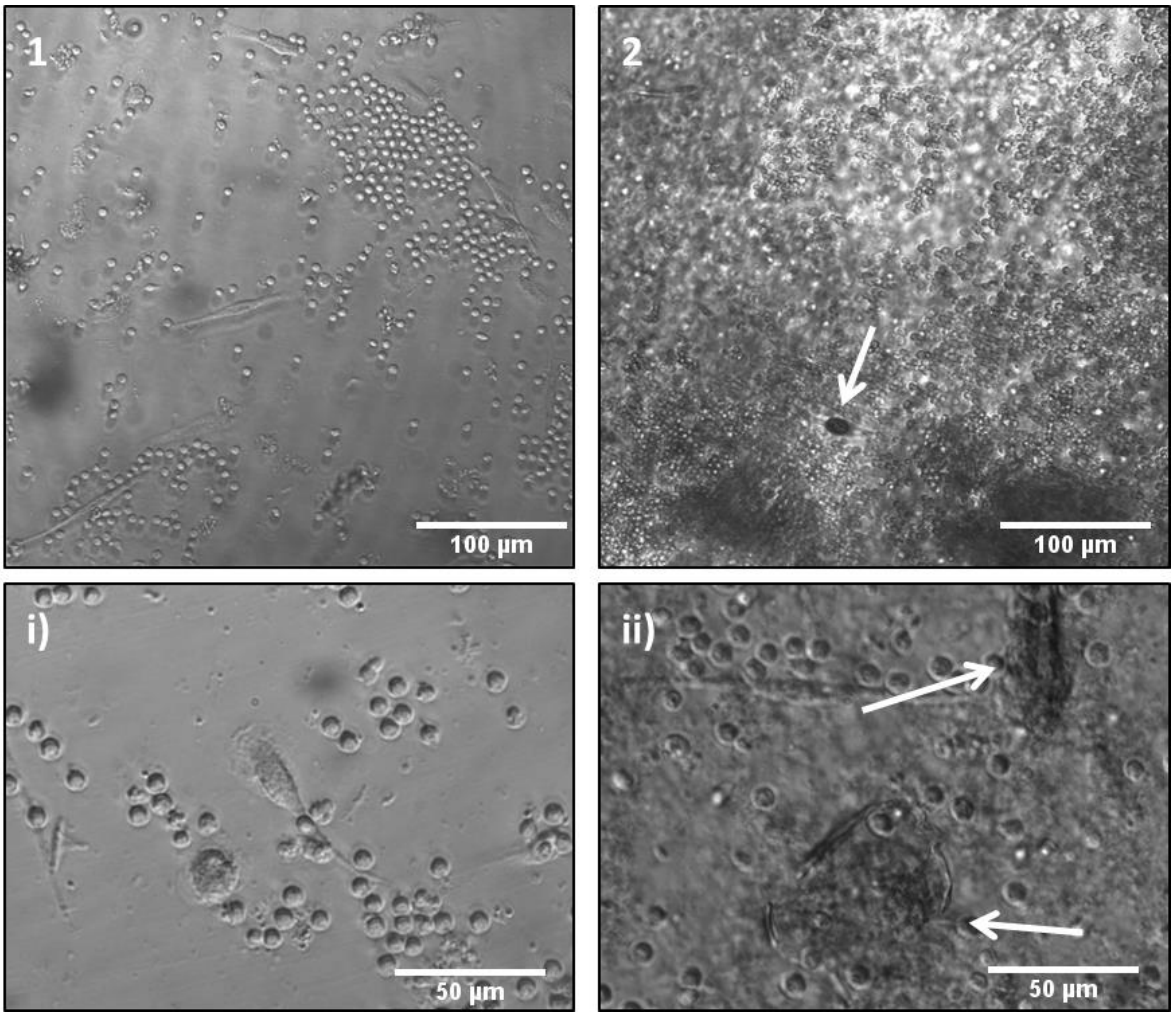

Figure 4-29 - PBMCs treated with PEG-GO (1) detail (i); and GO (2) detail (ii) The media in the sample treated with PEG-GO appears clear, with no obvious signs of flake agglomeration, and no flake aggregates observed in the macrophages. Whereas in the GO sample, the media appears cloudy, indicating flake agglomeration, and the macrophages appear very dark (white arrows), indicating signiicant flake uptake.

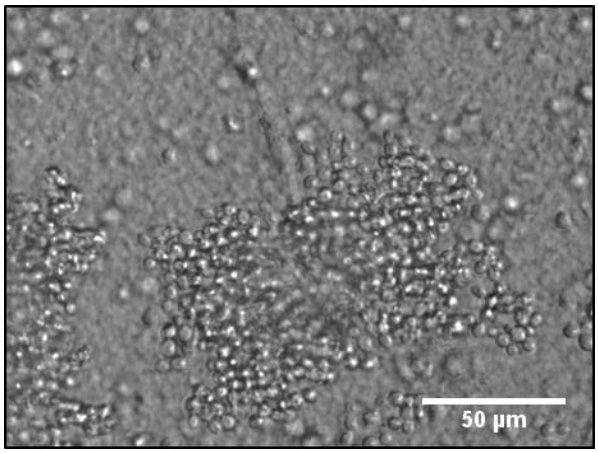

Figure 4-30 - Signs of lymphocyte agglutination in GO-treated samples Large numbers of small lymphocytes are observed crowded around a central macrophage.

To further investigate the interaction of flakes with the macrophages, the cultures were left for 1 week in the presence of GO to see how they differed. The majority of the lymphocytes were then removed and the remaining macrophages fixed and stained (see Figure 4-32).

For GO-treated cultures, significant intracellular material is observed within the phagocytic cells, which also present high degree of cytoplasmic vacuolation, indicated by the red arrows in Figure 4-32. These observations confirm that the instability of unfunctionalised GO preparations leads to significant macrophage uptake and activation.

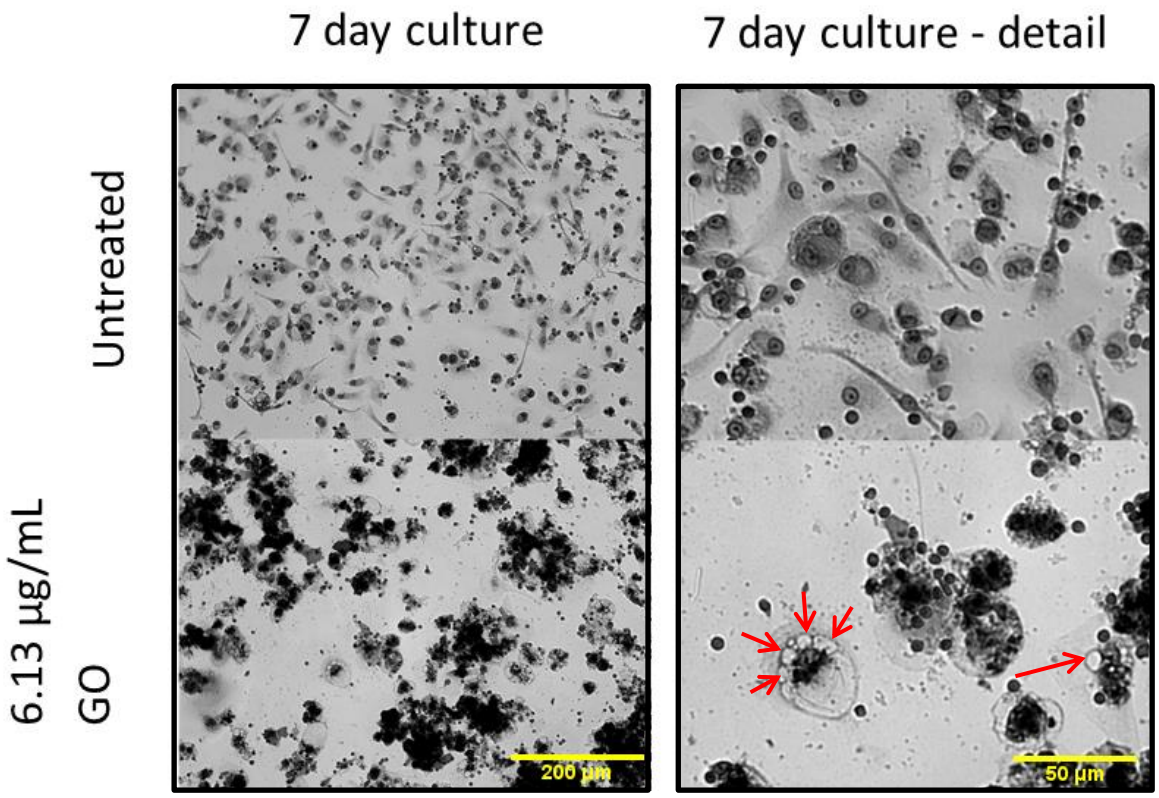

Figure 4-31 - Fixed and stained PBMCs after 7 day culture. Major remaining population is macrophages, their interactions with the GO present in the culture can be observed. Severe aggregation of GO flakes is observed in the lower panels, with localisation around the macrophages. Significant vacuolisation is also observed, indicated by the red arrows.

4.4.3.2.2 Flow cytometric studies

Flow cytometry provides significantly more information about sample viability and cellular effects than the use of a haemocytometer. The technique allows separate analysis of the different cell types within a mixed culture (see section 4.3.4.7.2, Figure 5-6) and a statistically relevant sample size. In addition, the fluorescence studies reported in Section 4.4.1.2.2, suggested that the technique can provide information about the behaviour of the graphene with which the cells have been treated, particularly with regards to the flakes' interactions with the cellular components and those of the biological medium in which they were cultured. Initial experiments were therefore designed to evaluate the use of flow cytometry for the assessment of graphene within live culture.

The scatter plots obtained using flow cytometry were gated based on both size and immunophenotype to separate different cell populations, including those that are apoptotic or necrotic, as described in Section 4.3.4.7.2, and illustrated in Figure 5-6, Figure 5-7 and Figure 5-8. Alongside gating strategies for apoptotic and necrotic cells, propidium iodide continued to be used to label the apoptotic or necrotic cells. The additional presence of graphene was assessed based on particle size, inherent fluorescence or quenching behaviour.

4.4.3.2.2.1 Cellular interactions with GO and PEG-GO

Using GO or PEG-GO, the interaction between the cells and the graphene was investigated using light scatter (FSC/SSC) and fluorescence. While PEG-GO was easily removed from cell suspensions using washing procedures, the instability of the GO meant that it remained in the sample. The GO is clearly observed in the FSC/SSC plot shown in blue in Figure 4-33, and its autofluorescence was recorded in the histogram (blue arrow Figure 4-33). Additional gating was undertaken to remove the signal associated with the GO, shown in the lower panel of Figure 4-33; the absence of the autofluorescence peak in the histogram confirms that the GO flake signals can be effectively identified and excluded from the analysis. In addition, the absence of a fluorescence peak when

only cellular events were observed suggested there was little colocalisation between the flakes the cells.

The samples treated with PEGylated GO presented a normal FSC/SSC plot; the PEG-GO was not observed, and the cell types were easily discernible through the gating strategies (Figure 5-34c and d). Alongside the microscopy results, this confirms little or no internalisation or interaction between the GO-PEG flakes and the cells.

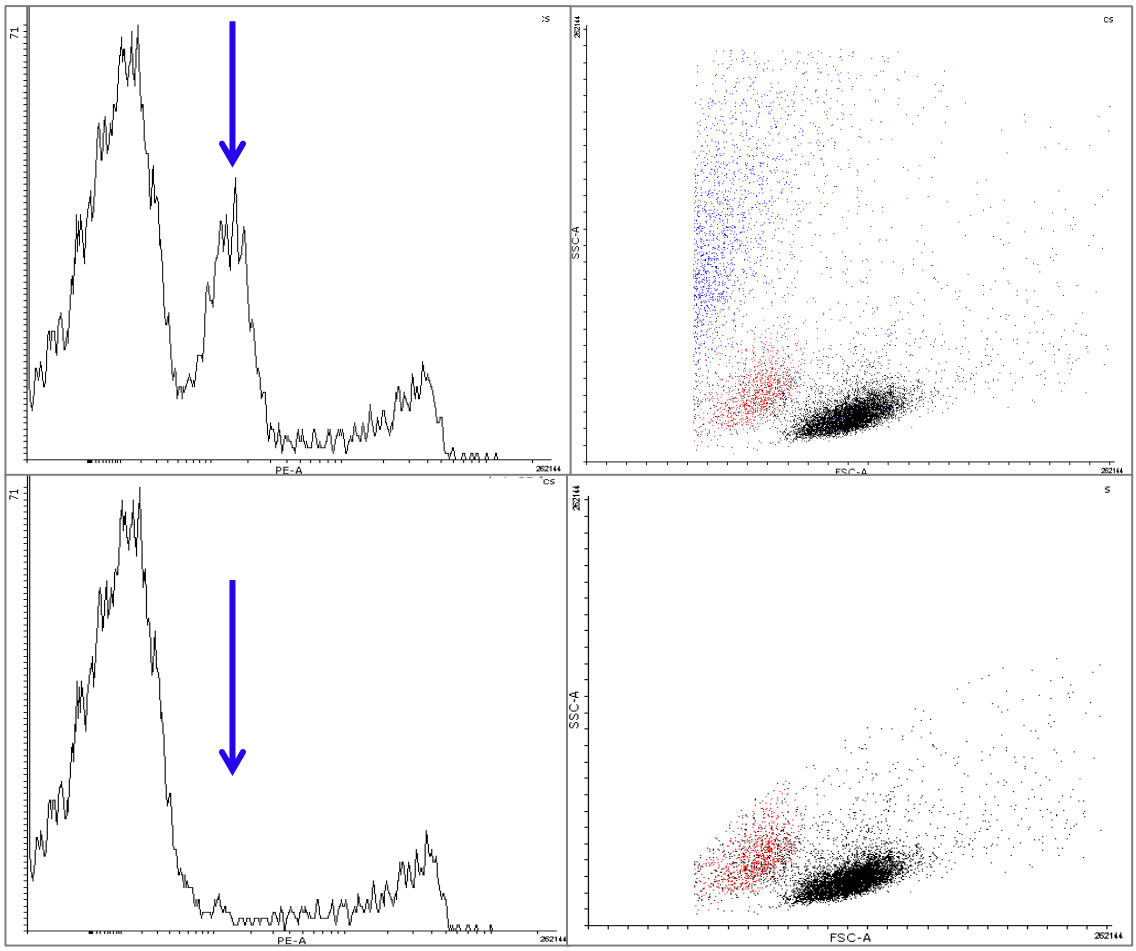

Figure 4-32 – Illustration of how GO flakes can be gated out of flow cytometric analysis of cells, confirmed using fluorescence

Top: GO 11.25 µg/mL. GO flakes are observed in both the scatter plot (marked blue) and the fluorescence histogram (middle peak – indicated by blue arrow)

Bottom: After gating – the fluorescence peak associated with GO completely disappears, illustrating that the GO has been successfully gated out.

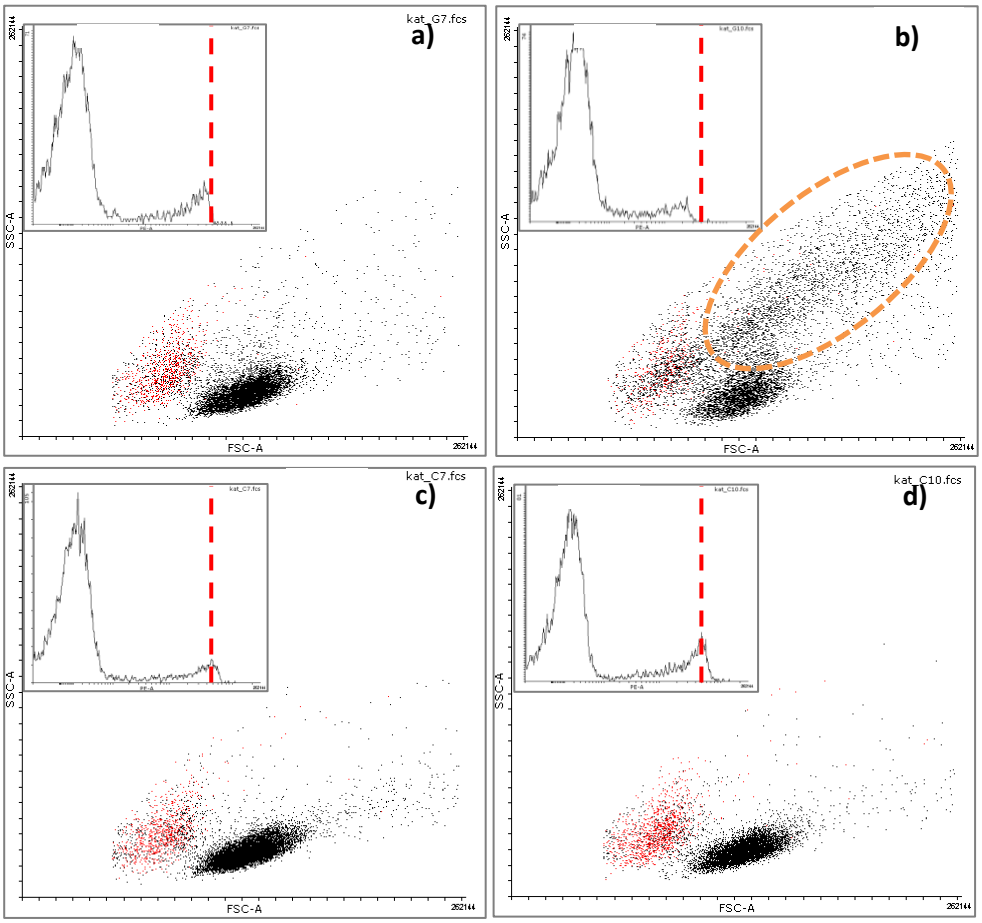

Figure 4-33 - Scatter plots and fluorescence histograms for a) GO 11.25 µg/mL; b) GO 90 µg/mL; c) PEG-GO 11.25 µg/mL; d) PEG-GO 90 µg/mL

When the cells were incubated with the highest GO concentration, an additional feature was observed on the scatter plot. Objects were recorded in a region of high SSC and FSC, highlighted with an orange circle in Figure 5-34. This fell outside of the regions where viable lymphocytes or dead cells are seen. This region did not present any fluorescent features, so was not thought to represent aggregates of GO or dead PI-stained cells. While this region could be associated with monocytes (Figure 5-6), however monocytes would not be expected to proliferate, and it had previously been observed that at 24 h most became adherent and therefore would be unlikely to be present in the sample that is analysed with the flow cytometer. Unfortunately, time pressures precluded the detailed further evaluation of this scatter plot feature.

An additional interesting feature was noted, related to the fluorescent peak associated with PI (illustrated in the histograms inset in Figure 5-34, where the red dashed line indicates the normal

fluorescence intensity of PI). In the presence of GO, the fluorescence of PI that was associated with dead cells was found to have lower intensity; this suggested that some quenching may have taken place, especially as GO and other GFNs are known to quench fluorescence. Drawing any strong conclusions from the quenching result is complex, however, as it is not known at what point the PI may have adsorbed onto the GO flakes – that is, before or after interaction with the cell chromosomes. It does, however, show that in the presence of GO, PI may not be a reliable method of assessing cell death, and reflects more widely on the challenges of assessing GO in flow cytometry, as it is a technique that predominantly employs fluorescence, and therefore quenching can be problematic.

4.4.3.2.2.2 Cell viability studies

In order to assess cell viability, the FSC/SSC plots were gated as described in Section 4.3.4.7.2, and the viabilities determined by assessing the relative number of live cells in the population; the results of which are shown in Figure 4-35. However, the observation of additional objects that fell outside of the live and dead gating in the culture treated with the highest concentration of GO (see Figure 5-34) led to a significant uncertainty in the analysis of cell viability. Uncertainties were

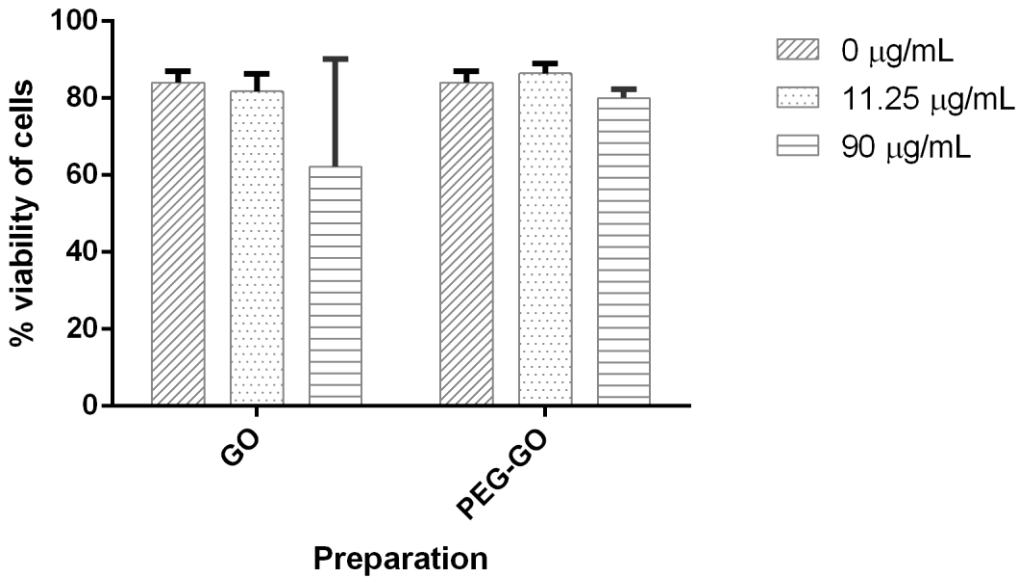

Figure 4-34 - Viability of PBMCs found using flow cytometry after treatment with GO or PEG-GO. Uncertainties were calculated by finding the difference between the number of events in the live gate and those ungated.

calculated by taking the number of events that fell outside of either the live or dead gated regions.

Figure 4-35 suggests there is very little difference in viability for cells treated with PEG-GO for either concentration tested in comparison to the untreated cells. At 11.25 μg/mL, very little difference in viability is observed for GO; the viability at 90 μg/mL appears reduced, however assessment was problematic due to the presence of objects that fell outside of either region; this led to the large uncertainties illustrated in the figure.

4.4.3.2.3 Assessing cellular viability with a mitochondrial function assay

The previous results using K562 cells suggested that GO affected a range of cellular processes, and that these effects might be best detected when the cells were actively dividing. To examine this further, the cell populations were stimulated into growth using phytohaemagglutinin (PHA), and their viability was assessed using an Alamar Blue assay. This assay provided some advantages when compared with flow cytometry, both due to the problems encountered in Section 4.4.3.2.2.2 with unfunctionalised GO, and since forward and side scatter characteristics of cells undergoing division are changed, making gating strategies complex to apply.

Alamar Blue provides a broader assessment of cell health by measuring cell metabolism. Healthy cells will reduce Alamar Blue present in the media through mitochondrial activity; this is reduced in unhealthy cells and absent in dead cells. Data from this assay therefore represent a broad assessment of cell number and metabolism, and are affected by proliferation, metabolic disturbance or death. The results are presented in Figure 4-36.

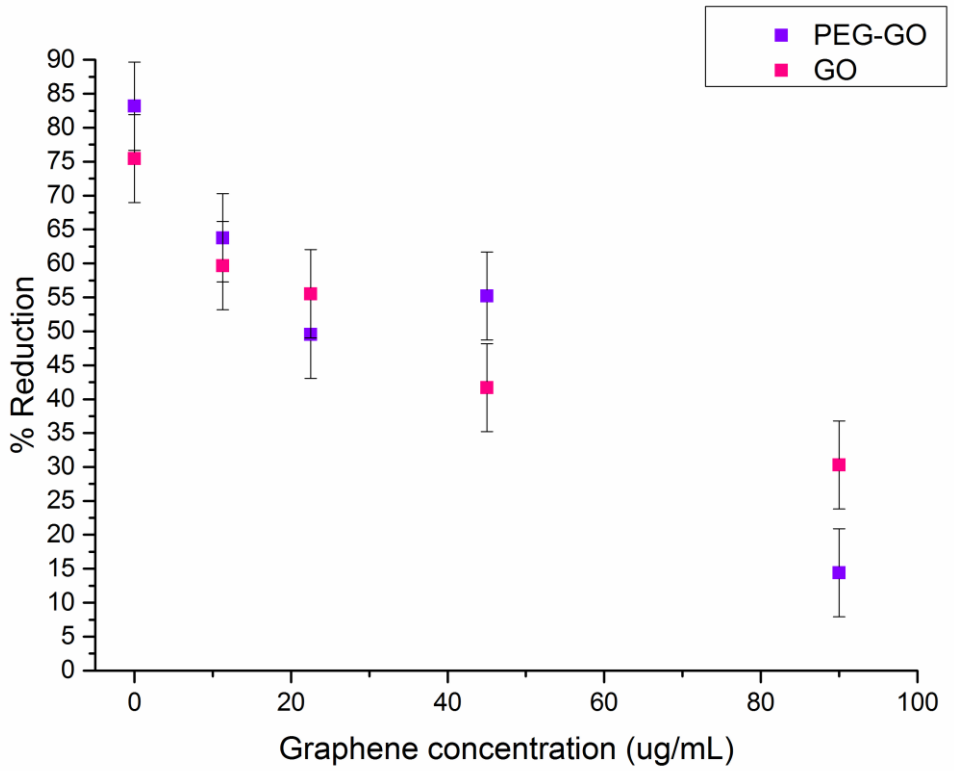

Figure 4-35 – Percentage reduction of Alamar Blue for PBMCs treated with GO and PEG-GO at a range of concentrations. Errors were calculated as the standard deviation on the mean.

For both GO and PEG-GO, increasing concentration leads to reduced cell health, with a noticeable difference in percentage reduction of Alamar Blue beginning at GO doses of 11.25 µg/mL. This is a similar trend to that seen with the K562 population in log phase growth when treated with GO (Figure 4-28). With regards to the PEG-GO samples, this is in significant contrast to the tendencies observed in both the morphological and viability studies performed using flow cytometry of the PBMCs at rest, as in these stimulated samples there is evidence for toxicity. As previously mentioned, cells are more sensitive to factors affecting their health when they are at their most metabolically active.

4.5 Discussion

Commercially acquired GO was purified and functionalised using methods detailed in the literature for improved biocompatibility [73, 114]. Thorough characterisation of the samples was undertaken using a range of established and novel techniques that made use of the inherent fluorescence of GO. Preliminary cell experiments were then performed to assess the interaction between the GO preparations and relevant cell types.

4.5.1 Comparative analysis of GO characterisation methods

Over the course of this work, it was found that many of the existing techniques used for characterising GO cannot easily measure the full range of flakes in a sample. For this reason, the inherent fluorescence of the material was harnessed so that RICS and flow cytometry could be applied. The results provided by both of the methods demonstrated their potential for wider use in the characterisation of GO, particularly for biological preparations.

Solution-based methods for characterising GO suspensions are convenient as they can characterise flakes *in situ*, the sample sizes analysed are statistically significant and often the measurements themselves are rapid. RICS is a fluorescence-based technique that utilises the hidden time structure in the images taken by a confocal microscope: as a fluorescent particle moves due to Brownian motion the fluorescence intensity measured per pixel in an image will fluctuate – the rate at which this occurs allows the diffusion coefficient to be determined [118]. The use of pixel dwell time, line rate and frame rate allows a far broader size range to be observed than is possible using DLS – with the R_h range encompassing the lateral size ranges measured by both AFM and optical microscopy. However, like DLS, RICS utilises the Stokes-Einstein equation [119], which assumes that the particles under investigation are hard spheres and therefore their only degrees of freedom are translational, and their diffusion characteristics will be symmetrical in all the Cartesian co-ordinates – as described earlier. The asymmetry of the

flakes may lead to spurious results, and the calculated R_h values may be different to the actual lateral dimensions of the flakes present, requiring calibration with an alternative method [64]. As none of the other techniques used in this work were able to measure the full range of flake sizes present, the distribution found by RICS could not be compared to a known distribution of flake sizes from each of the samples.

An interesting example of the challenges of using such methods with GO may have been highlighted in the measurements of wGO suspensions by DLS. When measured with the DLS, the distribution of R_h recorded for wGO had far smaller flakes in the suspension than uwGO, contrary to the results measured using RICS. However, the range recorded using DLS included apparent hydrodynamic radii that were < 1 nm; the presence of objects with lateral dimensions of this size is highly unlikely. However, since a thin flake such as GO has both translational and rotational degrees of freedom, the diffusion characteristics will be asymmetric with regards to diffusion that is normal or tangential to the flake basal plane [148], and as the flakes are also highly flexible, which may result in diffusion characteristics associated with bending and wrinkling. Therefore, these measurements may be due to the influence of edge-on diffusion (diffusion tangential to the basal plane) or bending and wrinkling of the flakes. While there are no reports of similar observations when using DLS to measure GO, despite how widely used it is, prior work on the scattering profiles of oblate objects in DLS has suggested that inherent flexibility of an object can influence the correlation curve [149], and therefore the distribution of R_h calculated. While this is a reasonable hypothesis, it is surprising that similar observations are not found in uwGO suspensions.

In addition, while RICS is superior to DLS in terms of the size range that it can capture, its dependency on both fluorescence and Brownian motion meant that behaviour change of the uwGO and wGO flakes in different complex media could not be assessed. The improved stability of PEG-GO in ionic solution was confirmed by the successful measurement of the flakes using RICS; however, the flake distribution observed using the RICS after the PEG-GO suspension was dispersed in saline provided surprising results, as the median and range of R_h observed was

smaller than those observed in pure water. This is the opposite of the expected change, if any electrostatically induced aggregation had occurred; however, it should be noted that the confocal set-up of a RICS experiment depends on a single focal plane, generally adjusted to be approximately in the centre of the volume in the well. Therefore, any precipitation of aggregates may lead to them not being captured by the technique.

DLS was also used to assess flakes' interactions with complex, biologically relevant media. Despite being broadly used to assess the adsorption of proteins (including BSA [150]) and polymers onto graphene and GO surfaces [151-153], DLS could not definitively confirm the interaction between GO and BSA, despite the interaction being well-documented [127, 136, 150, 154]; this was particularly apparent for wGO, in which no significant difference in the $1 \geq R_h \geq 500$ nm region was observed between samples, which is the range in which some difference was observed for uwGO. Therefore, flow cytometry was used as an alternative method of detecting interactions between BSA and GO; the intensity of the flakes' fluorescence was observed to be reduced in the presence of BSA and human AB serum (Section 4.4.1.2.2.2, Figure 4-18) and was considered to be due to quenching mechanisms by the serum proteins. As quenching requires molecular contact between the fluorophore and the quencher, it is commonly used to assess the interaction between two species [155]; the observation of quenching was therefore considered to be due to direct complexation of the serum proteins with GO flakes. The result was observed for both uwGO and wGO in both BSA and Human AB serum, and may provide a simple and fast method of assessing flake interactions with serum proteins. Flow cytometry has previously been used to analyse GO suspensions, the focus of which was predominantly on the use of forward and side scatter to define the flake sizes [107]. The forward and side scatter profile for the suspension reported by the authors was very different to that observed in the work reported here, despite the flakes in the suspension having a similar range to that quoted in the article; the authors also did not describe a method by which the flake sizes could be easily extracted. For these reasons, RICS is considered to be a superior method for flake sizing.

Some established techniques currently used the literature for graphene and GO characterisation do provide alternative characterisation techniques that allow the assessment of flake sizes and suspension stability. Transmission electron microscopy (TEM) [30, 64, 73, 121, 142, 156] has many of the benefits of AFM, including direct visualisation of nanoscale objects, but the technique can measure (depending on the set-up) from sub-nanometre ranges up to micron-sized objects, due to the very short wavelength of electrons, and the region of interest that the technique can capture is far larger than AFM, although the full range of flake sizes cannot be captured in one image, and generally requires magnification steps [157]. As a flake sizing method, TEM is a strong alternative to either AFM or optical microscopy, however its specialised set-up means that it is not available in many labs, and beam damage can occur to the flakes during measurement, particularly when performing high resolution measurements [158].

Despite the possibility of using both RICS and flow cytometry as more effective and high throughput techniques for the analysis of GO, their necessity also highlights the significant challenges associated with using GO in biological applications. The flakes are primarily very difficult to characterise using standard techniques due to the significant polydispersity of the samples. This feature is particularly problematic for biomedical application such as drug delivery.

4.5.2 Preparation of GO for biomedical applications

Multiple steps were taken to prepare GO that would be suitable for biomedical applications. Initially purification steps were undertaken to remove any residual contaminants and thicker or unreacted flakes. Following purification, the average lateral dimensions of the GO flakes were observed to decrease in measurements with RICS, optical microscopy and AFM. The flake thicknesses, as observed using both optical microscopy and AFM also appeared to decrease. However, as shown in the RICS results (Section 4.4.1.2.1, Figure 4-15), the distribution of lateral sizes in purified GO became tighter – with both the upper and lower limits of the distribution becoming closer to the median. This illustrates the importance of using a single method to gather the flake size distribution in order to gather a representative view of the flakes present. However,

while this result suggests that the suspension is more monodisperse, it is also in contradiction with the literature reference from which the protocol was extracted – in which it was found that multiple centrifugation steps led to a relatively monodisperse suspension of only the smallest and thinnest flakes [73]. It is thought that this result may be due to the second centrifugation step in the purification protocol; the suspension is repeatedly washed with warm water and centrifuged at very high rates (17000 x g), and supernatant is discarded to remove residual contaminants including mellitic acid. This step may therefore also reduce the presence of the very smallest flakes, as they may remain in suspension – resulting in the new distribution observed with washed GO. This change in the overall distribution – with the smallest flakes no longer present in suspension – may also explain the far worse stability of the washed GO flakes in media containing ionic and buffering agents (as observed from the correlation curve stability in the DLS measurements), however this was not confirmed. This result is problematic, as larger flakes have been widely correlated with greater toxicity; however XPS analysis showed that there were fewer residual contaminants present in the washed preparation, which is also an important determinant of toxicity. It may be preferable to perform additional sonication and size selection steps using density centrifugation separation in order to minimise contamination and obtain a suspension with the desired size range [101].

The purified GO was functionalised using 4-arm 10 kDa amine terminated PEG. While some other amine terminated PEG chains of smaller sizes and with only single chains were assessed in terms of their suitability for improving both flake stability and biocompatibility, problems with cross-linking and reduced stability in ionic solutions – with visible agglomerates after PEGylation and strong aggregation after the addition of ionic solutions – led to only the 10 kDa preparation being taken forward. Successful PEGylation was confirmed using XPS and AFM, and by observing the improved stability of the flakes in ionic solutions, both through DLS and RICS. The AFM results, however, illustrated that particularly on the larger flakes, the PEGylation was sparse, and not significantly observed at flake edges, where it has been hypothesised that the majority of the carboxylic acids reside on the flakes [31, 94]. However, as described in Section 4.1.2, the

structure of GO is still highly debated, and several reports in which an amidation step has been used for the functionalisation of the GO, an additional carboxylation step has been pursued to improve coverage [101, 106, 159]. In addition, the experimental procedure for PEGylation utilised the slow addition of GO flakes activated with EDC to an excess of PEG in order to minimise cross-linking, and while EDC is in part attractive due to its water solubility, the activated ester of the carboxylic acids will hydrolyse over time, which may have led to a less complete level of surface functionalisation than desired. This may have led to the aggregation of some of the flakes, evidence for which was observed using RICS.

The PEG-GO flake lateral dimensions measured using RICS were found to be larger than that of purified GO flakes. This result is surprising, as the PEGylation process involves the use of sonication, which leads to scission of GO flakes [81, 114, 160]. However, after the PEGylation is performed, the suspensions are washed repeatedly to remove all excess EDC and PEG; this is performed in a membrane filter centrifuge tube. The suspensions have a tendency to stick in the membranes and regularly need agitation to be resuspended; it not known whether this process effectively acts to size select the flakes, with the smallest remaining stuck in the membranes. Nevertheless, some of the outlier R_h values observed are larger than those observed in the purified suspensions; while RICS does not measure individual flakes, but fluorescence intensity fluctuations, and therefore caution should be exercised before comparing individual measurements, there is a possibility that some limited cross-linking between the flakes may have occurred during the PEGylation process, that was not as significant as observed with the other attempted preparations. The stability of the suspensions and the lack of obvious evidence observed in the AFM images means extensive cross linking is unlikely; however, the flake overlap that often occurs in the spin coating process (easily observed in the optical microscopy images for all samples Figure 5-12 and Figure 4-23) may have made some instances difficult to discern.

4.5.3 Interaction between graphene oxide preparations and white blood cells

Following the preparation and characterisation of GO and PEG-GO, preliminary cell experiments were performed to test the interactions between these GO preparations and cellular systems.

Initial experiments used the K562 cell lines using GO without PEGylation; a wide range of concentrations was tested, and the cell health was assessed by investigating cell number and viability through trypan blue exclusion. Both cell number and cell viability were assessed. The analysis confirmed that increased GO concentration was correlated with reduced cell viability. Effects were best seen when cells were in log-phase growth; with reduced cell number observed at 5 μg/mL and reduced viability at 50 μg/mL. Reports in the literature of the concentration of GO at which a toxic effect is observed have ranged from 1-100 μg/mL depending on cell type, method of GO preparation and the method by which toxicity was measured [105, 110, 161-163], therefore the ranges observed in this work fit into the reported range. These experiments were preliminary and were performed at a very early point in the project using unpurified or functionalised GO. Therefore the suspensions were highly polydisperse in terms of thickness and lateral dimensions and contained residual contaminants, all of which are known to affect toxicity of GO [72, 73, 105].

Subsequent experiments were performed using primary peripheral blood mononuclear cells; this culture provided a more complex environment, with the presence of phagocytic cells such as macrophages and a mixture of T-cells and B-cells. Flow cytometric analysis of toxicity showed little change in the viability at 11.25 μg/mL for either preparation of GO, and at 90 μg/mL no significant loss in viability was observed for the PEG-GO preparation. While a significant loss in viability was observed for GO at 90 μg/mL, this was complicated by the cellular objects that fell outside of the gates on the FSC/SSC plot, which led to large uncertainties. As the experiments with the K562s had shown the cells to be more sensitive to the presence of GO when undergoing log phase growth, the PBMCs were stimulated into proliferation using PHA. For both preparations, a strong trend correlating increasing GO and PEG-GO concentration and reduced

cell health was observed, with a decrease in viability from 11.25 µg/mL for both preparations, suggesting that during cell division PEG-GO may have toxic effects

Morphological examination of the PBMC preparations showed that despite the prior evidence of limited aggregation of the PEGylated flakes (Sections 4.4.2.3.1, Figure 4-27), the cell culture media remained clear without any evidence of aggregation. The morphologies of the different cell populations remained healthy and no evidence of significant macrophage uptake was observed. For cell cultures treated with unfunctionalised GO, on the other hand there was significant evidence of aggregation, and significant uptake by the macrophages was observed (Section 4.4.3.2.1, Figure 4-31). Further investigation of the morphology of the macrophages after longer culture times led to the observation of significant vacuolisation and evidence of macrophage activation (Section 4.4.3.2.1, Figure 4-32). These observations are in line with multiple reports in the literature in which significant macrophage uptake of GO was observed in macrophages from a range of human and animal sources both *in vivo* and *in vitro* [105, 125, 164-166] and evidence of activation through alterations in the cell morphology [105] and cytokine excretion [81, 167, 168].

Evidence of lymphocyte agglutination was also observed in the PBMC samples treated with unfunctionalised GO in the microscopy images (Section 4.4.3.2.1, Figure 4-30), and the flow cytometric analysis performed on the PBMCs at 90 µg/mL revealed an unidentified band of objects, which were likely to be cells, outside of the gates indicating the different cell populations. Reports in the literature regarding immunostimulation by GO have presented conflicting results; in some instances *in vitro* tests have reported GO does not cause immunostimulation [165, 166], whereas Yue *et al.* [105] recorded the secretion of interleukin-6 (IL-6) by macrophages after incubation with GO, which is known to stimulate T-cell proliferation [169] and *in vivo* experiments recorded the invasion of lymphocytes into the subcutaneous regions where GO had been introduced. Further work would need to be performed to elucidate whether the GO was indeed causing lymphocyte stimulation and the modes by which it was being caused – for instance whether the stimulation was primary or took place through the lymphocytes. In the experiments

performed by Yue *et al.* [105], it was found that the larger flakes, with average lateral dimensions of 2 μm, that caused the most significant excretion of IL-6. The GO suspensions used in this work were large – with lateral dimensions that far exceeded 2 μm, therefore any future experiments that examine this response should analyse any variation based on flake size. While time-constraints of the thesis precluded extensive cell culture work, this project has demonstrated the application of a range of techniques with different strengths that allow assessment of graphene behaviour in biological systems from initial preparation through to cell interaction.

5 Synthesis and bioactivity of BAT1 – a CXCR4 antagonist for therapeutics delivery targeting

5.1 Introduction

An essential element for targeted delivery of nanoparticles is the design and incorporation of a selective targeting ligand. CXCR4 is a cell surface receptor that is overexpressed in a number of cancers, including chronic lymphocytic leukaemia (CLL) [27, 170] – the focus of this project. Over the last 30 years a number of small molecule drugs, biomolecules peptides and polymers have been prepared that target this receptor, drawing on this work, a ligand was synthesised that would target CXCR4 and could easily be attached to GO.

5.1.1 Chemokines

Chemokines are low molecular weight chemotactic signalling proteins, which were first found to be associated with certain leukocytes, but are now known to play important roles with various other cells as well. After coupling with their conjugate receptor, cytokines trigger signalling cascades that lead to gradient-driven cellular migration [171-173]. Their main function is to facilitate the healthy homing and trafficking of haematopoietic cells, however some are also associated with organ development and angiogenesis, and may have non-chemotactic functions such as the promotion of survival or proliferation [170, 174]. Chemokines are divided into four major groups according to the number and placement of the cysteine residues (denoted by C) at their N-terminals: CXC, CC, C and CX_3C, where X denotes any amino acid other than cysteine; all bind to the family of G-protein coupled cell surface receptors known as seven-transmembrane domain receptors [171, 174]. The family can also be broadly split in terms of whether their role is inflammatory or homeostatic; homeostatic cytokines are particularly important in haematopoiesis and immune surveillance. In particular, one of the most important chemokines, CXCL12 (also known as SDF-1α/β) plays an important role in early neurogenesis and vasculogenesis, and is vital for healthy haematopoiesis, where it facilitates stem cell retention in the bone marrow niche. The primary receptor for CXCL12 is CXCR4, which is expressed across a number of healthy cells,

but is often overexpressed in a number of disease states, including chronic lymphocytic leukaemia (CLL). It is the CXCL12-CXCR4 chemotactic axis that is the focus of this chapter.

5.1.1.1 Cell surface receptor CXCR4

The conjugation of CXCR4 and its conjugate ligand, CXCL12, results in a signalling cascade (shown in Figure 5-1) that is associated with increased proliferation, survival, chemotaxis, intracellular calcium flux and gene transcription [175, 176]. When overexpressed in cancer cells, this translates to increased cancer cell survival, proliferation, invasion, and metastasis [172].

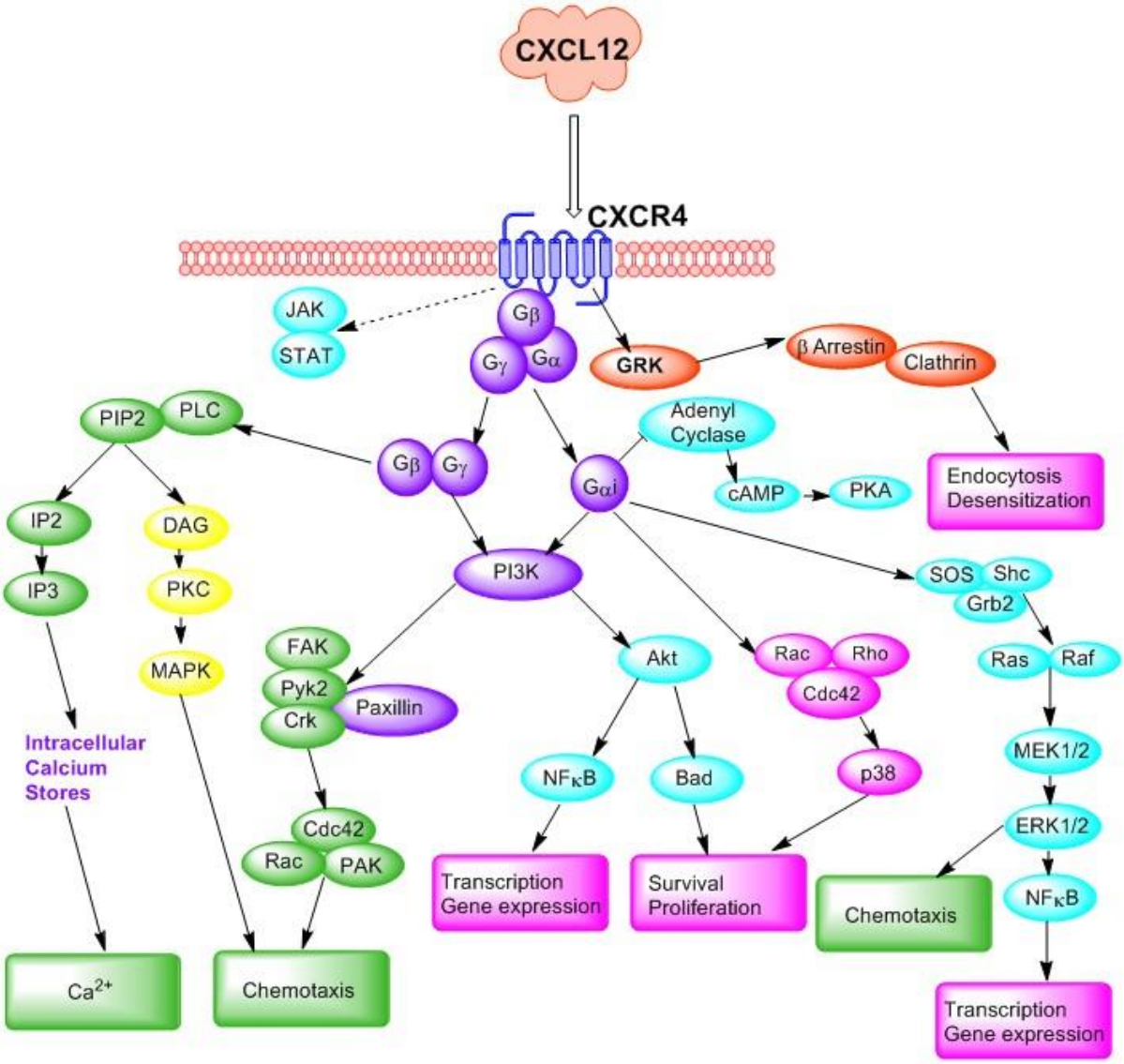

Figure 5-1 – A diagram of the CXCL12/CXCR4 cell signalling cascade. Adapted from Teicher & Fricker [214]

The receptor was first investigated in HIV research, as it is used by the virus to enter T-cells, but has since been found to be important in a number of other disease states [177-179], including its central role in cancers, in which overexpression is associated with worsened outcomes [170]. The key role that it plays in various cancers has led to interest in the CXCL12-CXCR4 axis as a therapeutic target, both with regards to inhibiting the pathway – either through CXCR4 downregulation using siRNA, by blocking its interaction with CXCL12 using antagonists, or exploiting its overexpression to deliver anticancer drugs [172, 180-195]. A number of CXCR4

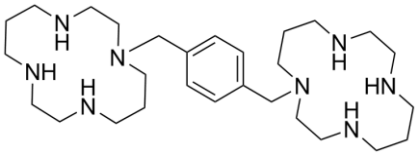

Figure 5-2 - The structure of AMD3100

antagonists have been developed, including various peptides [180-182, 185, 195], antibodies [183, 184, 196] and small organic molecules [187-189, 192, 194, 197]. Within the small organic molecule targeting agents, the most successful and only clinically approved is the bis(cyclam) AMD3100 (Mobozil, Plerixafor) – Figure 5-2 – which has also been used for targeted imaging work [190, 198]. In this work, this molecule was chosen as the basis of a targeting ligand for GO flakes.

5.1.2 AMD3100 in therapeutics delivery

As mentioned previously, the CXCR4 receptor was initially of interest due to its role in HIV entry, and after its initial formulation, it was hoped that AMD3100 could function as an anti-HIV drug [177-179]; by decreasing the number of CXCR4 receptors available on the cell surface it was thought that the ability of the virus to enter the cells would be reduced. However it is now predominantly used in the clinic to mobilise stem cells from the bone marrow to the blood stream; CXCL12 is produced by bone marrow stromal cells, and the interaction between the chemokine and the receptor CXCR4 functions to retain the stem cells in the bone marrow niche, which is disrupted by the antagonism of AMD3100 [199, 200]. The drug has also been used as a chemosensitiser in acute myeloid leukaemia [170]. The activation of CXCR4 by CXCL12 often leads to further chemoprotecting activity, for instance, interaction between CXCL12 and CXCR4 on

stromal cells – which are one of the predominant cell types that excrete CXCL12 also leads to the activation of adhesion molecules that trigger pro-survival signalling, and protects the cells from chemotherapy agents [170]. By interrupting the CXCR4/CXCL12 interaction, interactions between the stromal cells and cancer cells is disrupted, and the cells once again become vulnerable to chemotherapeutic agents.

The primary interaction between AMD3100 and the cell surface receptor CXCR4 is thought to occur *via* hydrogen bonding between its cyclams and the Asp^{171} and Asp^{262} residues of CXCR4 [201, 202], and the cyclams alone will in fact bind to CXCR4, but are a significantly less potent antagonist than AMD3100 [179].

With regards to its use in therapeutics targeting, the most prolific is the group of Prof. David Oupický have copolymerised AMD3100 through the tertiary amines of the cyclams with various other commercial polymer chains for therapeutics delivery, in which the polymeric plerixafor functioned as the encapsulating nanoparticle itself. Initially, the polymer was formed by reacting the amines on the cyclams with HMBA (N,N'-hexamethylenebisacrylamide), and further experiments have been performed that vary the polymeric linkers between the AMD3100 blocks – including the inclusion of both PEG [192] and cholesterol [193] to improve the stability of the nanoparticles. The polymeric plerixafor was able to successfully condense siRNA, and it was reported that the polymer retained its antagonistic effect; however, the polyplexes were found to be taken up through an alternative pathway and no colocalisation between the CXCR4 receptor and the internalised nanoparticles was observed [186]. Furthermore, while the polymeric plerixafor still resulted in the antagonism of CXCR4 and specific attachment and uptake, its antagonistic efficacy was significantly lower than AMD3100 alone. The polymerisation through the cyclams led to the formation of highly branched polymers, which may have interfered significantly with the cyclams' ability to interact with the CXCR4 receptor. In order to counter this, Oupický and co-workers formulated a new polymer, featuring unhindered individual cyclams that stretched off the main polymer backbone [194]. The new polymer was found to exhibit significant bioactivity, with EC_{50} values for monomers of different attachment chain lengths ranging from

21.3-56.8 ng/mL compared to the EC_{50} of 103 ng/mL for the original polymeric plerixafor in U2OS (osteosarcoma) cells. This illustrates the key role of the cyclams in the attachment of AMD3100 and its derivatives to CXCR4.

Several AMD3100 derivatives have also been synthesised by Poty *et al.* [190, 198] with tethers stretching off the central aromatic ring, which were functionalised with fluorescent and positron emission tomography sensitive moieties. Their derivatives were found to specifically target Jurkat cells, and after chelation with Ni in the cyclams, reached efficacies close to unfunctionalised AMD3100 [190]. Subsequent derivatives were able to target H69 xenografted tumours in animal models, however significant uptake into the liver, spleen, lung, bone marrow and adrenal glands [198].

5.1.3 Synthesis of an AMD3100 analogue - BAT1

In the approach considered here the central aromatic ring was used to attach a molecular tether, illustrated in Figure 5-3; this configuration aimed to reduce any interference with the interaction between the cyclams and their target, so maintaining the binding affinity of the molecule. Polyethylene glycol was chosen as the tether, both due to its biocompatibility and because the previous experiments with GO (Chapter 4) reported in this thesis show that PEG functionalisation provided the least toxic and most stable dispersions. The long-chain tether was designed to allow maximal movement of its functional end, and provide minimal steric interference. A PEG tether of well-defined length with an end primary amine group was chosen in order to allow ease of conjugation to other materials and molecules using EDC chemistry, as used in Chapter 4.

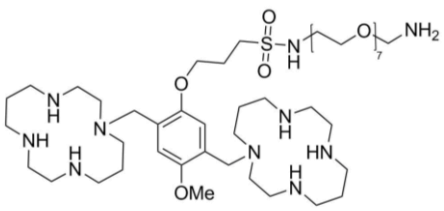

Figure 5-3 - AMD3100 analogue, BAT1

The short PEG chain of defined length was chosen to allow the molecule to be purified chromatographically, which requires molecules of identical structural form.

This chapter describes the synthesis and purification of the molecule, following which the toxicity and bioactivity of the molecule were assessed in primary CLL cells. This system is used as CLL cells are known to overexpress CXCR4 [26, 27] and allows characterisation of binding and bioactivity in a cell that is the most relevant for the desired application of the molecule.

5.2 Aims & Objectives

In this chapter the aim was to synthesise an analogue to the CXCR4 antagonist, AMD3100, that could be attached to graphene oxide flakes to act as a targeting ligand for CLL cells.

Following analysis of AMD3100 it was elected to modify the molecular structure of the drug through the incorporation of a polyethylene glycol chain with primary amine terminus to permit attachment to nanoparticles, including GO, while retaining the active binding site for the receptor.

Following synthesis and structural characterisation, analysis of the bioactivity and toxicity of the molecule alone and following conjugation to a second molecule was performed to assess binding characteristics and ensure specificity was retained.

5.3 Instrumentation

NMR spectra were recorded using a Bruker DPX 400 MHz spectrometer, in $CDCl_3$ or D_2O. Electrospray mass spectrometry was performed using an Agilent 6510 Quadrupole Time-of-Flight LC-MS and analysed using the in-built Agilent MassHunter Workstation software and ACD/Spectrus Processor™. Preparative and analytical high pressure liquid chromatography (HPLC) was performed using the Agilent 1260 Infinity LC with an Agilent ZORBAX Eclipse XDB reverse phase C8 column (150 x 4.6 mm) with a 5 μm particle size. Cells were deposited onto glass microscope slides before immunostaining using the Thermo Scientific™ Cytospin™ 4 Cytocentrifuge and visualisation of immunostained cells was performed using a Zeiss™ Axiovert™ epifluorescent microscope. Flow cytometry was performed as before (Section 4.3.4.7.2). Gel electrophoresis and western blotting equipment was purchased from Bio-Rad™ (UK).

5.4 Materials

5.4.1 Synthesis reagents

3-[2,5-Bis(chloromethyl)-4-methoxyphenoxy]-1-propanesulfonyl chloride, *N,N*-Diisopropylethylamine (99.5% biotech. grade with Sure/Seal™), 2,2,2-Trifluoroethanoic acid and trifluoroacetic anhydride, all deuterated solvents were obtained from Sigma Aldrich® Co. (UK). *N,N*-Dimethylformamide, 99.8% extra dry with AcroSeal, chloroform, petroleum ether, dichloromethane, acetonitrile, methanol, diethyl ether and ethyl acetate (all Analytical Reagent Grade) were obtained from Fisher Scientific.

(2-Aminoethyl)-O'-[2-(Boc-amino)ethyl]hexaethylene glycol was obtained from Polypure AS, Norway and tri-tert-butyl 1,4,8,11-tetraazacyclotetradecane-1,4,8-tricarboxylate was purchased from CheMatech, France.

5.4.2 Cell culture materials

Basic cell culture materials are as listed in Chapter 4, Section 4.3.1.1.

Primary human CLL cells used were held in frozen store following collection from patients with full REC approval for use in evaluation of new treatment strategies (REC reference 10/H1017/73). All samples had been collected with full consent for research use and are stored in pseudo-anonymised form with identity traced only through the collecting medical institution (Manchester Royal Infirmary, custodian Dr John Burthem). There are no direct or indirect medical implications for donors.

Phosphate buffered saline (PBS) and tris buffered saline (TBS) were purchased as tablets from Sigma Aldrich , UK, and dissolved in ddH_2O as suggested by the manufacturer.

Recombinant Human/Rhesus Macaque/Feline CXCL12 (carrier free), Mouse Anti-Human CXCR4 PE-conjugated Monoclonal Antibody (Clone #44717) and 1,1'-[1,4-Phenylenebis-(methylene)]-bis-(1,4,8,11-tetraazacyclotetradecane) octahydrochloride (AMD3100) were all purchased from R&D Systems® (UK). ProLong®Gold Antifade mountant with DAPI nucleic acid stain was purchased from ThermoFisher™ (UK). Rabbit Anti-Human CXCR4 [UMB2] Monoclonal Antibody was purchased from Abcam PLC (UK). p44/42 MAPK (Erk1/2) Antibody #9102 and Phospho-p44/42 MAPK (Erk1/2) (Thr202/Tyr204) Antibody #9101 for western blotting were purchased from Cell Signaling Technology®, Inc. (USA). Precision Plus Protein Standards Kaleidoscope loading marker was purchased from Bio-Rad™ (UK), Amersham ECL Prime western blotting detection reagent was purchased from GE Healthcare Life Sciences (UK).

5.4.2.1 Buffers

5.4.2.1.1 RIPA buffer

RIPA buffer was prepared as follows: Tris(hydroxymethyl)aminomethane (TRIS base) 50 mM, NaCl 150 mM, Triton-X-100 1% v/v, sodium deoxycholate monohydrate 0.275% w/v,

Ethylenediaminetetraacetic acid (EDTA) 1 mM, made up to volume with deionised water and adjusted to pH 7.4.

5.4.2.1.2 Laemmili buffer

Laemmili buffer was prepared as follows: sodium lauryl sulphate (SDS) 4% v/v, glycerol 20% v/v, tris(hydroxymethyl)aminomethane hydrochloride (TRIS HCl) 0.125 M, bromophenol blue 0.1% v/v; this can be made in advance with deionised water and kept at 4°C, allowing enough volume for 5% 2-mercaptoethanol to be added directly before use. pH 6.8.

5.4.2.1.3 Transfer buffer

For 1 L transfer buffer, the following was prepared: 100 mL 10X running buffer, 200 mL 100% methanol, 700 mL water were mixed thoroughly and stored at 2-4°C, and brought out for use when needed.

5.4.2.1.4 Running buffer

For 1 L 1X running buffer, the following was prepared: 3.02 g TRIS HCl (24 mM final concentration), 14.4 g glycine (191 mM final concentration), 1 g SDS (0.1% (w/v) final concentration) and the volume was made up to 1 L with ddH_2O and mixed well. The buffer could be stored at 2-4°C, and brought out for use when needed.

5.4.2.2 Gels

5.4.2.2.1 10% SDS-PAGE resolving gel

For 10 mL (enough for 2 gels with 0.75 mm spacer), the 10% SDS-PAGE resolving gel was prepared as follows: 3.3 mL 30% (v/v) acrylamide, 2.5 mL 1.5 M TRIS base at pH 8.8 (final concentration 375 mM), 4 mL water, 100 µL 10% (w/v) sodium dodecyl sulphate (SDS) are mixed well. The polymerising agents – 100 µL 10% (v/v) ammonium persulfate and 6.6 µL tetramethylethylenediamine (TEMED) should be added just before the gel is poured, after mixing well.

To prepare the gels, the gel plates were first assembled into a casting rack and the gel was poured to a level just below the comb-length and overlayed with ddH_2O to ensure that the gel set straight. The gel was then left to polymerise for 30 mins, or until set, and the water layer poured away to allow room for the stacking gel.

5.4.2.2.2 4% SDS-PAGE stacking gel

For 5 mL (enough for 2 gels with 0.75 mL spacer), the 4% SDS-PAGE stacking gel is prepared as follows: 0.675 mL 30% (v/v) acrylamide, 1.25 mL 0.5 M TRIS HCl at pH 6.8 (final concentration 125 mM), 3.075 mL water, 50 µL 10% (w/v) SDS are mixed well. The polymerising agents – 25 µL 10% ammonium persulfate and 5µL TEMED are added just before the gel is poured, after mixing well.

Stacking gel was poured on top of the set resolving gel in the assembled gel plates and the combs put in place. The gel was then left for 30 mins maximum to set before removing the comb.

5.4.2.3 Western Blotting materials

Polyvinylidene difluoride (PVDF) membrane and Whatman® 3MM blotting paper were purchased from Fisher Scientific (UK). All equipment necessary to perform western blotting was purchased from Bio-Rad™ (UK).

5.5 Methods

5.5.1 Synthesis

Synthesis was performed in three steps, as shown below. The numbers in bold codify the molecules used, for ease of reference.

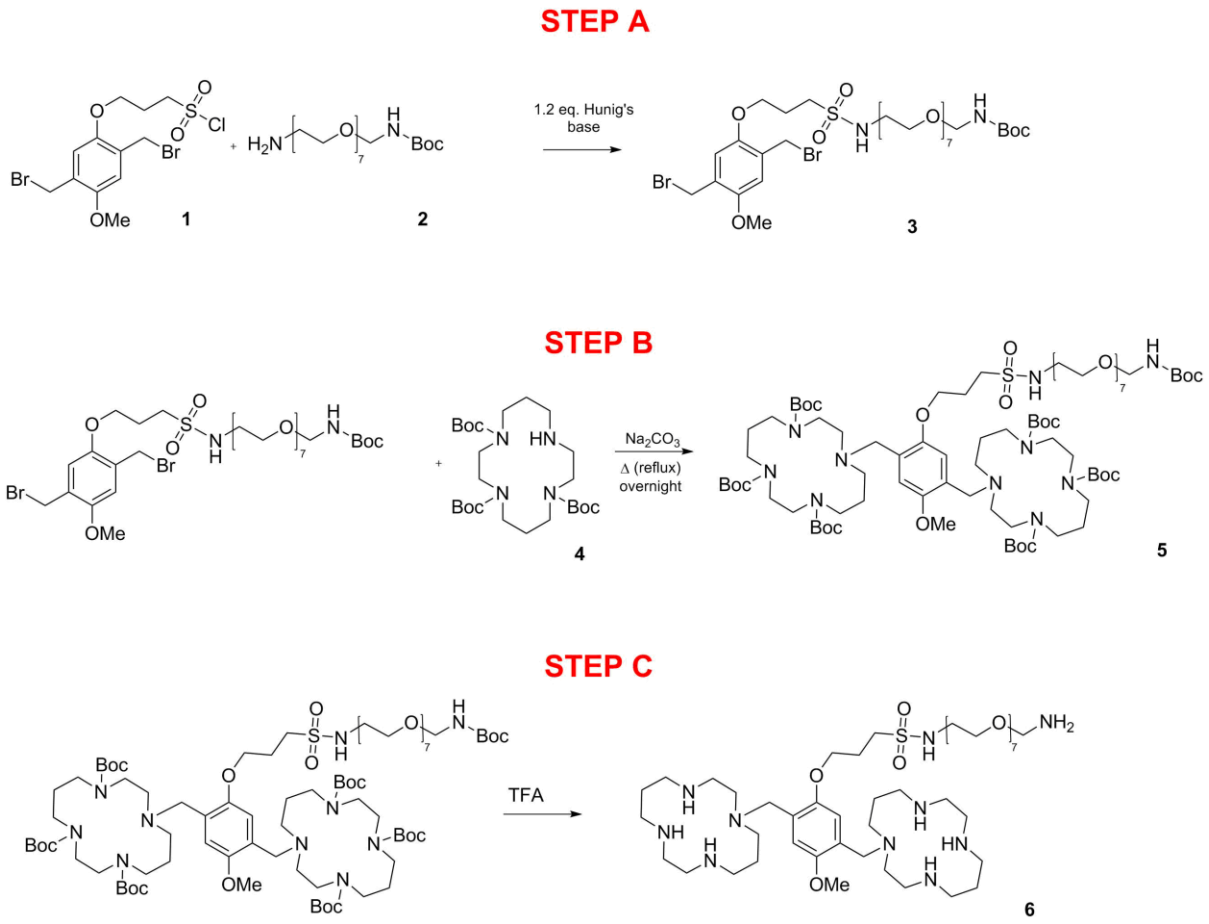

Schema 1 - Synthesis steps for BAT1

5.5.1.1 Step A - synthesis of molecule 3

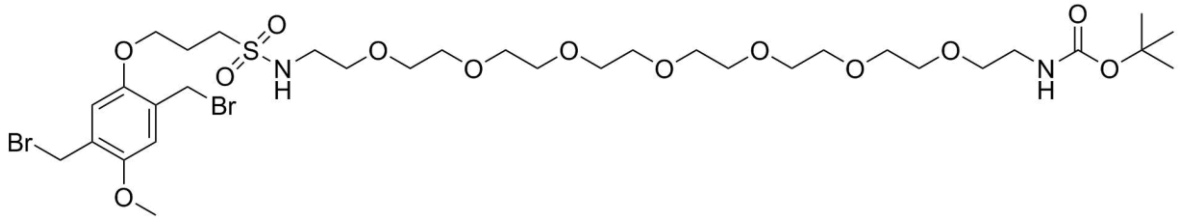

Figure 5-4 - Molecule 3 - result of synthesis step A

3-[2,5-Bis(bromomethyl)-4-methoxyphenoxy]-1-propanesulfonyl chloride (231 mg, 0.51mmols), O-(2-Aminoethyl)-O'-[2-(Boc-amino)ethyl]hexaethylene glycol (200 mg, 0.43 mmols), N,N-Diisopropylethylamine (DIPEA) (71 µL, 0.51 mmols) were added to dry N,N-Dimethylformamide (DMF) under inert conditions and the reaction was stirred under nitrogen for 48 h. The DMF and DIPEA were removed under reduced pressure using a rotary evaporator. The crude mixture was re-dissolved in chloroform and purified using flash column chromatography (10% (v/v) methanol in chloroform on silica), giving **3** as a yellow oil. R_f: 0.78 (10% (v/v) methanol in chloroform on silica). **Molecule 3** molecular weight: 882.7

5.5.1.2 Step B - synthesis of molecule 5

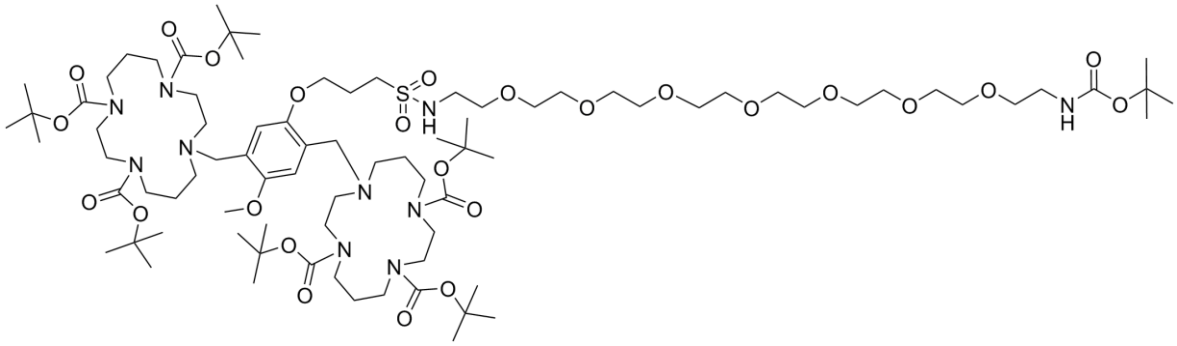

Figure 5-5 - Molecule 5, result of synthesis step B

Molecule **3** (50 mg, 56 µmols) and tri-tert-butyl 1,4,8,11-tetraazacyclotetradecane-1,4,8-tricarboxylate (67 mg, 134.4 µmols) were added to dry acetonitrile with sodium carbonate (12 mg, 112 µmols) and left stirring for 48 h under reflux. The reaction mixture was filtered using fluted filter paper to remove the sodium carbonate and the solvent was removed under reduced pressure using a rotary evaporator. The crude mixture was re-dissolved in ethyl acetate and purified using flash column chromatography (100% ethyl acetate (1.5 column lengths); 100% petroleum ether (1 column length); 5% (v/v) petroleum ether in ethanol (2 column lengths); 100 % petroleum ether (2 column lengths) on silica). The product was further purified using HPLC as described in Table 5-1. **Molecule 5** molecular weight: 1722.23

Table 5-1 - HPLC gradient for purification of molecule 5

Sample	Column	Eluent	Solvent B	Time (minutes)
Molecule **5**	C8 reverse phase	Solvent A: 0.1% (v/v) acetic acid in water Solvent B: 0.1% (v/v) acetic acid in acetonitrile	20%-40%	5
			40%-50%	40
			50%-100%	50
			100%	60

5.5.1.3 Step C - synthesis of molecule 6

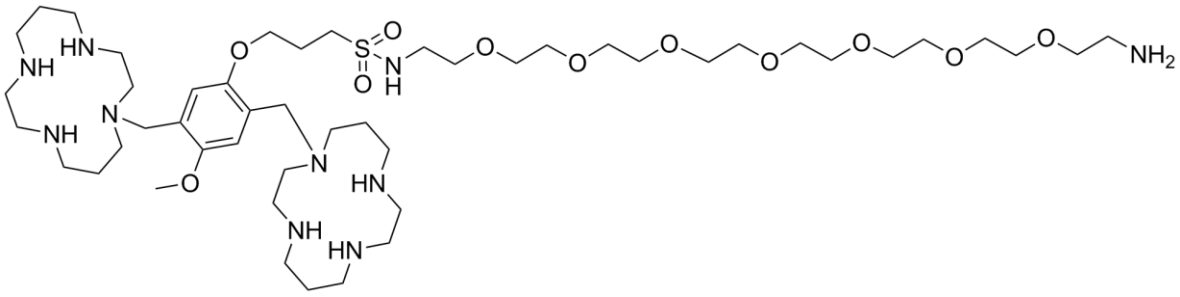

Figure 5-6 - Molecule 6 - or BAT1 - result of synthesis step C

Residual water was removed from 2,2,2-Trifluoroethanoic acid (TFA) by mixing 26 mmols TFA in 10 mL dry dichloromethane (DCM) and adding 7.1 µmols trifluoroacetic anhydride dropwise, stirring at 0 °C. The mixture was left stirring under inert conditions for 10 minutes. Molecule **5** was dissolved in dry DCM and added slowly to the TFA mixture, stirring, with the temperature retained at 0 °C and under inert conditions, before allowing the mixture to return slowly to room temperature (RT). The mixture was left stirring for 4 h, the DCM and residual TFA were removed under reduced pressure using a rotary evaporator. This reaction produces CO_2, therefore a partially inflated balloon was used to reduce back-pressure. To remove TFA salt, the product was further co-evaporated with ethoxyethane approximately 7 times. The final product was extracted with water and lyophilised, to give 5 mg final product. **Molecule 6** molecular weight: 1021.42

5.5.1.4 Fluorescent moiety attachment

Initial attachment experiments were carried out using Cyanine 5-NHS mono-reactive ester (Cy5-NHS ester), chosen for its ease of attachment to the primary amine terminus on the PEG tether of BAT1 and its ease of detection using flow cytometry.

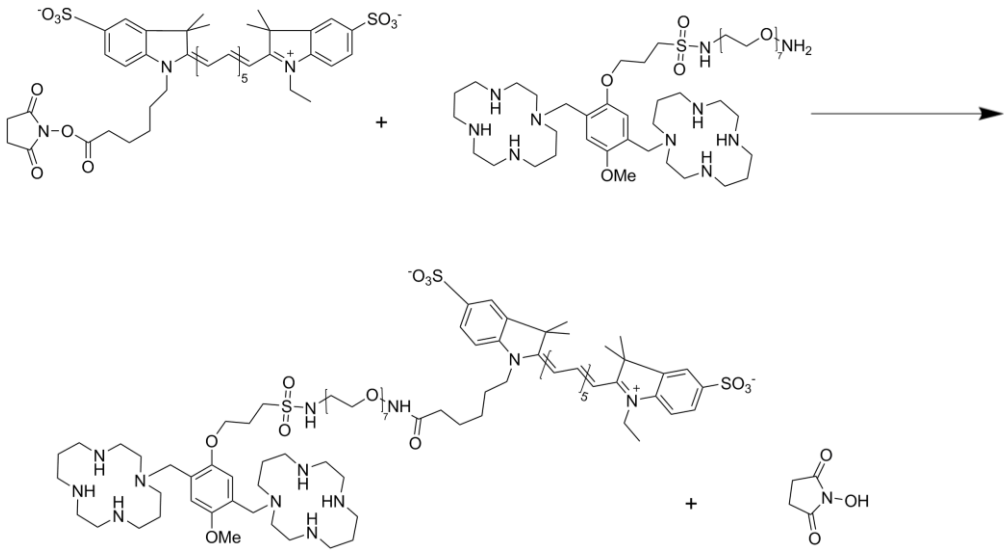

Figure 5-7 - Reaction procedure for BAT1/Cy5 conjugation

One molar equivalent of the Cy5-NHS ester was added to 1 mL of a 3 mM solution of BAT1 in PBS at pH 7.4. The mixture was left stirring overnight at RT, following which it was stored at -20 ^{o}C until needed. For control experiments the Cy5-NHS ester was left alone in PBS for 24 h, during which the NHS ester would be expected to hydrolyse, leaving a non-functional fluorescent molecule (Cy5). Throughout, both the Cy-5-BAT1 conjugate and the Cy5 alone were protected from light to reduce photobleaching.

5.5.2 Cell culture

5.5.2.1 Cryopreserved CLL samples

Samples of primary CLL cells in RPMI 1640 (Sigma Aldrich, UK) supplemented with 10% foetal calf serum (FCS), 1% l-glutamine, 1% penicillin streptomycin (complete media) (all ThermoFisher, UK) with a further 30% FCS and 10% dimethyl sulfoxide (DMSO), stored in liquid nitrogen were brought rapidly to room temperature. The cells were then washed by adding 10 mL RPMI complete media at 37°C dropwise; cells were then pelleted by centrifuging at 1400 rpm for 10 minutes. The supernatant was discarded and a volume of fresh media at 37°C was added to produce the cell density desired. Cells were cultured in an incubator at 37° with 5% CO_2, and both treated and harvested at the time points described for the respective experiments.

5.5.2.2 Flow cytometric analysis of CXCR4 expression and downregulation

Stock solutions of BAT1 and AMD3100 were prepared to give final concentrations of both molecules ranging from 2 nM – 20 µM, as shown in Table 5-2.

Table 5-2 - Concentrations of AMD3100 and BAT1 used for the assessment of potency against primary CLL cells

Stock concentrations	0.3 µM	3 µM	30 µM	300 µM	3 mM
Final concentrations	2 nM	20 nM	200 nM	2 µM	20 µM

Cells were plated at a density of $2x10^6$ cells/mL in a 96 well plate, and cultured for 24 h before incubation with AMD3100, BAT1, 200 ng CXCL12 (positive control) or PBS (negative control) for 3 h. 250 µL cells were then harvested from culture; cells that had become lightly adhered to the multiwell plate were resuspended by gently aspirating the media using a pipette. The cells were then transferred to a flow cytometry tube (Corning™ Falcon™, product #352054, Fisher Scientific, UK), which was kept on ice, and a PE-conjugated CXCR4 monoclonal antibody (Clone 44717, R&D Systems, UK) was added directly to the suspension at a concentration specified by the manufacturer. The cells were incubated with the anti-CXCR4 mAb for 15 minutes (on ice and

protected from light), prior to fixing with paraformaldehyde in TBS (final concentration 2%) for 15 minutes (on ice and protected from light). The cells were analysed using a BD FACSCanto II™ flow cytometer; for each sample the data for 10000 events was recorded. The PE-conjugated antibody was excited by a laser with a wavelength of 488 nm. The data recorded excluded debris by gating out the events with the lowest forward scatter; live and dead cells were separated by gating the populations based upon their forward and side scatter, in a manner described in Chapter 4, Section 4.3.4.7.2 for PBMCs.

The cell populations present in a CLL case are very different to those of a healthy PBMC donor, as the majority (> 90%) of the cells in a white blood cell population harvested from a CLL patient are expected to be B-cells. Therefore staining of the cell populations and regating was performed to confirm the cell populations present and their FSC/SSC profiles. Two CLL cases were stained using antibodies targeting the CD3 (T cells), CD14 (monocytes) and CD19 (B cells) receptors with forward and side scatter profiles used for gating purposes. Note that CD19 is expressed far more weakly on CLL cells than PBMCs, making a distinct population more difficult to observe [203]; however, the morphology is expected to be very similar to PBMCs, hence the gating region determined for PBMCs was used for the CLL samples. Examples shown in Figure 5-9 are for CLL7 (which was the case used throughout this Chapter) and Figure 5-8 are for CLL6, which presents a more mixed population.

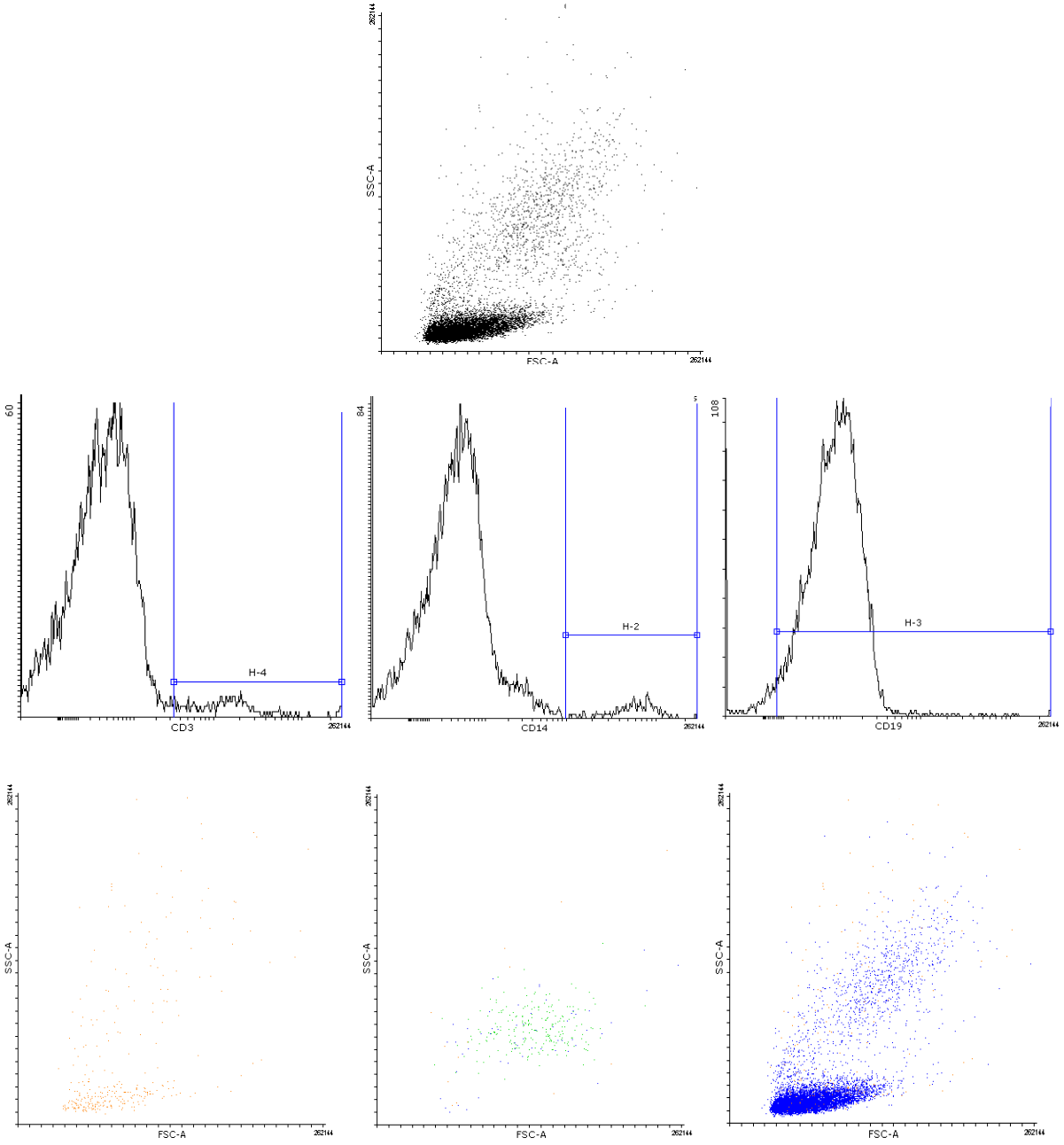

Figure 5-8 - Flow cytometric gating using antibody fluorescence to separate different white cell populations in a primary CLL culture. CLL6 case gated for CD3 (orange), CD14 (green) and CD19 (blue) respectively. This shows how the cell populations can vary between cases, but the majority of the cells are still B-cells. CD19 expression is lower on CLL B-cells than healthy B-cells (Ginaldi *et al.*[203]), as shown by the low fluorescence peak relative to the CD3 and CD14 staining.

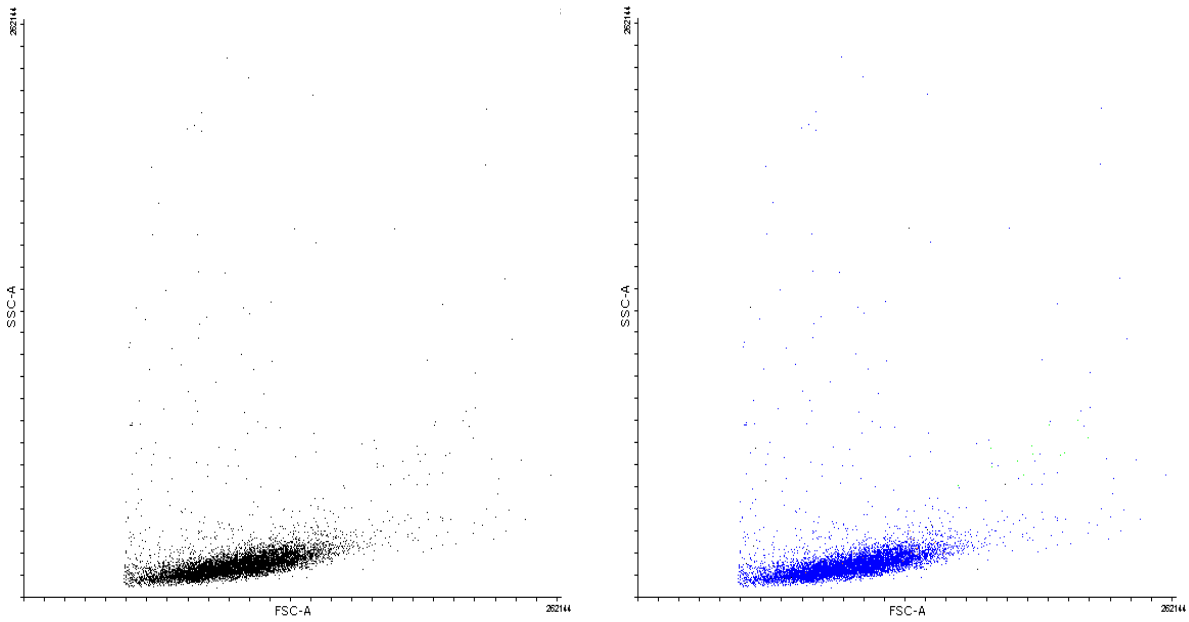

Figure 5-9 - FSC/SSC plots for CLL 7 day 0. Left- gated to remove debris, but without any gating for CD3, CD14 or CD19 expression. Right – the same FSC/SSC plot gated for CD3 (orange), CD14 (green) CD19 (blue). Shows that the majority of the cells present are B-cells.

All data were recorded using BD FACSDiva™ and analysed using Flowing Software 2.5.1.

5.5.2.3 Assay of CXCL12 signalling inhibition for Western Blot

Cells were plated at a density of $1x10^7$ cells/mL in a 12 well plate. After treatment with the relevant inhibitor for 3 h, as described in the previous section (5.5.2.2), 200 ng/mL CXCL12 (recombinant human/Rhesus Macaque/Feline, CF; R&D Systems) was added to each sample (except controls), incubated for 5 minutes, then put on ice. Cell suspensions were washed twice by centrifuging at 16000 RPM for 30 s and resuspending in ice cold PBS. Cells were again pelleted and the supernatant was discarded to obtain a dry pellet; RIPA buffer was added directly to the pellet to lyse the cells, and the pellet was resuspended by aspirating with a pipette. Suspensions were kept on ice for at least 10 minutes. Cell suspensions were then centrifuged as before to remove insoluble proteins and the supernatant was retained. An equal volume of 2X Laemmli

buffer with 5% 2-mercaptoethanol was added to the extracted protein and samples were heated to 95^{0}C for 5 min, before loading into the gel electrophoresis wells.

5.5.3 Western Blot

5.5.3.1 Gel electrophoresis

2-20 µg of protein from cell lysis in a maximum of 20 µL loading dye (2x Laemmli buffer with bromophenol blue and 5% β-mercaptoethanol) was heated at 95°C for 5 minutes. Meanwhile, the gels were placed into the gel tank and running buffer was poured into the centre and around the gel plate assembly. Protein samples were then loaded into each of the wells, with a protein molecular weight ladder (Precision Plus Protein standards Kaleidoscope, Bio-Rad™) in the end well. The gel was run at 150 V until the dye line was seen to reach the bottom of the gel.

5.5.3.2 Blotting

Polyvinylidene difluoride (PVDF) membrane was cut to size and pre-wet in methanol for 30 s, before washing in ddH_2O for 5 min, then the PVDF membrane, Whatman® 3MM blotting paper, gel from the electrophoresis procedure and gauze pads were all equilibrated in transfer buffer for 15 min. The blotting stack was then assembled as shown in Figure 5-10, ensuring no bubbles were present between the gel and the membrane.

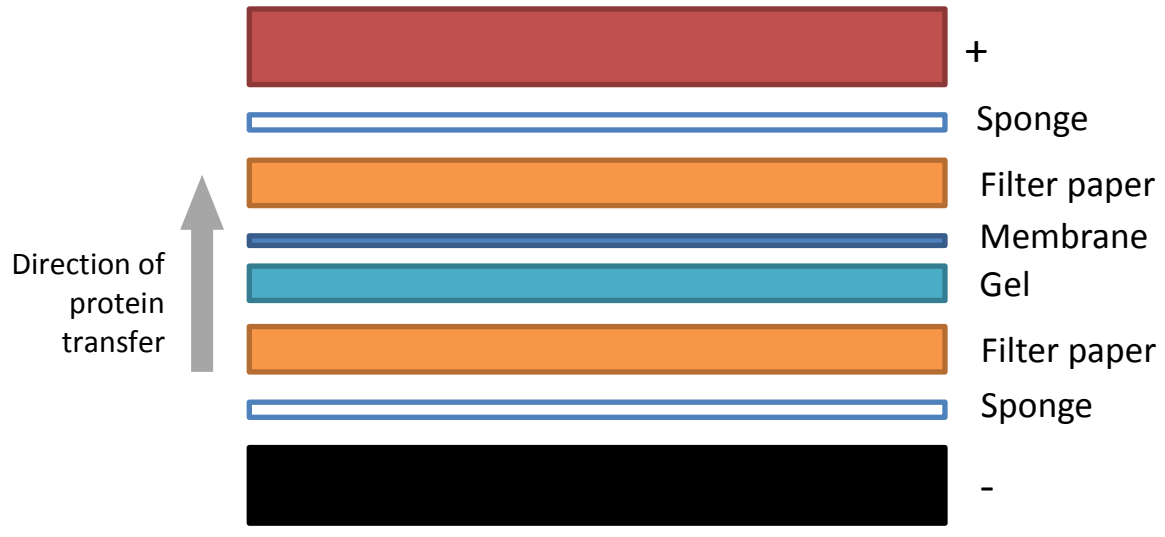

Figure 5-10 – Western blot membrane transfer apparatus

The stack was then transferred to the western blotting tank with a cooler unit, a magnetic stirrer bar added, and the tank filled with transfer buffer. The transfer was undertaken at 250 mA for 75 min while stirring and the success of the protein transfer checked by inspecting the migration of the pre-stained markers onto the PVDF membrane.

5.5.3.3 Antibody hybridisation

After the blotting step, the PVDF membrane was washed in a western box in 1x PBS and 0.1% (v/v) Tween-20 1x (PBS/T) for 5 min on a rocker. The membrane was then transferred into 10 mL of blocking buffer (1x PBS/T with 5% (v/v) BSA) and blocked for at least 1 h at RT on a rocker, after which it was washed in 1X PBS/T. The antibody was diluted to 1 in 1000 in 1 mL primary antibody dilution buffer (1X PBS/T with 3% (v/v) BSA) and pipetted onto saran wrap. . The membrane was then placed protein-side down onto the area containing the diluted antibody, ensuring no air bubbles were present, then covered while the membrane was incubated at RT on a rocker for 1 h or overnight at 4^0C. After incubation, the membrane was washed 3 times in 1x PBS/T (5 min per wash). The HRP-conjugated secondary antibody was diluted 1:10,000 in a volume sufficient to cover the membrane in the western box and incubated on a rocker for 1hr min, after which, the membrane was washed 3 times in 1x PBS/T (5 min per wash). For detection excess liquid was drained and the membrane was placed protein-side up on a sheet of plastic wrap. The luminescent reagent (ECL- GE Healthcare) was pipetted over the membrane at a dilution of 1:1 and incubated at RT for 1 min, after which the membrane was again drained and placed inside a plastic wallet for imaging. The Chemidoc XRS molecular imager (Bio-Rad™) was used for detection purposes.

5.5.4 Immunofluorescence

For dual CXCR4 staining, CLL cells cultured at $2x10^6$ cells/mL and treated with BAT1, AMD3100 or the appropriate blank in Corning® 96 well plates were extracted into microcentrifuge tubes and

stained with 5 µL mouse anti-human CXCR4 phycoerythrin-conjugated monoclonal antibody (Clone 44717) (R&D Systems Europe Ltd) for 30 minutes on ice; the cell suspension was then washed by centrifuging at 10000 rpm, discarding the supernatant and resuspending in cold RPMI complete. An antimouse secondary antibody stain was then added to the cell suspension at a dilution of 1:99, and incubated for a further 30 minutes on ice. The cell suspensions were then washed again as before and diluted to $1x10^6$ cells/mL. The cells were then deposited onto glass microscope slides using the Cytospin™ 4 Cytocentrifuge by aliquoting 100 µL of the cell suspension ($1x10^5$ cells) into the cytofunnels and centrifuging at 300 rpm for 10 minutes. Slides were air-dried overnight. Where cells were not being dual CXCR4 stained, they were diluted and spun onto the slides directly, at the same density as above, and air-dried overnight.

Prepared slides were fixed in 4% w/v paraformaldehyde for 15 minutes, and then washed twice for 7 minutes using TBS in a slide chamber. Cells were permeabilised using 0.2% v/v Triton-X-100 in TBS solution for 5 minutes and then washed as before, and blocked using 1% w/v BSA in TBS for 1 h. Slides were washed and the primary antibody applied at a dilution of 1 in 250 for 1 h. Slides were washed in TBS for 5 minutes in a slide chamber, and then incubated with the relevant species of secondary antibody. Slides were washed as before and left to air-dry, before mounting using ThermoFisher™ ProLong® Gold Antifade mountant with DAPI nucleic acid stain. Slides were then left to set for another 30 minutes before visualising on a Zeiss™ epifluorescence microscope.

5.6 Results

5.6.1 Synthesis

In order to prepare BAT1, a three step synthesis was devised. **Molecule 1** (3-[2,5-Bis(bromomethyl)-4-methoxyphenoxy]-1-propanesulfonyl chloride) was chosen as the sulfonyl chloride group could be easily converted to a sulphonamide by nucleophilic substitution to produce **molecule 3** and the bromine arms allowed us to follow the route devised by Guillaume *et al.* [204] to attach the cyclams (**5**). Finally the *tert*-butyloxycarbonyl (boc) protecting groups

would be removed using trifluoroacetic acid (TFA), in an approach commonly used in peptide synthesis to afford **molecule 6** (BAT1). The full synthesis is shown in Schema 1, Section 5.5.1.

5.6.1.1 Step A

5.6.1.1.1 Synthesis characteristics

Due to the presence of the strong leaving group, chlorine, sulfonyl chlorides are easily hydrolysed in the presence of water or any other nucleophilic molecules, therefore this reaction step was performed under nitrogen. The solubility of **molecule 1** in appropriate (aprotic, non-nucleophilic and dry) solvents was also found to be problematic. When dry, the reagent presented as an off-white powder, with hard clumps. The only non-nucleophilic solvent in which it was sparingly soluble was DMF, and this was initially aided by sonication. Low initial yields were initially thought to be due to this poor solubility, however when repeated several times it became apparent that the compounds were polymerising by non-nucleophilic substitution at the bromine positions; yields decreased further and visible polymerisation occurred upon addition of the DIPEA. It is thought that this was due to the degradation of the DMF into highly nucleophilic molecules [205]. The polymerisation process was then catalysed by the addition of the strong base DIPEA *via* a radical mechanism known as Gilch polymerisation [206], illustrated in Figure 5-11.

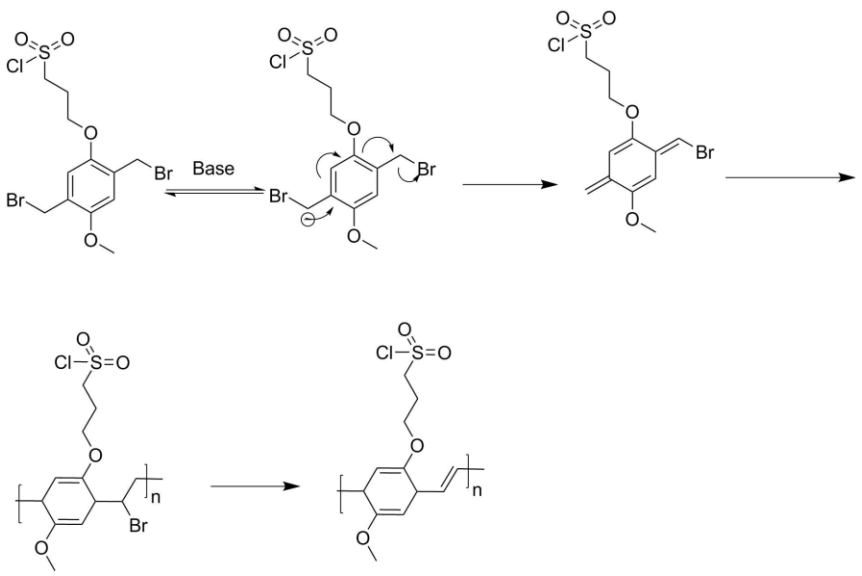

Figure 5-11 – Schematic representation of the Gilch polymerisation of molecule 1

Dry DMF was subsequently used and stored under inert conditions in the presence of molecular sieves. The reaction was prepared in a glove box, and took place in the presence of fine 3 Å molecular sieves. It has also been reported that DMF may degrade at elevated temperatures [207] – which may occur during sonication; therefore this technique was no longer used, and the larger clumps of **1** were ground using a pestle and mortar in the glove box before addition to the reaction mixture. **Molecule 3** was obtained and purified *via* flash column chromatography.

Despite the alterations to the synthesis method, the yields of the purified compound remained low (27%). Following a review of the literature, it was realised that the use of silica in the stationary phase and a chloroform:methanol mixture in the mobile phase during purification may also have caused polymerisation of **molecule 3**. If repeated in future the purification would be carried out using a neutral stationary phase such as alumina, and an alternative mobile phase that does not include any polar solvents.

5.6.1.1.2 NMR

Following purification, the fraction thought to contain **molecule 3** was characterised using NMR and mass spectrometry. Both chlorine and bromine are strong leaving groups, hence there was concern that substitution onto one of the bromine arms instead of the sulfonyl chloride group may occur, and that in this circumstance the chromatographic properties of the molecule could be similar to that of **molecule 3**.

Characterisation by NMR was able to provide information on the isolated molecule regarding its structure. For instance, the ratios of characteristic groups of **molecule 1** and **molecule 2** confirmed that **molecule 3** had been isolated from any starting materials or side products. With regards to the molecule structure, both the positions and the splitting patterns of the peaks indicated that the covalent bonds had been formed in the areas expected.

The NMR spectrum is shown in Figure 5-12, with the peak assignments listed in the box below. Importantly, by analysing the peaks associated with the PEG region (chemical shift at 3.61-3.66 for the majority of the chain) and the aromatic region defined by the aromatic positions of 1 and 4 (chemical shift of 6.94-6.87), the integration of indicated a 1:1 adduct of the **molecule 1** and **molecule 2**. This relationship also held for the (-CH_2Br) moieties, defined by positions 7 and 9 (chemical shifts of 4.52-.4.54 and 4.62-4.63).

In addition, the peak associated with the position labelled 15 on **molecule 3** (shown in Figure 5-12) has moved upfield compared to the chemical shift of the same position in **molecule 1**. This indicates that the protons in the CH_2 group at that position are experiencing the incident magnetic field less strongly [208], and therefore are more shielded by the electron cloud than the same hydrogens in the starting material. This would occur if a less electronegative atom were present in the neighbouring molecules than was present initially [208], as would be the case with the departure of the chlorine and its replacement with a nitrogen. The covalent bonding of the primary amine on **molecule 2** following substitution of the sulfonyl chloride (position 19) is confirmed by its shift significantly downfield to 5.28 ppm; whereas the protons on a primary amine are very labile, and therefore likely to be highly shielded and often very difficult to see, the reaction with the sulfonyl chloride leads to a significant deshielding by the two oxygens in the newly formed sulphonamide.

^{1}H NMR: (400 MHZ, $CDCl_3$, 25 °C): δ = 6.94-6.87 (m, 2H), 5.28 (m, 1H), 5.08 (s, 1H), 4.62-4.63 (dd, 2H, J = 3.1 Hz), 4.52-4.54 (dd, 2H, J = 3.1, 2.3 Hz), 4.14-4.17 (m, 2H), 3.86-3.88 (dd, 3H, J = 6.8 Hz, 2.6 Hz), 3.61-3.66 (m, 26H), 3.53-3.56 (t, 2H, J = 5 Hz), 3.30-3.37 (m, 6H), 2.32-2.40 (m, 2H), 1.45 (s, 9H). **MS** (ES^+): m/z 882.8 [M].

Figure 5-12 - Assigned NMR spectrum for molecule 3

The splitting patterns of the most important peaks were also investigated. The peak assigned to position 19 forms a broad triplet (shown in Figure 5-13b), indicating its coupling with the two protons present at position 20; if it had bound instead to the (-CH2) moiety present on the aromatic ring, the amine would be adjacent to two sets of protons, each set in a different chemical environment, and the splitting would be that of a triplet of triplets.

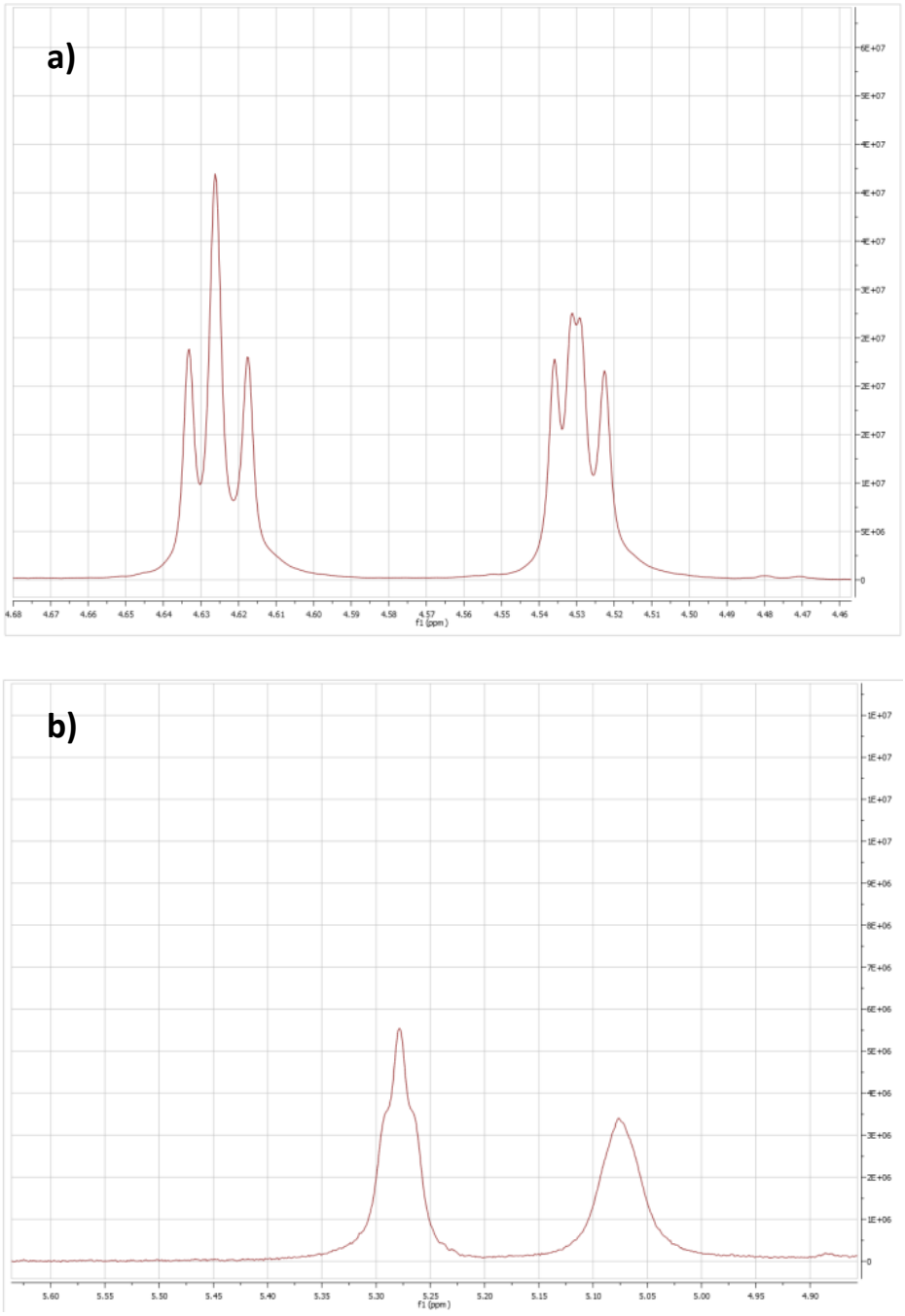

Figure 5-13 – Detail on some of the peak splitting for molecule 3 a) Peaks for positions 7 and 9 on molecule 3. Showing what initially looks like a triplet splitting, but the additional feature visible in the central peak on the peak associated with 9 shows that it is actually an unresolved doublet of doublets. b) Peaks assigned to positions 19 and 43. The broad triplet splitting on the peak assigned to 19 due to coupling with position 20.

The protons at positions 7 and 9 split into doublets of doublets – unresolved in the case of position 7, but weakly resolved for 9 – which demonstrates their coupling with positions 1 and 4, facilitated by the π-bonding orbital of the aromatic ring. Again, this leads to the conclusion that

the bromines could not have been substituted, otherwise a far more complicated splitting pattern would be observed.

Some additional sharp peaks are observed in the spectrum that are not associated with the structure of **molecule 3**. These were identified as residual DMF and chloroform [209].

5.6.1.1.3 Mass Spectrum

Following analysis with NMR, a mass spectrum was taken of the purified fraction; initially the spectrum appeared to present a fraction that was highly impure. Additional interrogation of the masses present and their isotopic fingerprints (listed in Table 5-3) revealed that there were in fact three highly similar molecules (named **molecule 3, 3i** and **3ii**) present in the fraction – in which the bromines on the arms of the molecule had been either singly or doubly substituted with chlorines, illustrated in Figure 5-16. The mechanism of the single and double chlorine substitution is illustrated in Figure 5-15; the nucleophilic substitution of the sulfonyl chloride on **molecule 1** in synthesis step A leads to the formation of HCl, which remains present as the reaction proceeds. As bromine is a stronger leaving group than chlorine, the substitution of bromine with chlorine is energetically favourable.

This is a variation in the structure that would not be easily detectable by NMR. In addition, the chemical similarity of the three molecules would make it likely that they would not be separated in the purification steps.

While this impurity may appear concerning, the chemical similarity of chlorine and bromine means that synthesis Step B can also proceed with **molecule 3i** and **molecule 3ii**. Both chlorine and bromine are strong leaving groups, therefore the nucleophilic substitution in Step B can still proceed – although it may be slower as it is not as strong a leaving group.

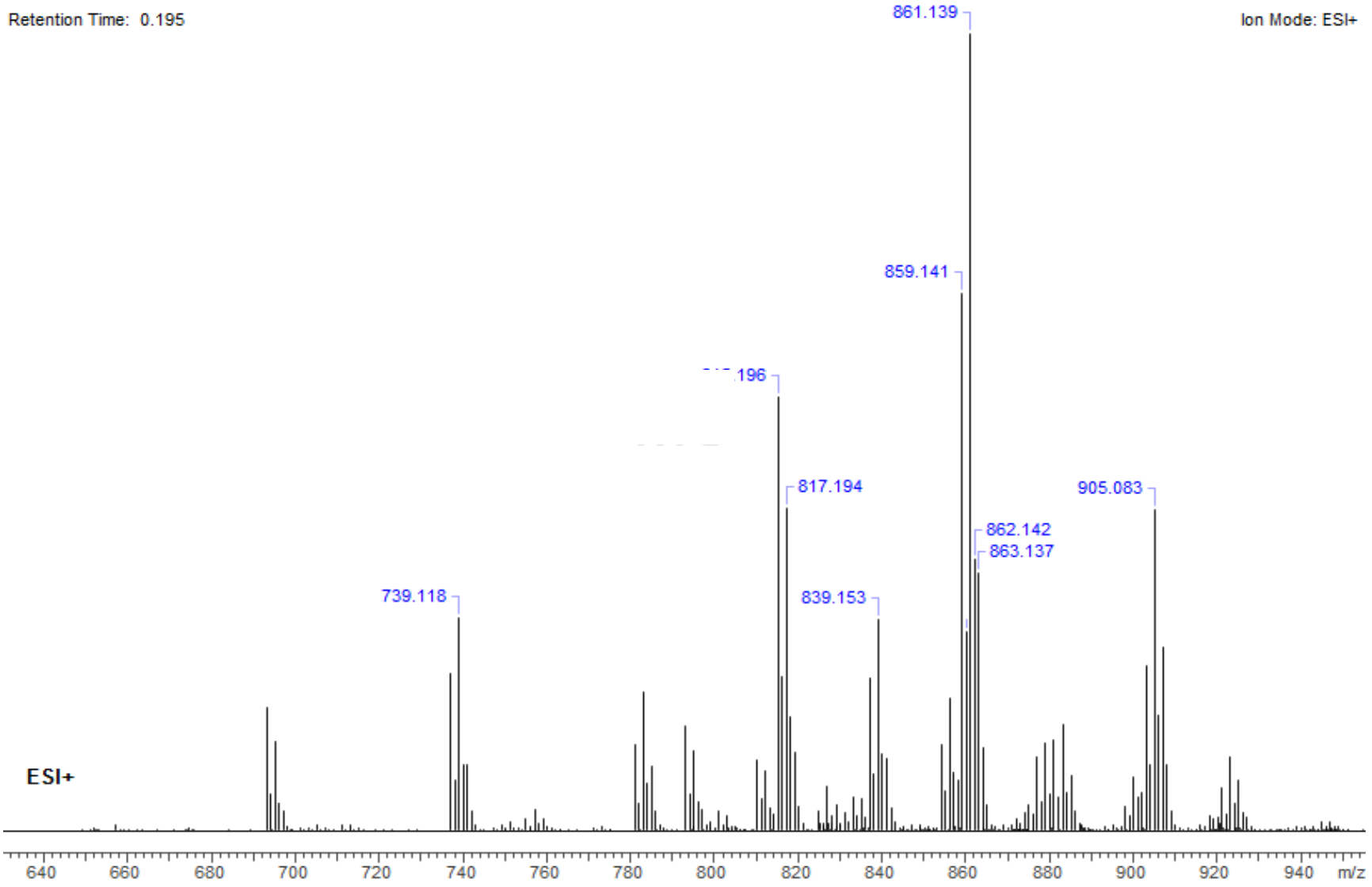

Figure 5-14 - Mass spectrum of purified fraction of molecule 3, indicating the presence of multiple chemical species.

Molecule 3

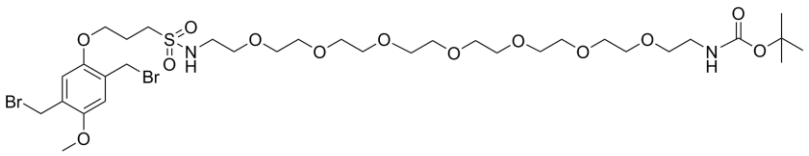

Molecule 3i

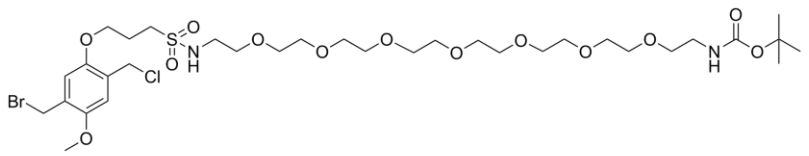

Molecule 3ii

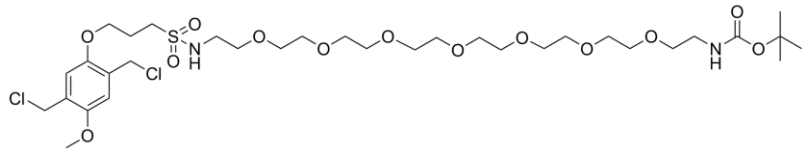

Figure 5-16 - The molecular structure of the three molecules present in the purified fraction, with molecule 3i and 3ii presenting single and double chlorine substitution on the bromine arms

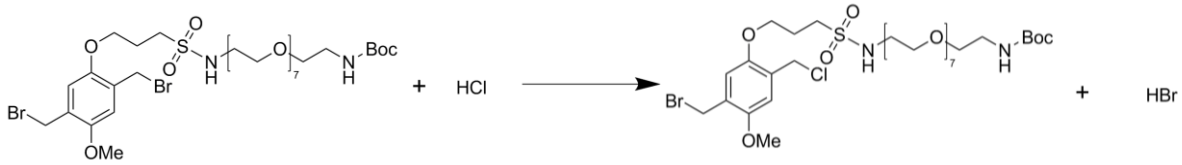

Figure 5-15 - Reaction mechanism for the single substitution of a bromine arm to afford molecule 3i. The same mechanism causes the double substitution

Table 5-1 - m/z peaks observed in the MS attributed to molecules 3, 3i and 3ii with the respective adducts attached. Peak attributation confirmed through isotopic fingerprint. Fragmentation products also observed but not listed

Compound	m/z	Adduct
Molecule 3	883.097	H^+
	905.083	Na^+
	923.046	Nb^+
Molecule 3i	837.156	H^+
	859.141	Na^+
Molecule 3ii	793.210	H^+
	815.196	Na^+

5.6.1.2 Step B

The fraction that included **molecules 3-3ii** was then reacted with tri-boc protected cyclams, in a method similar to that presented by Guillaume & Marshall [204]. The reaction was undertaken in in a dry solvent under an inert atmosphere to reduce the risk of either hydrolysis of the halogen arms or the polymerisation observed in Step A; an excess of $NaCO_3$ was used to deprotonate the free cyclam amine and facilitate the nucleophilic substitution of the halogen arms of **molecules 3-3ii**. The reaction was kept under observation using thin layer chromatography (TLC) to assess the point at which the reaction had reached completion, at which point the reaction mixture was filtered and the solvent removed by evaporation under reduced pressure.

5.6.1.2.1 HPLC purification

Purification both of **molecule 3-3ii** and **molecule 5** proved difficult due to the presence of the PEG chain, which causes streaking, resulting in the overlapping of fractions in the column. Initial purification after synthesis Step B was undertaken using flash column chromatography, however

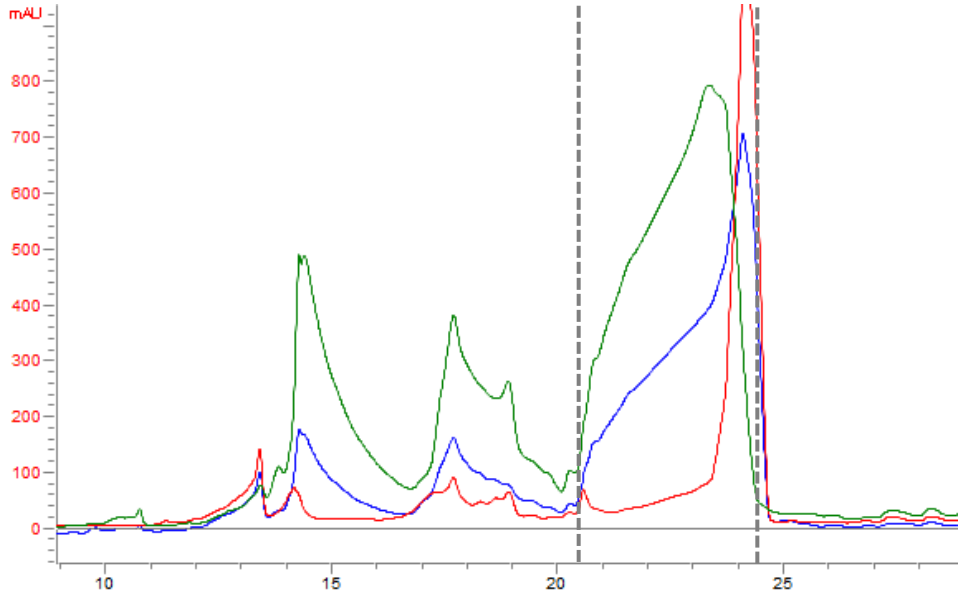

Figure 5-17 - Overlayed HPLC spectra of molecule 5 observed at 220 nm (blue), 254 nm (red), 290 nm (green)

other species remained present, hence it was necessary to use high pressure liquid chromatography (HPLC) with a reverse phase column to purify **molecule 5**, as described in Section 5.5.1.2. While the use of HPLC improved fraction separation, some overlap of products during

purification still remained, as illustrated in Figure 5-17; **molecule 5** is most strongly observed in the 290 nm absorption channel (the green trace in Figure 5-17), and the peak associated with its fraction is highlighted, stretching between 20 min 30 s and 24 min. There is a clear overlap with a separate species that absorbs most strongly in the 254 nm channel (the red trace in Figure 5-17). Care was therefore taken to take the only the fractions between 21-23 min.

5.6.1.2.2 NMR

After the purified fractions were collected, residual acetonitrile was removed by evaporation under reduced pressure, before the remaining water was removed through lyophilisation. The product was then characterised using NMR and mass spectrometry. For NMR, it was dissolved in deuterated chloroform. While the mass spectra showed that **molecule 5** was the major product, in the NMR spectrum (Figure 5-18), other peaks were shown to be present. The majority of the contaminants were from residual solvent, as observed in the NMR for **molecule 3**; however, at low ppm, peaks associated with residual contaminants are still observed. These are likely to be due to long hydrocarbon chains, including so-called 'NMR grease' [209]. The appearance of the additional peaks was of concern as they remain major in the spectrum, despite the additional HPLC purification step. It is possible that while **molecule 5** initially seemed to dissolve well in $CDCl_3$, its increased polarity may have led to the molecule coming out of solution. This is supported by the fact that a significant number of sweeps needed to be performed to attain a good signal to noise ratio. While the quantities of **molecule 5** being used were low due to the problems with step A and in the purification of this step, the resultant mass was still approximately 10 mg, which should have been enough to get a strong signal. In addition, its solubility in acetonitrile suggests that its polarity had significantly increased compared to **molecule 3**. Therefore the concentrations of the contaminant present may not be as significant as it appears from Figure 5-18.

Despite these problems, the NMR does support the successful conjugation of the cyclams to the bromine arms of **molecule 3**. Most significantly, the peaks associated with the protons on the

arms themselves (now labelled positions 7 and 8) have shifted upfield, now sitting in the same region as the PEG tether (chemical shift 3.56-3.58), which is expected if the conjugation has been successful. In addition, the ratio of protons attributed to the cyclams to those attributed to **molecule 5** is at 2:1, as expected for a successfully conjugated product.

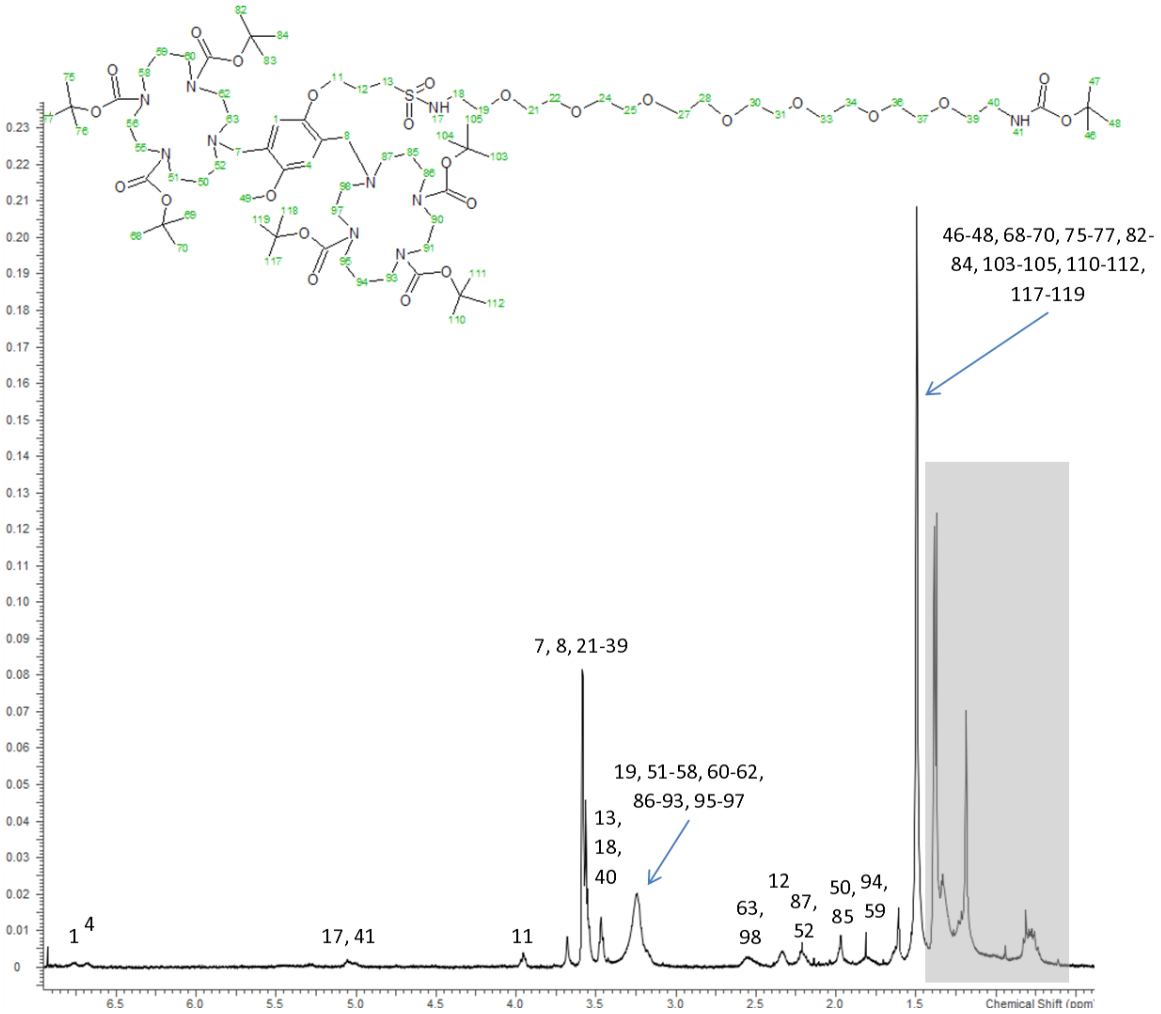

^{1}H NMR: (400 MHZ, $CDCl_3$, 25 °C): δ = 6.751 (br s, 1H), 6.689 (br s, 1H), 5.055 (br s, 2 H), 3.955 (t, 2H, J = 6.3 Hz), 3.679 (s, 3H), 3.579 (m, 30H), 3.459 (t, 6H, J = 5 Hz), 3.242 (br s, 26H), 2.551

Figure 5-18 - NMR spectrum of molecule 5, contaminant peaks observed

5.6.1.2.3 Mass spectrometry

The mass spectrum (MS) fingerprint of **molecule 5** was interrogated more thoroughly than that of **molecule 3** due to the weakness of the NMR spectrum. Figure 5-20 shows the full mass spectrum of the sample, with the peak associated with singly ionised **molecule 5** ($M + H^+$) highlighted and shown in detail on the right. The major peak is attributed to the doubly charged species ($M + 2H^+$), further clarified by its isotopic fingerprint, shown in Figure 5-19; each peak is 0.5 charge to mass units apart, and relates to the presence of 1, 2, 3, 4, 5 or 6 ^{13}C atoms present in the structure, with the peak intensity related to the probability of their presence, given the 1.107% abundance of ^{13}C in nature [210]. The peaks associated with **molecule 5** were the strongest in the spectra, and although MS is not a quantitative technique, it does suggest that this is the major product in the sample analysed. This further supports the conclusion that the weakness of the NMR spectrum was due to solubility issues in the chosen solvent. Step C was pursued without further purification.

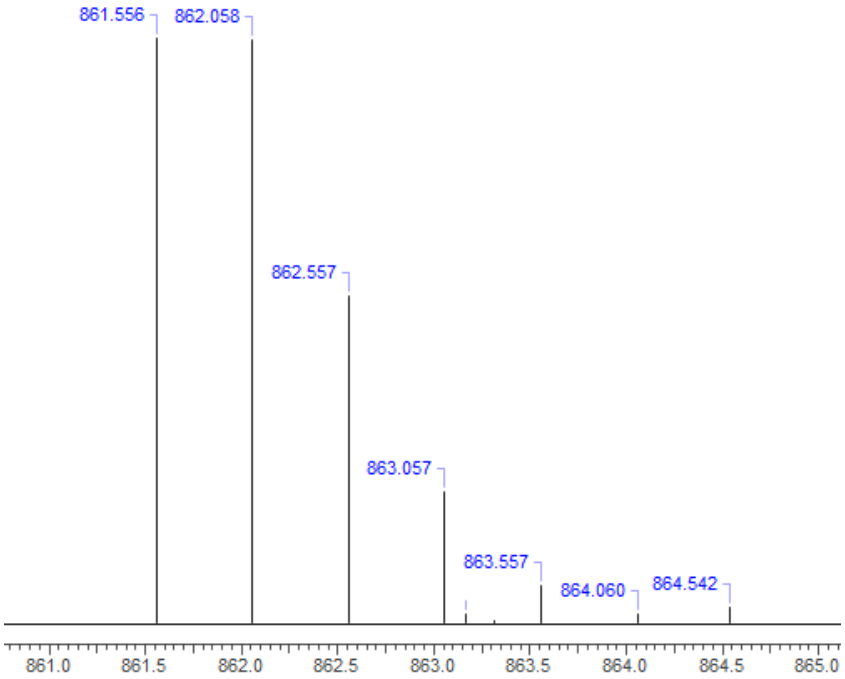

Figure 5-19 - Detail on the main peak in the mass spectrum of molecule 5, which is the doubly charged species, showing the isotopic fingerprint for molecule 5

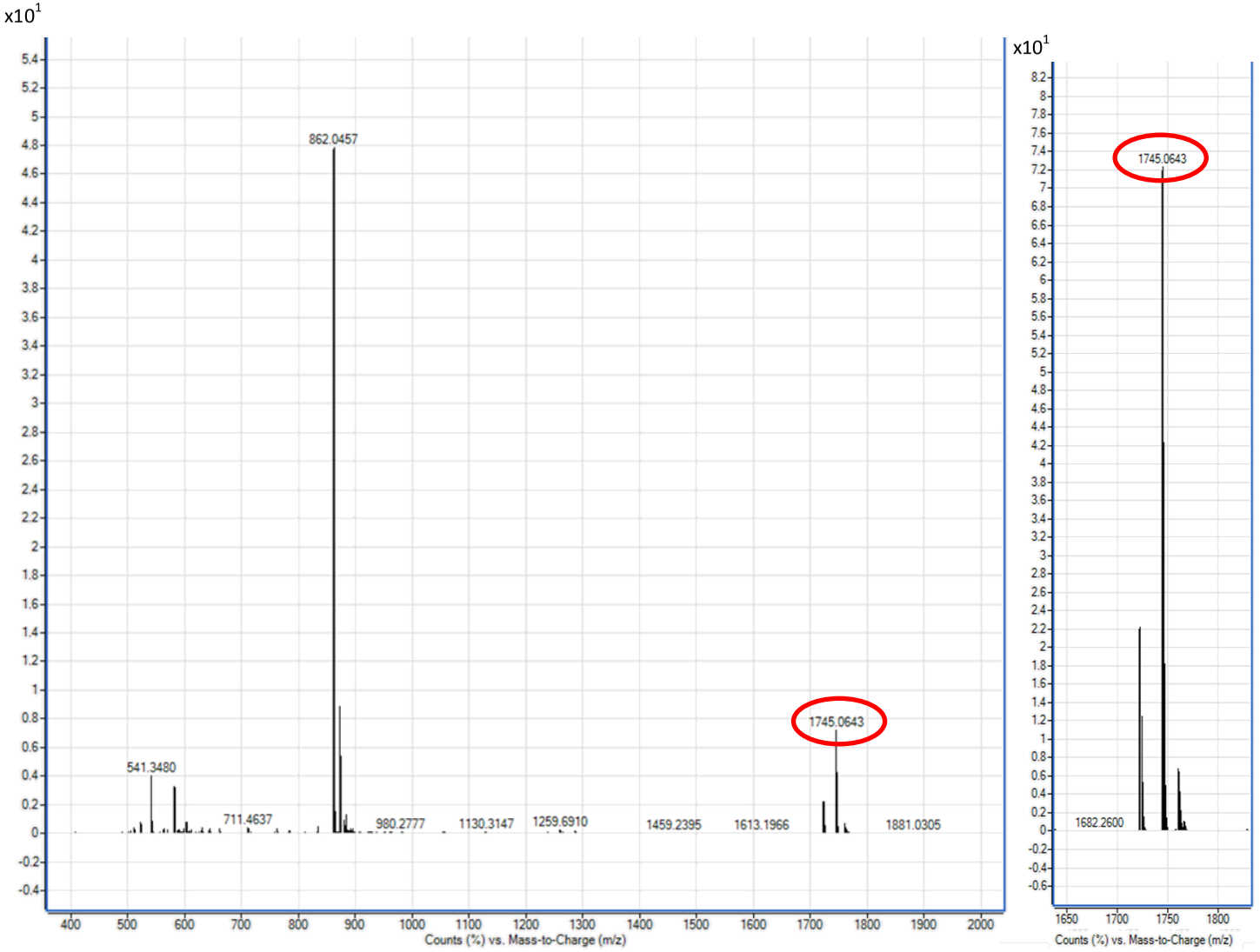

Figure 5-20 – Full mass spectrum of molecule 5, with the singly ionised peak highlighted. The peak at 541 is a triply charged molecule with no boc end group on the tether

5.6.1.3 Step C

Following characterisation of **molecule 5**, the final deprotection step was undertaken. The tert-Butoxylcarbonyl (boc) protecting groups present on **molecule 5** were cleaved using TFA in dry conditions, and the step was run to completion in order to avoid further purification. TFA salt was removed using diethyl ether co-evaporation. TFA unfortunately degrades rubber septa, and it is thought that for this reason additional impurities remained present in the final reaction mixture. After removal of the DCM under reduced pressure in which the reaction was performed, **molecule 6** (BAT1) was redissolved in water with the aim of excluding any hydrophobic polymeric molecules that may have been present, before lyophilisation.

5.6.1.3.1 Mass Spectrometry

Mass spectrometry was performed in the 900-1400 m/z region, and confirmed that BAT1 was both present and appeared to be the major product (although MS is not a quantitative technique), shown in Figure 5-21, where the isotopic fingerprint of the singly charged compound ($M + H^+$) and its sodium adduct are shown in detail below.

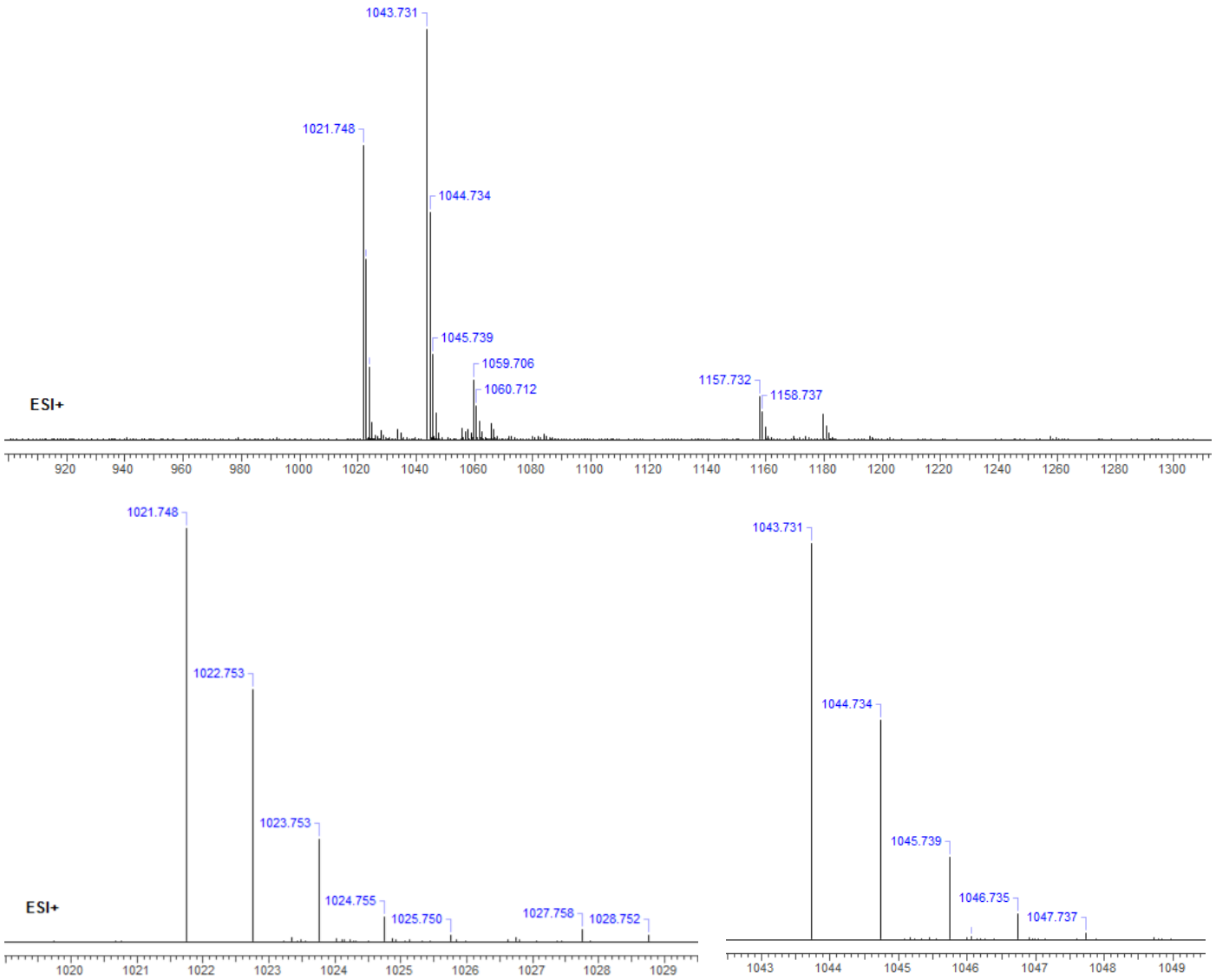

Figure 5-21 - Mass spectrum of BAT1, with the detail of the two major peaks highlighted below. The peaks at 1059, 1157 and 1179 are thought to be potassium, barium and terbium adducts, respectively.

5.6.1.3.2 NMR

Further characterisation was undertaken using NMR; BAT1 was dissolved in D_2O, as the molecule was extracted using water this was thought to be the best solvent for it to be characterised in. Similarly to Section 5.6.1.2, a significant number of sweeps were undertaken in order to gain sufficient peak intensity to characterise the molecule, and again, large residual solvent peaks appeared in the spectrum, particularly that of water, which may have been due to incomplete lyophilisation. In addition, peaks from residual diethyl ether from the co-evaporation step were observed, and are indicated in Figure 5-22. Given the volatility of diethyl ether, and that the solvent of the reaction mixture had first been removed under reduced pressure, followed by lyophilisation, the quantities that were present were expected to be very small. Secondly, the very strong water peak observed in the spectrum (not shown), indicates that while – as seen in previous spectra – there is always some undeuterated solvent present in NMR solvents, **molecule 6** may have had lower solubility in the D_2O than expected.

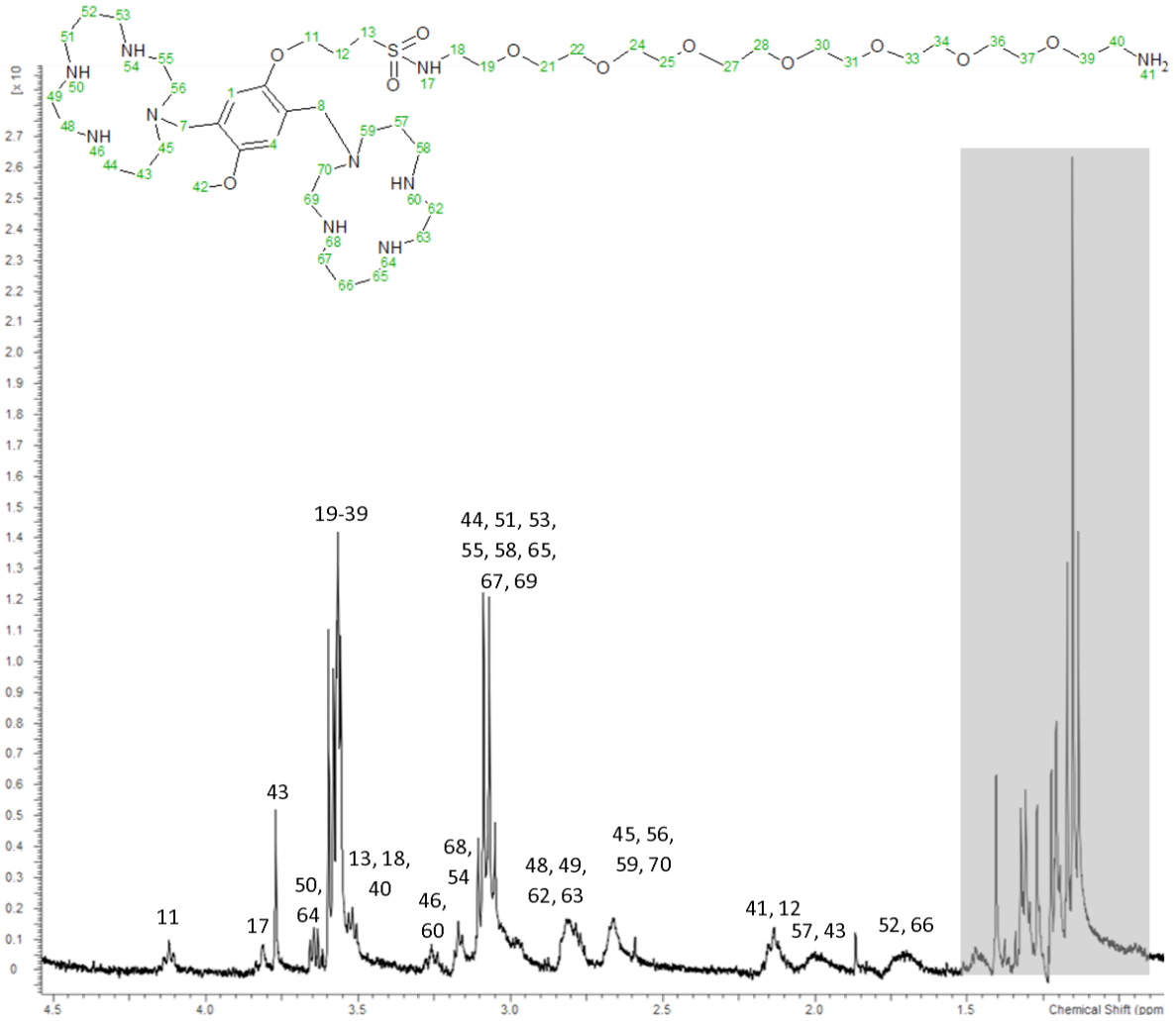

^{1}H NMR (400 MHz, D_2O, 25 °C): δ = 6.925 (s, 1H), 6.905 (s, 1H), 4.121 (t, 2H, J = 6.7 Hz), 3.81 (s, 1H), 3.77 (s, 3H), 3.645 (t, 2H, J = 5.3 Hz), 3.596 (s, 4H), 3.569 (m, 26 H), 3.519 (t, 6H, J = 5.2 Hz), 3.249 (t, 2 H, J=7.5 Hz), 3.166 (t, 3H, J = 5 Hz), 2.793 (br m, 10 H), 2.635 (m, 8H), 2.134 (t, 4H, J = 6.7 Hz), 1.999 (br s, 4H), 1.699 (br s, 4H)

Figure 5-22 - NMR spectrum for BAT1; the spectrum has been cropped due to the presence of a large water peak.

The molecule initially appeared to dissolve well in D_2O, but after characterisation was complete, some precipitate was observed at the bottom of the NMR tube, suggesting that not all of the compound had dissolved, or that it had come out of solution. This is surprising, given that the molecule was water extracted following the vacuum evaporation of its initial solvent, and it is not clear why such low solubility may have occurred.

The presence of the diethyl ether in the spectrum led to difficulties in resolving some of the peaks associated with the newly deprotected cyclams. However, it is known that the two multiplets of diethyl ether are related with a 2:3 ratio [211], so by comparing the volumes of the peaks and subtracting the discrepancy, the peak volume that may be attributed to the remaining protons present on the cyclams can be found. This was found to match well with the expected number of protons.

Importantly, however, the newly deprotected secondary amines on the cylams (the positions of which are labelled as 46, 50, 53, 60, 64 and 68) are now apparent as three triplets on the spectrum. Each of the protons in these amines is bound to two CH_2 groups on the neighbouring two carbons; for each set of protons the chemical environment is similar enough to make the four protons indistinguishable, leading to the triplet splitting. The peaks integrate to 6 protons in total, meaning that there was complete deprotection. Unfortunately the primary amine at position 41 is incredibly labile, making the peak difficult to resolve, if apparent at all.

5.6.1.3.3 Analytical HPLC

While both the NMR and the MS support the presence of BAT1 and that it is the major product present in solution, the spectra were not entirely satisfactory – the NMR spectrum in particular. For this reason it was decided that analytical HPLC should be carried out as a further method of assessing whether BAT1was indeed the major product present in the sample, the results of which are shown in Figure 5-23. While some smaller peaks are present, the single major peak at 3.402 min can clearly be identified as the major product, and was confirmed to be **molecule 6** with MS.

Due to the low yields, the problems of purification encountered previously and the molecule's relative purity, it was decided that the mixture would not be further purified before bioactivity testing. BAT1 was subsequently dissolved into PBS at pH 7.4 and kept at -20^{o}C in preparation for its introduction to cells.

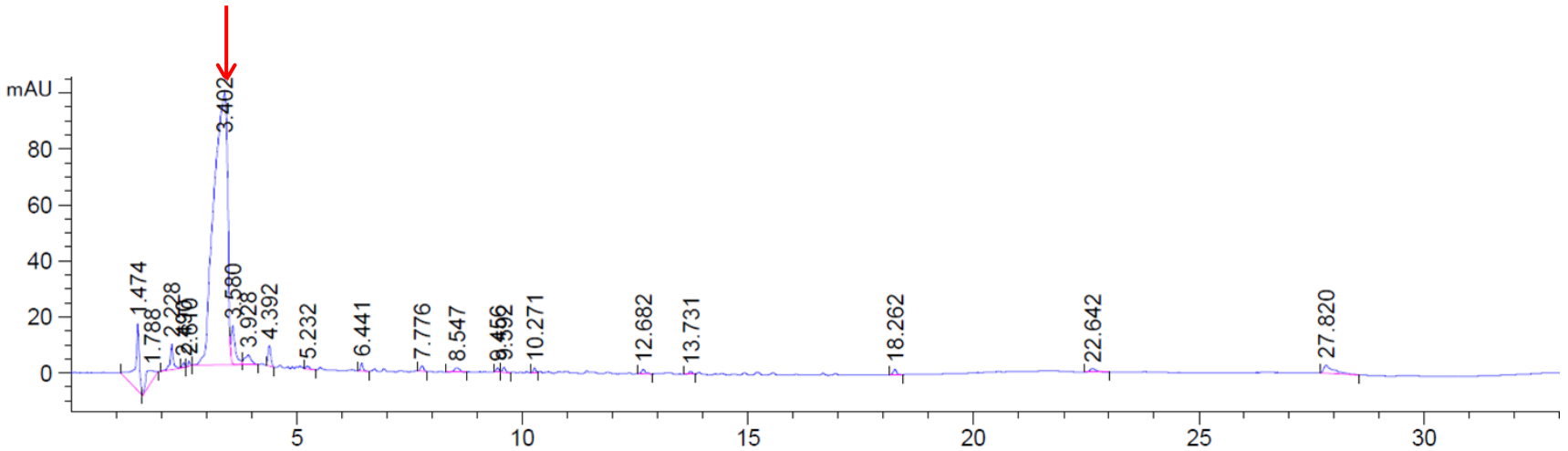

Figure 5-23 - Analytical HPLC of the purified BAT1 fraction taken at wavelength = 290 nm showing that the primary product in the mixture was molecule 6, MS confirmed

5.6.2 Bioactivity

Assays were performed to assess whether BAT1 would be an appropriate targeting ligand for GO. First, its binding to CXCR4, and its biological activity was compared to AMD3100 assessed, together with an assessment of any toxicity. Then its ability to specifically target a fluorescent molecule to CLL cells was determined.

In order to do this, both targeting competition and functional assays were performed that could confirm its antagonistic potency against CXCR4. In addition, the redistribution of the CXCR4 both on the cell surface and within the cytoplasm was assessed using immunostaining in order to see if there was any evidence of receptor internalisation or trafficking following the attachment of either AMD3100 orBAT1. Finally, the fluorophore Cy5 was attached to the primary amine end-group of the PEG tether of BAT1, as described in section 5.5.1.4 to assess whether the molecule's potency was altered.

5.6.2.1 Toxicity

As there was concern that BAT1 was not entirely pure, and the structural change to the molecule could induce unexpected toxic effects, the toxicity was assessed 24 h after addition of the

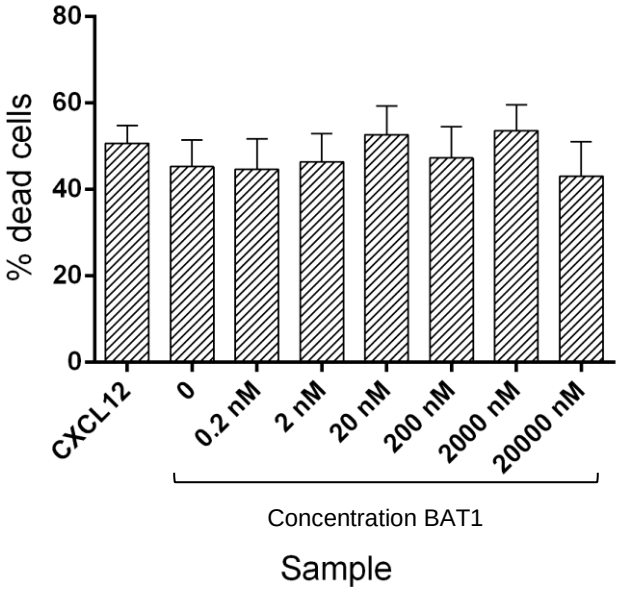

Figure 5-24 – Percentage dead CLL cells in the overall population at 24 h after treatment with BAT1 and relevant controls

molecule, using flow cytometry the same gating strategy as described in Chapter 4, Section 4.3.5.1.2. While the percentage dead population is high, there was no significant difference between those treated with BAT1 and those treated with PBS alone or CXCL12. While the percentage of dead cells was higher than desired, it is not unusual for CLL cells 24 h after incubation from storage; CLL B-cells are known to have very fragile cell membranes, which can cause high rates of death in cultures previously in liquid nitrogen storage [23]. It was therefore concluded that despite its impurity, BAT1 did not exhibit any significant toxicity that would prevent its further assessment.

5.6.2.2 Molecule potency

The potency of BAT1 was assessed using a competition assay, as described by Badr *et al.* [212]. Binding of CXCL12, AMD3100 and BAT1 was detected through the loss of CXCR4 cell surface receptors available to a fluorescently labelled anti-CXCR4 monoclonal antibody (PE-CXCR4-mAb), illustrated in Figure 5-25.

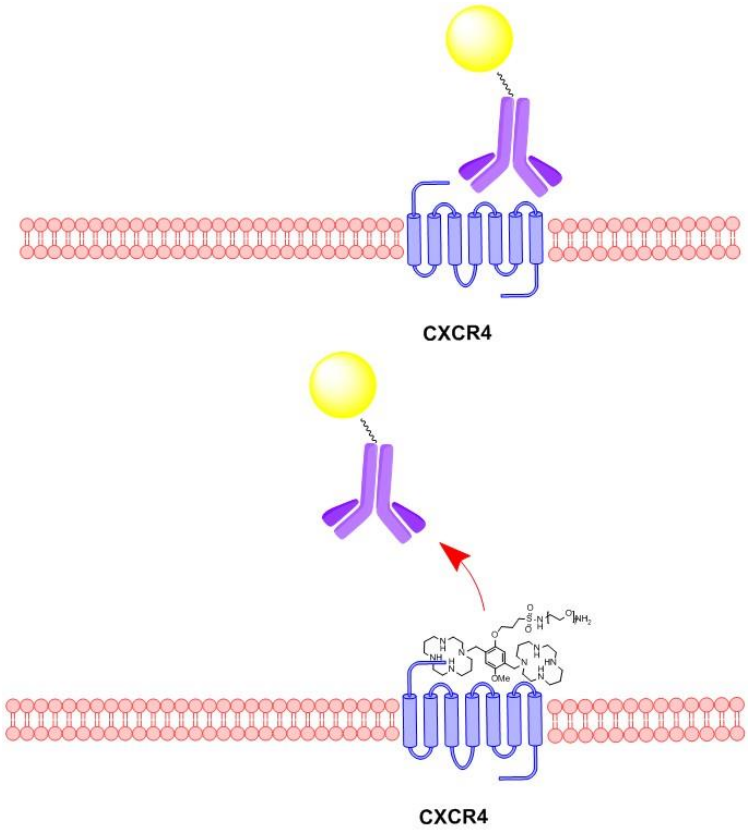

Figure 5-25 - Schematic of the mechanism behind the competition binding assay. If bound successfully, BAT1 should inhibit the binding of PE-CXCR4-mAb, resulting in a decrease in relative cell fluorescence

The concentration range tested (2 nM-20 μM) was chosen from the potencies of AMD3100 and its analogues reported in the literature [177-179, 190]; alterations to the central aromatic ring of AMD3100, while it is not thought to interact with the CXCR4 receptor itself, is recognised to potentially reduce its potency – possibly through steric hindrance. PBS with no drug and CXCL12 were used as negative and positive controls respectively. Primary chronic lymphocytic leukaemia B-cells were brought out of storage at - and cultured in a 96 well plate as described in Section 5.5.1; for primary CLL cells, cell viability stabilises and CXCR4 expression is at its highest at 24 h of culturing [213], hence this time point was chosen for the addition of drug.

After incubation with BAT1, AMD3100 or PBS, for 3 hours at concentrations between 0.2–20000 nM the cells were removed from culture and placed on ice to reduce the chance of receptor capping and internalisation before staining with the PE-CXCR4-mAb. After incubation with the PE-CXCR4-mAb, the cells were fixed and their fluorescence measured using flow cytometry. The events were gated on the forward/side scatter plot such that only the signal from live cells was collected (due to the decreased integrity of the cellular membrane of dead or dying cells, increased non-specific binding is likely to occur, which can lead to spurious results). The antagonism of the CXCR4 surface receptor was then assessed relative to the negative control, and a dose response curve was plotted for both BAT1and AMD3100 (Figure 5-26).

Figure 5-26 and Table 5-4 indicate that while the potency of BAT1 was significantly lower than that of AMD3100 (IC_{50} shown in Table 5-4), the efficacy is very similar. PE-CXCR4-mAb binding of cells treated with 20 μM BAT1was inhibited by 92.3%, whereas the inhibition provided by AMD3100 at 20 μM was 95.9%. This is significantly higher than other similar analogues of AMD3100 recently synthesised [190].

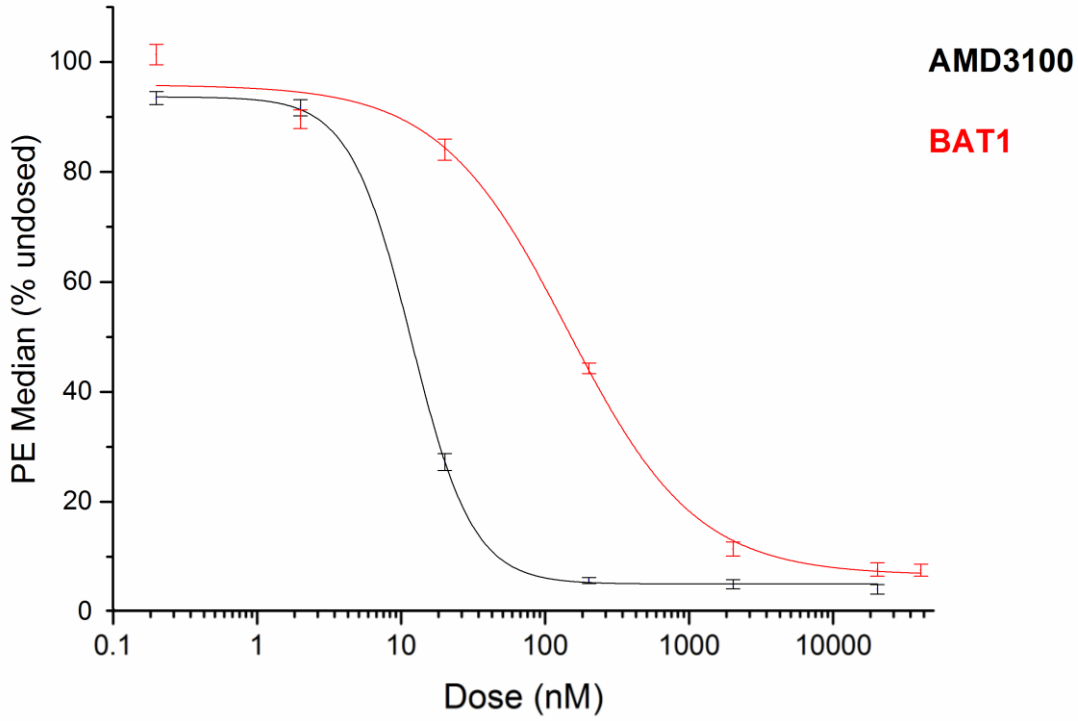

Figure 5-26 - Dose response curves for AMD3100 and BAT1, calculated using the competition binding assay

Table 5-2 - The half maximal inhibitory concentration of AMD3100 and BAT1 calculated using the competition binding assay

	IC_{50}
BAT1	142 nM
AMD3100	11.7 nM

Through this assay we were able to assess the molecules' specific binding affinity to CXCR4. It was considered valuable to also use a functional assay to assess whether BAT1 was able to prevent the cell signalling associated with CXCL12 complexation, therefore proving its dual function of specifically targeting cells that overexpressed the CXCR4 receptor and blocking the interaction with its conjugate ligand, which is associated with worsened survival outcomes in a range of cancers. For this purpose a western blot technique followed by immunohybridisation was used.

5.6.2.3 Molecule antagonism

One of the signalling pathways triggered by the binding of CXCL12 to CXCR4, described in detail in section 5.1.1.1 and illustrated in Figure 5-1, involves the phosphorylation of ERK 1 and 2. CLL cells express the intracellular signal molecules ERK 1 and 2 at relatively high levels, but with only a low level of baseline phosphorylation; after complexation with CXCL12 the protein becomes phosphorylated at greatly increased levels. The quantity of phosophorylated-ERK1/2 (p-ERK) relative to total ERK1/2 therefore provides insight into the extent of the interaction between

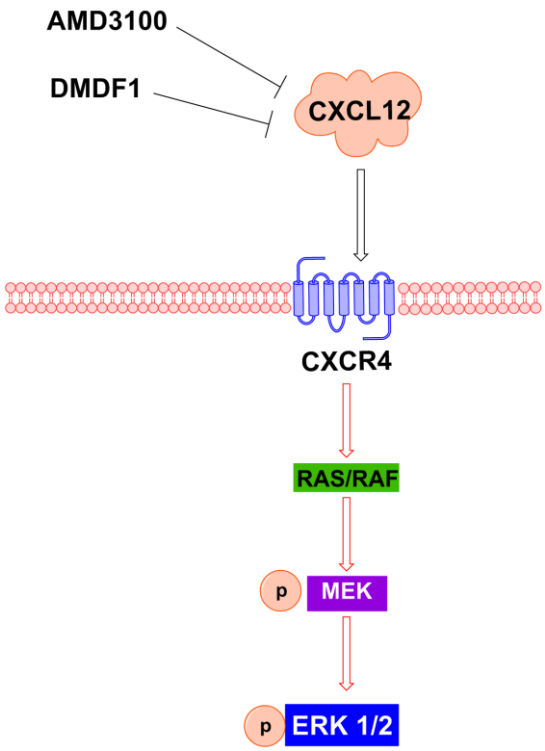

Figure 5-27 – A schematic of the RAS/RAF-MEK-ERK pathway after CXCL2 complexation with CXCR4

CXCR4 and CXCL12 [214]. This characteristic step in the RAS/RAF-MEK-ERK pathway – illustrated more simply in Figure 5-27 – can be easily detected using western blotting. This technique was therefore used to assess whether BAT1 retained its inhibitory effect on downstream signals through the RAS/RAF-MEK-ERK pathway.

Primary CLL cells from the same case were again incubated with BAT1 in the concentration range 20 nM-20 µM, for 3 h, and then treated with 200 ng/mL CXCL12 for 5 minutes, following which they were put on ice, prepared and lysed for western blot analysis, as described in section 5.5.3. As a positive control 20 µM AMD3100 was used, and both nil drug treatment and 20 µM **molecule 6** without CXCL12 addition were used as negative controls.

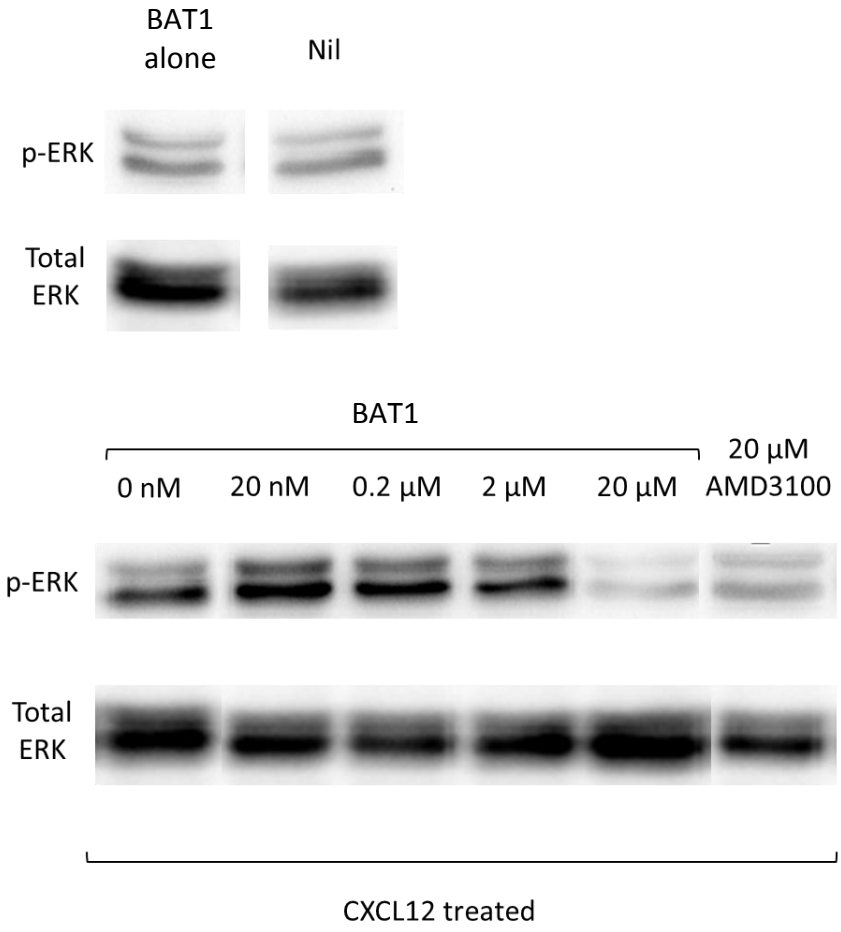

Figure 5-28 - Western blot analysis of phosphorylated ERK 1/2 after treatment with BAT1 and CXCL12. Inset: total ERK for the same samples.

Figure 5-28 shows the quantity of total ERK and p-ERK present in the cell lysates for the different treatments. The blots of total ERK show little variation in the quantities of ERK 1/2 present in the cells before lysing, and shows in turn that any variation in p-ERK 1/2 is due to blocking of the interaction of CXCR4 with CXCL12. The amount of total ERK 1/2 present in the cells tested provides a control to ensure equal presence of ERK1/2 in the samples. As shown in Figure 5-28, a

dose response inhibition of CXCR4-CXCL12 complexation and signalling is observed following treatment with BAT1. At 20 μM, inhibition of cell signalling is similar to that observed with 20 μM AMD3100, or with no CXCL12 exposure whatsoever, and at smaller doses the presence of phosphorylated ERK gets progressively higher. This confirms that BAT1is able to inhibit the activation of the RAS/RAF-MEK-ERK by CXCL12 to a similar extent as AMD3100 at the highest doses tested.

5.6.2.4 CXCR4 membrane and cytoplasmic redistribution

The aim in synthesising molecule **6** was in order to use it as a targeting ligand for therapeutics delivery vehicles. For most purposes, the vehicle would need to be internalised through some mechanism; preferable routes would avoid routes that result in trafficking to the endosomes and lysosomes to avoid degradation. While the CXCR4-CXCL12 complex is trafficked to the golgi [215] – avoiding the endosomes – after the RAS/RAF-MEK-ERK pathway is triggered, the majority of reports state that AMD3100 is not internalised at all [187, 201]. Some CXCR4 agonists have been shown to be internalised through endocytosis, as have larger materials attached to CXCR4 antagonists; however, as described earlier Li *et al.* [186] found that the AMD3100 polyplexes that were observed attached to the CXCR4 receptor remained external to the cell, although it is not clear whether those that entered through an alternative mechanism first attached to the cell surface through CXCR4-binding followed by release. It is therefore important to assess the redistribution of CXCR4 both on the membrane and in the cytoplasm of the CLL cells following treatment. Dual staining immunofluorescence studies were used to this end.

CLL cells from the same case were cultured for 24 h, and then treated with either 20 μMBAT1, 20 μM AMD3100, 200 ng/mL CXCL12 or blank PBS. After 3 h of incubation, membrane bound CXCR4 was stained *in vitro* while the cells were kept on ice; the cells were then washed and cytospun onto glass microscope slides, fixed and permeabilised, and their internal CXCR4 and nuclei were stained (described in detail in section 5.5.4). As shown in Figure 5-29, for both treatment with AMD3100 andBAT1, no CXCR4 staining is present on the membrane, whereas the staining inside

the cytoplasm remains indistinguishable from the untreated cells. The cells that had been treated with CXCL12 however show the presence of CXCR4 on the membrane – which is expected as the receptors are recycled back up to the membrane following the signalling cascade and internalisation – and in the golgi, which manifests as a bright spot situated next to the nucleus.

From these images it can be assumed that no trafficking of the CXCR4-BAT1 complex towards the

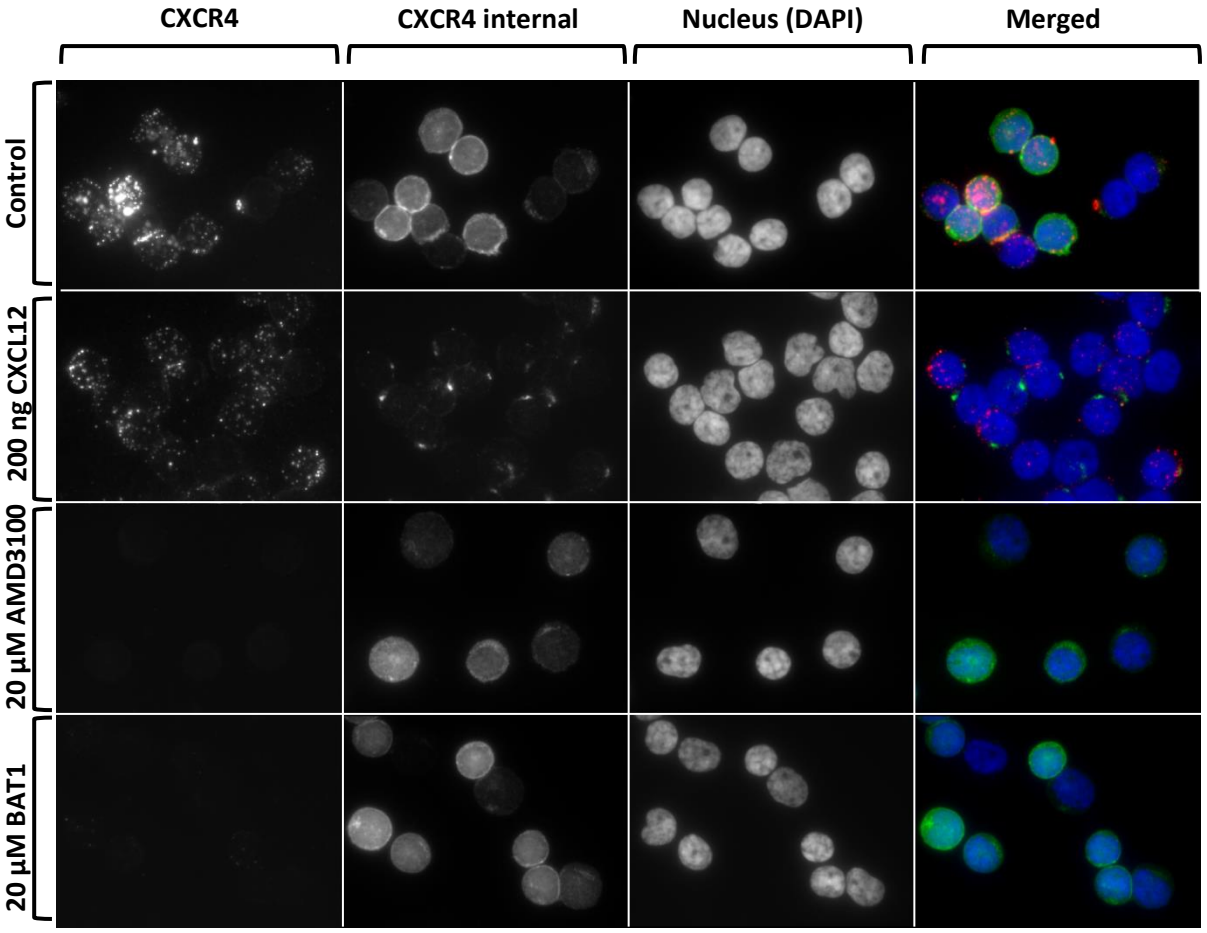

Figure 5-29 - Immunostained CLL cells following treatment with BAT1, AMD3100 or CXCL12. The distribution of the CXCR4 receptors both on the membrane and in the cytoplasm is shown in the first two columns, and highlighted in red and green respectively in the final column.

golgi or endosomes occurs, similarly with AMD3100. Drug complexation with CXCR4 also does not appear to result in the trafficking of cytoplasmic CXCR4 to the membrane, in order to replace those receptors that have been blocked, as both the brightness and homogeneity of cytoplasmic CXCR4 remains very similar to that of the untreated cells.

It is not clear, however, whether complexation with either AMD3100 or BAT1 results in any capping of the cell surface receptor, or whether it solely blocks the attachment of either CXCL12 or any other CXCR4 antibodies by attaching to the same region of the receptor.

5.6.2.4.1.1 Cy-5 conjugation

To assess whether the potency or efficacy of **BAT1** was affected upon conjugation to another molecule or material, a tester molecule was conjugated to the amine terminus of BAT1's PEG tether; a Cy-5 molecule with NHS ester was chosen due to its ease of attachment, and the ease with which attachment could be directly assessed using its fluorophore. Conjugation of the fluorophore to BAT1 is described in detail in Section 5.5.1.4, and the structure of the molecule is shown in Figure 5-30. Primary CLL lymphocytes were treated with Cy5-BAT1 at 0, 5 and 10 µM, either with or without pre-treatment with AMD3100 at 20 µM to demonstrate binding specificity. Unconjugated Cy5 was used as a negative control, and care was taken such that the NHS ester was no longer present on the molecule alone, as it would easily attach to the amines in the structures of proteins present in the suspension, other cell receptors and the cell membrane itself.

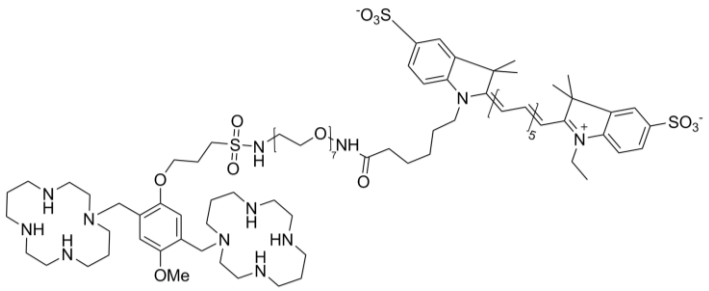

Figure 5-30 – BAT1/Cy 5 conjugate

After treatment with the either the BAT1/Cy5 conjugate or Cy5 alone, the cells were washed with 0.5% BSA in PBS and their relative fluorescence measured using flow cytometry. As before, the scatter plot was gated around the live cells to reduce the chance of non-specific binding producing spurious results (gating shown in Figure 5-31).

The competition assay (Section 5.6.2.2) tested BAT1's ability to reduce the binding of another molecule with affinity for the CXCR4 receptor (an anti-CXCR4 antibody); in this case the molecule's direct affinity for the CXCR4 receptor on cells was tested. While the antagonism of the receptor is important, as it proves that BAT1can have a dual purpose, its direct affinity to the cells being targeted is its most important function.

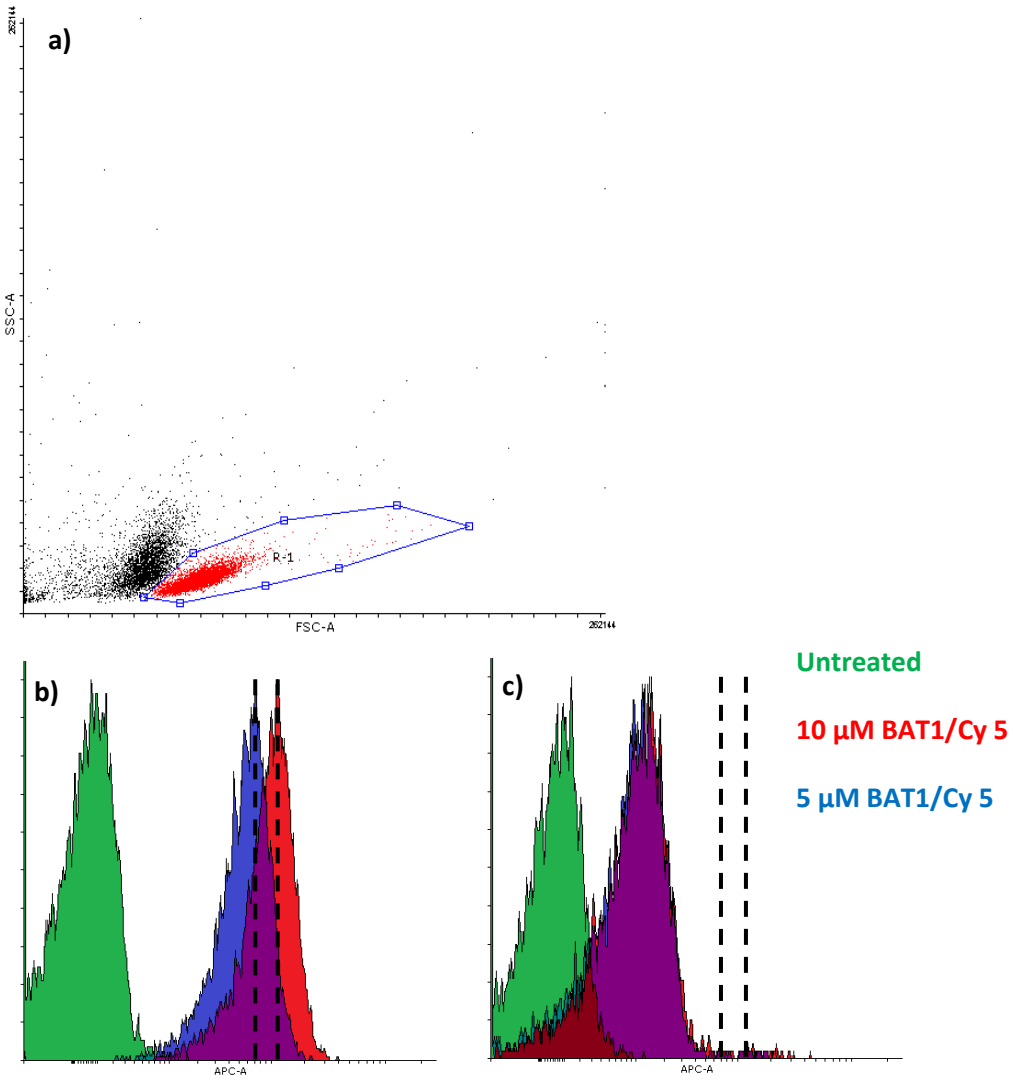

Figure 5-31 – Specific targeting of BAT1/Cy 5 conjugate to CXCR4 on CLL cells measured using flow cytometry a) Forward/side scatter plot for the CLL cells treated with the molecule 6/cy-5 conjugate; fluorescence intensity histograms for the cells that were b) incubated with the molecule 6/Cy-5 conjugate without any pre-treatment; c) incubated with the molecule 6/Cy5 conjugate after pre-treatment with AMD3100

As shown in Figure 5-31 and Figure 5-32, the cells that had been exposed to Cy5-BAT1 alone show increasing fluorescence intensity with increasing molecule concentration; however, following treatment with AMD3100 the intensity is knocked down significantly, with the average

fluorescence showing no significant difference to that seen at 0 µM Cy5-BAT1. This therefore shows that BAT1 can be used to specifically target fluorescent moieties to cells expressing CXCR4. While some non-specific binding was present in the samples treated with Cy5 alone, the difference in fluorescence between the two samples was significant, and the fluorescence of the cells pre-treated with AMD3100 followed by unconjugated Cy5 was not affected.

This experiment, therefore, acts as a proof of principle for the use of BAT1 as a ligand for the specific targeting of functional molecules to CLL B-cells.

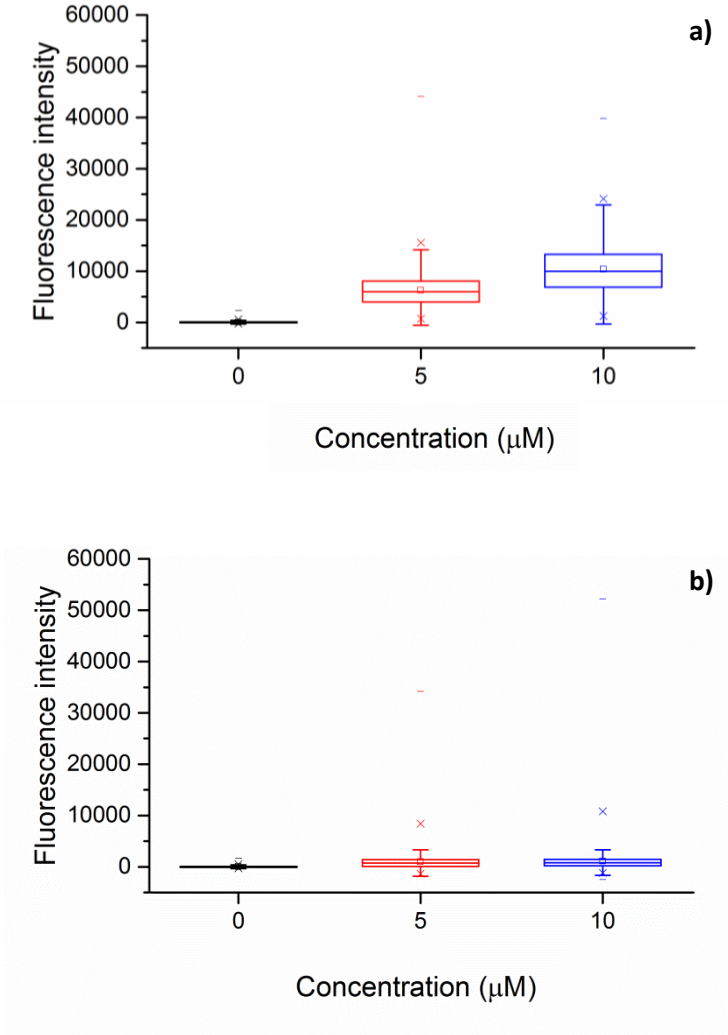

Figure 5-32 - Relative fluorescence of cells treated with Cy5-conjugated BAT1 at different concentrations, either a) without prior blocking with AMD3100; b) with prior blocking with AMD3100. Distributions are represented using box and whisker plots, with the whiskers representing the 1st and 4th quartile and the box representing the 2nd and 3rd, bisected by the median. □ is the arithmetic mean and x is the geometric mean.

5.7 Discussion

In this chapter the functional molecule BAT1, based on the CXCR4 antagonist AMD3100, was synthesised, structurally characterised and its antagonistic activity and function as a targeting ligand were tested. Challenges were encountered during the initial synthesis and purification steps, leading to low yields and the final molecule that was used not being entirely pure. However, the molecule was found to have low toxicity and exhibit bioactivity in primary CLL cells with an efficacy and potency comparable with other molecules of the bis(cyclam) class [178, 179]. Within this assessment, it was found that the drug's antagonism was effective with regards to attachment and cell signalling. The attachment of a fluorochrome to the PEG tether of BAT1 acted as a proof of principle for its use to specifically target functional molecules to cells that over-express CXCR4.

During the process of this work, two papers were published in which the synthesis of a similar molecule was synthesised for imaging purposes were published [190, 198]. Many of the aspects of the synthesis were similar to those used in this Chapter – in particular, making use of bis(bromine) arms for the attachment of tri-boc protected cyclams, and the attachment of functional molecules using the central aromatic ring, rather than the cyclams themselves, and in the subsequent paper PEG was used as a tether for the attachment of Ga^{68} for PET imaging purposes [198]. Interestingly, despite the structural similarity of the molecules, the efficacy of the molecule reported in [190] was significantly lower than both AMD3100 and BAT1 at the same 20 µM concentration, reaching a maximum inhibition of only 46% without the presence of chelated metal ions in the cyclams, and 84% following Ni^{2+} chelation, compared to 92.3% without chelation in this study. While a different *in vitro* system was used by the group – who used the popular T cell line Jurkat – it remains unclear why the efficacy would be affected. In addition, the step taken to transform the ester featured on the central aromatic ring into a primary amine required a significant excess of ethane-1,2-diamine (30 eq.) and the reaction took place over 6 days to gain a 60% yield. In the subsequent *in vivo* work, the authors encountered challenges with the biodistribution of the molecule, with large quantities detected in the liver, spleen, lung, kidney,

adrenal gland, bone and bone marrow in addition to the xenografted H69 tumour [198]. While the authors suggest that non-specific binding can be reduced by further tailoring the lipophilicity of their molecules – which are affected by the chelating group on the end of their PEG tether; however, for the majority of these regions, prior blocking with AMD3100 resulted in significantly lowered detection (only the kidney saw an increased quantity of detection after prior blocking), which suggests that the results are not purely due to non-specific binding, and instead reflects how widely expressed the receptor CXCR4 is. These results emphasise the importance of the application of the drug targeting system; in future work using BAT1 as a targeting ligand for therapeutics delivery vehicles to CLL, it is hoped that the combination of targeting, the use of CLL specific drugs such as Ibrutinib and the chemosensitising effect of CXCR4 antagonism will produce a significantly more potent therapy.

5.8 Future work

Future work would entail the repeated synthesis of BAT1, in which the purification steps would be altered such that the yields were improved – as discussed in Section 5.6.1.1. Alternative solvents would also be assessed for their ability to improve the strength of the NMR spectra in Steps B and C of the synthesis, as it is suspected that the poor quality of the spectra may have been due in a large part to solubility issues. Following these steps, the attachment of the molecule onto GO sheets, prepared as described in Chapter 2, would be investigated. It is expected that the PEG tether may need to be extended for such experiments, due to the problems of stability described in Chapter 2 when shorter single chain PEG chains were used. The inherent fluorescence of the GO flakes may be used in order to assess the attachment and intracellular trafficking of the flakes; while experiments in Section 5.6.2.4 showed that following CXCR4 complexation with BAT1 no redistribution of the CXCR4 receptor was observed, when attached to an object of dimensions ≥ 100 nm the object may be taken up by endocytosis. This is in part demonstrated by the specific internalisation found for the polymeric plerixafor nanoparticles used by Oupický *et al.* [187, 192, 193].

6 Conclusions

The aim of this project focused on the preparation of a graphene-based therapeutics delivery vehicle that could be targeted to malignant cells, in this case the B-cell malignancy CLL. Initial work focused on the possible use of pristine graphene, employing amino acids as novel exfoliating and suspending agents. The work used sonication methods similar to those detailed in the literature, and explored the relationship between amino acid structure and its interaction with the flakes in terms of the capacity to produce high yields of exfoliated graphene, the stability of the suspensions and the thickness of the resultant flakes. The lipophilicity of the amino acid structures and the inclusion of an aromatic ring were found to be correlated to flake thinness and suspension stability. However, severe instability of the suspensions was observed at the highest concentrations of the aromatic amino acids, with agglomeration and precipitation observed in some preparations within only 24 h. In addition – particularly in the later preparations – significant scission of the flakes' lateral dimensions was observed. The observation that apparently pristine graphitic material could be exfoliated and suspended in pure water led to the conclusion that the sonication method used was leading to a highly complex system that did not exhibit the homogeneity desired in a therapeutics delivery vehicle. In addition, the geometry of the flakes in terms of thickness and lateral dimensions led to concerns about potential toxicity. Flake thickness has been linked to toxicity – particularly *in vivo* [72, 73]– and the majority of the flakes observed were multilayer; in addition, flakes with very small lateral dimensions have been linked to increased genotoxicity [84, 85]. Therefore it was concluded that the suspensions would be unsuitable for use in therapeutics delivery. Nevertheless, the ubiquitousness of amino acids in biological environments, and the complex interactions with graphene and graphitic material identified in this work demand additional study, as such interactions may have a significant impact on the behaviour of GFNs in biological environments. In addition, the use of sonication – and probe sonication in particular – as a viable approach for the exfoliation of graphene and other 2D materials is called into question due to the lack of control of the system, with many groups turning to gentler methods such as shear mixing and ball milling.

The movement towards using GO for preparation as a therapeutics delivery vehicle stemmed from its more common use in the literature for this purpose, and from the flexibility of its structure with regards to functionalisation – where one can make use of both the polyaromatic basal plane and the oxygenated functional groups present. However, whereas the section of the work that focused on amino acids was designed to be simple and highly controlled – in which single amino acids were used with unfunctionalised pristine graphitic material of highly controlled lateral dimensions – GO that has been produced through the Hummer's Method is known to be highly heterogeneous both chemically and physically. Therefore a significant portion of the work focused on its characterisation, and the determination of whether efforts to reduce the heterogeneity were successful. It was found that the established methods that had been used were unable to provide sufficient information on the overall distribution of flake sizes due to the polydispersity of the samples, therefore the flakes' inherent fluorescence was exploited allowing RICS to be used to measure the distribution of apparent hydrodynamic radii for each sample. The broader size range that could be measured by the technique encompassed the ranges measured by both AFM and optical microscopy, therefore presenting a distribution that could be directly compared between preparations. In addition, the fluorescence of the flakes was used to assess the interaction between the GO flakes and both BSA and Human AB serum – demonstrating colocalisation through fluorescence quenching.

The GO used was commercially acquired, but further purified and functionalised in-house with the aim of improving its biocompatibility. The initial purification steps led to a suspension that contained fewer thick flakes, was less polydisperse laterally, and contained fewer residual contaminants. Following PEGylation, the suspension displayed improved stability in biologically relevant media; however the apparent hydrodynamic radii – as measured by RICS – were larger than those measured in the purified suspension. Nevertheless, the PEGylated flakes were shown to be more biocompatible than the unfunctionalised suspensions. Whereas unfunctionalised GO appeared to lead to cellular agglutination and macrophage activation, cells treated with PEGylated GO retained healthy morphologies and little change in viability when at rest. This

underscores the importance of further functionalising the flakes; although the dimensions are larger than desired (with some outlier flakes with dimensions > 10 μm), which has been reported to be a significant determinant of toxicity, this aspect was found to not be as important as surface chemistry of the flakes.

Despite the improved stability and biocompatibility of PEGylated GO, the problems associated with controlling both its size and surface chemistry, even before characterising the prepared suspension, mean that a significant amount of work needs to be performed in the field before the material can be considered to be suitable for use in drug delivery. The ongoing disagreements over the exact surface chemistry of GO highlight the current challenges in defining the material. This is in stark contrast to other nanoparticles used for drug delivery, where production methods such as extrusion for controlling the size of liposomes, and the wide choice of monomeric constituents for building polymeric nanoparticles lead to nanoparticles that are not only highly monodisperse in terms of their physical size, but have carefully controlled chemistry that can be tailored to the purpose in hand. It should be noted that the field of graphene is very young in comparison to liposomal and polymeric studies. A significant amount of work on the improvement of production methods in order to obtain graphene samples that are significantly more well defined is of utmost importance, particularly within the biological sphere.

The work in the final chapter focused on the synthesis of a targeting ligand suitable for attachment to PEGylated GO flakes – BAT1. Despite challenges in the synthesis resulting in lower yields than desired and a relative lack of purity of the final molecule, the toxicity was found to be low. Functional and competition assays confirmed that the targeting ligand had an antagonistic effect against its ligand CXCR4, and that following conjugation with a fluorescent moiety, retained its specificity. The PEG tether with primary amine terminus provides a flexible method of conjugating the ligand to numerous functional molecules and biomaterials including, but not limited to, GO. In the timescales of the project this unfortunately was not possible, and improved stability of GO flakes with short PEG chains would be required. However, future work is planned in which BAT1 will be conjugated to liposomes to target therapeutics to CLL; while GFNs provide a

model that is very promising, the immaturity of the field means that significant research is still required before their application in a clinical setting. The flexibility of BAT1 means that it may be applied to numerous biomaterials, and the use of liposomes provides a more developed therapeutics delivery vehicle, which can accelerate application of BAT1 into a clinical setting.

7 References

[1] C. McCallion, J. Burthem, K. Rees-Unwin, A. Golovanov, and A. Pluen, "Graphene in therapeutics delivery: Problems, solutions and future opportunities," *European Journal of Pharmaceutics and Biopharmaceutics,* vol. 104, pp. 235-250, Jul 2016.

[2] H. Hillaireau and P. Couvreur, "Nanocarriers' entry into the cell: relevance to drug delivery," *Cellular and Molecular Life Sciences,* vol. 66, no. 17, pp. 2873-2896, Sep 2009.

[3] G. Sahay, D. Y. Alakhova, and A. V. Kabanov, "Endocytosis of nanomedicines," *Journal of Controlled Release,* vol. 145, no. 3, pp. 182-195, Aug 3 2010.

[4] T. M. Allen and P. R. Cullis, "Liposomal drug delivery systems: From concept to clinical applications," *Advanced Drug Delivery Reviews,* vol. 65, no. 1, pp. 36-48, Jan 2013.

[5] J. M. Ageitos, et al., "Design Considerations for Properties of Nanocarriers on Disposition and Efficiency of Drug and Gene Delivery," *Nanomedicines: Design, Delivery and Detection,* RSC Drug Discovery Series, no. 51, pp. 1-354, 2016.

[6] A. Schroeder, C. G. Levins, C. Cortez, R. Langer, and D. G. Anderson, "Lipid-based nanotherapeutics for siRNA delivery," *Journal of Internal Medicine,* vol. 267, no. 1, pp. 9-21, Jan 2010.

[7] A. Hatefi and B. F. Canine, "Perspectives in vector development for systemic cancer gene therapy," *Gene Therapy and Molecular Biology,* vol. 13, no. 1, pp. 15-19, Jun 2009.

[8] E. Mastrobattista, M. van der Aa, W. E. Hennink, and D. J. A. Crommelin, "Artificial viruses: a nanotechnological approach to gene delivery,", *Nature Reviews Drug Discovery,* Article vol. 5, no. 2, pp. 115-121, Feb 2006.

[9] D. Lechardeur, A. S. Verkman, and G. L. Lukacs, "Intracellular routing of plasmid DNA during non-viral gene transfer," , *Advanced Drug Delivery Reviews,* Review vol. 57, no. 5, pp. 755-767, Apr 2005.

[10] K. M. Wagstaff and D. A. Jans, "Nucleocytoplasmic transport of DNA: enhancing non-viral gene transfer," *Biochemical Journal,* vol. 406, pp. 185-202, Sep 1 2007.

[11] Y. Arthanari, A. Pluen, R. Rajendran, H. Aojula, and C. Demonacos, "Delivery of therapeutic shRNA and siRNA by Tat fusion peptide targeting bcr-abl fusion gene in Chronic Myeloid Leukemia cells," *Journal of Controlled Release,* vol. 145, no. 3, pp. 272-280, Aug 3 2010.

[12] Z. Liu, J. T. Robinson, S. M. Tabakman, K. Yang, and H. Dai, "Carbon materials for drug delivery & cancer therapy," *Materials Today,* vol. 14, no. 7-8, pp. 316-323, Jul-Aug 2011.

[13] Z. Liu, S. Tabakman, K. Welsher, and H. Dai, "Carbon Nanotubes in Biology and Medicine: In vitro and in vivo Detection, Imaging and Drug Delivery," *Nano Research,* vol. 2, no. 2, pp. 85-120, Feb 2009.

[14] M. Prato, K. Kostarelos, and A. Bianco, "Functionalized carbon nanotubes in drug design and discovery," *Accounts of Chemical Research,* vol. 41, no. 1, pp. 60-68, Jan 2008.

[15] N. W. S. Kam, Z. Liu, and H. J. Dai, "Functionalization of carbon nanotubes via cleavable disulfide bonds for efficient intracellular delivery of siRNA and potent gene silencing," *Journal of the American Chemical Society,* vol. 127, no. 36, pp. 12492-12493, Sep 14 2005.

[16] A. K. Geim and K. S. Novoselov, "The rise of graphene," *Nature Materials,* vol. 6, no. 3, pp. 183-191, Mar 2007.

[17] C. F. Lopez, S. O. Nielsen, P. B. Moore, and M. L. Klein, "Understanding nature's design for a nanosyringe," *Proceedings of the National Academy of Sciences of the United States of America,* vol. 101, no. 13, pp. 4431-4434, Mar 30 2004.

[18] K. Kostarelos *et al.*, "Cellular uptake of functionalized carbon nanotubes is independent of functional group and cell type," *Nature Nanotechnology,* vol. 2, no. 2, pp. 108-113, Feb 2007.

[19] L. Lacerda *et al.*, "Translocation mechanisms of chemically functionalised carbon nanotubes across plasma membranes," *Biomaterials,* vol. 33, no. 11, pp. 3334-3343, Apr 2012.

[20] A. Bianco, "Graphene: Safe or Toxic? The Two Faces of the Medal,", *Angewandte Chemie-International Edition,* Review vol. 52, no. 19, pp. 4986-4997, 2013.

[21] A. Battigelli, C. Menard-Moyon, T. Da Ros, M. Prato, and A. Bianco, "Endowing carbon nanotubes with biological and biomedical properties by chemical modifications," *Advanced Drug Delivery Reviews,* vol. 65, no. 15, pp. 1899-1920, Dec 2013.

[22] T. Itkin *et al.*, "Distinct bone marrow blood vessels differentially regulate haematopoiesis," *Nature,* vol. 532, no. 7599, pp. 323-328, Apr 2016.

[23] L. Scarfo, A. J. M. Ferreri, and P. Ghia, "Chronic lymphocytic leukaemia," *Critical Reviews in Oncology Hematology,* vol. 104, pp. 169-182, Aug 2016.

[24] S. H. Faderl and H. Kantarjian, *"*Chronic Lymphocytic Leukemia", *Leukemias : principles and practice of therapy*, Wiley-Blackwell, pp. 297-339, 2011.

[25] S. Malek, *Advances in Chronic Lymphocytic Leukemia* (Advances in Experimental Medicine and Biology v.792). 2013.

[26] J. Barretina *et al.*, "CXCR4 and SDF-1 expression in B-cell chronic lymphocytic leukemia and stage of the disease," *Annals of Hematology,* vol. 82, no. 8, pp. 500-505, Aug 2003.

[27] R. Mohle, C. Failenschmid, F. Bautz, and L. Kanz, "Overexpression of the chemokine receptor CXCR4 in B cell chronic lymphocytic leukemia is associated with increased functional response to stromal cell-derived factor-1 (SDF-1)," *Leukemia,* vol. 13, no. 12, pp. 1954-1959, Dec 1999.

[28] A. Ciesielski *et al.*, "Harnessing the Liquid-Phase Exfoliation of Graphene Using Aliphatic Compounds: A Supramolecular Approach," *Angewandte Chemie-International Edition,* vol. 53, no. 39, pp. 10355-10361, Sep 2014.

[29] U. Khan, H. Porwal, A. O'Neill, K. Nawaz, P. May, and J. Coleman, "Solvent-Exfoliated Graphene at Extremely High Concentration," *Langmuir,* Article vol. 27, no. 15, pp. 9077-9082, 2011.

[30] M. Lotya, P. King, U. Khan, S. De, and J. Coleman, "High-Concentration, Surfactant-Stabilized Graphene Dispersions," *ACS Nano,* Article vol. 4, no. 6, pp. 3155-3162, 2010.

[31] D. R. Dreyer, S. Park, C. W. Bielawski, and R. S. Ruoff, "The chemistry of graphene oxide," *Chemical Society Reviews,* vol. 39, no. 1, pp. 228-240, 2010.

[32] O. Pupysheva, A. Farajian, C. Knick, A. Zhamu, and B. Jang, "Modeling Direct Exfoliation of Nanoscale Graphene Platelets," *Journal of Physical Chemistry C,* Article vol. 114, no. 49, pp. 21083-21087, 2010.

[33] J.-L. Capelo-Martínez, *Ultrasound in chemistry : analytical applications*, Wiley-VCH, 2009.

[34] T. Leong, M. Ashokkumar, and S. Kentish, "The Fundamentals of Power Ultrasound – A Review" *Acoustics Australia,* vol. 39, no. 2, pp. 54-63, Aug 2011.

[35] Y. Hernandez *et al.*, "High-yield production of graphene by liquid-phase exfoliation of graphite," *Nature Nanotechnology,* vol. 3, no. 9, pp. 563-568, Sep 2008.

[36] S. Sahoo, G. Hatui, P. Bhattacharya, S. Dhibar, and C. K. Das, "One pot synthesis of graphene by exfoliation of graphite in ODCB," *Scientific Research,* vol. 2, pp. 42-48, 2013.

[37] A. O'Neill, U. Khan, P. N. Nirmalraj, J. Boland, and J. N. Coleman, "Graphene Dispersion and Exfoliation in Low Boiling Point Solvents," *Journal of Physical Chemistry C,* vol. 115, no. 13, pp. 5422-5428, Apr 2011.

[38] G. P. Keeley, A. O'Neill, N. McEvoy, N. Peltekis, J. N. Coleman, and G. S. Duesberg, "Electrochemical ascorbic acid sensor based on DMF-exfoliated graphene," *Journal of Materials Chemistry,* vol. 20, no. 36, pp. 7864-7869, 2010.

[39] H. Yang *et al.*, "A simple method for graphene production based on exfoliation of graphite in water using 1-pyrenesulfonic acid sodium salt," *Carbon,* vol. 53, pp. 357-365, Mar 2013.

[40] X. H. An *et al.*, "Stable Aqueous Dispersions of Noncovalently Functionalized Graphene from Graphite and their Multifunctional High-Performance Applications," *Nano Letters,* vol. 10, no. 11, pp. 4295-4301, Nov 2010.

[41] M. Zhang *et al.*, "Production of Graphene Sheets by Direct Dispersion with Aromatic Healing Agents," *Small,* vol. 6, no. 10, pp. 1100-1107, May 2010.

[42] D. Parviz, S. Das, H. S. T. Ahmed, F. Irin, S. Bhattacharia, and M. J. Green, "Dispersions of Non-Covalently Functionalized Graphene with Minimal Stabilizer," *ACS Nano,* vol. 6, no. 10, pp. 8857-8867, Oct 2012.

[43] Q. Su, S. P. Pang, V. Alijani, C. Li, X. L. Feng, and K. Mullen, "Composites of Graphene with Large Aromatic Molecules," *Advanced Materials,* vol. 21, no. 31, pp. 3191-3195, Aug 2009.
[44] S. De *et al.*, "Flexible, Transparent, Conducting Films of Randomly Stacked Graphene from Surfactant-Stabilized, Oxide-Free Graphene Dispersions," *Small,* vol. 6, no. 3, pp. 458-464, Feb 2010.
[45] V. Leon *et al.*, "Few-layer graphenes from ball-milling of graphite with melamine," *Chemical Communications,* vol. 47, no. 39, pp. 10936-10938, 2011.
[46] M. Lotya *et al.*, "Liquid Phase Production of Graphene by Exfoliation of Graphite in Surfactant/Water Solutions," *Journal of the American Chemical Society,* Article vol. 131, no. 10, pp. 3611-3620, Mar 2009.
[47] Y. F. Li *et al.*, "Graphene microsheets enter cells through spontaneous membrane penetration at edge asperities and corner sites," *Proceedings of the National Academy of Sciences of the United States of America,* vol. 110, no. 30, pp. 12295-12300, Jul 2013.
[48] J.-W. T. Seo, A. A. Green, A. L. Antaris, and M. C. Hersam, "High-Concentration Aqueous Dispersions of Graphene Using Nonionic, Biocompatible Block Copolymers," *Journal of Physical Chemistry Letters,* vol. 2, no. 9, pp. 1004-1008, May 5 2011.
[49] H. A. X. Cai and P. Yao, "Gold nanoparticles with different amino acid surfaces: Serum albumin adsorption, intracellular uptake and cytotoxicity," *Colloids and Surfaces B-Biointerfaces,* vol. 123, pp. 900-906, Nov 2014.
[50] K. Dubey *et al.*, "Tyrosine- and tryptophan-coated gold nanoparticles inhibit amyloid aggregation of insulin," *Amino Acids,* vol. 47, no. 12, pp. 2551-2560, Dec 2015.
[51] J. Guo, L. Ren, R. Wang, C. Zhang, Y. Yang, and T. Liu, "Water dispersible graphene noncovalently functionalized with tryptophan and its poly(vinyl alcohol) nanocomposite," *Composites Part B-Engineering,* vol. 42, no. 8, pp. 2130-2135, Dec 2011.
[52] S. Mallakpour, A. Abdolmaleki, and S. Borandeh, "Covalently functionalized graphene sheets with biocompatible natural amino acids," *Applied Surface Science,* vol. 307, pp. 533-542, Jul 2014.
[53] K. Torii and Y. Iitaka, "Crystal structure of L-Valine," *Acta Crystallographica Section B-Structural Crystallography and Crystal Chemistry,* Article vol. B 26, pp. 1317-&, 1970 1970.
[54] C. Rajesh, C. Majumder, H. Mizuseki, and Y. Kawazoe, "A theoretical study on the interaction of aromatic amino acids with graphene and single walled carbon nanotube," *Journal of Chemical Physics,* vol. 130, no. 12, Mar 28 2009, Art. no. 124911.
[55] N. Dragneva, W. B. Floriano, D. Stauffer, R. C. Mawhinney, G. Fanchini, and O. Rubel, "Favorable adsorption of capped amino acids on graphene substrate driven by desolvation effect," (in English), *Journal of Chemical Physics,* Article vol. 139, no. 17, p. 6, Nov 2013, Art. no. 174711.
[56] H. Vovusha, S. Sanyal, and B. Sanyal, "Interaction of Nucleobases and Aromatic Amino Acids with Graphene Oxide and Graphene Flakes," *Journal of Physical Chemistry Letters,* vol. 4, no. 21, pp. 3710-3718, Nov 7 2013.
[57] Y. Q. Sun *et al.*, "Large scale preparation of graphene quantum dots from graphite with tunable fluorescence properties," *Physical Chemistry Chemical Physics,* vol. 15, no. 24, pp. 9907-9913, 2013.
[58] D. Li, M. B. Muller, S. Gilje, R. B. Kaner, and G. G. Wallace, "Processable aqueous dispersions of graphene nanosheets," *Nature Nanotechnology,* vol. 3, no. 2, pp. 101-105, Feb 2008.
[59] C. Casiraghi *et al.*, "Rayleigh imaging of graphene and graphene layers," *Nano Letters,* vol. 7, no. 9, pp. 2711-2717, Sep 2007.
[60] C. Backes *et al.*, "Spectroscopic metrics allow in situ measurement of mean size and thickness of liquid-exfoliated few-layer graphene nanosheets," *Nanoscale,* vol. 8, no. 7, pp. 4311-4323, 2016.
[61] U. Khan, A. O'Neill, M. Lotya, S. De, and J. Coleman, "High-Concentration Solvent Exfoliation of Graphene," *Small,* Article vol. 6, no. 7, pp. 864-871, 2010.
[62] D. Shaw, *Introduction to Colloid and Surface Chemistry*, Fourth ed. Elsevier, 1992, p. 306.

[63] J. Koetz and S. Kosmella, "Polyelectrolytes and Nanoparticles," *Polyelectrolytes and Nanoparticles,* pp. 1-105, 2007.
[64] M. Lotya, A. Rakovich, J. F. Donegan, and J. N. Coleman, "Measuring the lateral size of liquid-exfoliated nanosheets with dynamic light scattering," *Nanotechnology,* vol. 24, no. 26, Jul 2013.
[65] N. Jalili and K. Laxminarayana, "A review of atomic force microscopy imaging systems: application to molecular metrology and biological sciences," *Mechatronics,* vol. 14, no. 8, pp. 907-945, Oct 2004.
[66] U. Khan, A. O'Neill, H. Porwal, P. May, K. Nawaz, and J. N. Coleman, "Size selection of dispersed, exfoliated graphene flakes by controlled centrifugation," *Carbon,* vol. 50, no. 2, pp. 470-475, Feb 2012.
[67] T. E. Needham, A. N. Paruta, and Gerraugh.Rj, "Solubility of amino acids in pure solvent systems," *Journal of Pharmaceutical Sciences,* vol. 60, no. 4, pp. 565-&, 1971.
[68] P. B. Stathopulos, G. A. Scholz, Y. M. Hwang, J. A. O. Rumfeldt, J. R. Lepock, and E. M. Meiering, "Sonication of proteins causes formation of aggregates that resemble amyloid," *Protein Science,* vol. 13, no. 11, pp. 3017-3027, Nov 2004.
[69] C. H. B. Ng and W. Y. Fan, "Colloidal Beading: Sonication-Induced Stringing of Selenium Particles," *Langmuir,* vol. 30, no. 25, pp. 7313-7318, Jul 2014.
[70] P. Blake *et al.*, "Making graphene visible," *Applied Physics Letters,* vol. 91, no. 6, Aug 2007.
[71] Z. H. Chen, Y. M. Lin, M. J. Rooks, and P. Avouris, "Graphene nano-ribbon electronics," *Physica E-Low-Dimensional Systems & Nanostructures,* vol. 40, no. 2, pp. 228-232, Dec 2007.
[72] D. A. Jasim, C. Menard-Moyon, D. Begin, A. Bianco, and K. Kostarelos, "Tissue distribution and urinary excretion of intravenously administered chemically functionalized graphene oxide sheets," *Chemical Science,* vol. 6, no. 7, pp. 3952-3964, 2015.
[73] H. Ali-Boucetta, D. Bitounis, R. Raveendran-Nair, A. Servant, J. Van den Bossche, and K. Kostarelos, "Purified Graphene Oxide Dispersions Lack In Vitro Cytotoxicity and In Vivo Pathogenicity," *Advanced Healthcare Materials,* Article vol. 2, no. 3, pp. 433-441, Mar 2013.
[74] *The Merck index online: an encyclopedia of chemicals, drugs and biologicals*, RSC online. Available: https://www.rsc.org/merck-index?e=1 [Accessed: July 2013]
[75] D. A. Williams and T. L. Lemke, *Foye's principles of medicinal chemistry*, Lipincott Williams & Wilkins, 2002.
[76] S. Wang, M. Yi, and Z. G. Shen, "The effect of surfactants and their concentration on the liquid exfoliation of graphene," *Rsc Advances,* vol. 6, no. 61, pp. 56705-56710, 2016.
[77] Y. J. Lee *et al.*, "Structural rearrangement and dispersion of functionalized graphene sheets in aqueous solutions," *Colloid and Interface Science Communications,* vol. 8, pp. 1-5, Sep 2015.
[78] L. Adler-Abramovich *et al.*, "Phenylalanine assembly into toxic fibrils suggests amyloid etiology in phenylketonuria," *Nature Chemical Biology,* vol. 8, no. 8, pp. 701-706, Aug 2012.
[79] S. Perween, B. Chandanshive, H. C. Kotamarthi, and D. Khushalani, "Single amino acid based self-assembled structure," *Soft Matter,* vol. 9, no. 42, pp. 10141-10145, 2013.
[80] E. Y. Polyakova *et al.*, "Scanning Tunneling Microscopy and X-ray Photoelectron Spectroscopy Studies of Graphene Films Prepared by Sonication-Assisted Dispersion," *Acs Nano,* vol. 5, no. 8, pp. 6102-6108, Aug 2011.
[81] J. Russier *et al.*, "Evidencing the mask effect of graphene oxide: a comparative study on primary human and murine phagocytic cells," (in English), *Nanoscale,* Article vol. 5, no. 22, pp. 11234-11247, 2013.
[82] T. Skaltsas, X. Ke, C. Bittencourt, and N. Tagmatarchis, "Ultrasonication Induces Oxygenated Species and Defects onto Exfoliated Graphene," *The Journal of Physical Chemistry C,* 2013.
[83] A. Bellunato, H. A. Tash, Y. Cesa, and G. F. Schneider, "Chemistry at the Edge of Graphene," *Chemphyschem,* vol. 17, no. 6, pp. 785-801, Mar 2016.

[84] O. Akhavan, E. Ghaderi, and A. Akhavan, "Size-dependent genotoxicity of graphene nanoplatelets in human stem cells," *Biomaterials,* vol. 33, no. 32, pp. 8017-8025, Nov 2012.
[85] O. Akhavan, E. Ghaderi, H. Emamy, and F. Akhavan, "Genotoxicity of graphene nanoribbons in human mesenchymal stem cells," *Carbon,* vol. 54, pp. 419-431, Apr 2013.
[86] W. F. Zhao, F. E. Wu, H. Wu, and G. H. Chen, "Preparation of Colloidal Dispersions of Graphene Sheets in Organic Solvents by Using Ball Milling," *Journal of Nanomaterials,* 2010.
[87] K. R. Paton *et al.*, "Scalable production of large quantities of defect-free few-layer graphene by shear exfoliation in liquids," *Nature Materials,* vol. 13, no. 6, pp. 624-630, Jun 2014.
[88] T. Ramanathan *et al.*, "Functionalized graphene sheets for polymer nanocomposites," *Nature Nanotechnology,* vol. 3, no. 6, pp. 327-331, Jun 2008.
[89] L. Liu, Z. G. Shen, M. Yi, X. J. Zhang, and S. L. Ma, "A green, rapid and size-controlled production of high-quality graphene sheets by hydrodynamic forces," *Rsc Advances,* vol. 4, no. 69, pp. 36464-36470, 2014.
[90] E. Varrla *et al.*, "Turbulence-assisted shear exfoliation of graphene using household detergent and a kitchen blender," *Nanoscale,* vol. 6, no. 20, pp. 11810-11819, 2014.
[91] B. Paulchamy, G. Arthi, and B. Lignesh, "A simple approach to stepwise synthesis of graphene oxide nanomaterial," *Journal of Nanomedicine and Nanotechnology,* 2015.
[92] A. M. Dimiev and T. A. Polson, "Contesting the two-component structural model of graphene oxide and reexamining the chemistry of graphene oxide in basic media," *Carbon,* vol. 93, pp. 544-554, Nov 2015.
[93] K. P. Loh, Q. L. Bao, G. Eda, and M. Chhowalla, "Graphene oxide as a chemically tunable platform for optical applications," *Nature Chemistry,* vol. 2, no. 12, pp. 1015-1024, Dec 2010.
[94] J. P. Rourke *et al.*, "The Real Graphene Oxide Revealed: Stripping the Oxidative Debris from the Graphene-like Sheets," *Angewandte Chemie-International Edition,* vol. 50, no. 14, pp. 3173-3177, 2011.
[95] K. Loh, Q. Bao, P. Ang, and J. Yang, "The chemistry of graphene," *Journal of Materials Chemistry,* Article vol. 20, no. 12, pp. 2277-2289, 2010.
[96] H. R. Thomas, C. Valles, R. J. Young, I. A. Kinloch, N. R. Wilson, and J. P. Rourke, "Identifying the fluorescence of graphene oxide," *Journal of Materials Chemistry C,* vol. 1, no. 2, pp. 338-342, 2013.
[97] S. H. Dave, C. Gong, A. w. Robertson, J. H. Warner, and J. C. Grossman, "Chemistry and Structure of Graphene Oxide via Direct Imaging," *ACS Nano,* vol. 10, no. 8, pp. 7515-7522, 2016.
[98] C.-H. Lu, C.-L. Zhu, J. Li, J.-J. Liu, X. Chen, and H.-H. Yang, "Using graphene to protect DNA from cleavage during cellular delivery," *Chemical Communications,* vol. 46, no. 18, pp. 3116-3118, 2010.
[99] R. S. Swathi and K. L. Sebastian, "Long range resonance energy transfer from a dye molecule to graphene has (distance)(-4) dependence," *Journal of Chemical Physics,* Letter vol. 130, no. 8, p. 3, Feb 2009
[100] L. Yang, C. H. Liu, W. Ren, and Z. P. Li, "Graphene Surface-Anchored Fluorescence Sensor for Sensitive Detection of MicroRNA Coupled with Enzyme-Free Signal Amplification of Hybridization Chain Reaction," *ACS Applied Materials & Interfaces,* Article vol. 4, no. 12, pp. 6450-6453, Dec 2012.
[101] X. Sun *et al.*, "Nano-Graphene Oxide for Cellular Imaging and Drug Delivery," *Nano Research,* vol. 1, no. 3, pp. 203-212, Sep 2008.
[102] Z. T. Luo, P. M. Vora, E. J. Mele, A. T. C. Johnson, and J. M. Kikkawa, "Photoluminescence and band gap modulation in graphene oxide," *Applied Physics Letters,* vol. 94, no. 11, Mar 2009.
[103] C. T. Chien *et al.*, "Tunable Photoluminescence from Graphene Oxide," *Angewandte Chemie-International Edition,* vol. 51, no. 27, pp. 6662-6666, 2012.

[104] J. Z. Shang, L. Ma, J. W. Li, W. Ai, T. Yu, and G. G. Gurzadyan, "The Origin of Fluorescence from Graphene Oxide," *Scientific Reports,* vol. 2, Nov 2012.
[105] H. Yue *et al.*, "The role of the lateral dimension of graphene oxide in the regulation of cellular responses," *Biomaterials,* vol. 33, no. 16, pp. 4013-4021, Jun 2012.
[106] Z. Liu, J. T. Robinson, X. Sun, and H. Dai, "PEGylated nanographene oxide for delivery of water-insoluble cancer drugs," *Journal of the American Chemical Society,* vol. 130, no. 33, pp. 10876-10877, Aug 20 2008.
[107] S. K. Singh, M. K. Singh, M. K. Nayak, S. Kumari, J. J. A. Gracio, and D. Dash, "Size distribution analysis and physical/fluorescence characterization of graphene oxide sheets by flow cytometry," *Carbon,* vol. 49, no. 2, pp. 684-692, Feb 2011.
[108] Z. Hamrang, A. Pluen, E. Zindy, and D. Clarke, "Raster image correlation spectroscopy as a novel tool for the quantitative assessment of protein diffusional behaviour in solution," *Journal of Pharmaceutical Sciences,* vol. 101, no. 6, pp. 2082-2093, Jun 2012.
[109] Z. Hamrang *et al.*, "Characterisation of Stress-Induced Aggregate Size Distributions and Morphological Changes of a Bi-Specific Antibody Using Orthogonal Techniques," *Journal of Pharmaceutical Sciences,* vol. 104, no. 8, pp. 2473-2481, Aug 2015.
[110] S. Das *et al.*, "Oxygenated Functional Group Density on Graphene Oxide: Its Effect on Cell Toxicity," *Particle & Particle Systems Characterization,* Article vol. 30, no. 2, pp. 148-157, Feb 2013.
[111] A. Sasidharan *et al.*, "Differential nano-bio interactions and toxicity effects of pristine versus functionalized graphene," *Nanoscale,* vol. 3, no. 6, pp. 2461-2464, 2011 2011.
[112] H. P. Koeffler and D. W. Golde, "Human Myeloid-Leukemia cell lines – a review," *Blood,* vol. 56, no. 3, pp. 344-350, 1980.
[113] J. Melo, T. Hughes, and J. Apperly, "Chronic Myeloid Leukaemia," *Hematology Am Soc Hematol Educ Program*, pp. 132-152, 2003
[114] K. Yang, L. Feng, H. Hong, W. Cai, and Z. Liu, "Preparation and functionalization of graphene nanocomposites for biomedical applications," *Nature Protocols,* vol. 8, no. 12, pp. 2392-2403, Dec 2013.
[115] S. Hofmann, *Auger- and X-ray photoelectron spectroscopy in materials science : a user-oriented guide,* Springer series in surface sciences 49, 2013.
[116] C. Kittel, *Introduction to solid state physics*, 8th Ed., Wiley, 2005.
[117] J. I. Paredes, S. Villar-Rodil, A. Martinez-Alonso, and J. M. D. Tascon, "Graphene oxide dispersions in organic solvents," *Langmuir,* vol. 24, no. 19, pp. 10560-10564, Oct 7 2008.
[118] M. A. Digman, P. Sengupta, P. W. Wiseman, C. M. Brown, A. R. Horwitz, and E. Gratton, "Fluctuation correlation spectroscopy with a laser-scanning microscope: Exploiting the hidden time structure," *Biophysical Journal,* vol. 88, no. 5, pp. L33-L36, May 2005.
[119] M. A. Digman, C. M. Brown, P. Sengupta, P. W. Wiseman, A. R. Horwitz, and E. Gratton, "Measuring fast dynamics in solutions and cells with a laser scanning microscope," *Biophysical Journal,* vol. 89, no. 2, pp. 1317-1327, Aug 2005.
[120] X. F. Cao *et al.*, "Functionalized Graphene Oxide with Hepatocyte Targeting as Anti-Tumor Drug and Gene Intracellular Transporters," *Journal of Nanoscience and Nanotechnology,* Article vol. 15, no. 3, pp. 2052-2059, Mar 2015.
[121] R. Imani, S. H. Emami, and S. Faghihi, "Nano-graphene oxide carboxylation for efficient bioconjugation applications: a quantitative optimization approach," *Journal of Nanoparticle Research,* Article vol. 17, no. 2, p. 15, Feb 2015.
[122] R. Imani, S. H. Emami, and S. Faghihi, "Synthesis and characterization of an octaarginine functionalized graphene oxide nano-carrier for gene delivery applications," *Physical Chemistry Chemical Physics,* Article vol. 17, no. 9, pp. 6328-6339, 2015.
[123] T. Lammel, P. Boisseaux, M. L. Fernandez-Cruz, and J. M. Navas, "Internalization and cytotoxicity of graphene oxide and carboxyl graphene nanoplatelets in the human hepatocellular carcinoma cell line Hep G2," *Particle and Fibre Toxicology,* Article vol. 10, p. 21, Jul 2013.
[124] A. Bachmatiuk, "Characterisation Techniques," *Graphene: Fundamentals and Emergent Applications,* pp. 229-237, 2013.

[125] M. J. Feito *et al.*, "In vitro evaluation of graphene oxide nanosheets on immune function," *Journal of Colloid and Interface Science,* vol. 432, pp. 221-228, Oct 2014.
[126] H. Bao *et al.*, "Chitosan-Functionalized Graphene Oxide as a Nanocarrier for Drug and Gene Delivery," *Small,* vol. 7, no. 11, pp. 1569-1578, Jun 6 2011.
[127] S. Ahadian *et al.*, "Facile and green production of aqueous graphene dispersions for biomedical applications," *Nanoscale,* Article vol. 7, no. 15, pp. 6436-6443, 2015.
[128] Y. J. Li *et al.*, "Surface Coating-Dependent Cytotoxicity and Degradation of Graphene Derivatives: Towards the Design of Non-Toxic, Degradable Nano-Graphene," *Small,* vol. 10, no. 8, pp. 1544-1554, Apr 2014.
[129] H. Kim and W. J. Kim, "Photothermally Controlled Gene Delivery by Reduced Graphene Oxide-Polyethylenimine Nanocomposite," *Small,* vol. 10, no. 1, pp. 117-126, Jan 15 2014.
[130] M. Rothe, T. Gruber, S. Groger, J. Balbach, K. Saalwachter, and M. Roos, "Transient binding accounts for apparent violation of the generalized Stokes-Einstein relation in crowded protein solutions," *Physical Chemistry Chemical Physics,* vol. 18, no. 27, pp. 18006-18014, Jul 2016.
[131] M. I. Mishchenko, J. W. Hovenier, and L. D. Travis, “Light scattering by nonspherical particles : theory, measurements, and applications”, *Measurement Science and Technology*, Vol. 11, No. 12, 2000.
[132] M. I. Mishchenko and L. D. Travis, "Intensity and polarization of light scattered by size distributions of randomly oriented nonspherical particles," presented at the Progress in Electromagnetics Research Symposium, Jet Propulsion Laboratory, NASA, USA, 1993.
[133] A. Chandra, S. Deshpande, D. B. Shinde, V. K. Pillai, and N. Singh, "Mitigating the Cytotoxicity of Graphene Quantum Dots and Enhancing Their Applications in Bioimaging and Drug Delivery," *ACS Macro Letters,* Article vol. 3, no. 10, pp. 1064-1068, Oct 2014.
[134] L. Z. Feng, K. Y. Li, X. Z. Shi, M. Gao, J. Liu, and Z. Liu, "Smart pH-Responsive Nanocarriers Based on Nano-Graphene Oxide for Combined Chemo- and Photothermal Therapy Overcoming Drug Resistance," *Advanced Healthcare Materials,* Article vol. 3, no. 8, pp. 1261-1271, Aug 2014.
[135] T. L. Moore, R. Podilakrishna, A. Rao, and F. Alexis, "Systemic Administration of Polymer-Coated Nano-Graphene to Deliver Drugs to Glioblastoma," *Particle & Particle Systems Characterization,* Article vol. 31, no. 8, pp. 886-894, Aug 2014.
[136] X. F. Tan *et al.*, "Functionalization of Graphene Oxide Generates a Unique Interface for Selective Serum Protein Interactions," *ACS Applied Materials & Interfaces,* Article vol. 5, no. 4, pp. 1370-1377, Feb 2013.
[137] S. K. Singh, M. K. Singh, P. P. Kulkarni, V. K. Sonkar, J. J. A. Gracio, and D. Dash, "Amine-Modified Graphene. Thrombo-Protective Safer Alternative to Graphene Oxide for Biomedical Applications," *Acs Nano,* vol. 6, no. 3, pp. 2731-2740, Mar 2012.
[138] N. Han *et al.*, "Improved heat dissipation in gallium nitride light-emitting diodes with embedded graphene oxide pattern," *Nature Communications,* vol. 4, Feb 2013.
[139] S. C. Wu, G. D. Wen, R. Schlogl, and D. S. Su, "Carbon nanotubes oxidized by a green method as efficient metal-free catalysts for nitroarene reduction," *Physical Chemistry Chemical Physics,* vol. 17, no. 3, pp. 1567-1571, 2015.
[140] B. Yu *et al.*, "Functionalized graphene oxide/phosphoramide oligomer hybrids flame retardant prepared via in situ polymerization for improving the fire safety of polypropylene," *Rsc Advances,* vol. 4, no. 60, pp. 31782-31794, 2014.
[141] C. A. Tao *et al.*, "Fabrication of pH-sensitive graphene oxide-drug supramolecular hydrogels as controlled release systems," *Journal of Materials Chemistry,* vol. 22, no. 47, pp. 24856-24861, 2012.
[142] C. K. Chua, A. Ambrosi, and M. Pumera, "Graphene oxide reduction by standard industrial reducing agent: thiourea dioxide," *Journal of Materials Chemistry,* vol. 22, no. 22, pp. 11054-11061, 2012.
[143] H. P. Viet *et al.*, "Chemical functionalization of graphene sheets by solvothermal reduction of a graphene oxide suspension in N-methyl-2-pyrrolidone," *Journal of Materials Chemistry,* vol. 21, no. 10, pp. 3371-3377, 2011.

[144] A. Ganguly, S. Sharma, P. Papakonstantinou, and J. Hamilton, "Probing the Thermal Deoxygenation of Graphene Oxide Using High-Resolution In Situ X-ray-Based Spectroscopies," *Journal of Physical Chemistry C,* vol. 115, no. 34, pp. 17009-17019, Sep 2011.

[145] N. Ajenjo, D. S. Aaronson, E. Ceballos, C. Richard, J. Leon, and P. Crespo, "Myeloid leukemia cell growth and differentiation are independent of mitogen-activated protein kinase ERK1/2 activation," *Journal of Biological Chemistry,* vol. 275, no. 10, pp. 7189-7197, Mar 2000.

[146] Y. H. Lee and C. A. Peng, "Enhanced retroviral gene delivery in ultrasonic standing wave fields," *Gene Therapy,* vol. 12, no. 7, pp. 625-633, Apr 2005.

[147] J. L. Lewis *et al.*, "The influence of INK4 proteins on growth and self-renewal kinetics of hematopoietic progenitor cells," *Blood,* vol. 97, no. 9, pp. 2604-2610, May 2001.

[148] S. Fujime and K. Kubota, "Dynamic light-light scattering from dilute suspensions of thin disks and thin rods as limiting forms of cylinder, ellipsoid and ellipsoidal shell of revolution," *Biophysical Chemistry,* vol. 23, no. 1-2, pp. 1-13, Nov 1985.

[149] K. Kubota, Y. Tominaga, S. Fujime, J. Otomo, and A. Ikegami, "Dynamic light-scatering study of suspensions of purple membrane," *Biophysical Chemistry,* vol. 23, no. 1-2, pp. 15-29, Nov 1985.

[150] C. Cheng *et al.*, "Biopolymer functionalized reduced graphene oxide with enhanced biocompatibility via mussel inspired coatings/anchors," *Journal of Materials Chemistry B,* vol. 1, no. 3, pp. 265-275, 2013.

[151] S. H. Li *et al.*, "Strong and Selective Adsorption of Lysozyme on Graphene Oxide," *ACS Applied Materials & Interfaces,* vol. 6, no. 8, pp. 5704-5712, Apr 2014.

[152] B. J. Hong, O. C. Compton, Z. An, I. Eryazici, and S. T. Nguyen, "Successful Stabilization of Graphene Oxide in Electrolyte Solutions: Enhancement of Biofunctionalization and Cellular Uptake," *Acs Nano,* vol. 6, no. 1, pp. 63-73, Jan 2012.

[153] L. Feng *et al.*, "Polyethylene Glycol and Polyethylenimine Dual-Functionalized Nano-Graphene Oxide for Photothermally Enhanced Gene Delivery," *Small,* vol. 9, no. 11, pp. 1989-1997, Jun 10 2013.

[154] Y. W. Liu, J. Bai, X. D. Jia, X. E. Jiang, and Z. Guo, "Fabrication of Multifunctional SiO2@GN-Serum Composites for Chemo-Photothermal Synergistic Therapy," *ACS Applied Materials & Interfaces,* Article vol. 7, no. 1, pp. 112-121, Jan 2015.

[155] J. R. Lakowicz, *Principles of fluorescence spectroscopy*, 3rd Ed., Springer, 2006.

[156] M. Chu *et al.*, "Biocompatible polyethylenimine-graft-dextran catiomer for highly efficient gene delivery assisted by a nuclear targeting ligand," *Polymer Chemistry,* vol. 4, no. 8, pp. 2528-2539, 2013.

[157] D. B. Williams and C. B. Carter, *Transmission electron microscopy : a textbook for materials science*, Springer, 2009.

[158] R. S. Pantelic, J. C. Meyer, U. Kaiser, and H. Stahlberg, "The application of graphene as a sample support in transmission electron microscopy," *Solid State Communications,* vol. 152, no. 15, pp. 1375-1382, Aug 2012.

[159] W. Zhang, Z. Guo, D. Huang, Z. Liu, X. Guo, and H. Zhong, "Synergistic effect of chemo-photothermal therapy using PEGylated graphene oxide," *Biomaterials,* vol. 32, no. 33, pp. 8555-8561, Nov 2011.

[160] S. K. Singh *et al.*, "Thrombus Inducing Property of Atomically Thin Graphene Oxide Sheets," *Acs Nano,* vol. 5, no. 6, pp. 4987-4996, Jun 2011.

[161] E. Hashemi, O. Akhavan, M. Shamsara, R. Rahighi, A. Esfandiar, and A. R. Tayefeh, "Cyto and genotoxicities of graphene oxide and reduced graphene oxide sheets on spermatozoa," *Rsc Advances,* vol. 4, no. 52, pp. 27213-27223, 2014.

[162] S. M. Chowdhury *et al.*, "In Vitro Hematological and In Vivo Vasoactivity Assessment of Dextran Functionalized Graphene," *Scientific Reports,* vol. 3, Sep 4 2013.

[163] S. M. Chowdhury, G. Lalwani, K. Zhang, J. Y. Yang, K. Neville, and B. Sitharaman, "Cell specific cytotoxicity and uptake of graphene nanoribbons," *Biomaterials,* vol. 34, no. 1, pp. 283-293, Jan 2013.

[164] C. M. Girish, A. Sasidharan, G. S. Gowd, S. Nair, and M. Koyakutty, "Confocal Raman Imaging Study Showing Macrophage Mediated Biodegradation of Graphene In Vivo," (in English), *Advanced Healthcare Materials,* Article vol. 2, no. 11, pp. 1489-1500, Nov 2013.
[165] A. Sasidharan *et al.*, "Hemocompatibility and Macrophage Response of Pristine and Functionalized Graphene," *Small,* vol. 8, no. 8, pp. 1251-1263, Apr 2012.
[166] Z. J. Ding, Z. J. Zhang, H. W. Ma, and Y. Y. Chen, "In Vitro Hemocompatibility and Toxic Mechanism of Graphene Oxide on Human Peripheral Blood T Lymphocytes and Serum Albumin," *ACS Applied Materials & Interfaces,* Article vol. 6, no. 22, pp. 19797-19807, Nov 2014.
[167] G.-Y. Chen *et al.*, "Simultaneous induction of autophagy and toll-like receptor signaling pathways by graphene oxide," *Biomaterials,* vol. 33, no. 27, pp. 6559-6569, Sep 2012.
[168] H. Zhou *et al.*, "The interactions between pristine graphene and macrophages and the production of cytokines/chemokines via TLR- and NF-kappa B-related signaling pathways," *Biomaterials,* vol. 33, no. 29, pp. 6933-6942, Oct 2012.
[169] O. Dienz and M. Rincon, "The effects of IL-6 on CD4 T cell responses," *Clinical Immunology,* vol. 130, no. 1, pp. 27-33, Jan 2009.
[170] U. M. Domanska *et al.*, "A review on CXCR4/CXCL12 axis in oncology: No place to hide," *European Journal of Cancer,* vol. 49, no. 1, pp. 219-230, Jan 2013.
[171] T. M. Calderon and J. W. Berman, "Overview and history of chemokines and their receptors," *Chemokines, Chemokine Receptors, and Disease,* vol. 55, pp. 1-47, 2005.
[172] Y. Wang, Y. Xie, and D. Oupicky, "Potential of CXCR4/CXCL12 Chemokine Axis in Cancer Drug Delivery," *Current Pharmacology Reports,* vol. 2, no. 1, pp. 1-10, 2016.
[173] B. Alberts and et al., *Molecular biology of the cell*, 4th Ed., Garland Science, 2002.
[174] A. J. Kastin, *Handbook of biologically active peptides*, Elsevier, 2006.
[175] R. K. Ganju *et al.*, "The alpha-chemokine, stromal cell-derived factor-1 alpha, binds to the transmembrane G-protein-coupled CXCR-4 receptor and activates multiple signal transduction pathways," *Journal of Biological Chemistry,* vol. 273, no. 36, pp. 23169-23175, Sep 1998.
[176] M. Burger *et al.*, "Small peptide inhibitors of the CXCR4 chemokine receptor (CD184) antagonize the activation, migration, and antiapoptotic responses of CXCL12 in chronic lymphocytic leukemia B cells," *Blood,* vol. 106, no. 5, pp. 1824-1830, Sep 1 2005.
[177] G. J. Bridger *et al.*, "Synthesis and structure-activity-relationships of phenylenebis(methylene)-linked bis-tetraazamacrocycles that inhibit HIV replication – effects of macrocyclic ring size and substituents on the aromatic linker," *Journal of Medicinal Chemistry,* vol. 38, no. 2, pp. 366-378, Jan 20 1995.
[178] E. De Clercq *et al.*, "Highly potent and selective-inhibition of human-immunodeficiency-virus by the bicyclam derivative JM3100," *Antimicrobial Agents and Chemotherapy,* vol. 38, no. 4, pp. 668-674, Apr 1994.
[179] Y. Inouye *et al.*, "Dimeric macrocyclic polyamines with potent inhibitory activity against human-immunodeficiency-virus," *Antiviral Chemistry & Chemotherapy,* vol. 6, no. 5, pp. 337-344, Sep 1995.
[180] C. Chittasupho, K. Lirdprapamongkol, P. Kewsuwan, and N. Sarisuta, "Targeted delivery of doxorubicin to A549 lung cancer cells by CXCR4 antagonist conjugated PLGA nanoparticles," *European Journal of Pharmaceutics and Biopharmaceutics,* vol. 88, no. 2, pp. 529-538, Oct 2014.
[181] W. H. P. Driessen, N. Fujii, H. Tamamura, and S. M. Sullivan, "Development of peptide-targeted lipoplexes to CXCR4-expressing rat glioma cells and rat proliferating endothelial cells," *Molecular Therapy,* vol. 16, no. 3, pp. 516-524, Mar 2008.
[182] A. Egorova, M. Bogacheva, A. Shubina, V. Baranov, and A. Kiselev, "Development of a receptor-targeted gene delivery system using CXCR4 ligand-conjugated cross-linking peptides," *Journal of Gene Medicine,* vol. 16, no. 11-12, pp. 336-351, Nov-Dec 2014.
[183] P. Guo, J. O. You, J. Yang, M. A. Moses, and D. T. Auguste, "Using breast cancer cell CXCR4 surface expression to predict liposome binding and cytotoxicity," *Biomaterials,* vol. 33, no. 32, pp. 8104-8110, Nov 2012.

[184] P. Guo, J. O. You, J. Yang, D. Jia, M. A. Moses, and D. T. Auguste, "Inhibiting Metastatic Breast Cancer Cell Migration via the Synergy of Targeted, pH-triggered siRNA Delivery and Chemokine Axis Blockade," *Molecular Pharmaceutics,* vol. 11, no. 3, pp. 755-765, Mar 2014.

[185] H. Hanaoka *et al.*, "Development of a In-111-labeled peptide derivative targeting a chemokine receptor, CXCR4, for imaging tumors," *Nuclear Medicine and Biology,* vol. 33, no. 4, pp. 489-494, May 2006.

[186] J. Li, Y. Zhu, S. T. Hazeldine, C. Li, and D. Oupicky, "Dual-Function CXCR4 Antagonist Polyplexes To Deliver Gene Therapy and Inhibit Cancer Cell Invasion," *Angewandte Chemie-International Edition,* vol. 51, no. 35, pp. 8740-8743, 2012.

[187] J. Li and D. Oupicky, "Effect of biodegradability on CXCR4 antagonism, transfection efficacy and antimetastatic activity of polymeric Plerixafor," *Biomaterials,* vol. 35, no. 21, pp. 5572-5579, Jul 2014.

[188] J. Li *et al.*, "Examination of Structure-Activity Relationship of Viologen-Based Dendrimers as CXCR4 Antagonists and Gene Carriers," *Bioconjugate Chemistry,* vol. 25, no. 5, pp. 907-917, May 2014.

[189] A. C. Misra, K. E. Luker, H. Durmaz, G. D. Luker, and J. Lahann, "CXCR4-Targeted Nanocarriers for Triple Negative Breast Cancers," *Biomacromolecules,* vol. 16, no. 8, pp. 2412-2417, Aug 2015.

[190] S. Poty *et al.*, "New AMD3100 derivatives for CXCR4 chemokine receptor targeted molecular imaging studies: synthesis, anti-HIV-1 evaluation and binding affinities," *Dalton Transactions,* vol. 44, no. 11, pp. 5004-5016, 2015.

[191] E. L. Snyder *et al.*, "Enhanced targeting and killing of tumor cells expressing the CXC chemokine receptor 4 by transducible anticancer peptides," *Cancer Research,* vol. 65, no. 23, pp. 10646-10650, Dec 2005.

[192] Y. Wang, J. Li, and D. Oupicky, "Polymeric Plerixafor: Effect of PEGylation on CXCR4 Antagonism, Cancer Cell Invasion, and DNA Transfection," *Pharmaceutical Research,* vol. 31, no. 12, pp. 3538-3548, Dec 2014.

[193] Y. Wang, J. Li, Y. Chen, and D. Oupicky, "Balancing polymer hydrophobicity for ligand presentation and siRNA delivery in dual function CXCR4 inhibiting polyplexes," *Biomaterials Science,* vol. 3, no. 7, pp. 1114-1123, 2015.

[194] Y. Wang, S. T. Hazeldine, J. Li, and D. Oupicky, "Development of Functional Poly(amido amine) CXCR4 Antagonists with the Ability to Mobilize Leukocytes and Deliver Nucleic Acids," *Advanced Healthcare Materials,* vol. 4, no. 5, pp. 729-738, Apr 2015.

[195] R. T. Wang, X. Y. Zhi, S. Y. Yao, and Y. Zhang, "LFC131 peptide-conjugated polymeric nanoparticles for the effective delivery of docetaxel in CXCR4 overexpressed lung cancer cells," *Colloids and Surfaces B-Biointerfaces,* vol. 133, pp. 43-50, Sep 2015.

[196] S. Nimmagadda, M. Pullambhatla, and M. G. Pomper, "Immunoimaging of CXCR4 Expression in Brain Tumor Xenografts Using SPECT/CT," *Journal of Nuclear Medicine,* vol. 50, no. 7, pp. 1124-1130, Jul 2009.

[197] B. Le Bon, N. Van Craynest, J. M. Daoudi, C. Di Giorgio, A. J. Domb, and P. Vierling, "AMD3100 conjugates as components of targeted nonviral gene delivery systems: Synthesis and in vitro transfection efficiency of CXCR4-expressing cells," *Bioconjugate Chemistry,* vol. 15, no. 2, pp. 413-423, Mar-Apr 2004.

[198] S. Poty *et al.*, "AMD3100: A Versatile Platform for CXCR4 Targeting Ga-68-Based Radiopharmaceuticals," *Bioconjugate Chemistry,* vol. 27, no. 3, pp. 752-761, Mar 2016.

[199] S. P. Fricker, "Physiology and Pharmacology of Plerixafor," *Transfusion Medicine and Hemotherapy,* vol. 40, no. 4, pp. 237-245, 2013.

[200] V. Amendola, G. Bergamaschi, L. Fabbrizzi, M. Licchelli, and C. Mangano, "The interaction of Mozobil (TM) with carboxylates," *Organic & Biomolecular Chemistry,* vol. 14, no. 3, pp. 905-912, 2016.

[201] L. O. Gerlach, R. T. Skerlj, G. J. Bridger, and T. W. Schwartz, "Molecular interactions of cyclam and bicyclam non-peptide antagonists with the CXCR4 chemokine receptor," *Journal of Biological Chemistry,* vol. 276, no. 17, pp. 14153-14160, Apr 27 2001.

[202] S. Hatse *et al.*, "Mutation of Asp(171) and Asp(262) of the chemokine receptor CXCR4 impairs its coreceptor function for human immunodeficiency virus-1 entry and abrogates the antagonistic activity of AMD3100," *Molecular Pharmacology,* vol. 60, no. 1, pp. 164-173, Jul 2001.

[203] L. Ginaldi, M. De Martinis, E. Matutes, N. Farahat, R. Morilla, and D. Catovsky, "Levels of expression of CD19 and CD20 in chronic B cell leukaemias," *Journal of Clinical Pathology,* vol. 51, no. 5, pp. 364-369, May 1998.

[204] D. Guillaume and G. R. Marshall, "Efficient one-pot synthesis of JM3100," *Synthetic Communications,* vol. 28, no. 15, pp. 2903-2906, 1998.

[205] E. Buncel and E. A. Symons, "Inherent instability of dimethylformamide-water systems containing hydroxide ion," *Journal of the Chemical Society D-Chemical Communications,* no. 3, pp. 164-165, 1970.

[206] S. H. Jin *et al.*, "Synthesis and EL properties of light-emitting polymers by Gilch polymerization," *Molecular Crystals and Liquid Crystals,* vol. 444, pp. 1-11, 2006.

[207] H. C. Yau, M. K. Bayazit, J. H. G. Steinke, and M. S. P. Shaffer, "Sonochemical degradation of N-methylpyrrolidone and its influence on single walled carbon nanotube dispersion," *Chemical Communications,* vol. 51, no. 93, pp. 16621-16624, 2015.

[208] D. H. Williams and I. Fleming, *Spectroscopic methods in organic chemistry*. 1995.

[209] G. R. Fulmer *et al.*, "NMR Chemical Shifts of Trace Impurities: Common Laboratory Solvents, Organics, and Gases in Deuterated Solvents Relevant to the Organometallic Chemist," *Organometallics,* vol. 29, no. 9, pp. 2176-2179, May 2010.

[210] K. J. R. Rosman and P. Taylor, "IUPAC Subcommittee for Isotopic Abundance Measurements," *Pure Applied Chemistry,* vol. 71, pp. 1593-1607, 1999.

[211] R. S. Macomber, *A complete introduction to modern NMR spectroscopy*, Wiley-Interscience, 1998.

[212] G. Badr, E. A. Lefevre, and M. Mohany, "Thymoquinone Inhibits the CXCL12-Induced Chemotaxis of Multiple Myeloma Cells and Increases Their Susceptibility to Fas-Mediated Apoptosis," *Plos One,* vol. 6, no. 9, Sep 2011.

[213] V. Coelho *et al.*, "Identification in CLL of circulating intraclonal subgroups with varying B-cell receptor expression and function," *Blood,* vol. 122, no. 15, pp. 2664-2672, Oct 2013.

[214] B. A. Teicher and S. P. Fricker, "CXCL12 (SDF-1)/CXCR4 Pathway in Cancer," *Clinical Cancer Research,* vol. 16, no. 11, pp. 2927-2931, Jun 2010.

[215] E. B. Cepeda *et al.*, "Mechanisms regulating cell membrane localization of the chemokine receptor CXCR4 in human hepatocarcinoma cells," *Biochimica Et Biophysica Acta-Molecular Cell Research,* vol. 1853, no. 5, pp. 1205-1218, May 2015.

8 Appendix

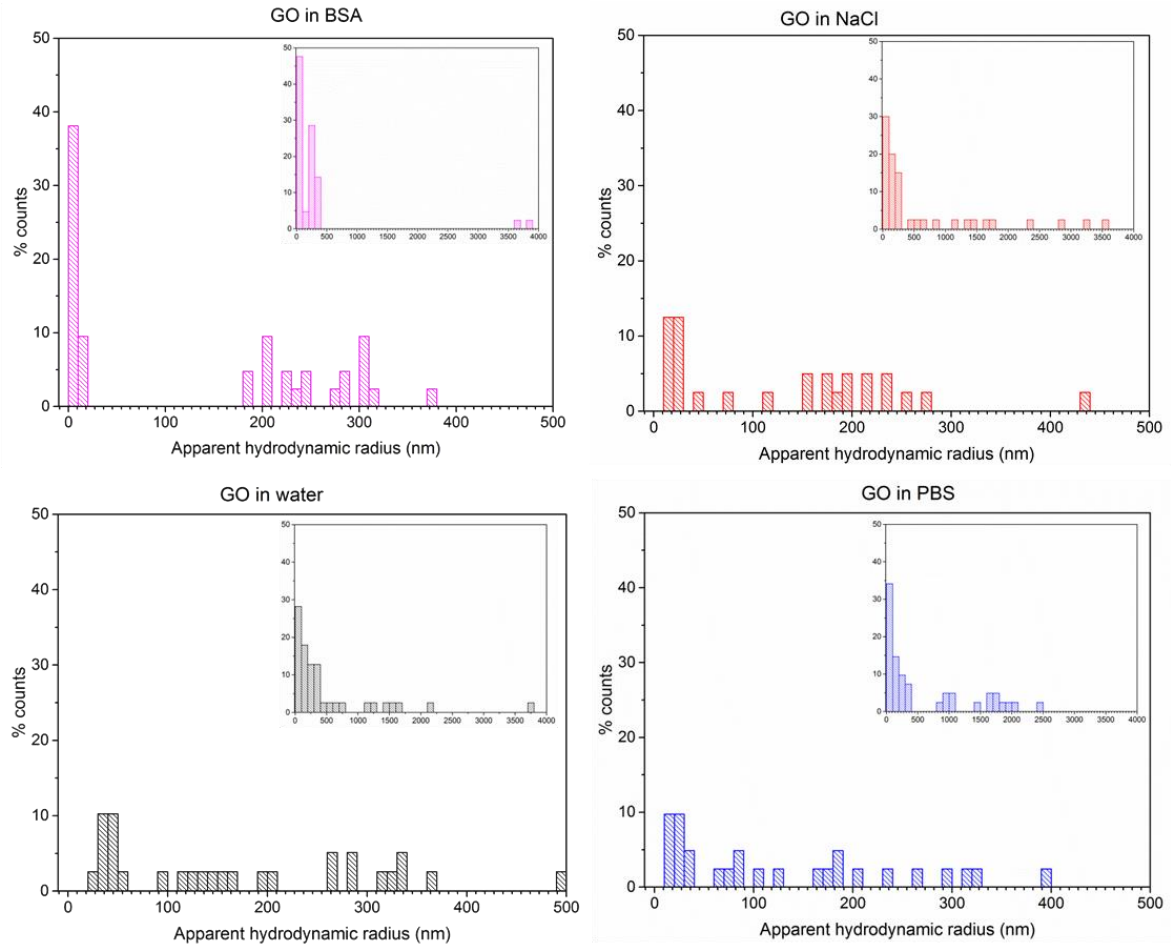

Figure 7-1 – Histograms with 10 nm binning showing the distribution of apparent hydrodynamic radii for all preparations of unwashed GO, for 0 ≤ apparent hydrodynamic radii ≤ 500 nm, with the full scale at 100 nm binning inset

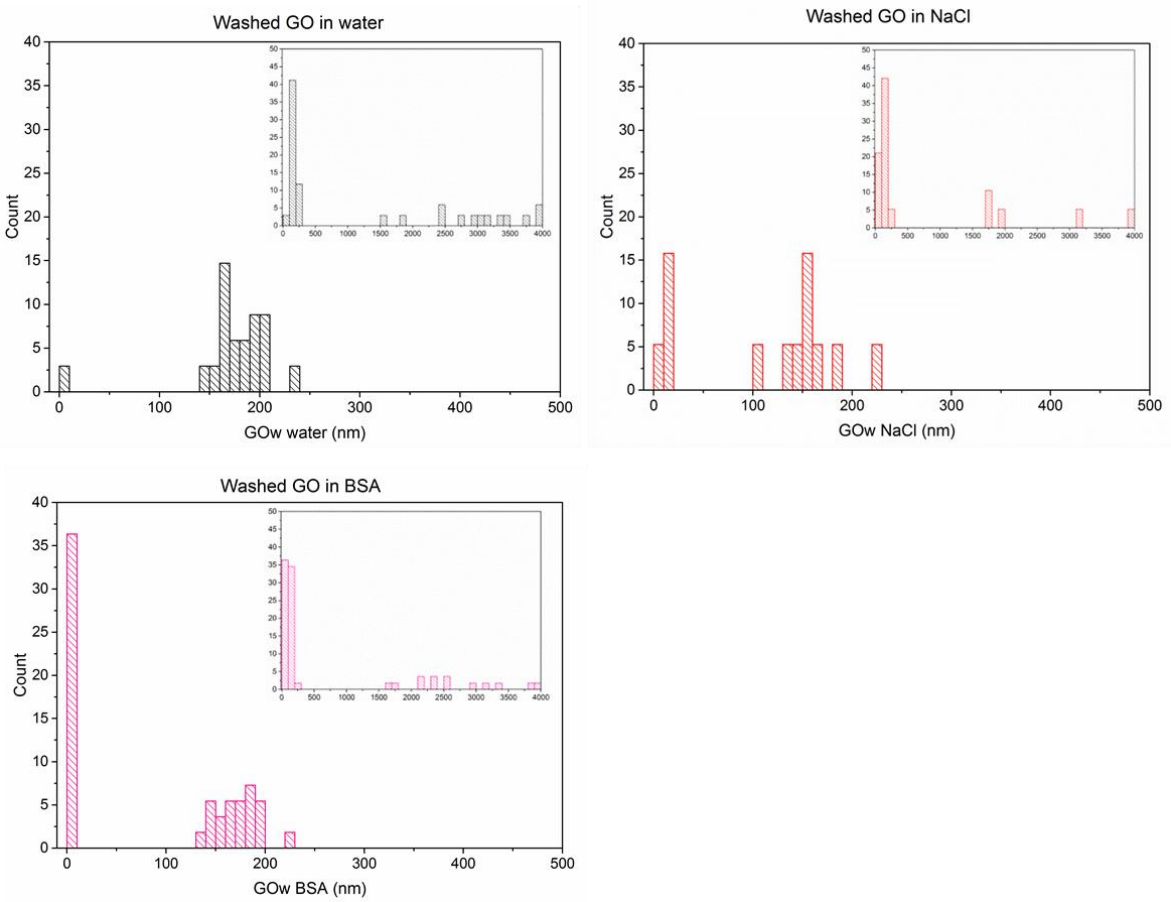

Figure 8-2 - Histograms with 10 nm binning showing the distribution of apparent hydrodynamic radii for all preparations of washed GO, for 0 ≤ apparent hydrodynamic radii ≤ 500 nm, with the full scale at 100 nm binning inset